Fakultät für
Mathematik, Informatik
und Naturwissenschaften

RWTH AACHEN
UNIVERSITY

Neural activity dynamics in experimental recordings and simulated networks

Von der Fakultät für Mathematik, Informatik und Naturwissenschaften der RWTH Aachen
University zur Erlangung des akademischen Grades eines Doktors der Naturwissenschaften
genehmigte Dissertation

vorgelegt von

Simon Essink, M.Sc.

aus

Emmerich am Rhein

Berichter: *Prof. Sonja Grün*
Prof. Björn Kampa

Tag der mündlichen Prüfung: *12.12.2023*

Diese Dissertation ist auf den Internetseiten der Universitätsbibliothek verfügbar.

NEURAL ACTIVITY DYNAMICS IN EXPERIMENTAL RECORDINGS AND SIMULATED NETWORKS

SIMON ESSINK, M.SC.

Bonn
April 2023

SUPERVISORS:

Prof. Sonja Grün
Prof. Björn Kampa
Dr. Junji Ito

Simon Essink: *Neural activity dynamics in experimental recordings and simulated networks,* An attempt to bridge disciplines in the computational neurosciences, © April 2023

EIDESSTATTLICHE ERKLÄRUNG

Ich, Simon Essink,
erkläre hiermit, dass diese Dissertation und die darin dargelegten Inhalte die eigenen sind und selbstständig, als Ergebnis der eigenen originären Forschung, erarbeitet wurden.
Hiermit erkläre ich an Eides statt:

1. Diese Arbeit wurde vollständig oder größenteils in der Phase als Doktorand dieser Fakultät und Universität angefertigt;
2. Sofern irgendein Bestandteil dieser Dissertation zuvor für einen akademischen Abschluss oder eine andere Qualifikation an dieser oder einer anderen Institution verwendet wurde, wurde dies klar angezeigt;
3. Wenn immer andere eigene oder Veröffentlichungen Dritter herangezogen wurden, wurden diese klar benannt;
4. Wenn aus anderen eigenen oder Veröffentlichungen Dritter zitiert wurde, wurde stets die Quelle hierfür angegeben. Diese Dissertation ist vollständig meine eigene Arbeit, mit der Ausnahme solcher Zitate;
5. Alle wesentlichen Quellen von Unterstützung wurden benannt;
6. Wenn immer ein Teil dieser Dissertation auf der Zusammenarbeit mit anderen basiert, wurde von mir klar gekennzeichnet, was von anderen und was von mir selbst erarbeitet wurde.
7. Ein Teil oder Teile dieser Arbeit wurden zuvor veröffentlicht und zwar in: *siehe Publikationsliste*

Bonn, April 2023

Simon Essink, M.Sc.

The brain is a world consisting of a number of unexplored continents
and great stretches of unknown territory.

— Santiago Ramón y Cajal

ABSTRACT

Empirical, data-driven approaches and theoretical, model-driven approaches to investigate the brain largely co-exist. With the intention to foster synergies, this thesis explores the intricacies of each of these two approaches.

In the first study, we investigate the neural underpinnings of eye-hand coordination by analyzing spiking activity recorded via multi-electrode arrays from behaving monkeys within the Vision-for-Action experiment. Before exploring movement-related activity along the dorsal visual stream, we follow the dataset's evolution from the raw recording data to preprocessed datasets with integrated metadata as well as spike sorting, and deal with potential artifacts by characterizing and excluding them. To isolate the effect of movement variables from simultaneously occurring behaviors (e.g., vision and eye movements) on the spiking activity of single neurons, we use Generalized Linear Models (GLMs).

In particular, we reproduce the observation of a bimodal distribution of preferred directions of neurons in M1/PMd for hand movements restricted to the horizontal plane and report similar bimodal distributions in V1/V2, DP, 7a.

In a second project, we research high-frequency oscillations ($\sim$ 300 Hz) that are predicted by simulations of biologically constrained, large-scale, spiking neural network models of a cortical microcircuit. To understand the model prediction mechanistically, we approximate the network dynamics via mean-field and linear response theory and find three network ingredients that impact the power spectrum of the population activity: the anatomical connectivity, the delay distributions, and the transfer functions. Assuming the model prediction is accurate, we argue that high-frequency oscillations should be detectable via population measures as the local field potential.

ZUSAMMENFASSUNG

Empirische, datengestützte Ansätze und theoretische, modellgestützte Ansätze zur Erforschung des Gehirns existieren weitestgehend unabhängig voneinander. Mit der Absicht, Synergien zu fördern, erforscht diese Arbeit die Feinheiten beider Ansätze.

In der ersten Studie werden die neuronalen Grundlagen der Koordination von Auge und Hand untersucht, indem Spike-Aktivitäten, die über Multielektroden-Arrays im Rahmen des Vision-for-Action Experiments in Affen aufgezeichnet wurden, analysiert werden. Bevor die bewegungsbezogene Aktivität entlang des dorsalen Sehstroms untersucht wird, wird die Entwicklung des Datensatzes von den Rohdaten bis hin zu vorverarbeiteten Daten mit integrierten Metadaten und Spike Sortings erläutert. Artefakte werden charakterisiert und entfernt. Um die Auswirkungen von Bewegungsvariablen von simultan stattfindenden Prozessen (z. B. Sehen und Bewegung der Augen) auf die Spike-Aktivität einzelner Neuronen zu isolieren, werden Generalized Linear Models (GLMs) verwendet.

Insbesondere wird die Beobachtung einer bimodalen Verteilung der bevorzugten Richtungen von Neuronen in M1/PMd für Handbewegungen, die auf die horizontale Ebene beschränkt sind, reproduziert und durch die Beobachtung einer ähnlichen bimodalen Verteilung in V1/V2, DP, 7a erweitert.

In einem zweiten Projekt werden hochfrequente Oszillationen ($\sim 300\,\mathrm{Hz}$) erforscht, die in Simulationen von biologisch eingeschränkten, großskaligen, spikenden neuronalen Netzwerkmodellen eines kortikalen Mikroschaltkreises auftreten. Um die Modellvorhersage mechanistisch zu verstehen, wird die Netzwerkdynamik durch Mean-Field- und Linear Response Theorie angenähert und es werden drei Netzwerkbestandteile ausgemacht, die die spektrale Leistungsdichte der Populationsaktivität beeinflussen: die anatomische Konnektivität, die Delay-Verteilungen und die Übertragungsfunktionen. Unter der Annahme, dass die Modellvorhersage zutreffend ist, wird argumentiert, dass hochfrequente Oszillationen über Populationsmessungen wie beispielsweise das lokale Feldpotenzial nachweisbar sein sollten.

PUBLICATIONS

The thesis at hand builds upon the following publications:

NNMT: Mean-Field Based Analysis Tools for Neuronal Network Models

by Moritz Layer, Johanna Senk, Simon Essink, Alexander van Meegen, Hannah Bos and Moritz Helias

Published in *Frontiers in Neuroinformatics*, 16, p. 835657. doi: `https://doi.org/10.3389/fninf.2022.835657`.

Parts of this publication enter Chapter 6

AUTHOR CONTRIBUTIONS

CHAPTER 2: NEUROSCIENTIFIC BACKGROUND

The author performed the literature research and wrote the chapter under the supervision of Junji Ito and Sonja Grün. Alexa Riehle and Thomas Brochier contributed valuable literature citations.

CHAPTER 3: SETUP, DATA AND PREPROCESSING

The author wrote this chapter and gathered the information presented in this chapter under supervision of Junji Ito and Sonja Grün as part of an enormous collaborative effort of the labs of Sonja Grün and Thomas Brochier.

The labs of Sonja Grün and Thomas Brochier jointly designed the experiment. The lab of Thomas Brochier set up (in particular Marcel Jan de Haan and Frédéric V. Barthélemy) and performed the experiments (Marcel Jan de Haan, Frédéric V. Barthélemy, Lucio Condro and Shrabasti Jana).

The author contributed to the preprocessing pipeline which Julia Sprenger and Alexander Kleinjohann mainly developed under the supervision of Michael Denker.

CHAPTER 4: ARTIFACTS

The author wrote this chapter. The author detected and characterized the artifacts together with Alexander Kleinjohann under the supervision of Junji Ito and Sonja Grün.

The author investigated the sources of the artifacts in close exchange with Alexander Kleinjohann, Frédéric V. Barthélemy, Regimantas Jurkus and Cristiano Köhler.

The author implemented and evaluated the proposed removal methods with Alexander Kleinjohann. Jonas Oberste-Frielinghaus and Junji Ito contributed insights into the crosstalk mechanisms and the reasoning for channel exclusions presented in Section 4.6.

Alexa Riehle and Frédéric V. Barthélemy performed the manual spike sortings. The author conducted the automatic spike sorting using SpikeInterface and applied the procedure as detailed in Section 4.6.

Results from this chapter are planned to be published.

CHAPTER 5: SINGLE UNIT ACTIVITY ANALYSIS

The author wrote this chapter, developed and implemented the analysis pipeline, visualized the results, and interpreted the data under supervision of Junji Ito and Sonja Grün. Junji Ito helped in the conceptualization of the storyline and proofread parts of the chapter. Frédéric V. Barthélemy, Thomas Brochier, and Alexa Riehle helped with insights on the behavioral data.

CHAPTER 6: SIMULATIONS AND THEIR THEORETICAL DESCRIPTION

The content of this chapter is partly reproduced from Layer et al. (2022b). Hannah Bos and Moritz Helias developed and implemented the code base and the initial version of the toolbox. Moritz Layer, Johanna Senk, and the author designed the current version of the toolbox. Moritz Layer implemented the current version of the toolbox, vectorized and generalized tools, developed and implemented the test suite, wrote the documentation, and created the example shown in Section 6.2.3.1. Alexander van Meegen improved the numerics of the firing rate integration. The author implemented integration tests, improved the functions related to the `sensitivity_measure`, and created the examples shown in Section 6.2.4. Moritz Layer, Johanna Senk, the author, Alexander van Meegen, and Moritz Helias wrote the text.

Results from this chapter are planned to be published.

CHAPTER 7: VSTRIPES — ULTRA-HIGH-FREQUENCY OSCILLATIONS IN THE MICROCIRCUIT MODEL

The author simulated the different networks, implemented the analysis and drafted the initial version of the text presented in this chapter under supervision of Sonja Grün, Markus Diesmann and Moritz Helias. Renan Oliveira Shimoura, Johanna Senk, Sacha Jennifer van Albada, Moritz Helias, Hans Ekkehard Plesser and Markus Diesmann contributed to the text. Renan Oliveira Shimoura ran analyses on the isolated V1 model from the multi-area model presented in Section 7.2.2.2.

The author co-supervised Runar Helin, who worked on this topic in his master's thesis with Hans Ekkehard Plesser. Runar Helin contributed the formalizations of the delay distribution and their impact in Section A.5.1, excluded simulation artifacts to be the origin of synchronization in Section A.5.2, and implemented initial analysis codes.

Results from this chapter are planned to be published.

Friends and family near,
Together we are stronger,
The Force is with us.

— Haiku by ChatGPT

ACKNOWLEDGMENTS

This work would not have come into being without the direct or indirect support of countless people. To adequately do justice to all the people involved and to enumerate their contributions throughout the last four years, I would probably have to write another dissertation. Nevertheless, I try to thank the main actors and apologize to all those who are not mentioned here.

First of all, there is my doctoral mother Prof. Sonja Grün, who, with a leap of faith, hired me, then gave me the freedom to formulate and pursue my own ideas and projects and, in all of this, always infected me with her enthusiasm for research.

I'd like to thank Prof. Björn Kampa for his assistance and comments during our meetings and for agreeing to act as my second supervisor.

I was also able to learn a great deal from Dr. Junji Ito, who was not only able to provide expert advice in all matters, but also intercepted my sometimes strongly and emotionally charged scientific opinions with his calm and unagitated manner, thus opening up a more rational approach for me.

In addition to this direct support, I would like to thank the whole INM-6 at Forschungszentrum Jülich, including the management by Sonja Grün and Markus Diesmann, the secretaries, the scientific coordination team, the IT and all PIs and students. I found the (deeply human) way people treat each other and the way they work together extremely pleasant and beneficial.

I don't know if it's the good leadership, the exciting research or a happy little accident, in any case, INM-6 seems to attract wonderful people and I consider myself very lucky to have been able to spend so much time with them. Without the collegial support, the doctoral doubts would certainly have become overwhelming.

Indispensable was especially Alexander Kleinjohann, with whom I fathomed all depths of electrophysiology, who always had an open ear (probably that's why he developed such an outstanding good taste in music), for whom no gravel is too coarse and who taught me the magic of shortcuts in initially painful pair-coding sessions, in addition to being the only one who knows about litscherature!

I would like to single out my compagnons from the pre-Corona office: Michael Dick, David Berling and Lorenzo Tiberi; thank you for putting up with my whining and keeping me happy with ever-elusive smells.

Although it would be necessary to unpack at least one anecdote about every single person, here, alphabetical and incomplete, more incredibly great, inspiring personalities:

Agnes Korcsak-Gorzo, Aitor Morales, Alessandra Stella, Alexander van Meegen, Anno Kurth, Barna Zajzon, Cristiano Koehler, David Dahmen, Jasper Albers, Jonas Oberste-Frielinghaus, Johanna Senk, Julia Sprenger, Kirsten Fischer, Michael Denker, Moritz Helias, Moritz Layer, Peter Bouss, Regimantas Jurkus, Renan Shimoura, Robin Gutzen, Sacha van Albada, Sven Krauße, Tobias Schulte to Brinke, Tom Tetzlaff, Younes Bouhadjar.

In the same breath as INM-6, I would also like to thank our experimental collaborators in Marseille, including Frédéric Barthélemy, Marcel de Haan, Thomas Brochier, Alexa Riehle, and my collaborators in Norway, Runar Helin and Hans Ekkehard Plesser.

Thank you, Marianna, for wandering through the V4A data with me during your master's thesis, your perseverance and consistency were impressive!

Thanks, Erik, for the intense library sessions, I really enjoyed watching you soak up information like a sponge!

Shoutout to great friends: Max F., Klausi (&SaarLorLuxis), Hubi&Melli, Simili, Holle, Luc (&Fietsetrüppchen), Paulchen, Thorsti, Max Z. (&Master Physiker), Fredi (&Nicas).

A thousand thanks to my parents, who supported me unconditionally, for the many cheering phone calls, for everything...And do you know my big brother? He's super cool! You want one like him too! Thanks, Brudi!

Maria, thanks for everything, du bisn Bötz!

CONTENTS

LIST OF FIGURES

LIST OF TABLES

ACRONYMS

EPSP	excitatory postsynaptic potential
IPSP	inhibitory postsynaptic potential
GABA	gamma-aminobutyric acid
LIF	leaky integrate-and-fire model
SUA	single unit activity
MUA	multi unit activity
SNR	signal-to-noise ratio
V4A	Vision-for-Action
MEA	multi-electrode array
NSP	neural signal processor
LGA	land grid array
LFP	local field potential
RMS	root mean square
PCA	principle component analysis
ISI	inter-spike interval
arc	arcuate sulcus

iocs	inferior occipital sulcus
itps	intraparietal sulcus
cs	central sulcus
lf	lateral fissure
ls	lunate sulcus
prs	principal sulcus
sts	superior temporal sulcus
V1	primary visual cortex
V2	secondary visual cortex
V3	tertiary visual cortex
DP	dorsal prelunate
7a	area 7a
PPC	posterior parietal cortex
M1	primary motor cortex
PMd	dorsal premotor cortex
PMv	ventral premotor cortex
F5	ventral premotor cortex
F7	pre-dorsal premotor cortex
MT	middle temporal area
MST	middle superior temporal area
SC	superior colliculus
LIP	lateral intraparietal area
FEF	frontal eye field
LGN	lateral geniculate nucleus
MD	mediodorsal nucleus
EMG	electromyography
PSD	power spectral density
GLM	generalized linear model
RF	receptive field
PD	preferred direction
OTL	optimal time lag
KDE	kernel density estimate
PSTH	peri-stimulus time histogram
BMI	brain-machine interface
RNN	recurrent neural network
BPTT	back-propagation through time
LIF	leaky integrate-and-fire

Il faut savoir que, d'une part, les plaisirs, les joies, les ris et les jeux, d'autre part, les chagrins, les peines, les mécontentements et les plaintes ne nous proviennent que de là (le cerveau). C'est par là surtout que nous pensons, comprenons, voyons, entendons, que nous connaissons le laid et le beau, le mal et le bien, l'agréable et le désagréable, soit que nous les reconnaissions par l'utilité qu'elles nous procurent, ressentant, dans cette utilité même, le plaisir et le déplaisir, suivant les opportunités, les mêmes objets ne nous plaisant pas.

— Hippocrates, 460-377 BC

1

INTRODUCTION

The brain is arguably the most complex organ of the human body, and its crucial role in our functioning has been philosophized upon since the time of the sophists in ancient Greece (Breitenfeld et al., 2014). Unlike Aristotle, who believed the heart to be the crucial organ and the brain to merely cool down the blood (Clarke et al., 1963), Hippocrates, as cited above, foresaw the brain's paramount importance.

Centuries of effort into the investigation of the brain, termed neuroscience, enlightened us with insights into basic human capabilities ranging from the instincts of breathing and sleeping via sensory perception and movement control to complex emotions and social interactions.

Modern neurosciences reflect the demand to advance understanding of this fascinating multi-scale organ through various approaches on different spatial and temporal scales, synthesizing insights from physics, biology, medicine, and psychology research. However, it is unclear which line of research brings us closer to unraveling the brain's mysteries. Can we merely rely on fMRI studies of the BOLD signal in humans to understand which brain regions activate during a specific task? Is it crucial to first explain the membrane potential of a single neuron in the behaving fruit fly to comprehend the mechanisms behind Alzheimer's disease?

Within the scope of this thesis, we deal with projects located in two subfields: Systems neuroscience and computational neuroscience.

Common to both systems and computational neuroscience is, however, the assumption that the basic building block constituting the brain is the neuron. This point of view was established in the late 19th century due to Golgi (1873), who invented the silver-staining of neural tissue and Ramón y Cajal (1888), who used such stainings for astonishingly detailed drawings of single neurons, but also intricate networks thereof. Both received a joint Nobel prize in 1906 for their contributions.

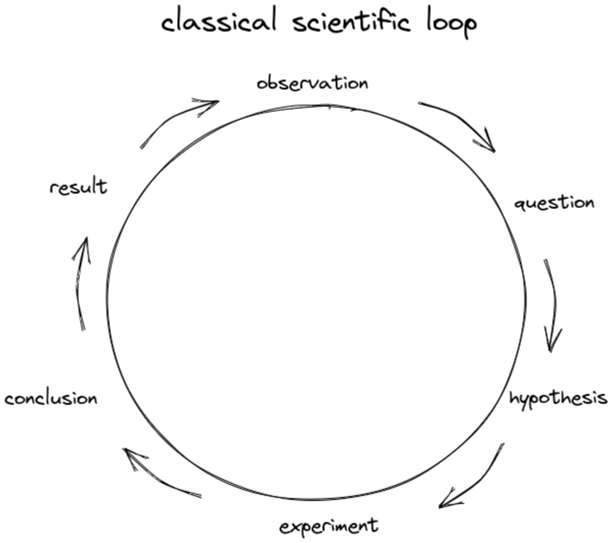

Figure 1.1: Illustration of the scientific loop.

But while systems and behavioral neuroscience focus on understanding brain subsystems and their functions through experiments and therefore follow a top-down approach, computational neuroscience, younger and steadily advancing with computing technology, utilizes simulations and theoretical descriptions to achieve a mechanistic, bottom-up understanding of experimental findings. In their common quest — understanding how the brain works —, they have a symbiotic history, these subfields remain separate (De Schutter, 2008) due to increasing specialization and complexity. Yet, the need for integrative approaches that combine experimental and computational techniques is of utmost importance.

Arguing in favor of this hypothesis, consider the scientific loop as depicted in Figure 1.1, which represents an idealization of the scientific process. The observation of an unknown feature in experimental data, a prediction from simulations, or analytical descriptions lead to a question that can be formulated as a falsifiable hypothesis. An experiment must be designed to test this hypothesis, which can be performed in vitro (including computational approaches) or in vivo. The obtained knowledge is then converted into a result, which can lead to new observations depending on the outcome.

The reality is that the brain is analyzed in diverse scientific subfields, and the gaps between the research directions are significant, making it difficult for researchers to communicate across communities and keep track of all the findings. Progress in experimental possibilities allows simultaneous recording from multiple brain regions, while systematic examinations of connectivity and neuron densities enable biologically realistic simulations.

However, while experiments explore functional relationships, simulations have not yet reached the same level. Reconciliation between experiment and simulation/theory is crucial for advancing our understanding of the brain.

This thesis presents two lines of projects that, if treated independently, would each be considered to belong to just one subfield, either experimental neuroscience or computational/theoretical neuroscience. For one part, we will dive deep into an experimental setup, preprocess the data, investigate behavioral data, and relate it to neuronal activity in specific macaque brain regions. For the other part, we will perform simulations of spiking neural networks and examine the network dynamics using theoretical tools.

The goal of combining these projects into one thesis is to understand the intricacies of each of the two research approaches to finally bridge the gap between them, profit from this synergy, and eventually gain a more comprehensive understanding of how the brain works.

Next, we will briefly establish the prerequisites that are needed for the following chapters. The focus lies on the basic building block of the brain: the neuron.

1.1 PREREQUISITES

The brain consists of two categories of cells: neurons and glia. While neurons are believed to play a key role in the brain's functioning, the glia's role is less clear and is often attributed a mere supporting function.

1.1.1 *The neuron*

Neurons communicate through electrical and chemical signals transmitted between neurons at connection points, the *synapse*. As depicted in Figure 1.2, a neuron consists of a cell body, the *soma*, the signal-receiving branches, the *dendrites*, and outward projecting branches, the *axons*. Signals are received at the dendrites, integrated at the cell body, and propagated down the axon as an action potential. The *axon terminal* may connect with a synapse or a muscle. *Myelin* sheets, which cover the axons intermitted with gaps, known as *nodes of Ranvier*, insulate the "cable" and allow for faster conduction speeds of a signal (Purves et al., 2018).

THE ACTION POTENTIAL The *action potential* (see Figure 1.3), also commonly called *spike*, is a large yet brisk ($\sim 1-2\,\mathrm{ms}$) deflection of the membrane potential that is generated at the part of the cell body called the *axon hillock* if sufficiently many incoming signals add up to cross a certain threshold.

The membrane potential is the difference in ion concentration between the inside and outside of a neuron. At rest, the membrane potential is around $-70\,\mathrm{mV}$, governed by the Nernst potential that

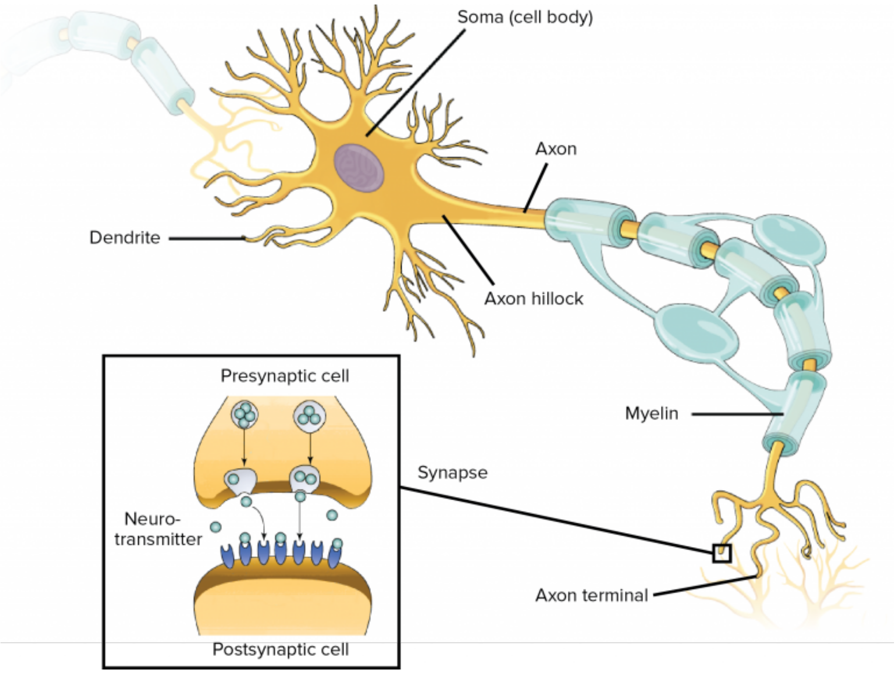

Figure 1.2: Sketch of a neuron. Image from "Neurons and glial cells" in Clark et al. (2018) licensed under Creative Commons Attribution License v4.0.

describes the equilibrium potential for a given ion type. The cell membrane consists of a lipid bilayer with many ion channels (e.g., voltage-gated) and ion pumps (Kandel et al., 2013; Purves et al., 2018) and thus allows for the exchange of ions if the channels are open or at the expanse of energy to engage the pumps. Relevant ions involved in neuronal signaling are potassium (K^+), sodium (Na^+), chloride (Cl^-), and calcium (Ca^{2+}) (Purves et al., 2018).

Depolarization is the process by which the membrane potential becomes more positive. This can occur through incoming signals, which might add up, if sufficiently synchronized. If the excitation threshold is exceeded, a cascade of events follows: voltage-gated ion channels open, leading to complete depolarization (peak action potential) until Na^+-channels close repolarization (Kandel et al., 2013). The Na^+ channels stay closed for a certain amount of time, preventing further action potentials called the *refractory period*.

When a neuron receives a signal, sodium channels in the membrane open and allow positively charged sodium ions (Na^+) to flow into the cell, which depolarizes the membrane and triggers the action potential. As the membrane potential becomes more positive during depolarization, potassium channels open and allow positively charged potassium ions (K^+) to flow out of the cell, which repolarizes the membrane and returns it to its resting potential.

THE SYNAPSE AND NEUROTRANSMITTERS Synapses typically connect the axon terminal of a presynaptic neuron with the dendritic spine of a postsynaptic neuron (see inset in Figure 1.3). There are two types of synapses: chemical and electrical. Chemical synapses involve the release of neurotransmitters from the presynaptic neuron in the synaptic cleft, which then bind to receptors on the postsynaptic neuron. Electrical synapses involve direct communication between neurons through gap junctions.

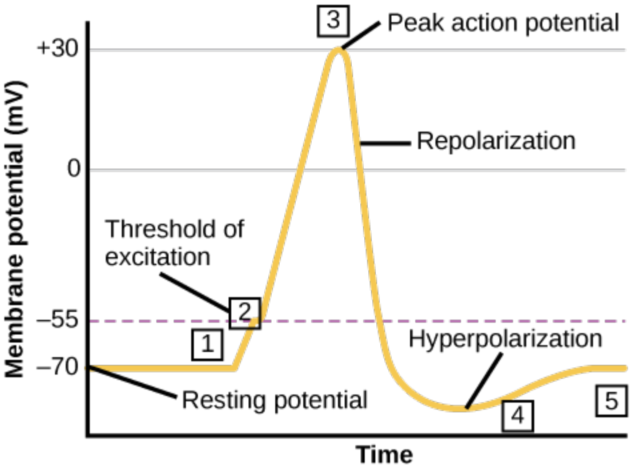

Figure 1.3: Sketch of an action potential. Image from "Neurons and glial cells" in Clark et al. (2018) licensed under Creative Commons Attribution License v4.0.

At chemical synapses, calcium ions (Ca^{2+}) are involved in triggering the release of neurotransmitters from the presynaptic neuron. When an action potential reaches the end of an axon, it triggers calcium channels to open and allows calcium ions to flow into the cell. This influx of calcium then leads to a fusion of vesicles containing neurotransmitters with the membrane. It causes the release of neurotransmitter molecules from the axon terminal into the synaptic cleft. The released neurotransmitters then diffuse across the synaptic cleft and bind to specific receptors on the postsynaptic membrane, triggering a response in the postsynaptic neuron.

Neurotransmitters can have excitatory or inhibitory effects on the postsynaptic neuron, depending on the specific receptor subtypes they bind to. Depolarization results in an excitatory postsynaptic potential (EPSP), while hyperpolarization leads to an inhibitory postsynaptic potential (IPSP). There is a transmission delay of roughly 1 ms caused by chemical transmission (Clark et al., 2018). Furthermore, the unidirectional nature of synaptic transmission allows for complex information processing in the brain (Kandel et al., 2013). Common neurotransmitters observed in the brain are glutamate (acting excitatory), gamma-aminobutyric acid (GABA) (inhibitory), acetylcholine (excitatory), dopamine (both excitatory and inhibitory), and serotonin (both excitatory and inhibitory).

Electrical synapses are far less common than chemical synapses but involve direct communication between neurons through gap junctions. These synapses allow for faster communication than chemical synapses (Connors et al., 2004).

EXTRACELLULAR ELECTROPHYSIOLGY Electrodes that are sufficiently sensitive and located in the neural tissue can detect the deflections caused by action potentials of nearby neurons. Unlike intracellular recordings, which require placing an electrode inside a neuron (or on the membrane —called patch-clamping), extracellular recordings detect the electrical signals that neurons emit into the extracellular space.

Extracellular recordings can be done using several types of electrodes, including single-wire electrodes, multi-wire electrodes, and microelectrode arrays. The choice of electrode depends on the specific experiment and the desired level of spatial resolution.

Nowadays, extracellular recordings can be used to study the activity of many neurons simultaneously. To understand how groups of neurons work together to generate behavior or process information. Additionally, extracellular recordings can be done in awake, behaving animals, which allows researchers to study neural activity under naturalistic conditions (see Chapter 3).

DIVERSITY OF NEURON TYPES The brain contains an incredibly diverse array of neuron types, each with their unique properties and functions. Neurons vary widely in shape (unipolar, bipolar, multipolar), size, and connectivity. This diversity is critical for enabling the complex computations and behaviors characteristic of the brain. Two large research consortia that have recently been working to uncover this diversity's full extent are The Blue Brain Project (Erö et al., 2018) and the Allen Institute for Brain Science (Sunkin et al., 2012). By combining cutting-edge techniques like whole-cell patch clamping and single-cell RNA sequencing, these projects are helping to catalog and categorize the many different types of neurons found in the brain.

GLIA CELLS Glia cells are non-neuronal cells that are believed to play a crucial role in supporting neural tissue. These cells provide structural and functional support to neurons by maintaining the extracellular environment necessary for neuronal function. Glia cells participate in the formation and maintenance of synapses, facilitate the transmission of nerve impulses, and regulate the chemical composition of the extracellular fluid. Recently, evidence for a potential functional role of astrocytes has been accumulated (Delepine et al., 2023; Rasmussen et al., 2023).

1.1.2 *Neuron models*

The biological, chemical, and physical details of an action potential generation for a single neuron, starting from signal reception at the synapse to the cascades of ion flux in and out of the cell, are fascinating. However, it is crucial to find a level of modeling that is simple and at the same time describes the desired phenomena sufficiently well. In practice, the trade-off gave rise to a zoo of different models (Herz et al., 2006).

In computational neurosciences, different complexity levels are required. A single neuron's dynamics must be simple enough and computationally efficient to simulate large-scale networks. These, in turn, allow us to study phenomena that emerge only due to the interaction of many neurons. Thus, biological details (likely) can be reduced to a minimum as in binary neurons or, already more advanced, the leaky integrate-and-fire (LIF) (Gerstner et al., 2014), which will be introduced below.

However, if the dynamics of the membrane potential of a single neuron recorded via whole-cell patch clamping are to be explained, more complex models are necessary. Representatives of such models are the rather complicated Izhikevich model (Izhikevich, 2003) and the famous Hodgkin-Huxley model (Hodgkin et al., 1952).

LEAKY INTEGRATE-AND-FIRE (LIF) Neurons can be understood as input-output devices based on their basic components (dendrites, soma, axon). The LIF neuron model describes the dynamics of the membrane potential via a system of coupled differential equations

$$\tau_m \frac{dV(t)}{dt} = -V + R_m I(t) \quad , \tag{1.1}$$

$$\tau_s \frac{dI(t)}{dt} = -I(t) + \tau_s \eta(t) \quad . \tag{1.2}$$

with V denoting the membrane potential, R_m the membrane resistance, τ_m the membrane time constant and $I(t)$ the time-dependent incoming synaptic current induced by the input $\eta(t)$. The membrane time constant and resistance are related to the membrane capacitance through $C_m = \frac{\tau_m}{R_m}$. The membrane potential is rescaled to zero in the absence of inputs. The dynamics of the synapse are here defined as an exponential post-synaptic current.

The firing mechanism is included in the LIF as follows: When $V(t)$ reaches the threshold potential $V_{\text{threshold}}$, the membrane potential is clamped to the reset potential V_{reset} for a refractory period τ_{ref}. After the refractory period the membrane potential evolves according to the equations again. The reaching of the threshold with subsequent depolarization corresponds to one action potential (or spike).

1.1.3 *Large-scale organization*

Neurons form connections, and the density of neurons is different across areas and layers of the *cortex*, the outer sheet of the brain. This can be visualized through staining techniques such as done by Golgi as well as Cajal Golgi (1873) and Ramón y Cajal (1888). Stereotypical connections between and within layers are found throughout the cortex (Mountcastle, 1997). The cortical column, proposed by Mountcastle, is a basic unit of cortical organization and is often referred to as a *microcircuit*.

1.1.4 *Information encoding hypotheses*

The way that neurons encode and communicate information is one of the fundamental questions in neuroscience that remain unresolved, despite the fact that spikes are regarded as the fundamental components of neural communication.

Based on the observation that multiple inputs are required for a neuron to cross its threshold potential, two major theories have emerged. The first theory, known as rate coding, proposes that information is encoded in the modulation of a neuron's firing rate (Georgopoulos et al., 1982; Hubel et al., 1962; Shadlen et al., 1994), as opposed to the precise timing of individual pulses. The second theory, temporal coding (Abeles et al., 1994; Gautrais et al., 1998; Torre et al., 2016), suggests that precise spike timing and coordination between neurons on a shorter timescale play a crucial role in information encoding and processing. Recent studies suggest that both mechanisms may coexist in the brain, despite the fact that these two hypotheses are often viewed as exclusive alternatives. Additional theories, including population coding and sparse coding, have been proposed to explain neural coding.

1.2 ORGANIZATION OF THE THESIS

In the introduction, I already stated that I will present research from two distinct neuroscience subfields. Indeed, writing this thesis proved difficult: If I had condensed the breadth of prior knowledge that I deemed necessary for the reader to have into one single "Neuroscientific Background" chapter, this would have had a sedative effect exceeding that of commonly used anesthetics.

To keep the overall introduction short, only the most crucial background is supplied here. Each of the thesis' two parts — Part i and Part ii —, introduces its own neuroscientific background (Chapter 2 and Chapter 6).

1.2.1 *Research questions*

The two research questions that guided my work are:

1. Is the bimodality of the distribution of preferred directions (PDs) that has been observed in primary motor cortex (M1) and dorsal premotor cortex (PMd)/ventral premotor cortex (PMv) also present in the parietal and visual cortex of macaque monkeys that perform a visually guided reaching task?
2. Are oscillatory synchronizations of the spiking activity observed as vertical stripes of raster diagrams in simulations of a microcircuit model composed of LIF neurons a valid prediction of the model? Should they be observable in experimental data, and can we mechanistically understand them?

Besides having the overarching aim to bridge between disciplines, I worked on projects that are deeply rooted in the research agenda of the INM-6 at the Forschungszentrum Jülich. Here, I will briefly motivate each research question and then present the outline.

1.2.2 *Systems neuroscience question*

Let us, for a moment, imagine the voluntary act of brushing your teeth in the morning: You enter the bathroom with the intent to brush your teeth — you learned that maintaining dental hygiene is important —, move towards the sink, focus your eyes on the toothbrush and initiate a movement towards it. The movement starts with pure reaching and ends with a grasp of the brush. Even without conscious thought, somehow, you estimate the distance between your current hand position and the brush correctly, activate the correct sequence of muscles in the shoulder, elbow, and hand, and finally adjust the position of your fingers so that the grasp is secured by applying the necessary amount of grip force. After that, you make a swift eye movement (saccade) targeted at the toothpaste, grasp it with the other hand, demonstrate tremendous coordination by screwing it open while holding the toothbrush in the other hand, and eventually squeeze the right amount of paste on the brush. After placing the toothpaste back, you move the toothbrush to your teeth and start scrubbing.

Due to the visual feedback from the mirror and a sense of the posture of your arm with respect to the body (proprioception), you manage to guide it to the mouth instead of your nose.

Several senses are involved in performing this seemingly simple task, and thus it is apparent that not just one brain area governs the neural basis of this process.

Hand-eye coordination is a crucial component of our everyday behavior. The Vision-for-Action (V4A) experiment aims to probe the neural mechanisms that govern hand-eye coordination. Previous research suggests that in the brain, besides the visual and motor cortices, areas in the dorsal visual stream play a crucial role in this process.

BRIEF DESCRIPTION OF THE EXPERIMENT In the Vision-for-Action (V4A) experiment, rhesus monkeys (*macaca mulatta*) are trained to perform various visually guided hand movement tasks.

Extracellular neural activity is recorded simultaneously with four Utah arrays with 32 electrodes each inserted in the primary visual cortex (V1), secondary visual cortex (V2), dorsal prelunate (DP) and area 7a (7a), and one array of 96 electrodes in the primary motor cortex (M1)/dorsal premotor cortex (PMd). A two-joint (shoulder and elbow) robotic exoskeleton system is used to record the monkey's arm and hand movements. It restricts movements to a 2D horizontal plane. Eye movements are recorded via an infrared light source and camera. Furthermore, a head-fixation mask was used to ensure the head position's stability.

PURPOSE OF THE EXPERIMENT With neural activity recorded from areas along the dorsal visual stream and the motor cortex and behavioral recordings from the arm and eye during tasks that allow for naturalistic behavior, this dataset yields a reach platform for various investigations.

This multi-purpose nature of the data from the V4A experiment is exciting yet challenging to analyze. Rough research ideas immediately meet the eye, such as:

- Can we observe interarea coordination?
- How is visual input transformed into motor output?
- What do the areas in posterior parietal cortex (PPC) encode?

Some of the above and more questions were tackled during my exploration of the data, yet I deemed them not conclusive enough to be included here (see dashed circles on the left in Figure 1.4).

BIMODALITY OF PREFERRED DIRECTION Literature research revealed a phenomenon observed in the community of motor control: Single neurons in M1 encode the direction of hand movement in their firing rate. The direction of hand movement that leads to maximal firing is termed the PD (Georgopoulos et al., 1982). Across many recorded neurons, the distribution of PDs was assumed to be uniform. Indeed for movements in 3D, this was confirmed (Caminiti et al., 1990; Schwartz et al., 1988) with a notable exception by Naselaris et al. (2006). However, for movements constrained to 2D, as in the V4A experiment, this distribution of PDs showed a systematic bias (Scott et al., 2001b, 1997) that could be traced back to the biomechanics of the arm (Codol et al., 2023; Lillicrap et al., 2013; Verduzco-Flores et al., 2022). Unexpectedly, in addition to M1, the same bimodality could also be observed in neurons from premotor areas (Suminski et al., 2015).

Given these observations and the recorded datasets of the V4A experiment, we hence ask:

Is the bimodality of the distribution of PDs that has been observed in M1 and PMd/PMv also present in the parietal and visual cortex of macaque monkeys that perform a visually guided reaching task?

1.2.3 *Computational neuroscience question*

Richard Feynman's famous quote aptly summarizes the physicist's approach to ensuring proper understanding of a matter "What I cannot create, I do not understand".

BALANCED NETWORKS In line with this tradition, computational neuroscientists have not stopped at realistically modeling single neurons (see Section 1.1.2) but went beyond to build models composed of individual neurons (e.g., binary neurons (van Vreeswijk et al., 1996)) whose population neural activity statistically resembles what is observed in experimental data. In particular, networks were found to exhibit "realistic" (neither too high firing rates nor silent) spiking activity statistics if excitation and inhibition are in balance (Amit et al., 1997b; Brunel, 2000; van Vreeswijk et al., 1998).

THE MICROCIRCUIT MODEL While very successful and exhibiting features like efficient information processing and noise robustness associated with biological neural networks, these artificially balanced networks were only weakly constrained by known biological data. One answer to this issue is data-constrained spiking neural networks (Shimoura et al., 2021): Technical advances nowadays allow for the measurement of anatomical data (e.g., layer resolved (excitatory/inhibitory) neuron densities connection probabilities between neuron population) or even morphological data of neurons.

The Potjans-Diesmann model (Potjans et al., 2014a), developed at our institute, aims at modeling a layered cortical microcircuit of 1 mm^2 with 4 layers (L23, L4, L5, L6) with a total of 77169 neurons. Each layer consists of one excitatory and inhibitory population. The connectivity between the different populations is derived from experimental data. The single neurons are modeled as LIF. Crucially, the density of neurons in this model is large enough such that the majority of inputs to a neuron originate in the model and thus reduce the assumptions that are required on externally supplied background activity.

The model successfully reproduces layer and population-specific firing rates as observed in vivo experiments. Yet, raster diagrams of the spiking activity that it generates display population (and even

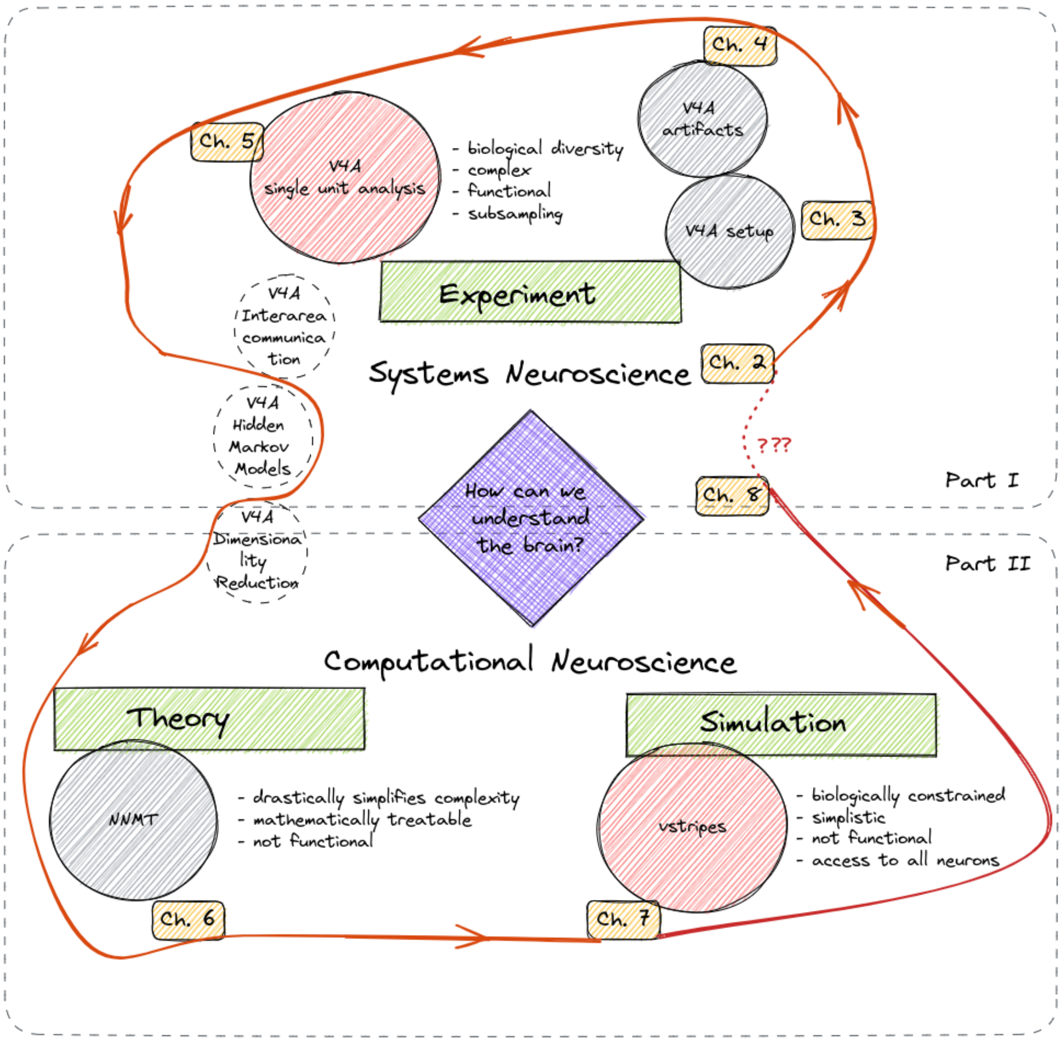

Figure 1.4: Projects overview. Grey-circled chapters are merely the means to the red-circled chapters. The dashed and white circles are open projects not presented in this thesis.

model-wide) synchronizations that have, up to now, not been observed in vivo. Hence, we ask ourselves:

Are oscillatory synchronizations of the spiking activity observed as vertical stripes of raster diagrams in simulations of a microcircuit model composed of LIF neurons a valid prediction of the model? Should they be observable in experimental data, and can we mechanistically understand them?

1.2.4 *Outline*

After having motivated the two guiding questions, let us have a look at the structure of this document by following the red thread in Figure 1.4.

In the first part (Part i), we delve into the analysis of electrophysiological data from the V4A experiment, beginning with a systems neuroscience review in Chapter 2, which includes information on the macaque brain anatomy, the visual system, motor control and the PPC. Being equipped with new knowledge, details on the setup, the recorded data, subjects and tasks, and the preprocessing pipeline that renders the data accessible for analysis will be explained in Chapter 3. In the early stages of our data analysis, we encountered potential artifacts that will be characterized and (at least partly) dealt with in Chapter 4 before we can tackle our research question in Chapter 5.

The second part (Part ii) starts with a presentation of a theoretical description of spiking neural networks (Chapter 6) and then investigates the ultra-high-frequency oscillations in the microcircuit model in Chapter 7.

Lastly, in Chapter 8, we summarize the results, discuss what we learned, and dare to give an outlook — now that we have gained insights from and even contributed to two fascinating neuroscience research directions.

Part I

ANALYSIS OF ELECTROPHYSIOLOGICAL DATA FROM THE VISION-FOR-ACTION EXPERIMENT

Our knowledge can only be finite,
while our ignorance must necessarily be infinite.

— Karl Popper

2

NEUROSCIENTIFIC BACKGROUND — SYSTEMS NEUROSCIENCE

This part of the thesis presents the analysis of data from the Vision-for-Action (V4A) experiment.

In this chapter, I supply an overview of the neuroscientific background that I consider relevant for interpreting this dataset.

The control of limb movements requires the coordination of sensory information and therefore engages multiple neuronal structures. In visually guided reaching tasks, vision is the primary sense that needs to be processed; hence, eye movements are necessary. In this section, we briefly review foundational knowledge of the visual system, the circuitry involved in saccade generation, the neural basis for motor control, the role of the posterior parietal cortex (PPC), and finally, concepts on their interaction in eye-hand coordination.

Most of the mentioned studies involve primates or humans if not stated otherwise.

We start with a brief description of the macaque brain anatomy and specify the locations of our recordings sites, which shall serve as an orientation during the subsequent discussion on important literature.

2.1 MACAQUE BRAIN ANATOMY

The cerebrum of the rhesus macaque, analogous to the human cerebrum, consists of two hemispheres connected via the corpus callosum. Historically, a subdivision into four different lobes according to prominent sulci or fissures (see Figure 2.1), as well as functional differences, has prevailed: The frontal lobe, the temporal lobe, the parietal lobe, and the occipital lobe (Gray et al., 1918; Kandel et al., 1991).

A substantial part of the occipital lobe is composed of visual areas. Visual stimuli that hit the retina in the back of the eye evoke neural signals that travel via the corpus callosum to the contra-lateral hemisphere and then via the lateral geniculate nucleus (LGN) in the thalamus to the visual cortex. In the visual cortex, the visual stimuli traverse the visual hierarchy (see Felleman et al. (1991)), starting with the primary visual cortex (V1), also called the striate cortex, followed by the secondary visual cortex (V2), then higher areas, and eventually, the temporal and parietal lobe.

The terms ipsilateral and contralateral refer to whether something (such as a stimulus, body component, or movement) on one side of the body is processed by the same or opposite hemisphere of the brain. Thus, the processing of vision occurs in the contralateral hemisphere.

Two distinct visual pathways associated with disparate functions have been proposed (Goodale et al., 1992a; Ungerleider et al., 1982): The ventral stream, also called the "What" or "Vision-for-Recognition" pathway, and the dorsal stream, also called the "Where", "How" or "Vision-for-Action" pathway.

The dorsal stream leads via the extrastriate visual cortices (e.g., V2, V3) and the prelunate gyrus, the gyrus anterior to the lunate sulcus (ls), to the posterior parietal cortex (PPC). The area called dorsal prelunate (DP), which will be relevant later on, is located on the medial part of the prelunate gyrus.

The PPC involves areas posterior to the postcentral gyrus, the gyrus posterior to the central sulcus (cs), with several somatosensory areas, and anterior to the superior temporal sulcus (sts). Within PPC, it is common to distinguish between the superior parietal lobule and the inferior parietal lobule, which lie medial and lateral with respect to the intraparietal sulcus, respectively. The area 7a (7a), another area of importance in the following, is located on the medial end of the gyrus between the superior temporal sulcus (sts) and intraparietal sulcus (itps).

In the frontal lobe, the primary motor cortex (M1) and the adjacent dorsal premotor cortex (PMd) and ventral premotor cortex (PMv) are located anterior to the central sulcus (cs). Several brain areas, more rostral to that, belong to the prefrontal cortex.

Having this rough overview in mind, we start the neuroscientific background with a brief description of the visual system.

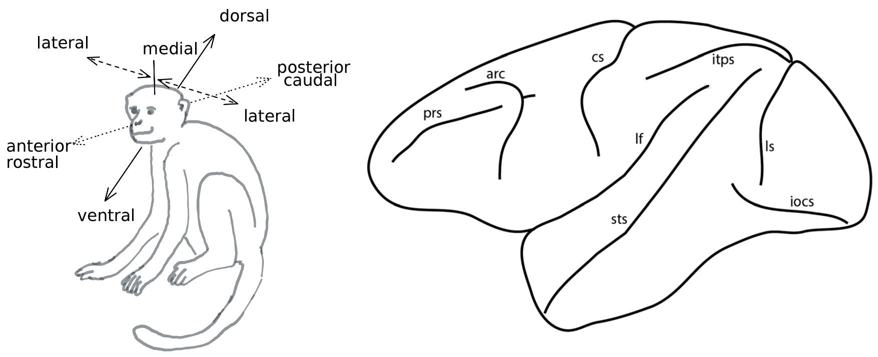

Figure 2.1: Left: Sketch of a monkey illustrating directional references that are commonly used to describe the brain anatomy. Right: Lateral view of the macaque monkey brain with sulci. Abbreviations: arc: arcuate sulcus, iocs: inferior occipital sulcus, itps: intraparietal sulcus, cs: central sulcus, lf: lateral fissure, ls: lunate sulcus, prs: principal sulcus, sts: superior temporal sulcus. Reproduced with permission from Springer Nature from Figure 5 in Rushmore et al. (2021).

2.2 THE VISUAL SYSTEM

The primate body perceives light emitted or reflected from objects in the three-dimensional world through the eye. It serves as a lens that projects incoming photons onto the retina at the back of the eye. Each area in the visual field maps a specific location on the retina; this is called visuotopic (or retinotopic) mapping. In the visual system, a neuron's receptive field (RF) is the portion of the visual field that excites it (Kuffler, 1953).

Eccentricity is the angular distance of a visual stimulus from the focus of vision. The density of cones is highest at the fovea, the center of vision, then decreases for larger eccentricity. Rod density, in contrast, peaks for $\sim 25^\circ$ eccentricity (Curcio et al., 1990; Wells-Gray et al., 2016), which explains why the dimmest stars on the night sky always seem to evade the focus of vision.

The retina consists of cones and rods, the photoreceptors. While cones react to colored light in specific wavelengths (similar to the RGB color space axes), rods are responsible for vision in dim light. After processing in the inner and outer nuclear layers, the photoreceptor activity is essentially compressed and converges into retinal ganglion cells whose axons constitute the optic nerve (Kandel et al., 2013). Per eye, this optic nerve connects to the optic chiasm, where the fibers cross from one hemisphere to the other. From here on, the visual signals are processed contralaterally, e.g., the right hemifield perceived by the right eye, is processed in the brain's left hemisphere.

From the optic chiasm, the optic nerve projects to the lateral geniculate nucleus (LGN), a structure located in the thalamus that sends axons to the primary visual cortex (V1). Different layers of the LGN relay the ipsi- and contralateral visual signals of the same hemifield and innervate with different layers in V1.

2.2.1 *Visuotopic mapping*

Neurons in the primary visual cortex (V1) exhibit a visuotopic mapping. Analogously to the density of photoreceptors in the retina, the center of vision is represented by the largest cortical volume with neurons that have small, precise, RFs. The larger the eccentricity of the visual field, the smaller the part of V1 that represents it, and the larger the corresponding RFs (Kandel et al., 2013). The visuotopic organization of visual cortex is illustrated in the maps in panels B and C of Figure 2.2.

Besides the visuotopic mapping, neurons in V1 are organized in cortical columns that are selective to the orientation and direction of moved edges (Hubel et al., 1959), receive predominantly input from one eye (ocular-dominance), vary in color preference and exhibit patchy, lateral connections to other nearby columns.

2.2.2 *Hierarchical structure*

The connectivity between visual areas follows a hierarchical structure (Felleman et al., 1991). V1, also called striate cortex, in this classical picture projects to V2, which in turn projects to tertiary visual cortex (V3), both accounted to be extrastriate areas. With each step in the hierarchy, single neurons encode more complex features of the visual scene. One factor that enables this is convergence; many neurons of V1 project to fewer neurons in V2 and so on.

This hierarchy, furthermore, seems to be split into two pathways, the dorsal and the ventral pathway Figure 2.2D. Interestingly, these two pathways largely overlap with the two parallel pathways that originate with two distinct types of ganglion cells (parvocellular and magnocellular) in the retina, are processed in particular layers at the level of LGN, and project to different parts of layer IV in V1 (Medathati et al., 2016; Yoonessi et al., 2011).

There are feedforward and feedback connections to other areas (Wang et al., 2022b) which are shown to be layer dependent (Rockland, 2022; Rockland et al., 1979).

Influential theories inspired by the hierarchical anatomy and function of the visual system, whose details are out of the scope of this little review, have been proposed and lead to ideas on convolutional neural networks and eventually deep learning (Fukushima, 1988; LeCun et al., 2015; Marr, 1982).

High-resolution vision is only possible due to the high cone density in the fovea. Eye movements are necessary to bring objects of a visual scene into the fovea.

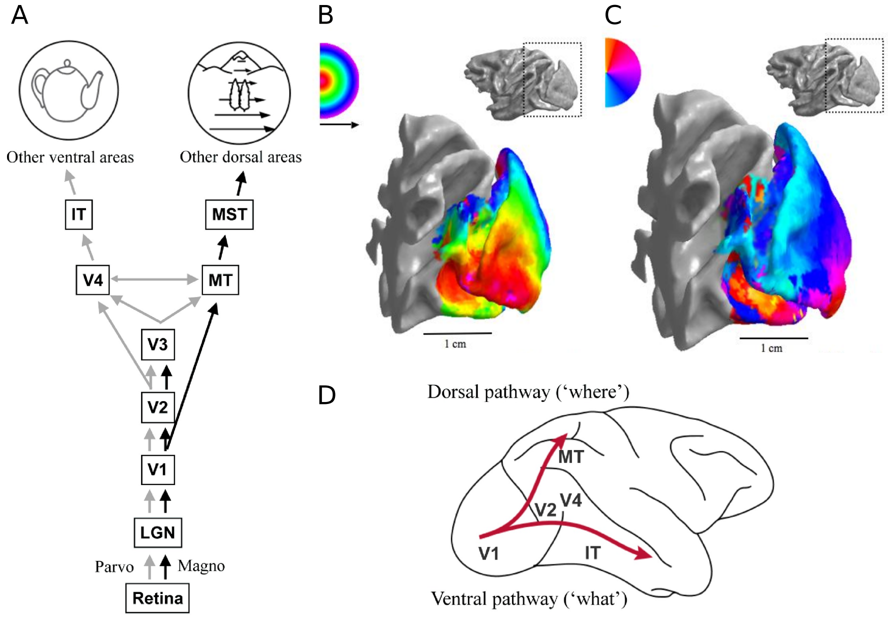

Figure 2.2: Illustrations on the visual system. A: Block diagram of the main nodes involved in the two visual pathways. Gray arrows indicate the ventral pathway, which coincides with the parvocellular pathway, and similarly, black arrows indicate the dorsal pathway (magnocellular). The figure is taken from (Medathati et al., 2016). B: Radial and C: angular component of the retinotopic maps in the macaque visual cortex, color codes as shown in the insets. Figures reused with permission from Prof. Brian Wandell, whose Lab distributed them as displayed in Prof. Heeger's lecture using data from (Brewer et al., 2002; Dougherty et al., 2003). D: Brain sketch illustrating the two visual pathways. Figure taken from (Medathati et al., 2016)

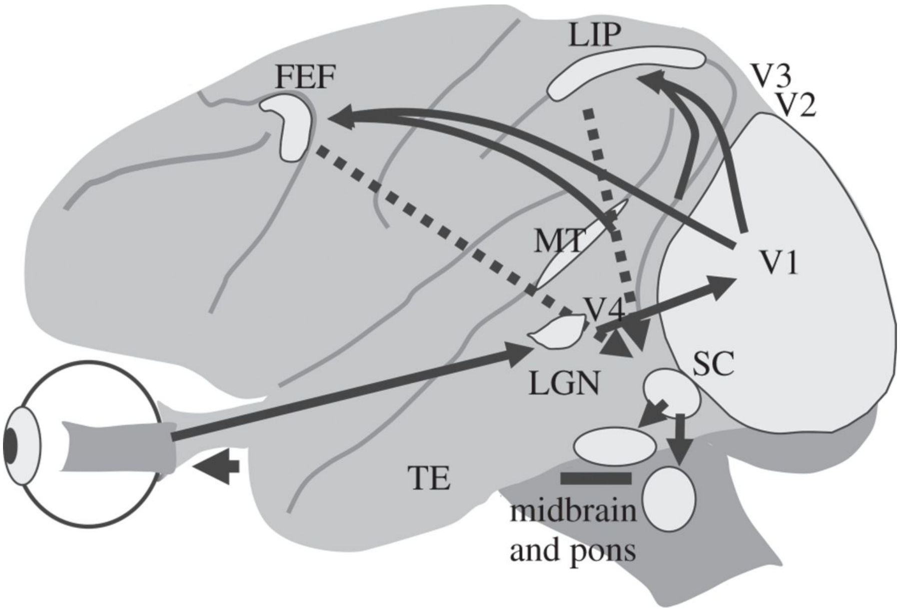

Figure 2.3: Neural circuitry involved in the generation of eye movements (both saccades and smooth pursuit). Created by Wurtz, CC BY 4.0, presented in (Wurtz, 2015), file obtained from Wikimedia Commons.

2.2.3 *Saccade generation*

Eye movements have been characterized into several categories: Saccades are rapid and ballistic jumps of both eye positions in the ocular cavity to foveate a new target during a fixation period. In contrast to the brisk movement during saccades, the smooth pursuit is a continuous movement of both eyes to follow a moving visual target. Humans perform $3-4$ eye saccades per second, and most of these are thought to happen subconsciously and involuntarily, but some also are volitional (McDowell et al., 2008).

Curiously, patients with blindsight *lost visual awareness due to damage in V1, yet retain the ability to perform visuomotor tasks and to correctly guide saccades (Kato et al., 2021).*

The circuitry that generates saccades is closely linked to the visual system. It includes some low-level structures in the midbrain (brainstem and superior colliculus (SC)) and some higher-level structures in the parietal and frontal cortex as illustrated in Figure 2.3.

The six muscle bundles (three agonist-antagonist pairs) that control the eye are driven by the cranial nerve nuclei in the brainstem (Kandel et al., 2013). These nuclei receive direct input from the SC. The upper layer of SC has a retinotopic map of the visual field, and conversely, neurons have receptive fields (RFs). In contrast to V1, these neurons are not tuned to any features of the visual stimuli. The (sensory) upper layer projects to the lower layer, where neurons are organized in movement fields that encode the vector from the current eye position to the RFs of the upper layer. Stimulation of these movement fields evokes a saccade along this vector and thus leads to the foveation of a corresponding stimulus.

Besides SC, also the lateral intraparietal area (LIP) and thefrontal eye field (FEF) are engaged in saccade generation.

Targeted inactivations or lesions of these areas revealed interesting connections: If SC is blocked, V1, V2, and LIP can't generate saccades anymore, but FEF has a direct connection to the eye muscle control in the brainstem and can still produce saccades. Furthermore, short latency saccades called express saccades were not observed anymore (McPeek et al., 2004; Zhaoping, 2014). If FEF is lesioned or inactivated, non-visually-guided saccades (e.g., memory-guided) saccades could not be generated (Sommer et al., 1997).

2.2.4 *Saccadic remapping*

It has been shown that neurons in LIP (Duhamel et al., 1992) , FEF (Umeno et al., 1997) and the deep layers of SC (Walker et al., 1995) transiently shift their visual RFs prior to saccades. This affects three situations: 1. They already respond to stimuli that are not yet in their RF but will be after the upcoming saccade (predictive remapping) 2. They cease to respond to stimuli in the RF once a new saccade plan moves the eyes away. 3. A remembered stimulus at the remapped RF, that is no longer present, evokes a response after the saccade (Kusunoki et al., 2003; Sun et al., 2016).

Recommended read: Duhamel et al. (1992)

Remapping has also been suggested in some extrastriate areas (Nakamura et al., 2002)

For FEF, evidence for a bottom-up mechanism enabling the remapping has been found: The saccade-generating SC sends a corollary discharge or efference copy of the oculomotor command via the mediodorsal nucleus (MD) to the FEF, which in turn can prepare for upcoming visual stimuli (Fukutomi et al., 2020; Sommer et al., 2002).

2.2.4.1 *Visual masking and saccadic suppression*

The visual perception appears rather stable to us, despite the high frequency of discontinuous jumps in the retinal image. The perceived images of a visual scene are generated during periods of fixation, where the eye position is still. But what happens during a saccade? How does the brain decide whether the eye is moving or the object that was kept in focus is moving?

Visual masking is one mechanism that could stabilize the perceived image: It has been demonstrated that the perception of a low-contrast image is eliminated if a high-contrast image is presented in quick succession (Kandel et al., 2013). The low-contrast image is said to be masked by the high-contrast image.

A second mechanism contributing to a stable visual percept is saccadic suppression. There is evidence that V1 (McFarland et al., 2015), V4 (Denagamage et al., 2021; Zanos et al., 2016), middle temporal area (MT) and middle superior temporal area (MST) (Niknam et al., 2019; Thiele et al., 2002) are suppressed around the time of a saccade.

Denagamage et al. (2021) investigated saccadic suppression in V4, observed suppression at the input layer IV prior to saccades, and hypothesized the pulvinar to be a likely source for such suppression signals.

Imagine you sit on the train and stare out of the window. You spot a deer on the field, and to maintain the focus, you perform a saccade counteracting the train's movement. In such a situation, perception during a saccade is possible!

2.2.4.2 *Saccadic main sequence*

The dynamics of saccades are well understood: With increasing saccade amplitude, the duration and peak velocity increase (Dai et al., 2016; Gibaldi et al., 2021). The observation that peak velocity increases linearly for small amplitude saccades until it saturates for larger amplitudes was termed the saccadic main sequence (Bahill et al., 1975).

Next, we look into the control of limbs and, thus, muscles around the body which is distinct from the saccade-generating circuitry.

2.3 MOTOR CONTROL

At first glance, body muscles are controlled through cortical projections from the primary motor cortex (M1) downwards the spinal cord, where motor neurons activate, innervate with muscles, and lead to their contraction. However, the network involved in planning and controlling the signals generated by M1 is much more intricate than meets the eye. In this section, I will start explaining on the level of muscles and progressively broaden the picture. The focus will lie on the control of arm movements, as needed for the analysis of data during a visually guided reaching task in the upcoming chapters.

2.3.1 *Muscles*

The axons of motor neurons exit the spinal cord at the ventral root, branch off at the muscle and connect via neuromuscular synapses (also neuromuscular junction) to a few to hundreds of muscle fibers (Kandel et al., 2013). The combination of the motor neuron and innervated muscle fibers is called the motor unit. Each muscle consists of a few hundred to thousands of muscle fibers, and most muscles are driven by hundreds of motor units.

The force exerted by a muscle depends on the motor units recruited and the firing rate. The recruitment of motor neurons with higher required muscle force follows the size principle: First, the smallest neuron is activated, then gradually, larger neurons are engaged. In contrast to the naive expectation that M1 governs muscle recruitment, one consequence of this finding is that a mechanism in the spinal cord decides upon the precise motor neuron to be activated (Kandel et al., 2013).

Muscles can be classified based on their role in movement. Agonist muscles are responsible for generating movement, while antagonist muscles work in opposition to agonist muscles to control movement. A triphasic activation pattern of muscles for example consists of three distinct phases of activity with agonist-antagonist-agonist activation.

Another classification is between flexor and extensor muscles. Flexor muscles are responsible for bending joints and decreasing the angle between two body parts, while extensor muscles are responsible for straightening joints and increasing the angle between two body parts (Kandel et al., 2013).

But how does the cortex control neurons in the spinal cord and thus muscles?

2.3.2 *Primary motor cortex (M1)*

The controversies about what neurons in M1, or sometimes agranular cortex due to the lack of a granular layer, encode and how they contribute to voluntary arm movement motivated a long series of investigations in the 20th century. The starting point was experiments by Evarts (1968), who recorded single neurons in M1 while a monkey moved a bar back and forth. They were able to show that neural activity correlates with the amount of force, a kinetic variable, suggesting that neurons directly control muscle activation. Opposing this view, Georgopoulos et al. (1982) found that during arm reaching, requiring multiple joints and muscles, M1 neurons were tuned to direction, a kinematic variable.

Georgopoulos demonstrated in his seminar paper that approximately one-third of the recorded neurons exhibited cosine-like directional tuning, which can be characterized by a preferred direction (PD) and a modulation depth. This notion of a PD will be crucial in Chapter 5.

The debate between the encoding of kinetic or kinematic variables dominated for several decades: While direct projections down the spinal cord appear to require no additional processing (pro kinetics), a kinematic variable encoding would necessitate that downstream regions convert the signals to the appropriate muscle commands (Sergio et al., 2005). Schwartz (1994) found a dependency of hand movement velocity and the success in decoding movement from the neuronal population vector (Georgopoulos et al., 1983, 1988; Georgopoulos et al., 1986), a weighted sum of the PDs of single neurons, argued in favor of the kinematic perspective.

Todorov (2003) attempts to reconcile these views and, in particular, the multitude of correlated variables with M1 neural activity by arguing in favor of direct cortical control of muscle activation.

In Omrani et al. (2017), N.G. Hatsopoulos is cited: “So, we can all agree that M1 is not one thing”. He argues to differentiate between caudal M1, which exhibits more monosynaptic connections to spinal motoneurons, and rostral M1.

Griffin et al. (2020) evidence in an impressive study via careful analysis of the temporal relationship between the single unit and electromyography (EMG) recordings that M1 neurons send premovement suppression signals to prevent an antagonist muscle from opposing the movement generated by an agonist's muscle.

More recently, activity in the motor cortex has been analyzed taking a dynamical systems perspective (see reviews by Vyas et al. (2020) and Wang et al. (2022c)). In these studies, the emphasis shifts from encoding a single neuron to examining how population activity patterns in the motor cortex temporally evolve to produce a particular behavioral output.

2.3.2.1 *Premotor cortex*

Motor cortex, previously categorized into primary and supplementary motor areas by Brodmann (1909), nowadays is known to have many subdivisions (Graziano et al., 2007; Luppino et al., 2000; Matelli et al., 1985; Rapan, 2021; Strick et al., 2021) with different naming conventions (see Table 2.1).

Full Name	**Short Name**	**Brodmann**	**Matelli 1985**
Primary motor cortex	M1	area 4	F1
Dorsal premotor cortex	PMd	area 6	F2
Supplementary motor area proper		area 6	F3
Ventral premotor cortex caudal	PMv	area 6	F4
Ventral premotor cortex rostral	PMv	area 6	F5
Pre-supplementary motor area		area 6	F6
Pre-dorsal premotor cortex		area 6	F7

Table 2.1: Naming of motor areas. See Graziano et al. (2007) for a visualization of their locations in the cortex.

Both PMd and PMv were shown to have a modulatory effect on M1 (Côté et al., 2017), yet they might also directly influence muscle activity: e.g., Strick et al. (2021) review the existence of disynaptic connections of premotor areas to spinal neurons. While PMd is associated with preparatory signals (Kaufman et al., 2013), PMv discharge correlates with the purpose of a motor act and not with the individual movements that constitute it (Kandel et al., 2013; Rizzolatti et al., 2014).

Notably, as it might be relevant for the study of PDs: Glaser et al. (2018) report that the preferred direction depends on the position of the hand and, thus, on the probability of an upcoming movement in a certain direction.

2.4 THE ROLE OF THE POSTERIOR PARIETAL CORTEX (PPC)

According to the chapter on "Voluntary Movement: The Parietal and Premotor Cortex" in Kandel et al. (2013), one of the key functions of the PPC is to integrate information from different sensory modalities, including vision, touch, and proprioception, to guide movements and actions.

In particular, the PPC is thought to be involved in transforming visual information about the location of objects in the environment into motor commands for the movement of the eyes and limbs. For example, when we reach for an object, the PPC is thought to integrate information about the location of the object in visual space, the position and movement of the eyes, and the position and movement of the hand and arm, to plan and execute a precise and coordinated reaching movement (Battaglia-Mayer et al., 2006).

PPC plays a crucial role in eye-hand coordination, which is the ability to coordinate eye movements with hand movements to reach and manipulate objects in the environment (Battaglia-Mayer, 2019).

PPC has been associated, in particular, with the intention of performing an action (e.g. hand movement or eye movement) (Andersen et al., 2002). The same team of researchers argue that PPC would thus be a favorable implantation site for brain-machine interfaces (BMIs) (Andersen et al., 2022, 2014).

Rigotti et al. (2013) established the term mixed selectivity for neurons in the prefrontal cortex. Single neurons in PPC were found to exhibit mixed selectivity (Diomedi et al., 2020; Hadjidimitrakis et al., 2019; Zhang et al., 2017). Thus the firing rate of a neuron is associated with multiple different behavioral modalities.

By definition, PPC is the posterior part of the parietal lobe. This region is often subdivided into the superior and inferior parietal lobules (Gamberini et al., 2021).

Inferior parietal lobule

The inferior parietal lobule is located lateral to the intraparietal sulcus and medial from the lunate fissure, which merges with the superior temporal sulcus (cf. Figure 2.1). Brodmann (1909) called the complete gyrus Area 7 (sometimes short BA7), which was later subdivided by Vogt et al. (1919) and von Bonin et al. (1947) into the posterior 7a (or PG) and the anterior 7b (or PF). The modern view on the structural organization is dominated by Pandya et al. (1982), who suggest a split of Area 7 into four divisions, from caudal to rostral: Opt, PG, PFG, and PF (also Gregoriou et al. (2006)). For a recent re-evaluation on this parcellation based on receptor densities, see Niu et al. (2021).

The cytoarchitecture (Caspers et al., 2011) and receptor densities (Niu, 2022) in the macaque inferior parietal lobule resemble a potential homolog area in the human angular gyrus (see e.g., Numssen et al. (2021)).

The inferior parietal lobule is activated during multiple modalities (Mountcastle et al., 1975) and assumed to play a role in multi-sensory integration during motor behavior (both eye and limb) (Andersen, 1987; Avila et al., 2019; Borra et al., 2017; Rozzi et al., 2008).

Here, we briefly give more detailed information on 7a and DP, as we record from these in V4A experiment.

2.4.0.1 *Area 7a (7a)*

CONNECTIVITY 7a is part of the dorsal visual stream and reciprocally connected with visual areas Andersen et al. (1990a) and Wang et al. (2022b). 7a receives disynaptic output connections from hippocampus (Clower et al., n.d.) several motor areas (especially to ventral premotor cortex (F5) and pre-dorsal premotor cortex (F7)) (Rapan, 2021; Rizzolatti et al., 2014).

Furthermore, it receives feedback input from other parietal and frontal areas (Gregoriou et al., 2006; Lewis et al., 2000; Niu et al., 2021; Rozzi et al., 2006; Stepniewska et al., 2005).

FUNCTIONAL ROLE Neurons in 7a activate during saccades (Andersen et al., 1990b; Barash et al., 1991) and hand reaches (Heider et al., 2010, 2014; Hyvärinen et al., 1974; MacKay, 1992), exhibit gain modulation of large visuotopic RFs due to eye (Andersen et al., 1990b; Andersen et al., 1985; Bremmer et al., 1998; Siegel et al., 2003) and hand (Buneo et al., 2012) position, are responsive to optical flow stimuli (Heider, 2005; Raffi et al., 2007) or visual motion stimuli (Merchant et al., 2004), modulate their activity with (covert) attention (Constantinidis et al., 1996, 2001; Quraishi et al., 2007; Raffi et al., 2005; Steinmetz et al., 1994) and also show somatosensory properties (Rozzi et al., 2008).

Rozzi et al. (2008) demonstrate a gradient from more oculomotor-related activity on the medial end of the inferior parietal lobule towards more limb-movement-related activity in the lateral end of 7a.

In Andersen et al. (2002), the encoding of motor action intent of several areas in the PPC has been reviewed. In line with this view, Li et al. (2022) show that 7a not only activates due to sensory triggers (latency $\sim 100 - 150\,\text{ms}$) but also represents pre-movement activity for an upcoming movement during a manual interception task (lead $\sim 50\,\text{ms}$).

Mirror neurons (Gallese et al., 1996; Rizzolatti, 1994; Rizzolatti et al., 2014, 2004, 1996), that activate during the mere observation of an action, have also been reported in 7a (Fogassi et al., 2005; Rozzi et al., 2008; Yokoyama et al., 2021).

Evidence points at preference towards lower eye position and lower visual receptive fields which, however, are variable in time and depend on the task and attentional state (Heider et al., 2010, 2014; Karkhanis et al., 2014; Merchant et al., 2004; Wang et al., 2022b). Battaglia-Mayer et al., 2005 found an over-representation of eye movements towards the contralateral side and eye position signals in the contralateral space.

Due to the vastly distinct response patterns in 7a, several studies (Battaglia-Mayer et al., 2007; Merchant et al., 2004) suggest a subdivision of the neuronal population. The large area covered by 7a, with demonstrated functional differences (see Rozzi et al. (2008)), likely is one cause of this.

2.4.0.2 *Dorsal prelunate (DP)*

The (extrastriate) DP is located on the dorsomedial portion of the prelunate gyrus and merges into the visual area V4 on the ventral end (Asanuma et al., 1985).

CONNECTIVITY May et al. (1986) states that DP has prominent connections with LIP, 7a, and areas along the anterior bank of the caudal superior temporal sulcus. It exhibits direct feedback connections to V1 (Wang et al., 2022b) and is connected to various other parietal areas. Andersen et al. (1990a) found connections with V3A, LIP, 7a, V4, MST, PO, 46, and 8a. According to Felleman et al. (1991) it is lower in the anatomical hierarchy than 7a.

FUNCTIONAL ROLE Neurons in DP respond to saccades and gaze position (with a latency of $70 - 150\,\mathrm{ms}$) (Andersen et al., 1990a; Li et al., 1989), and are modulated by attention. Several reports state that DP exhibits RFs in the (contralateral) far lower visual field (Arcaro et al., 2011; Maguire et al., 1984), however, Heider (2005) also finds a representation of the upper visual field.

2.5 REFERENCE FRAMES AND COORDINATE SYSTEMS

To discuss these issues, a bit of terminology is necessary:

The terms reference frame and coordinate system are used as in the physics literature. Reference frames in neuroscience are commonly categorized into allocentric, with external objects as the point of reference, and egocentric, with some body part as point of reference (Crawford et al., 2011). To define a point relative to the origin in a certain reference frame, a set of (typically 3-D) base vectors or coordinate axes can be defined (e.g., cartesian or spherical) (Soechting et al., 1992).

In order to guide an accurate movement of an effector (e.g., hand, eye), we use our senses (e.g., vision, touch, hearing, smell, proprioception, and the vestibular sense).

Information about the external world is also called extrinsic (e.g., object to object or object to body distance), while information about the body itself is referred to as intrinsic (e.g., set of muscle lengths and set of joint angles) (Kandel et al., 2013).

Each of the senses represents information about the external world in a certain manner: Their corresponding primary sensory cortices — if existent — use a sense-specific reference frame. Vision manifests itself in the activation of RFs organized in a visuotopic map in V1 (see Figure 2.2), touch with a somatotopic map.

Auditory stimuli are coded in a head-centered reference frame (Cohen et al., 2002).

One of the key sensory receptors involved in proprioception is the muscle spindle, which is a specialized sensory receptor located in skeletal muscles that is sensitive to changes in muscle length and tension.

Neurons in LIP respond to auditory stimuli in an eye-centered reference frame (Stricanne et al., 1996).

The vestibular sense is governed by the three semicircular canals of the vestibular system located in the inner ear. Each of these canals defines a plane along which movement of the body leads to movement of fluid inside the canals into the contrary direction (due to inertia), which in turn tilts the hair cells embedded in the cupula and triggers electrical signals (Kandel et al., 2013).

A classical idea states that all information represented in different reference frames merge into one abstract, universal representation in the parietal cortex and that this reference frame is used to inform movements (Battaglia-Mayer, 2019; Cohen et al., 2002). However, the existence of a unique reference frame has not been proven.

Gain modulation due to the eye position (Andersen et al., 1985) was computationally shown to arise in recurrent neural networks (RNNs) trained with back-propagation through time (BPTT) (Zipser et al., 1988).

3

SETUP, DATA AND PREPROCESSING

In the previous chapters, we gave a brief overview of the Vision-for-Action (V4A) experiment and supplied relevant background knowledge.

This chapter describes the setup in more detail and sketches the path from the source data files obtained during the recording to the files with fully integrated metadata used in the analyses that will be presented in the following chapters.

The V4A experiment is run in the context of a collaboration between two laboratories: The Lab of Prof. Thomas Brochier at the Institut de Neurosciences de la Timone, Centre National de la Recherche Scientifique-Aix-Marseille Université carried out the actual experiments, while the Lab of Sonja Grün at Institute of Neuroscience and Medicine (INM-6) and Institute for Advanced Simulation (IAS-6) and JARA Brain Institute I (INM-10), Forschungszentrum Jülich, Jülich, Germany, were mostly concerned with data management, preprocessing and analysis. The split of responsibilities was not strict: Analyses were also performed in Marseille, and researchers from Juelich participated in improving the setup.

3.1 SETUP OVERVIEW

The setup of the V4A experiment was designed to flexibly probe neural activity along the dorsal visual pathway during visually guided behavior of rhesus monkeys (*macaca mulatta*).

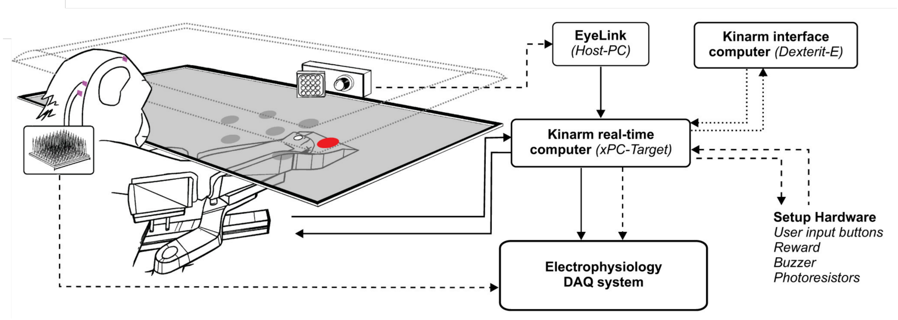

Figure 3.1: Experimental Setup. Figure taken from de Haan et al. (2018). The experimental subject, a macaque monkey, is seated in an exoskeleton device (KINARM) in front of a work area. The work area consists of a semitransparent mirror, which allows for observation of the arm underneath (in lighted condition) and reflects the display of a downward-facing screen, e.g., target or a hand cursor feedback. One eye is tracked by an infrared light source and camera (Eyelink). The monkey is implanted with multiple Utah arrays that record extracellular potentials along the dorsal visual stream and motor cortex. Lines illustrate the analog (solid), digital (dashed), or via Ethernet (dotted) signal flow between devices and computers (boxes). At the last stage, all signals, behavioral and electrophysiological, enter the data acquisition (DAQ) system (henceforth called neural signal processor (NSP)), from where they are time synced and stored.

Two components were necessary to achieve this: recordings of the monkey's behavior and electrophysiological recordings.

Here I will first give an overview of the setup, then dive into the details of the recorded data, briefly describe the preprocessing pipeline, supply background knowledge on the experimental subjects and explain the behavioral tasks.

As illustrated in Figure 3.1, the monkey was seated in a chair in front of a work area. The monkey's head direction was fixed with a mask (Barthélemy, 2023) designed to enable the monkey to view the whole extent of the work area. Attached to the chair was a motorized exoskeleton (KINARM Exoskeleton Laboratory, BKIN Technologies) in which the monkey's upper arm and forearm were placed.

The work area is part of a virtual reality system: It is a semitransparent mirror that reflects the image of a downward-facing computer screen. The hand underneath the mirror could be illuminated to enable direct visual feedback of the hand/arm (de Haan et al., 2018). The benefit of this setup is that both visual target and hand movements happen in the same plane, such that the monkey can use direct, natural mapping.

For Jazz the semitransparent mirror was replaced with a true mirror.

In the following, we discuss recordings during which the room is darkened, and the computer screen supplies the hand feedback.

An eye-tracking system (EyeLink system, SR Research[1]) that records the movement of one eye was attached at the rear end of the work area.

Neural activity was recorded via multiple neural implants called multi-electrode arrays (MEAs), more precisely Utah arrays (Blackrock Microsystems, Salt Lake City, UT, USA [2]) (Campbell et al., Aug./1991; Nordhausen et al., 1996). The two experimental subjects recorded until the writing of this thesis, *Enya* and *Jazz*, were implanted with four Utah arrays with 36 electrodes each in the left primary visual cortex (V1), secondary visual cortex (V2), dorsal prelunate (DP) and area 7a (7a), and one array with 100 electrodes in primary motor cortex (M1)/dorsal premotor cortex (PMd). Note that 4 electrodes per array are inactive.

The four smaller arrays are connected to one connector with 128 contacts, while the M1/PMd-array connects to a separate connector. These two connectors were embedded in the skull, fixed through bone cement, and constituted the starting point of two data streams outside the brain (more details in Section 3.2.5).

These two data streams were processed by two synchronized real-time computers (cf. electrophysiology data acquisition (DAQ) system in Figure 3.1), called the NSPs. The signals about the task, eye tracking, and hand/arm behavior from the KINARM real-time computer also entered the NSPs as analog inputs and were therefore synchronized as well. Furthermore, the NSP performed an online spike-sorting, which will be discussed in more detail in Section A.1. Details on the hierarchy of computers processing the Eyelink, the KINARM interface computer, the KINARM real-time computer, and the NSPs are explained in (de Haan et al., 2018).

Each NSP sent small packages of data to a computer running software `Cerebus Central` (Blackrock Microsystems, Salt Lake City, UT, USA, `www.blackrockmicro.com`) to store the data in different files with proprietary data format from Blackrock: The raw neural signals are stored in a `.ns6`-file, while the analog signals and the extracted waveforms were stored in a `.ns2`-file. The spiketimes and information on the online sorting were stored in a `.nev`-file. As a result, two sets of these three data files are stored, one for the visual-parietal arrays and one for the motor array.

3.2 RECORDED DATA

In the following subsections, I will discuss the recorded data in more detail and mention a few preprocessing steps that are needed to use them. An extensive discussion of all the preprocessing steps is beyond the scope of this thesis.

---

[1] `https//www.sr-research.com`

[2] `www.blackrockmicro.com`

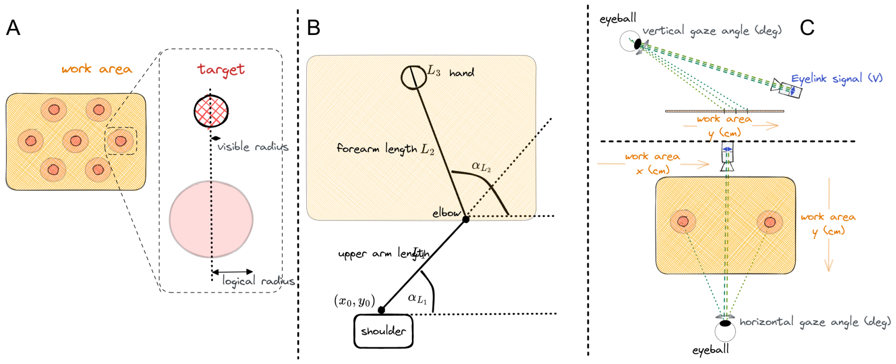

Figure 3.2: Behavioral data sketches. A: A display of the work area with the targets positioned at the vertices of a hexagon. Right to the work area is a zoom of a target decomposed into the visible and logical part. B: Top view of a KINARM exoskeleton sketch. The shoulder was anchored by the device and defines the position relative to the work area. Lengths of the upper arm L_1, forearm L_2, and fingertip L_3 are listed in Table 3.1. C: Sketches of the Eyelink geometry. The upper part shows a side view of the setup, while the lower part shows a top view. A change in the (eyeball) gaze direction would lead to a changed reflection of infrared signals registered by the Eyelink camera and translated into a modified output voltage. The colors chosen in this figure are not the ones used in the experiment: For maximal detectability and small targets, the screen background was black and targets were white. The logic radii were not visible to the monkey and were introduced to allow for less restricted, ballistic movements.

3.2.1 *Hand movement data*

The KINARM exoskeleton outputs a voltage signal sampled at 1 kHz for each shoulder and elbow joint, which can be converted into the corresponding angles. The necessary conversion is detailed in the Simulink model (see source files `Landing_task.mdl` or `Drawing_task_6targets.mdl`). The resulting x and y positions of the hand were stored in both `.ns2`, for the visual-parietal stream and the motor stream, for all sessions.

The central panel in Figure 3.2 sketches the top view on the KINARM and defines the required lengths and angles. The corresponding values used for both subjects, *Enya* and *Jazz*, are listed in Table 3.1.

The conversion from angles to the hand position was performed online, and the resulting hand positions were stored for every session. However, the joint angle signals are not recorded for all experimental sessions. However, if at least one angle is recorded, all quantities shown in Figure 3.2B can be reconstructed.

RECONSTRUCTION OF THE ANGLES Here we exploit simple, trigonometric relationships to obtain either α_{L_1} or α_{L_2}. Because the hand was

human readable name	variable name	value	unit
shoulder x	x_0	0.275	cm
shoulder y	y_0	-26.250	cm
upper arm length	L_1	12.6	cm
forearm length	L_2	23.0	cm
fingertip offset	L_3	-0.1	cm

Table 3.1: Kinarm parameters. The shoulder x/y position is given with respect to the screen origin, which is at the bottom-center of the screen. The screen is thus not centered with respect to the body but rather shifted to the right.

aligned with the forearm, it was included in its total length, therefore in the following, the fingertip is neglected.

The x and y positions of the shoulder, elbow and hand (neglecting the fingertip offset) are given by:

$$x_{\text{shoulder}} = x_0 \tag{3.1}$$

$$y_{\text{shoulder}} = y_0 \quad , \tag{3.2}$$

$$x_{\text{elbow}} = x_{\text{shoulder}} + L_1 \cos \alpha_{L_1} \tag{3.3}$$

$$y_{\text{elbow}} = y_{\text{shoulder}} + L_1 \sin \alpha_{L_1} \quad , \tag{3.4}$$

and

$$x_{\text{hand}} = x_{\text{shoulder}} + L_1 \cos \alpha_{L_1} + L_2 \cos \alpha_{L_2} \tag{3.5}$$

$$y_{\text{hand}} = y_{\text{shoulder}} + L_1 \sin \alpha_{L_1} + L_2 \sin \alpha_{L_2} \quad . \tag{3.6}$$

In most sessions, the angle α_{L_2} was recorded; the missing shoulder joint angle can then be obtained by

$$\alpha_{L_1} = \arccos \frac{x_{\text{hand}} - x_{\text{shoulder}} - L_2 \cos \alpha_{L_2}}{L_1} \quad . \tag{3.7}$$

HAND MOVEMENT SEGMENTATION The continuous hand movement behavior of the monkey can be split into movement segments. Given the time-dependent x and y position of the hand, we calculated velocities in x- and y-direction by taking the first derivative with a Savitzky-Golay filter with the window length $w_{\text{SG hand}} = 101\,\text{ms}$ and the polynomial order $p_{\text{SG hand}} = 3$. We calculated the absolute velocity of the resulting 2-D velocity vector by taking its norm.

Movement segments were then defined between minima of the absolute velocity if 1. the peak velocity between minima was larger than a minimum peak velocity of $v_{\text{minimal peak}} = 1\,\text{cm/s}$ and 2. the depth of the minimum was not too shallow. The minimum required depth of velocity minima, relative to the height of the nearest velocity peak, considered for segmentation was $d_{\text{minimal relative}=0.1}$.

3.2.2 *Eye movement data*

The EyeLink 1000 allows for the non-invasive detection of eye movement. It emits infrared light, which is reflected by the eye. The change in reflection is then detected with a camera (see details in de Haan et al. (2018) and sketches in Figure 3.2C).

As a result, we recorded a voltage signal sampled at 1 kHz between $-5\,\text{V}$ and $+5\,\text{V}$ for the vertical and horizontal direction, which had to be linked to the actual gaze direction (in degree relative to the straight forward gaze direction) or the corresponding focus of the eye on the work area (in centimeters).

To obtain this mapping, ideally, prior to each experimental session, an eye calibration was performed.

CALIBRATION For all sessions recorded with *Enya* and recordings with *Jazz* until mid-2022 the calibration consisted of the presentation of a regular 5×5 grid of targets (later changed to only 17 targets). The targets were presented in reading order, and the x, y voltage of the eye signal during the corresponding fixations were recorded for 100 ms each. The optimal mapping was then obtained by fitting a second-order polynomial to the average voltage during the fixation per target and the fixed target positions in centimeters.

In de Haan et al. (2018), a fourth-order polynomial was proposed because it yielded the best fit for fixations inside the calibration area. Unfortunately, this high-order fit did not generalize well and resulted in a weird-looking warp of the eye positions for gazes above the work area.

The quality of the eye calibration using the above method relying on the static fixations turned out to be difficult to evaluate for the experimenters. Hence, a new calibration method, in which the monkey is required to follow (pursue) a horizontally moving target, is being developed and tested at the time of writing.

SACCADE EXTRACTION The eye movement behavior is characterized by brisk jumps of the eye position, called saccades. We detect saccades by thresholding the norm of the 2-D eye velocity vector obtained by application of the first derivative with a Savitzky-Golay filter with the window length $w_{\text{SG eye}} = 9\,\text{ms}$ and the polynomial order $p_{\text{SG eye}} = 3$. In addition to the threshold, a few heuristically determined criteria were employed. The parameters are listed in Table 3.2.

3.2.3 *Task data*

A MATLAB Simulink model controlled the experimental task and therefore used the data from the KINARM exoskeleton and the Eyelink.

name	value	unit
saccade velocity threshold	50	deg/s
minimal saccade duration	10	ms
maximal saccade duration	100	ms
minimal saccade peak velocity	60	deg/s
minimal saccade peak velocity	20000	deg/s
minimal saccade peak acceleration	4000000	deg/s^2
minimal saccade peak acceleration	0.1	deg/s^2

Table 3.2: Saccade detection parameters.

Targets appearing in the work area are specified by their visible radius and their logical radius (see Figure 3.2A). The latter is not visible, yet defines the region around the visible target that the monkey needs to enter in a reaching task such that it counts as successfully reached.

CONSTRAINT ON THE WORK AREA The targets lay on the vertices of a hexagon to maximally exploit the usable work area. The horizontal work area allows the targets to fall in the same plane as the monkey's hand movement. However, the region that is reachable by the monkey is limited by their arm lengths. Furthermore, the KINARM chair with an attached mask forces the monkey's head to be guided straight ahead. To see the work area, the monkey's gaze downward is quite steep, with the nose as an obstacle. To maximize its surface, the work area was thus not centered but slightly shifted to the right relative to the monkey.

TASK CODES Each event of the task (e.g., trial start, a hand entering target 2, reward start, and so on) was stored in the data with a timestamp and a 16 bit task code. The precise nature of the task codes can be decoded into a machine- and human-readable format via semi-automatically written descriptors that depend on the behavioral task.

LATENCY OF SCREEN The experimenters found that there is a systematic delay between the time stamp of the target onset and the actual appearance on the downward-facing screen (see corresponding discussion in de Haan et al. (2018)). We did not account for this delay in the following analyses due to inherent variability. Preliminary investigations by the experimenters by recording the luminance on the work area via photo receptors revealed three sources for the delayed appearance:

1. 43 ms due to communication and the graphic card drive

2. $0 - 16\,\text{ms}$ with a linear relationship of the vertical distance between the target and the top of the screen.
3. $0 - 16\,\text{ms}$ due to the refresh rate of the screen

The first two issues are deterministic and should be corrected in the future. For the second point, the relationship between the target's vertical position and the delay can be calculated by knowing the target coordinates. The last point, however, is more difficult to take into account.

3.2.4 *Choice of recorded analog signals*

Each of the two NSPs can process 16 analog signals and store them in a `.ns2`-file; thus, in addition to the neural activity, the recording setup can store up to 32 analog signals.

The experimenters decided to store the x- and y-positions of the hand, eye, and target positions with each NSPs, yielding redundancy and thus robustness against signal loss or failure from one NSP. This choice also allows running analyses on only one dataset (motor or visual-parietal) without the necessity to load everything.

To be able to reconstruct eventual data gaps due to package losses during the transmission from the NSP to the computer, two analog signals with phase-shifted sync pulses are stored.

Given these constraints, there are $8/16$ channels undetermined per NSP. The choice of how to occupy these remaining channels changed over time. In most cases, additionally stored signals are raw eye signals, the angles, velocities or acceleration of the KINARM joints, the eye diameter, or photoresistors measuring the luminance.

3.2.5 *Electrophysiological data*

This subsection describes the electrophysiological data flow from arrays to neural signal processors (NSPs) as illustrated in Figure 3.3.

Four Utah arrays (6x6 electrode grid, 32 active electrodes out of 36) were implanted along the dorsal visual stream in V1, V2, DP, and 7a. One Utah array (10x10 electrode grid, 96 active electrodes out of 100) was implanted in the hand/arm region of M1/PMd. The V1 and V2 array's location was chosen to obtain overlapping receptive fields. All array placements were guided by anatomical markers.

In this paragraph, the data flow of the recorded neural signals as illustrated in Figure 3.3 will be explained. At the electrode, a potential difference to the reference electrode is recorded. The single wires per electrode are connected to the array's backside (called bonding pad), are bundled in groups of 32 wires, and, within one cable, are guided to the connector (CerePort). During surgery, pictures were taken to allow for future localization of cortical areas that lay under the arrays

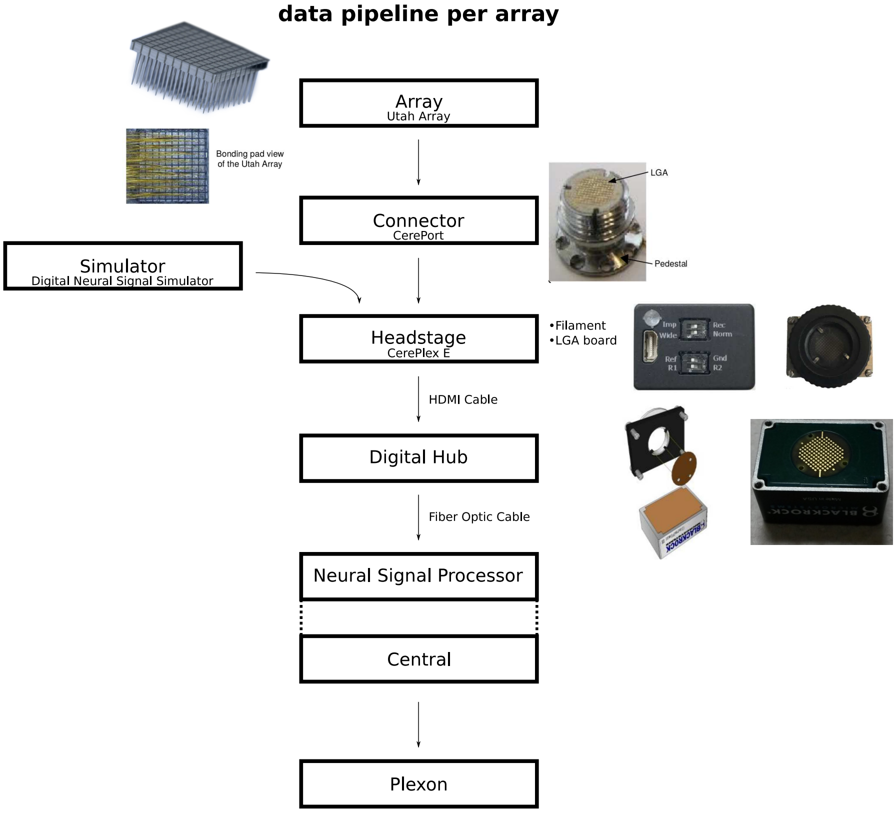

Figure 3.3: Electrophysiological data flow with illustrations of the involved devices.

and to keep track of the array orientation by using the wire bundle as a side reference. The connector's inner part is filled with a silicon-like gel. Inside this isolating gel, the cable bundle splits again into single wires, which are then connected to the back side of the grid-organized pin ensemble (called land grid array (LGA)). The headstage (CerePlex E) is the device that can be screwed on top of the connector to connect to the LGA with an exact counterpart. In order to guide the electrical signal from one LGA pin to its counterpart, an insolation membrane that allows only for current to propagate orthogonally to its surface (called filament film) is used.

The wires stemming from the four visual-parietal arrays were gathered in one connector (CerePort) attached to the right occipital bone, while the wires from the motor array were guided to a separate connector that was secured to the right parietal bone.

The resulting two streams of analog signals (sampled at 30 kHz) were band-pass filtered between 0.3 Hz-7500 Hz and digitized in the headstage minimizing the chances to collect ambient noise in the data. These filters are applied online/during runtime by the hardware and are zero-phase filters (causal filters, see (Yael et al., 2018)). The digital signal was then sent to the digital hub via a mini-HDMI cable, where it was converted to an optical signal. From there, it is sent via an optic fiber cable to the neural signal processor (NSP).

Each electrode of the Utah array records a voltage: The potential difference between the tip of the electrode and a reference electrode. The headstage offers the choice between two reference signals, from which only the reference yielding the best signals was used per experimental subject and kept consistent across sessions. The sampling rate of this signal was 30 kHz. According to the Nyquist-Shannon theorem, the highest frequency that can be resolved with a signal of this sampling rate is $f_{\text{max}} = 15\,\text{kHz}$.

The tip of the electrode is located in the neural tissue, and the voltage will contain signals induced by its surrounding: This can be low-frequency fluctuations of the overall potential or very local and fast changes in electrical potential due to a nearby neuron firing an action potential.

As a consequence, two types of signals are commonly extracted from such a signal:

1. the low-frequency content of the signal, the local field potential (LFP)
2. the high-frequency content of the signal, spiking activity.

The spiking activity recorded on one single electrode might stem from multiple neurons. Therefore a process called spike sorting (in-depth discussion in Section A.1) was employed. In short, spike sorting assigns action potentials with the same prototypical waveform shape to a unit, a putative neuron.

3.3 EXPERIMENTAL SUBJECTS

Up until the writing of this thesis, three subjects performed tasks in the V4A experiment, *Yamako*, *Enya* and *Jazz*.

Yamako was the first macaque to be trained to work in the setup and yielded only behavioral data, which were presented in de Haan et al. (2018). Unfortunately, *Yamako* died during the surgery for array implantation.

Enya, born on April 29, 2010, is female and reported to have a very nice character. She participated in the Reach-to-Grasp (R2G) experiment before and thus she already was used to training for a motor task. Training on the V4A experiment started on March 17, 2017. She performed the hand movements with the right arm and, consequently, during the surgery on December 07, 2017, arrays were implanted in the (contralateral) left hemisphere (see Figure 3.4). The left eye was used for eye tracking.

Jazz, born on May 26, 2014, is male and also reported to have a very nice character. Training on the V4A experiment started on July 11, 2017.

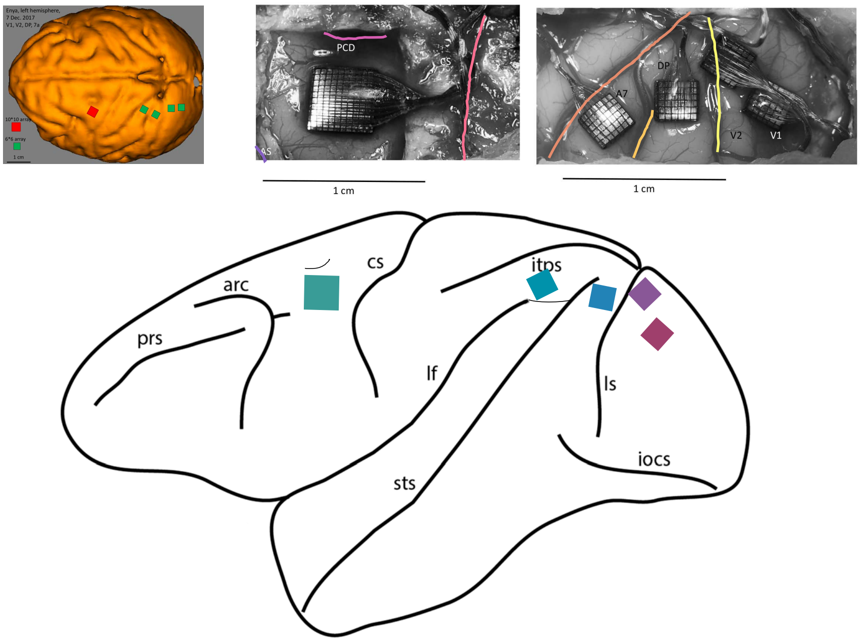

Figure 3.4: Array placement *Enya*.

As this was the first experiment he took part in, his training naturally took longer. He performed the hand movements with the right arm and, consequently, during the surgery on January 08, 2020, arrays were implanted in the (contralateral) left hemisphere (see Figure 3.5). The left eye is used for eye tracking.

3.4 BEHAVIORAL TASKS

In this thesis, we analyze data from two visually guided motor tasks that we termed the *landing task* and the *drawing task*.

Besides these two tasks, the monkeys have performed more tasks in the V4A experiment, that we will not explain here.

3.4.1 *Landing task*

In the landing task, the monkey had to perform subsequent, point-to-point, hand reaches landing within the logical radius of each subsequently shown target of a given landing sequence within certain time limits. The landing sequence is a unique sequence of target positions, starting with the central position and followed subsequently by three peripheral positions, chosen from six possible peripheral target positions located at the corners of a hexagon centered at the center target.

Per recording session, the monkeys were required to fulfill 120 trials. A trial is defined as the time between an initial presentation of a new landing sequence (called trial type presentation), starting with the

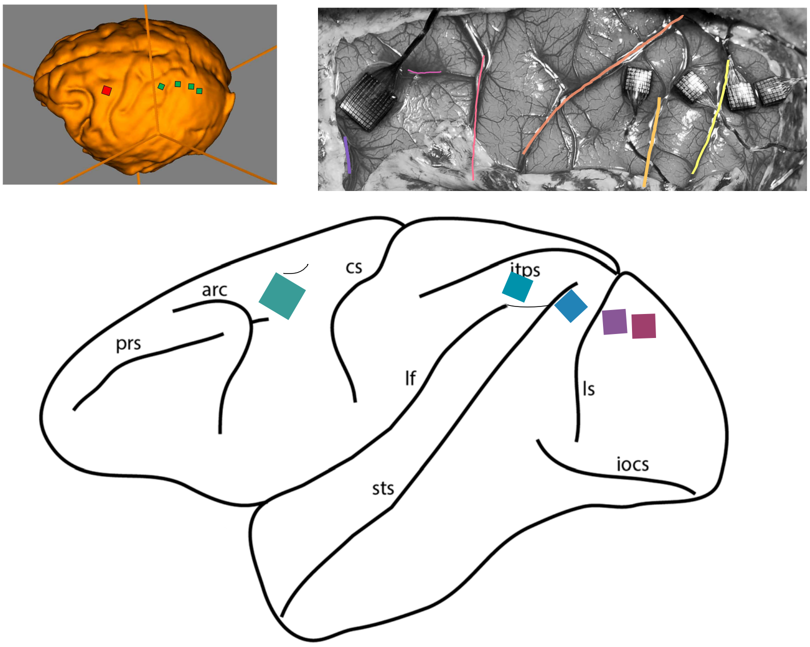

Figure 3.5: Array placement *Jazz*.

first target, and its completion ending with a reward. The monkey was presented with 12 different landing sequences in random order, yielding ten repetitions of the same landing sequence per session.

Note that the precise task definitions might vary from session to session: for training purposes or to test different behavioral hypotheses, some sessions have eight landing sequences, while others have 12 different landing sequences. Also, the required durations for the landing, as well as the radii of the targets, varied.

Each time the experimental system presents the landing sequence (trial type presentation), starting with the first target and the monkey performs the task until either success or failure; we call this an attempt. Attempts can thus be either unsuccessful, leading to a new attempt of the same trial-type presentation, or successful, ending the trial and leading to the first attempt of the next trial-type presentation. Unsuccessful attempts are grouped into time-out errors (the monkey fails to perform the reaches within the given time limits) or anticipation errors (the monkey leaves the current target before the next target is lit up or overshoots the target). Monkeys were slightly water-deprived before the experiments and received water drops as a reward for completing a trial.

Refer to the displays of the behavioral in Figure 5.3 and Figure 5.4 as well as for the spike data in Figure 5.8, that are presented in the next chapter, for a visualization of a landing sequence.

3.4.2 *Drawing task*

In the drawing task, each trial starts with the illumination of the central target, which indicates the hand's starting position to the monkey. After 200 ms, the central target was turned off and replaced by the six peripheral targets. The monkey was then required to hover over all targets without any constraints on the order and very little time pressure (maximum 1 s between each target). Upon successfully reaching towards all the targets, the monkey receives a water reward.

3.5 PREPROCESSING PIPELINE

The recording setup outputs two sets of files: {`.ns6`, `.ns2` and `.nev`} per session. These are stored with many metadata files, e.g., array specifications, Simulink model files, and task-specific code descriptors, to name just a few, in a folder with the following unique format: `[subject-ID][date in yymmdd format]-[short task name]-[3-digit session-ID]`. For example, y180306-land-001 would stand for the first recording session on March 06, 2018, with *Enya* performing a landing task, and j210208-draw-002 would be the second recording session with *Jazz* on February 08, 2021, performing a drawing task.

After being stored on the local server in Marseille called *congloue*, the data is transferred to the local server in Jülich called *hambach*.

Fun fact: The small and large Congloué are two little islands near the coast of Marseille, while Hambach is a small village close to Jülich.

The multitude of data files and formats makes it difficult for an end user to deal with the raw data. Furthermore, several preprocessing steps have to be performed on the behavioral data (e.g., convert signals from volts to centimeters, hand movement segmentation, and eye segmentation) and the electrophysiological data (integrate spike sorting, extract LFP signal by filtering and downsampling). Our Lab developed a preprocessing pipeline to avoid each end user needing to perform this preprocessing, leading to a zoo of different routines. This pipeline uses the software Snakemake (Köster et al., 2012) and multiple Python scripts organized in data and metadata apps. This allows for a modular and extensible way of merging the raw data files into a well-organized and usable output file.

The final output is a `.nix`-file that has a standardized format and allows the application of the same analysis on several sessions. The preprocessing output is furthermore version-controlled via GIN[3].

Details on the preprocessing pipeline can be found in the thesis by Alexander Kleinjohann.

In the previous chapter, we introduced the V4A project and reviewed the neuroscientific background, while this chapter explained the setup, data, and task. We now have all prerequisites to look at the actual data. But before we present the main neuroscientific analysis, the next

---

[3] GIN, `https://gin.g-node.org/`

chapter will discuss artifacts that were found in preliminary analyses and that ideally should be dealt with to obtain trustworthy data.

Make the best use of what is in your power,
and take the rest as it happens.

— Epictetus

4

ARTIFACTS

Initial analyses of the electrophysiological data from the Vision-for-Action (V4A) project revealed potential non-neuronal data called artifacts. This chapter seeks to characterize these artifacts, to argue for and against their artifactual nature, and to suggest potential origins in the arrangement.

Finally, to make the recorded data safely usable, we propose a preprocessing stage that removes the most significant artifacts from the recorded data even before spike sorting.

While long-term degradation of Utah recordings (Sponheim et al., 2021) and potential scarring of the neural tissue (through explant analyses) have been discussed in literature (Patel et al., 2022; Woeppel et al., 2021), artifacts in the recorded data are rarely mentioned.

4.1 DESCRIPTION OF POTENTIAL NON-NEURONAL DATA

Early visualizations of the single unit activity (SUA) spiketrains extracted via a manual spike sorting procedure, as explained in Paragraph A.1.2, revealed that some spikes from different units are highly coordinated. In the raster plot shown in Figure 4.1, where spikes are aligned to the first peripheral target onset in the landing task, especially spiketrains from primary motor cortex (M1)/dorsal premotor cortex (PMd) look surprisingly similar.

The binning of the spiking activity with sampling rate precision (30 kHz) into a time histogram exhibits multiple peaks.

We compare the empirical distribution of time histogram entries (complexity distribution, (Louis et al., 2010)) with the distribution that is expected if the fine temporal structure of the spiking activity is explicitly destroyed by dithering each spike in a certain dithering window (here $w_{\text{dither}} = 10\,\text{ms}$). With many parallel spiketrains, a certain amount of synchronization at sampling rate precision is expected by chance. A direct comparison of these distributions in Figure 4.1 shows our data's excess synchrony.

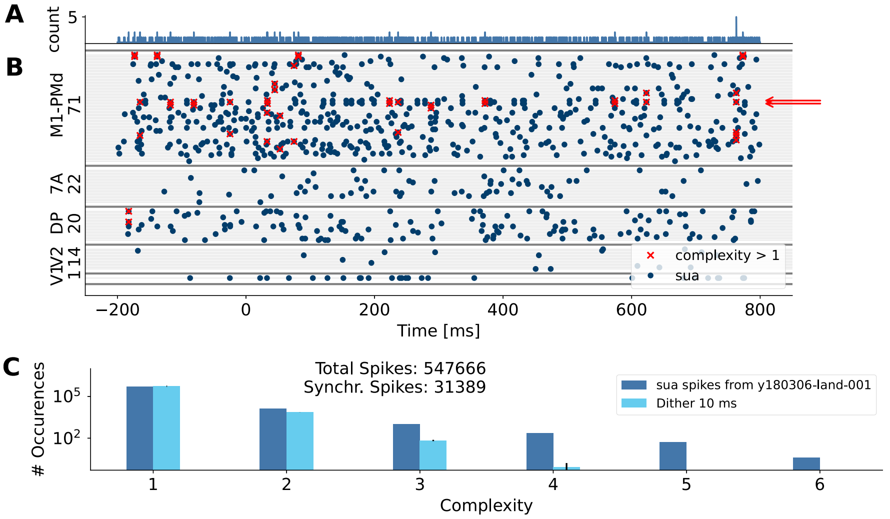

Figure 4.1: Synchrofacts in SUAs. The raster plot (**B**) shows the spike times of all SUAs recorded in the session `y180306-land-001`. Times are relative to the first peripheral target onset ($t_{\text{target onset}} = 107.9676\,\text{s}$, right target, marked with dashed vertical line). Each row contains the spiketrain of one single unit; rows are sorted by recording area. The total number of units per recording is printed on the panel's left. Spikes that are recorded on the same sampling time point across different units (detected via `elephant.spike_train_synchrony.Synchrotool` with `spread`$= 0$) are marked with a red cross. The two red, horizontal arrows point at two spiketrains in M1/PMd which are similar and exhibit several synchronous spikes. A zoom of the shaded area between $t \in 700, 800\,\text{ms}$ will be shown in Figure 4.2. The top panel (**A**) shows a histogram at sampling rate precision (bin size $b = 1/30000\,\text{s}$) of all the SUAs. The panel on the bottom (**C**) shows distributions of histogram entries (complexity distributions) from empirical (blue) and dithered (light blue) data from the whole duration of the sessions on a log-scale. The dithered data shown here are the mean of five dithering surrogate datasets, and the error bars show the standard deviation.

Note that the typical duration of one action potential is around $1-2$ ms (see Section 1.1). A synchronization at sampling rate precision would require a way of synchronizing faster than spike transmission, which is unlikely.

In the following, we will refer to synchrofacts (Torre et al., 2016) as hyper-synchronous putative spikes at sampling rate precision of the recording system, sometimes involving a large number of channels, which are unlikely to represent neuronal activity. The order of a synchrofact is defined by the number of putative synchronous spikes (e.g., three spikes being synchronous at sampling rate precision would be called a synchrofact of order 3).

Up to now, we looked at the spike sorted SUA, in fact, also other threshold crossings (multi unit activity (MUA) and noise units) are affected by excessive synchronization. To illustrate this, Figure 4.2 shows a zoom into the greyly shaded time stretch from Figure 4.1 containing spiketrains of all unit types.

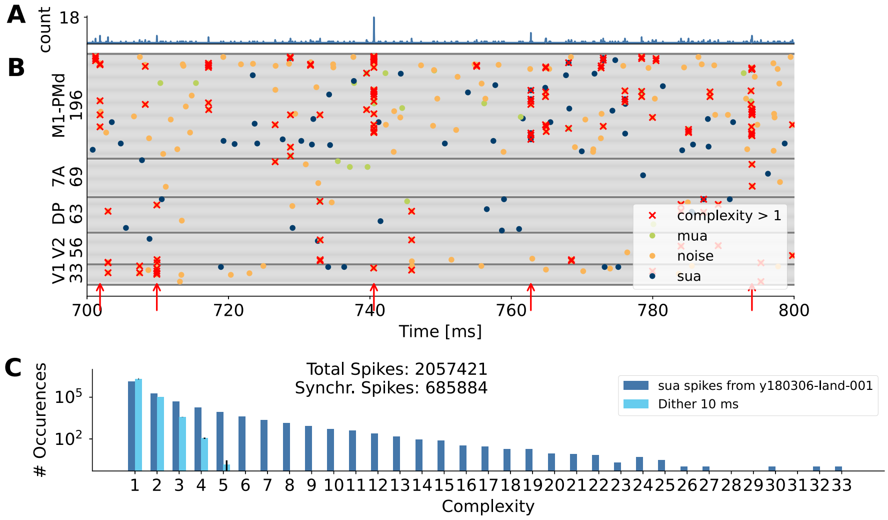

Figure 4.2: Synchrofacts in all unit types. The figures are organized as Figure 4.1 and show a zoom of the greyly shaded area from that figure. Besides SUA, this plot also includes MUA and threshold crossings, which have been classified as noise. The red vertical arrows point at events for which the number of synchronous spikes over all shown units is larger than 4.

While the display in Figure 4.1 suggests that only some SUA spiketrains are highly correlated, the occurrence of synchrofacts in all types of units, predominantly in noise units (see Figure 4.2), indicates that the origin might be observable in the raw data traces.

Qua natura, there is a relationship between the raw signals and the spikes sorted into SUA, MUA, and noise units. Thus, the spike sorting procedure is naturally reflected in the spiking activity.

A crucial parameter is the threshold that is used to extract the spikes. As described in Section A.1, to obtain spike-sorted data, a few preprocessing steps have been performed: First, the raw recorded extracellular voltages are spectrally band-pass filtered between 250 Hz and 7500 Hz. Second, for the displayed session `y180306-land-001`, threshold crossings are extracted from these filtered data by a threshold that has been set by the experimenter during each recording session (online) (see Paragraph A.1.2). Third, the extracted waveforms of the threshold crossing events are grouped into analyzed SUA MUA and noise units during manual spike sorting by the experimenter independently per channel. Hence, the spike sorter does not detect potentially synchronous spike waveforms on multiple channels.

The following section illustrates this intricate relationship between raw signals, synchrofacts, and spike sorting output.

4.2 CHARACTERIZATION OF ARTIFACTS

The visual inspection of the spike-sorted units and the corresponding high-pass filtered raw signals around time points of high-order synchrofacts lead to a characterization of three main artifact types, which will be explained in the following.

4.2.1 *Crosstalk*

We refer to pairs of channels showing a high cross-correlation across all frequency bands as *crosstalking*. This crosstalk eventually leads to simultaneous threshold crossings. Figure 4.3 shows the band-pass filtered signals and the resulting spike times of sorted units of some channels of the motor array. It is clearly visible that the signals of channels 91, 92, 93, and 96 are highly similar and essentially exhibit the same spikes.

It is likely that the spike originates in the channel where the spike waveform has the highest amplitude (here, channel 96) and then bleeds over to the other channels with different strengths. The spike observed at $t \sim 7.4\,\mathrm{ms}$ on channel 91 does not seem to affect the other channels except for channel 92. This hints at the nature of the coupling that leads to the crosstalk and would argue against a reciprocal (symmetric) bleeding of signals between channels.

In this display, the similarity of waveforms is rather obvious; during spike sorting, however, as explained in Paragraph A.1.2, each channel is treated independently, such that these similarities of signals easily go unnoticed.

Figure 4.4 illustrates crosstalk at the example of the visual and parietal arrays. The cross-correlation coefficient between two signals is a simple measure to uncover a stable similarity at the level of the band-pass filtered raw signals (as observed in Figure 4.3). The low-frequency content of the electrophysiological signal (e.g., local field potential (LFP)) is known to be similar across the spatial scale of a Utah array.

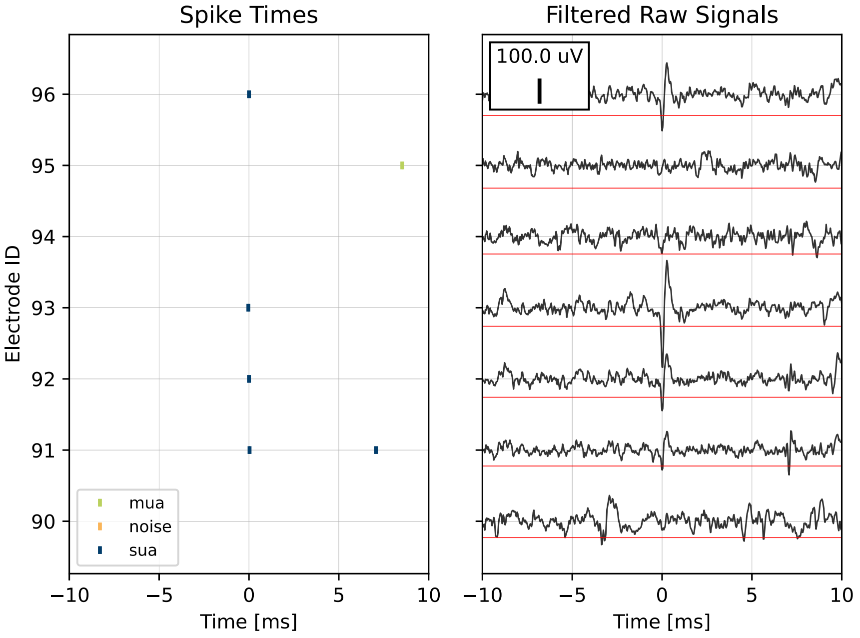

Figure 4.3: Spike times and filtered raw signals showing crosstalk signature. Both panels are aligned to $t = 16.46587\,\mathrm{s}$ and show data from the motor array in `y180116-land-001`. The red lines on the right panels show the spike extraction threshold set by the experimenter during the recording session. This type of figure has been developed by Sprenger, 2014.

The high-frequency content, however, is expected to be dampened by the neural tissue and not measurable on several electrodes. In this example, cross-correlation coefficients between electrodes on the secondary visual cortex (V2) array seem excessively correlated.

It is, however, difficult to clearly define pairs of channels to be crosstalking as we do not find a sharp bimodal distribution of the cross-correlation coefficients, but rather a smooth distribution; thus, no threshold can be set.

Panel **B** in Figure 4.4 relates the cross-correlation coefficient to the percentage of synchrofacts contained in the spiking of a unit. We observe the tendency that a higher cross-correlation leads to more synchrofacts. The point clouds suggest that setting a threshold to separate the good and bad units or channels is reasonable.

Figure 4.4 shows that crosstalking channels tend to be close on the array mapping and/or the connector mapping. The same plot for the motor array can be found in the appendix Figure A.1.

Notably, the composition of crosstalking channels appears to be changing across sessions (data not shown here).

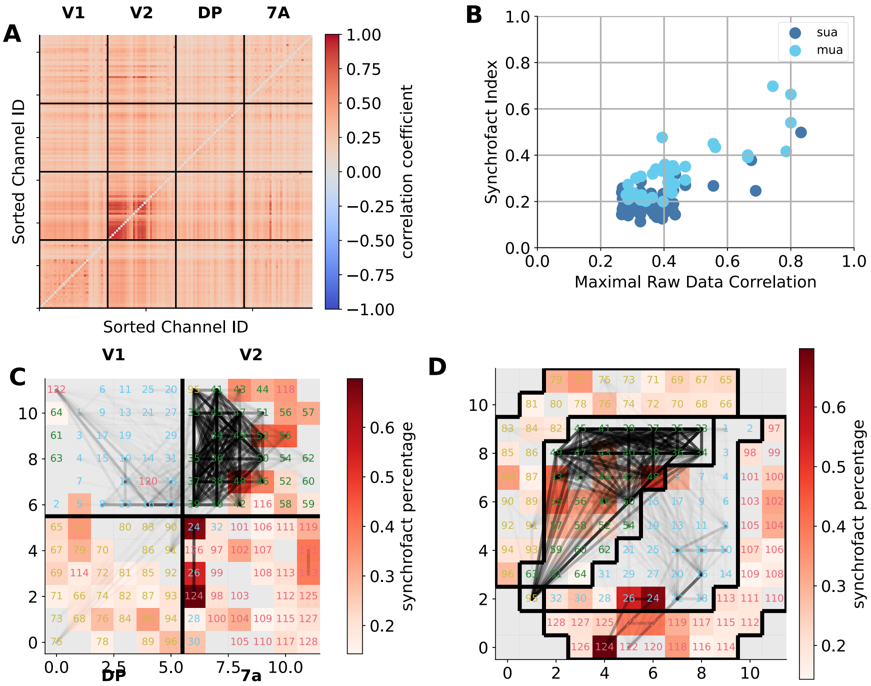

Figure 4.4: Panel illustrating features of the artifact called crosstalk. The data presented in this figure stem from the visual-parietal arrays recorded in session `y180306-land-001`. **A**: Matrix showing the cross-correlation coefficient calculated between pairs of channels. The raw recorded extracellular voltages are spectrally band-pass filtered between 250 Hz and 7500 Hz with a fourth-order Butterworth filter prior to calculating the correlation coefficient over the whole duration of the session. **B**: Scatter plot relating the maximal raw data correlation (maximal value of a row in panel A) on the x-axis to the percentage of spikes participating in synchrofacts of a certain unit (SUA in blue or MUA in light blue) on the y-axis. Here, the synchrofact detection was performed only across the visual-parietal areas with a `spread`$= 2$ (as was chosen to be the case in the preprocessing pipeline). The lower two panels show the topography on the array (left, **C**) and the connector (right, **D**). Each little square belongs to a channel with the channel ID (number) being colored according to the physical connector (bank) demarcated in panel **D**. The shades of red illustrate the average synchrofacts percentage across all units on that channel. Connections between channels are fully transparent up to a cross-correlation coefficient of $c_{X,Y} > 0.4$. The transparency decreases with rising coefficient and vanishes for $c_{X,Y} = 1$.

4.2.2 *Common noise*

We refer to simultaneous deflections (blips) visible on all channels of the array as common noise, as they are common to all channels of an array or even the connector. These deflections mostly do not resemble a spike; however, they lead to threshold crossing and might mistakenly end up in a sorted unit (see channel 43 in Figure 4.5).

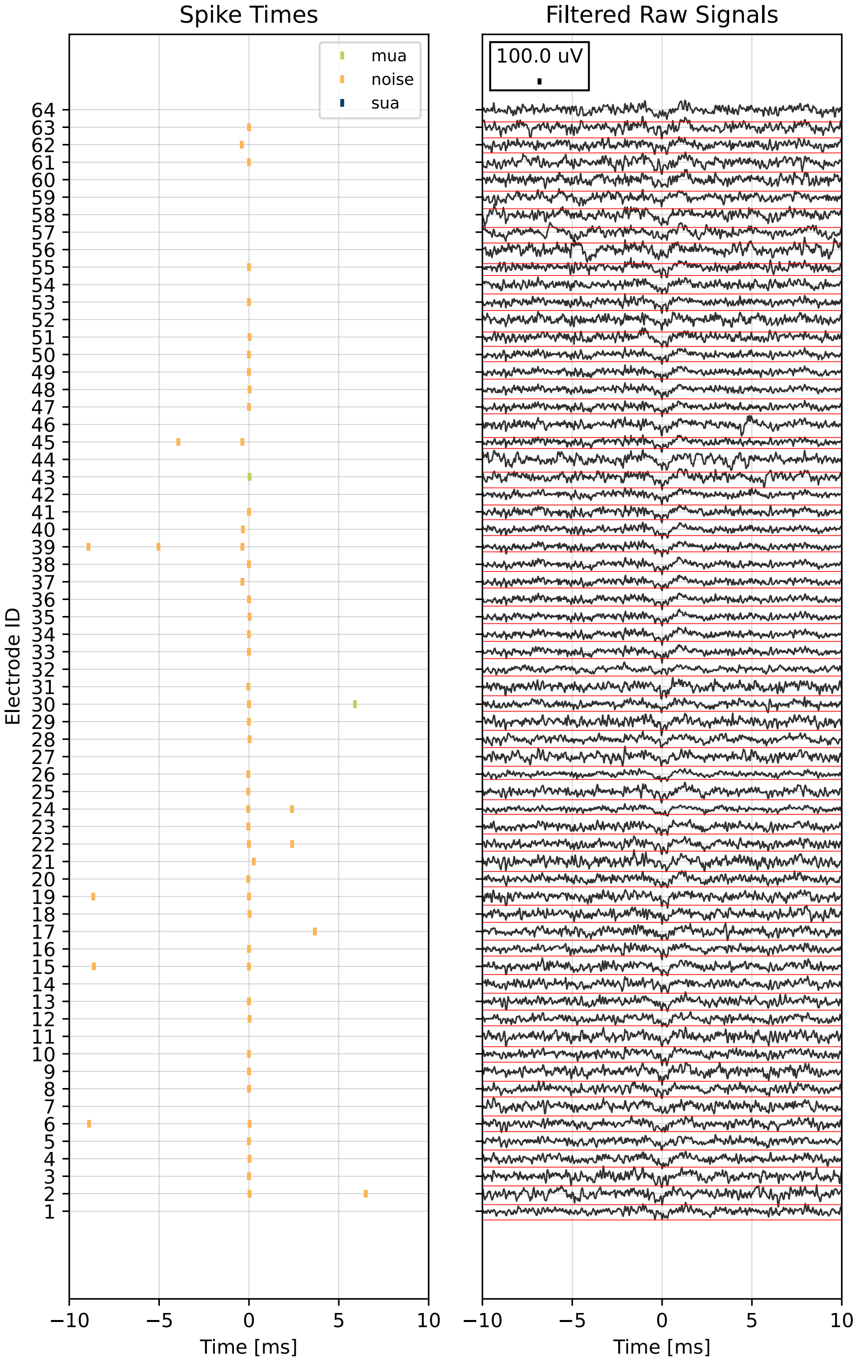

Figure 4.5: Spike times and filtered raw signals showing a common noise signature called long blip. Both panels are aligned to $t = 125.8169\,\mathrm{s}$ and show data from the visual-parietal arrays in `y180306-land-001`. The figure shows the same details as Figure 4.3

Furthermore, we distinguished between fast and slow blips (Table 4.1) because the distribution of blip widths turned out to be bimodal. An example of a slow (long) blip is shown in Figure 4.5 and an example of a fast (short) blip can be found in the appendix Figure A.2. The width of these deflections can be used to estimate their frequency content.

blip type	width	frequency
slow	$\sim 1\,\text{ms}$	1000 Hz
fast	$\leq 0.25\,\text{ms}$	$\geq$ 4000 Hz

Table 4.1: Frequency content of slow (long) and fast (short) blips.

Indeed, we find (see Figure 4.6) that the power spectrum shows a broad region of elevated power between $\sim 2000 - 5000\,\text{Hz}$, particularly in the channels of the visual and parietal arrays, which by visual inspection showed more deflections than the motor array.

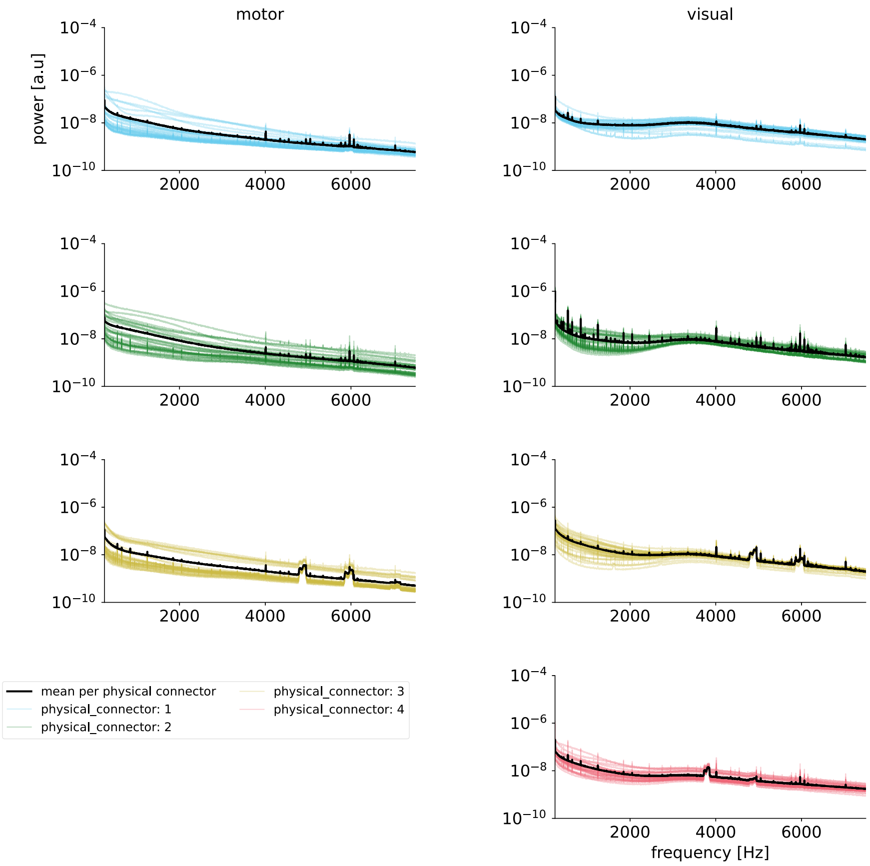

Figure 4.6: Power spectral densities PSD reflect common noise. Power spectral densitys (PSDs) of all recording channels in the motor (left) and the visual-parietal arrays (right). The traces are colored according to the physical connector bank on the connector.

Besides the above-mentioned elevation in power, we furthermore discovered sharp peaks in the power spectra.

4.2.3 *Peaks in power spectrum*

We termed this artifact peaks in the power spectrum or narrow-band oscillatory noise. With these terms, we refer to the signals that give rise to sharp peaks in the power spectrum which typically have a width of $\sim 5 - 50\,\text{Hz}$ and are observed in frequencies from $\sim 2000 - 15000\,\text{Hz}$.

While most of these peaks remain stable at a certain frequency, others move over time and thus wash out (see Figure 4.7). These ones give rise to broader peaks with a power spectral density higher than the average but lower than those of the sharp peaks.

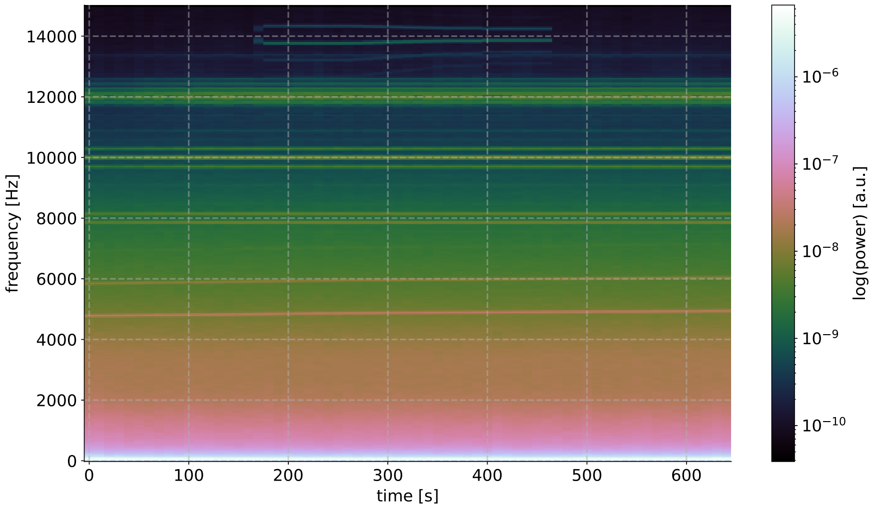

Figure 4.7: Time-resolved PSD of channel 70 from the visual-parietal arrays from session `y180306-land-001`. The time axis was segmented into $\Delta t = 10\,\text{s}$ chunks and the PSD per segment was obtained via `scipy.signal.welch()` with `nperseg`$= 600$. Color encodes the power on a logarithmic scale. Note that the elevations between $\sim 4000 - 6000\,\text{Hz}$, visible as broad peaks in Figure 4.6, and around $\sim 14000\,\text{Hz}$ drift over time

Typically the groups of channels which show those sharp peaks belong to the same *bank* of the Blackrock system. This is illustrated in Figure 4.8, where the relative peak height of the PSDs is plotted on the array and connector mapping. A similar observation, that the signals within a cable bundle or connector bank show correlated signals has been made previously (Mineault, 2011).

Up to now, we have not found an isolated effect of these peaks on the spiking activity.

4.2.4 *Superposition of problems*

The three artifact types defined above co-exist in the data and are intertwined with actual neuronal activity. The simplest model, yet an illustrative one, would be a linear superposition of signal components:

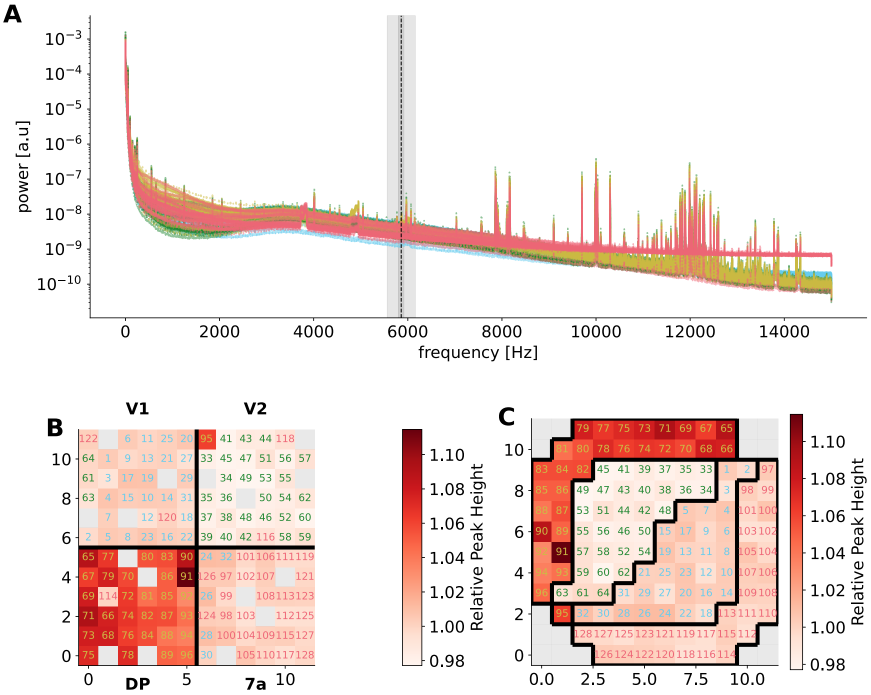

Figure 4.8: Peaks in PSDs related to connector bank. Panel **A** shows the PSD of all channels from the visual-parietal arrays from session `y180306-land-001`. The traces are colored according to the physical connector bank on the connector, same as in Figure 4.6. The signals are shown as stored in the `.ns6`-file, i.e. no further filtering was applied. To estimate the relative peak height around 5860 Hz the mean peak power in the range frequency $f_{\text{peak}} = 5860\,\text{Hz} \pm 60\,\text{Hz}$ (centered shade) was related to the mean baseline power in the range frequency $f_{\text{baseline}} \in 5560 - 6160\,\text{Hz}$ (surrounding shade). These relative peak heights per channel are shown in the form of a heatmap in the array mapping (left, **B**) and the connector mapping (right, **C**).

$$X_{\text{signal}} = X_{\text{neuronal}} + X_{\text{crosstalk}} + X_{\text{common noise}} + X_{\text{peaks in PSD}} + X_{?} \quad (4.1)$$

where $X_?$ stands for signatures that might be due to artifacts but are not yet captured by the three artifact types discussed above.

The idea of the superposition of signals allows for a more differentiated analysis: From the analysis of crosstalk in Figure 4.4, we know that most channels in area V2 are highly correlated (channel IDs $\sim 30 - 50$). With this information, Figure 4.5 can be interpreted more carefully: A close look at $\sim 30 - 50$ reveals a close similarity of the overall signals, a signature of crosstalk. However, the blip is observed not only in those "crosstalking" channels but across all the displayed channels, likely being caused separately from the crosstalk.

4.2.5 *Synchrofacts are symptoms of underlying artifacts*

The idea of a superposition of problematic signal components allows for a broader perspective on the discussion about synchrofacts: Synchrofacts seem to be a common symptom of various types of underlying noise signals. Above, we reasoned that at least crosstalk and common noise can give rise to synchrofacts. The impact of the narrow-band oscillatory noise on synchrofacts was not conclusively shown.

A further complication in the discussion about synchrofacts is imposed by the nonlinear spike sorting process to go from (noisy) raw signals to sorted units. Given contaminated signals, whether or not they suffer from synchrofact crucially depends on the spike extraction threshold and the judgment of the person who sorts the data, when a waveform belongs to a SUA, MUA or noise unit.

In particular, the spike extraction threshold, which used to be set online during the experiment, has an impact: The more permissive the threshold was chosen, the more potential artifacts are also reflected in the threshold crossings, making it more difficult for the spike sorter to reject non-neural crossings.

Example 1: A deflection on all channels, also called common noise, might lead to several simultaneous threshold crossings and thus to a synchrofact of a high order (as high as there are synchronous threshold crossings). Such a deflection might, for example, be caused by switching on/off a lamp.

Example 2: Channel A shows a spike. Channel A crosstalks to Channel B, then simultaneously, you observe a spike in Channel B. Thus, you see a synchrofact of order 2.

4.3 HYPOTHESIZED SOURCES IN THE SETUP

In previously recorded data from a similar experimental setup for the reach-to-grasp project (R2G, (Brochier et al., 2018)), resembling synchronous events have been identified and linked to the raw voltage data (Sprenger, 2014).

The main cause for synchrofacts in the old dataset was hypothesized to be the analog signal transmission from the headstage to the digital hub via the so-called patient cable, which was likely prone to perturbations by electrical noise.

In the V4A-setup, however, signals are already digitized at the headstage (see Figure 3.3). To resolve the issues at the source, it is necessary to understand the origins of the signatures that were described above. The following paragraph is admittedly speculative, yet reflects the state-of-the-art understanding of our collaborative investigations into the matter.

CROSSTALK We hypothesize that crosstalk arises due to physically touching cables (e.g. due to broken isolation in a wire bundle leading from the array to the connector, or touching wires on the back of the array).

During the implantation of the arrays, the relatively long cable bundles (primary visual cortex (V1): 4 cm, V2: 5 cm, dorsal prelunate (DP): 6 cm, area 7a (7a): 8 cm) leading from the array to the connector pedestal have to be accomodated below the skull.

Blackrock supplies a tool name the "Digital Neural Signal Simulator" (see Figure 3.3), which can be used to replace signals from a connector with artificial ones. We used this device to test the setup, observed no crosstalk in the simulated signals, and concluded that crosstalk is produced in a prior stage of signal transmission (e.g., prior to or at the connector level).

The contacts of connector land grid array (LGA) connect to the headstage through a filament: It is supposed to guide the electrical current from one contact on the connector to the corresponding contact on the headstage. We tested the effects of pollution on the performance of the filament: E.g. clogged the filament with blood or left residual cleaning alcohol undried. We observed that this might lead to crosstalk at between contacts. However, regular cleaning and replacement of the filament can prevent this from happening.

The large group of highly correlated channels in V2 (see Figure 4.4), however, seems not to persist across all sessions. Late sessions (e.g. `j210913-land-001`) in Jazz do not show these correlations. The lab book during this period of recordings reports that the combination between Cereplex and connector was changed (e.g. the Cereplex that was previously used to connect to the motor array was switched to the visual connector and vice versa).

COMMON NOISE As the deflections considered as the artifact common noise can be observed on all arrays simultaneously, we assume that they stem from electromagnetic waves traveling through the setup. Alternatively, the ground signal of the electrical grid in the building where the experiments are performed fluctuations during events like switching on or off a lamp. Interestingly, the effect is stronger on all arrays in the visual and parietal areas.

PEAKS IN POWER SPECTRUM The signature of a sharp peak in the power spectral density is also observed in systems suffering from ground loops (Gaboian, 2000). We suggest that a ground loop might be the cause.

In the V4A setup two parallel data streams run from the array/-connector to the neural signal processor (NSP) (see Figure 3.3). A huge noise signal is present if the two HDMI cables leading from the headstages to the digital hubs are not bridged. We observed that the amplitude of the power spectral density peaks is drastically influenced by the connection between these two HDMI cables and a custom solution for bridging them was ordered from Blackrock and used henceforth. The precise date can be inferred from a change of Cereplexes, which happened simultaneously.

4.4 REMOVAL OF ARTIFACTS

Artifacts can be removed in two stages:

1. The *setup* can be improved in order to eliminate artifacts
2. The *recorded signal* can be post-processed, and the identified signatures can be removed as well as possible.

In the long run, it is best to try to remove any issue in the setup (if possible) and resort to the post-ancestry only if necessary. However, the latter is also necessary because many recorded sessions contain the discussed artifacts, and we need to deal with them.

4.4.1 *Removal of artifact sources in the setup*

For the removal of the artifact sources, thorough before-and-after testing needs to be implemented to judge the effectiveness of a given measure.

Given the signatures and hypothesized sources, we, first of all, advise for preventative measures prior to the implantation of another experimental subject. This entails testing the arrays and cable bundles for crosstalk.

Furthermore, we propose regular impedance measurements (Cody et al., 2018) of the electrodes to track eventual degradation. Prior to each experiment, a live preview of cross-correlated channels and high-frequency noise could give the incentive to clean the connector, screw it tightly to the headstage or check the bridging cable between the connectors.

To check the impact of a fluctuating ground signal on the setup, we proposed to test a DC power source to run the whole equipment.

4.4.2 *Removal of artifacts in existing data*

Crosstalk can be detected by calculating the cross-correlations and relating these to the number of synchrofacts shown in Figure 4.4. A threshold, which has to be chosen, can then be used to identify problematic channels or units, and these can be annotated. Based on this annotation the user can subsequently decide to include or exclude the data from analyses.

As for the common noise, a re-referencing technique could be employed. Methods could consist of removing the median signal across all channels from each channel as commonly used by the community, or calculating the a principle component analysis (PCA) and removing the first component. The latter allows for more local removal of a noise component.

SpikeInterface (Buccino et al., 2020), currently discusses the implementation of such a functionality.

The impact of the peaks in the power spectrum on synchrofacts is not yet conclusive. A possible way of removing the peaks one by one could be a sequential application joint decorrelation (De Cheveigné et al., 2014), a versatile dimensionality reduction method.

4.5 LIMITATIONS

Any method of removing artifacts requires a measure of success to answer the question: When are we satisfied? This is problematic, as the signals have no ground truth to test against.

In the end, any scientific outcome should, however, be rather robust against the details of preprocessing as the precise spike sorting routine.

For a large part of this these, the measure of success was to reduce the number of synchrofacts present in the data to the level that is expected by chance.

In such a scenario, the evaluation of methods that manipulate the raw signals, as, e.g., a sequential application of joint decorrelation, unfortunately, requires a new spike extraction and a new spike sorting. As explained in Section A.1 this is a lengthy process and showed not to be practical without automatic spike sorting routines.

Within the scope of this thesis, we did implement a pipeline with artifact characterization and artifact removal on the raw data, but the crucial step of subsequent spike sorting and, thus, evaluation was lacking. Recent developments in the accessibility of automatic spike sorting methods (e.g., SpikeInterface) make such an endeavor possible.

4.6 EMPLOYED WAY OF ENSURING USABILITY OF DATA

Due to the lack of conclusive measures of success for the artifacts common noise and peaks in the power spectrum, we dealt with the artifact crosstalk for subsequent analyses.

In the first step, we analyzed manually sorted sessions. Therefore, we chose to annotate those channels and units that are exceedingly correlated to any other channel and also exhibit a large synchrofact percentage (see Figure 4.4). The single unit analysis presented in the next chapter, was performed on all sorted units (SUA and MUA), but for the end result, only those meeting a strict selection by quality metrics were permitted. The selection criteria were a larger firing rate than 1 Hz and a waveform signal-to-noise ratio (SNR) larger than 2.5 (for details, see Section A.1).

With this procedure, a reasonable amount of units in M1/PMd were gathered across the manually sorted sessions. Due to a low number of recorded units in V1, a large part of rejected channels in V2 and the overall smaller arrays in the visual-parietal recording sites, the number of neurons that remained after the strict selection was very low (see in Table 4.2 row with Alexa and Fred as sorter).

To overcome this bottleneck, only the visual-parietal area has been automatically spike sorted for more sessions (see details Section A.1.3). Knowing that a large part of the data is contaminated with crosstalk, we aimed to reject these channels even before sorting. To achieve that, we band-pass filtered the raw signals between 250 Hz and 7500 Hz and extracted threshold crossings per channel by setting a threshold as

$$\mathrm{Thr} = -5 \cdot \mathrm{median}\left(\frac{|x|}{0.6745}\right) \tag{4.2}$$

where $|x|$ denotes the median absolute deviation of the voltage.

With the resulting spiketrains from threshold crossings, we replicated the plots as in Figure 4.4**B** by calculating a synchrofact percentage per channel. We then used these plots (see Figure 4.9) to manually set rejection thresholds for the maximum correlation between channels and the synchrofact index. Only channels that lie below these two thresholds were subsequently automatically spike-sorted and used for analysis. In Figure 4.10 the result of such a procedure is visualized for three different sortings. Not that for the sorting of Alexa without channel rejection most complexities show more occurrences than the dither (chance synchrony) prediction.

For Mountainsort4 we chose the parameters listed in Table A.2. Here, the adjacency radius is -1 and was set as default. It allows spikes to be detectable on all channels. We observed in complexity distributions that this setting effectively removes any synchrofacts, including chance synchrony.

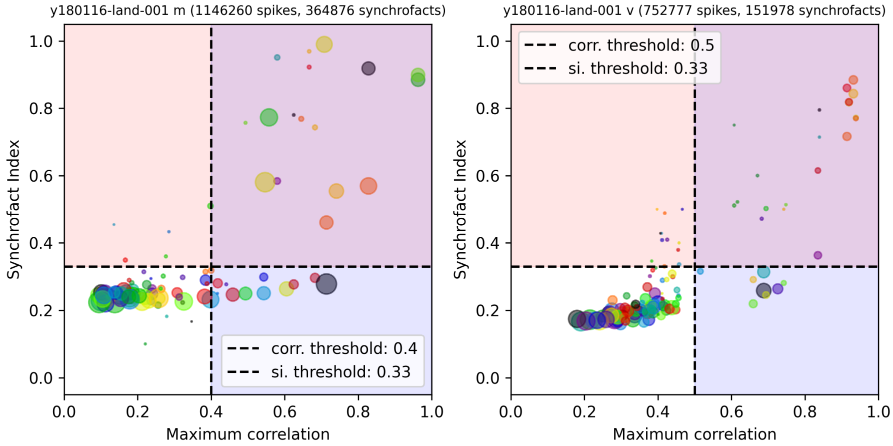

Figure 4.9: Crosstalk exclusion thresholds that were chosen for `y180116-land-001` shown in a scatter plot as in Figure 4.4**B**. Each circle corresponds to one channel. The size of the circle is proportional to the amount of detected threshold crossings. The colors are random. Only channels below the horizontal and left to the vertical line (area without shade) were chosen for the analysis.

In the following analyses, we will use the Mountainsort4 sorting. As we will look into the rate coding of the neurons, it probably does not hurt to be very conservative and remove any synchrony. A similarly conservative choice of synchrofact removal was taken in (Torre et al., 2016).

Table 4.2 lists all used sessions and the numbers of units before and after rejection for all the different spike sortings that were used. Table 4.3 summarizes the former table and lists the number of neurons pooled over sessions.

[ht]

session name	sorter	V1/ V2	V1/ V2$_{\text{strict}}$	DP	DP$_{\text{strict}}$	7a	7a$_{\text{strict}}$	M1/ PMd	M1/ PMd$_{\text{strict}}$
y180116 land 001	Alexa	44	21	41	20	41	16	118	51
	Fred	✗	✗	✗	✗	✗	✗	✗	✗
	mountainsort4	16	14	28	21	28	15	✗	✗
	tridesclous	5	5	12	11	14	12	✗	✗
y180221 land 002	Alexa	20	5	33	11	39	20	113	29
	Fred	✗	✗	✗	✗	✗	✗	✗	✗
	mountainsort4	4	4	14	10	24	15	✗	✗
	tridesclous	1	1	8	7	17	15	✗	✗
y180306 land 001	Alexa	24	7	31	16	37	14	101	31
	Fred	✗	✗	✗	✗	✗	✗	✗	✗
	mountainsort4	8	5	22	17	22	15	✗	✗

session name	sorter	V1/ V2	V1/ V2$_{\text{strict}}$	DP	DP$_{\text{strict}}$	7a	7a$_{\text{strict}}$	M1/ PMd	M1/ PMd$_{\text{strict}}$
	tridesclous	4	3	11	11	9	8	✗	✗
y180306	Alexa	25	10	31	14	38	14	102	33
draw	Fred	✗	✗	✗	✗	✗	✗	✗	✗
002	mountainsort4	7	6	24	20	22	17	✗	✗
	tridesclous	2	2	12	11	11	9	✗	✗
j210204	Alexa	✗	✗	✗	✗	✗	✗	✗	✗
land	Fred	63	1	40	5	41	5	155	58
001	mountainsort4	2	1	6	5	6	3	✗	✗
	tridesclous	✗	✗	3	2	6	5	✗	✗
j210208	Alexa	✗	✗	✗	✗	✗	✗	✗	✗
land	Fred	31	2	24	4	26	2	110	43
001	mountainsort4	1	1	5	5	4	2	✗	✗
	tridesclous	✗	✗	2	2	3	2	✗	✗
j210212	Alexa	✗	✗	✗	✗	✗	✗	✗	✗
land	Fred	✗	✗	✗	✗	✗	✗	✗	✗
001	mountainsort4	1	1	6	5	7	6	✗	✗
	tridesclous	✗	✗	3	3	6	5	✗	✗
j210223	Alexa	✗	✗	✗	✗	✗	✗	✗	✗
draw	Fred	✗	✗	✗	✗	✗	✗	✗	✗
002	mountainsort4	✗	✗	8	8	3	3	✗	✗
	tridesclous	✗	✗	4	4	2	2	✗	✗
j210301	Alexa	✗	✗	✗	✗	✗	✗	✗	✗
draw	Fred	✗	✗	✗	✗	✗	✗	✗	✗
001	mountainsort4	✗	✗	5	5	5	5	✗	✗
	tridesclous	✗	✗	1	1	3	3	✗	✗
j210601	Alexa	✗	✗	✗	✗	✗	✗	✗	✗
land	Fred	✗	✗	✗	✗	✗	✗	✗	✗
001	mountainsort4	2	1	10	9	4	2	✗	✗
	tridesclous	✗	✗	7	7	4	2	✗	✗
j210608	Alexa	✗	✗	✗	✗	✗	✗	✗	✗
land	Fred	✗	✗	✗	✗	✗	✗	✗	✗
001	mountainsort4	1	✗	13	9	9	8	✗	✗
	tridesclous	✗	✗	9	9	7	7	✗	✗
j210729	Alexa	✗	✗	✗	✗	✗	✗	✗	✗
draw	Fred	✗	✗	✗	✗	✗	✗	✗	✗
001	mountainsort4	6	5	14	13	11	11	✗	✗

session name	sorter	V1/ V2	V1/ V2$_{\text{strict}}$	DP	DP$_{\text{strict}}$	7a	7a$_{\text{strict}}$	M1/ PMd	M1/ PMd$_{\text{strict}}$
	tridesclous	1	1	10	9	8	8	✗	✗
j210901 draw 001	Alexa	✗	✗	✗	✗	✗	✗	✗	✗
	Fred	✗	✗	✗	✗	✗	✗	✗	✗
	mountainsort4	5	5	14	13	8	6	✗	✗
	tridesclous	4	4	9	9	7	4	✗	✗
j210913 land 001	Alexa	✗	✗	✗	✗	✗	✗	✗	✗
	Fred	✗	✗	✗	✗	✗	✗	✗	✗
	mountainsort4	8	5	12	11	11	7	✗	✗
	tridesclous	3	3	4	4	11	8	✗	✗
j211007 land 001	Alexa	✗	✗	✗	✗	✗	✗	✗	✗
	Fred	✗	✗	✗	✗	✗	✗	✗	✗
	mountainsort4	7	5	11	10	12	10	✗	✗
	tridesclous	4	4	4	4	8	8	✗	✗
j211103 land 002	Alexa	✗	✗	✗	✗	✗	✗	✗	✗
	Fred	✗	✗	✗	✗	✗	✗	✗	✗
	mountainsort4	7	4	13	9	10	5	✗	✗
	tridesclous	4	4	7	7	9	7	✗	✗

Table 4.2: Table summarizing the unit count in each area per session and sorter.

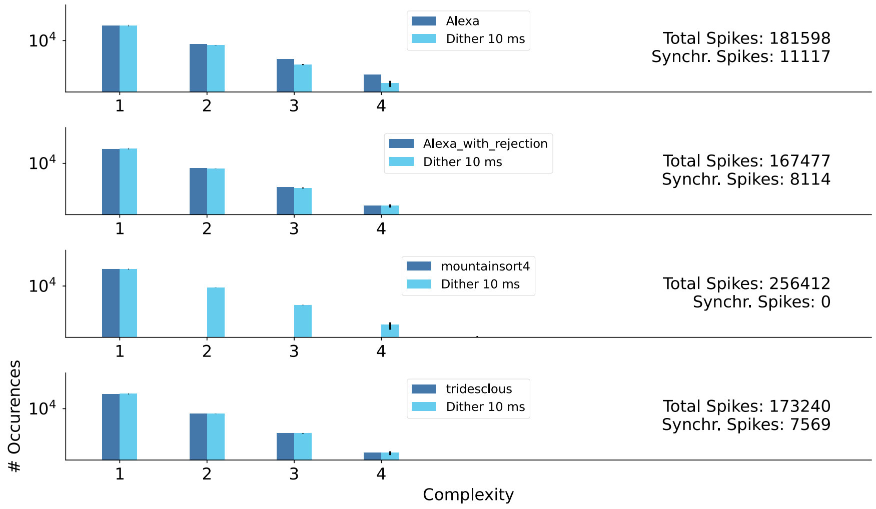

Figure 4.10: Complexities (after channel rejection) for different sorters for all visual-parietal channels in `y180306-land-001`.

subject	sorter	V1/V2$_{\text{strict}}$	DP$_{\text{strict}}$	7a$_{\text{strict}}$	M1/PMd$_{\text{strict}}$
Enya	Alexa	43	61	64	144
	Fred	✗	✗	✗	✗
	mountainsort4	29	68	62	✗
	tridesclous	11	40	44	✗
Jazz	Alexa	✗	✗	✗	✗
	Fred	3	9	7	101
	mountainsort4	28	102	68	✗
	tridesclous	16	61	61	✗

Table 4.3: Table summarizing the unit count in each area per sorter pooled across sessions.

With the end of this chapter, we conclude the preliminaries for the actual investigation of the data to answer the research question:

Is the bimodality of the distribution of preferred directions (PDs) that has been observed in M1 and PMd/ventral premotor cortex (PMv) also present in the parietal and visual cortex of macaque monkeys that perform a visually guided reaching task?

We have reviewed the literature on the cortical systems involved in eye-hand coordination, have explained the details of the experimental setup, including necessary preprocessing steps and finally excluded the most severe cause of artifacts to avoid systematic biases in the recorded data.

Freedom is what you do with what's been done to you.

— Jean-Paul Sartre

5

SINGLE UNIT ACTIVITY ANALYSIS

In the previous chapters, we first reviewed neuroscientific background (Chapter 2), then exhibited the details of the experimental setup (Chapter 3) of the Vision-for-Action (V4A)-project and finally characterized artifacts in the neural recordings (Chapter 4) and proposed a way of dealing with the apparent issues. All of these are necessary prerequisites to answer scientific questions with experimental data. In this chapter, I present an analysis of the single unit activity that we isolated as explained in the end of the last chapter.

5.1 INTRODUCTION

Awake animals and humans constantly interact with their environment: grabbing the toothbrush in the morning, reaching for the coffee mug, and opening the laptop lid to start working; in all these circumstances, we exert meaningful control of bodily action, which requires sensory perception of body posture and external world. This is often referred to as the action-perception loop (Noel et al., 2022).

Visually guided reaching tasks, by definition, emphasize the importance of visual information to perform concerted sequences of muscle activations that eventually lead to desired limb movements.

Research suggests that visual information enters the cortex in the primary visual cortex, and, subsequently flows along the ventral and the dorsal pathway (Ungerleider et al., 1982) (see Section 2.1). The ventral stream, which projects to the inferotemporal cortex, is associated with recognition or perception, and thus was also termed the *what* or *vision-for-perception* pathway. In contrast, the dorsal stream projects to the posterior parietal cortex, is related to spatial vision, and called *where* or *vision-for-action* pathway due to its crucial role in movement execution (Goodale et al., 1992b).

As reviewed in Section 2.2, most of the occipital cortex is occupied by visual areas, in particular the primary visual cortex (V1) and higher order areas (Felleman et al., 1991). Although visual areas are shown to receive feedback connections from higher-order cortices (Wang et al., 2022b), the dominant factor governing their activations seem to be visual variables. Talluri et al. (2022) recently demonstrated that spontaneous movements explain only a small part of the variance measured in the macaque V1. This is in contrast to observations in mice (Musall et al., 2019; Stringer et al., 2019a), which show strong V1 activations also for other behaviors, e.g., movements.

Following the two visual pathway hypothesis, areas in the posterior parietal cortex have been shown to integrate sensory information of various modalities and to be activated prior to eye or limb movements (see Section 2.4 for a literature review). Such neural activations have been interpreted to code the intent or motor plan rather than the actual execution. The prevailing hypothesis is that motor intent is subsequently transmitted to premotor and motor cortex, from which corticomotoneuronal cells have descending connections to motor neurons in the spinal cord (Strick et al., 2021) that ennervate muscles (see Section 2.3.1).

Although the debate about what neurons in the motor cortex encode is not yet resolved (cf. Section 2.3.2), it is well established that the majority of neurons in the limb area of M1 are tuned to the direction of limb movement, which classically is described by a cosine tuning

(Amirikian et al., 2000; Georgopoulos et al., 1982) that is characterized by a preferred direction (PD).

For movements in 3D, the distribution of PDs across neurons was demonstrated to be uniform (Caminiti et al., 1990; Schwartz et al., 1988). If the hand is constrained to a 2D plane by means of an exoskeleton (KINARM), the distribution of PDs across neurons, however, was shown to be bimodal (Scott et al., 2001b, 1997). Modeling studies (Codol et al., 2023; Lillicrap et al., 2013; Verduzco-Flores et al., 2022) which take into account the biomechanics of arm and constrained movement of the hand in 2D. They demonstrate that for 2D hand movements there is are directions for which groups of muscles required maximum contraction. Furthermore, across muscles, as muscles are grouped in agonist-antagonist pairs, the contraction depending on the movement angle in 2D is bimodal. In consequence, they suggest that the bimodality in PDs reflects the bimodal activations of muscles.

Recently, Suminski et al. (2015) have shown that the bimodality of the distribution of PDs extends to areas PMd and ventral premotor cortex (PMv), and, hence concluded that even these pre-motor areas are subject to the biomechanistic properties of the limb. Given this finding, one can ask whether a bimodality of PDs would be observable in further areas.

As reviewed in Section 2.4, activity in the posterior parietal cortex has been shown to respond to several modalities: eye movements (saccades), body movement, and different sensory stimuli. While movement-related activity has been demonstrated in several areas in the posterior parietal cortex (Battaglia-Mayer et al., 2000, 2007; Diomedi et al., 2021), to our knowledge the existence of a tuning for hand movement direction with an emphasis on the expect bias of PDs when the hand is constrained to 2D, has not been investigated along the dorsal visual pathway.

In this chapter, we want to answer this question by analyzing the data recorded in the V4A project as detailed in Chapter 3. In a first step, we confirm that the bias in the PDs distribution in M1/PMd is reproduced with our data and then proceed to the question: Can we observe a bimodality of PDs to hand movement along the dorsal visual pathway?

DISENTANGLING OF MULTIPLE BEHAVIORAL INFLUENCES The mixed selectivity of neurons in posterior parietal cortex (PPC), however, hinders a naive extraction of neural tuning to hand movement in integrated visuo-motor task. Effects due to visual perception and eye movements, which happen in a correlated manner to the hand movement, might evoke neural responses that then can falsely be confounded as responses to simulataneously occuring movements.

One way to deal with these confound effects is to explicitly model the neural activity of every single neuron via a rich set of behavioral regressors and, by that, isolate the unique effect of the behavior of importance. The Poisson Generalized linear model (GLM) (McCullagh et al., 1989a) is a widely used modeling approach in the neurosciences to describe the dependence of the spike count of a neuron to a variety of regressor variables (Lepage et al., 2012; Truccolo et al., 2005; Vaccari et al., 2021).

APPROACH We aim to answer the question of whether a firing rate tuning towards hand movement direction can be observed in areas along the dorsal visual pathway. If tunings exist, we furthermore ask whether the distributions of PDs in these areas are biased towards a bimodality. To this aim, we perform the following analyses:

In a first step, we employ per neuron a naive Poisson GLM modeling approach with just the sine and cosine of the instantaneous movement angle as regressors. This preliminary analysis will reveal tendencies towards a bimodal distribution of PDs in each of the recording areas. To exclude possible confounding variables, such as coincidentally triggered sensory receptive fields of neurons in certain movement directions, in a second step, we devise a more complex GLMs to describe the spike count vector via a large collection of regressors that we group into the modalities: *visual*, *eye position*, *saccade*, *hand position* and *movement*.

We make use of a procedure detailed in (Diomedi et al., 2020; Vaccari et al., 2021) to uncover overall tendencies in selectivity towards these regressor blocks in each of the recorded regions and thereby confirm the expectation of a progressive decrease of the influence of visual variables along the dorsal visual pathway and, conversely, an increase of the influence of hand movement variables.

At this stage, having confirmed that many neurons, especially in the parietal areas, are selective for movement variables, we proceed and investigate the tuning functions to hand movement direction by explicitly removing confounding variables and find that the tendency of a bimodal distribution of PDs survives.

5.2 MATERIAL AND METHODS

5.2.1 *Experiment*

In the present chapter, we analyze data from the V4A experiment which was performed with macaque monkeys. For details on the experimental setup refer to Chapter 3. The monkeys perform two variants of visuomotor coordination tasks: the *landing task* and the *drawing task* (see Section 3.4), which are supposed to probe various behavioral modalities from simple visual stimuli, proprioceptive perception and saccades to movement execution.

Note that for the purpose of this analysis, we do not cut the session into successful trials and do not discard unsuccessful trials or eventual intertrial periods. We removed the first and last 10 s of each of the recordings to avoid artifacts in the signals due to the beginning or end of the session.

5.2.1.1 *Behavioral data*

We are making use of different behavioral data recorded at a sampling rate of $f_s = 1\,\mathrm{kHz}$. Specific details can be found in Section 3.2. Limb movement is constrained to the horizontal plane by the KINARM (KINARM Exoskeleton Laboratory, BKIN Technologies) and enables the recording of the instantaneous hand position. Eye movement is tracked via the EyeLink (EyeLink system, SR Research[1]). The experiments are held in a dark room, such that all visual stimuli should be task-related and located in the work area.

5.2.1.2 *Neural data*

The recording of the neuronal signals with devices from Blackrock and more specifically chronically implanted Utah arrays is explained in Section 3.2.5. In the previous chapter (Chapter 4) we discussed apparent artifacts in these electrophysiological recordings. To avoid contamination of our results with crosstalk, we employed the procedure as explained in Section 4.6.

As a result we are analyzing units from manually sorted sessions for primary motor cortex (M1)/dorsal premotor cortex (PMd), but rely on units from automatically sorted units (see Section A.1) for primary visual cortex (V1)/secondary visual cortex (V2), dorsal prelunate (DP) and area 7a (7a). A summary of neuron numbers per session can be found in Table 4.2. For the sake of this analysis we assume that neurons recorded in different sessions are independent from each other, yielding the numbers of neurons shown in Table 4.3.

5.2.2 *Generalized linear models (GLMs)*

In systems neuroscience, it is common to use either encoding or decoding model to make sense of neural activity. Encoding models try to answer the question of what a neuron's activity encodes. On the contrary, decoding models aim at decoding behavioral observations (e.g. movements, decisions, etc.) given neural activity.

GLMs (McCullagh et al., 1989b) belong to the broad category of encoding models: With their help, it is possible to disentangle the effects that various variables have on the activity of a neuron.

---

[1] `https//www.sr-research.com`

5.2.2.1 *Formulation*

In contrast to a *general* linear model, *generalized* linear models do not exhibit a linear relationship between the independent variable and dependent variables (also called regressors or covariates, respectively).

In general, a generalized linear model can be written in vector form as

$$\vec{\lambda} = f(\mathbf{X}\vec{\beta}) \quad , \tag{5.1}$$

or with indices as

$$\lambda_t = f(\beta_0 X_{0,t} + \beta_1 X_{1,t} + \beta_2 X_{2,t} + \cdots + \beta_N X_{N,t}) \quad , \tag{5.2}$$

where λ is the dependent variable, f is a nonlinear link function, $\mathbf{X}$ the design matrix with the i-th independent variable $X_{i,t}$ as row and β the coefficients of the model, i.e. the free parameters that need to be determined via a fitting procedure.

In the neural context, it is useful to model the the firing rate λ of an underlying Poisson process as the dependent variable. Typically, this is done by assuming that the random variable Y is the spike count y_t in a certain time interval and that this follows a Poisson distribution

$$p(Y = y_t) = \frac{\lambda_t^{y_t} e^{-\lambda_t}}{y_t!} \quad . \tag{5.3}$$

In the Poisson generalized linear model (GLM) (also called the linear-nonlinear cascade model), the logarithm of the positive rate of the Poisson process is modeled to be linearly related to a sum of regressors as

$$\log \lambda_t = \mathbf{X}\vec{\beta} = \beta_0 X_{0,t} + \beta_1 X_{1,t} + \beta_2 X_{2,t} + \cdots + \beta_N X_{N,t} \quad , \tag{5.4}$$

with the zero-th row of the design matrix $\mathbf{X}$ being the intercept $\vec{X}_0 = \vec{1}$ with $\vec{1}$ the unity vector. By removing the logarithm on the left, we can identify the link function in our problem to be $f = \exp()$:

$$\begin{aligned}
\lambda_t &= f(\mathbf{X}\vec{\beta}) && (5.5)\\
&= f\left(\vec{\beta}^T \vec{x}_t\right) && (5.6)\\
&= \exp\left(\beta_0 X_{0,t} + \beta_1 X_{1,t} + \beta_2 X_{2,t} + \cdots + \beta_N X_{N,t}\right) \quad . && (5.7)
\end{aligned}$$

The encoding distribution, or likelihood, is then obtained by plugging Equation 5.7 into Equation 5.3:

$$p\left(y_t \mid \vec{\beta}, \vec{x}_t\right) = p\left(Y = y_t \mid \lambda_t = f\left(\vec{\beta}^T \vec{x}_t\right)\right) \tag{5.8}$$

$$= \frac{\left[f\left(\vec{\beta}^T \vec{x}_t\right)\right]^{y_t}}{y_t!} e^{-f\left(\vec{\beta}^T \vec{x}_t\right)} \tag{5.9}$$

For a Poisson generalized linear model the log-likehood is far simpler to calculate

$$\log \mathcal{L} = \log \mathcal{L}(\vec{\beta} \mid \boldsymbol{X}) \tag{5.10}$$

$$= \log p\left(y_t \mid \vec{\beta}, \vec{x}_t\right) \tag{5.11}$$

$$= \log \prod_{t=1}^{T} \frac{\left[f\left(\vec{\beta}^T \vec{x}_t\right)\right]^{y_t}}{y_t!} e^{-f\left(\vec{\beta}^T \vec{x}_t\right)} \tag{5.12}$$

$$= \sum_{t=1}^{T} \left(y_t \log f\left(\vec{\beta}^T \vec{x}_t\right) - f\left(\vec{\beta}^T \vec{x}_t\right) - \underbrace{\log y_t!}_{\text{constant}} \right) \tag{5.13}$$

and inserting the exponential link function $f = \exp()$ and making use of Equation 5.2.

$$\log \mathcal{L} = -\sum_t \lambda_t + \sum_t y_t \log \lambda_t - \sum_t \log(y_t!) \quad , \tag{5.14}$$

where λ_i is the mean of the Poisson distribution at time bin t and equals the predicted firing rate given the spike count y_t. The last term is constant and often omitted, sometimes expressed in a Gamma function $y_t! = \Gamma(y_t + 1)$ and can be conveniently calculated with `scipy.special.gammaln`.

In order to obtain the free parameters β_i ($i \in 0, \ldots N$) of this model, we want to maximize the likelihood of observing the data given the model. As the logarithm is monotically increasing, we can also maximize the log-likelihood by setting its first derivative to zero

$$\frac{\partial \log \mathcal{L}(\vec{\beta} \mid \boldsymbol{X})}{\partial \vec{\beta}} = 0 \quad . \tag{5.15}$$

A solution to this equation is guaranteed (see Paninski (2004b)) as the negative log-likelihood is required to be a convex function and can be minimized via methods such as gradient descent. Optimization yields a set of optimal $\beta_i = \hat{\beta}_i$.

This optimization problem can equivalently formulated as

$$\hat{\beta}_i = \underset{\beta}{\operatorname{argmax}} (\log \mathcal{L}) \tag{5.16}$$

with argmax_β representing the choice of those β values that maximize the log-likelihood, or in other words the posterior distribution of the data given the model.

5.2.2.2 *Regularization*

The naive gradient descent of the model is prone to over-fitting and non-convergence (Farhoodi et al., 2021; Stevenson, 2018).

To remedy such situations different kinds of *regularizations* have been investigated. The regularization imposes a further constraint on the values of β_i by modifying the optimization problem to

$$\hat{\beta}_i = \underset{\beta}{\text{argmax}} \left(\log \mathcal{L} - \text{penalty} \right) \quad . \tag{5.17}$$

Elastic-net regularization (Jas et al., 2020; Zou et al., 2005) combines two types of penalties known as Lasso (Tibshirani, 1996) and Ridge regularizations (Hoerl et al., 1970)

$$\text{penalty}_{\text{elastic net}} = \lambda_{\text{reg}} \sum_{i=0}^{N} \left(\alpha \left| \beta_i \right| + (1 - \alpha) \left| \beta_i \right|^2 \right) \quad . \tag{5.18}$$

where the regularization parameter λ_{reg} controls the effect of penalization and needs to be estimated by proper cross-validation.

If $\alpha = 1$ we recover pure Lasso regularization, which uses the $L1$-norm

From a Bayesian point of view, the L2-penalty is analogous to the choise of a Gaussian prior over the weights, while the L1-penalty is equivalent to a zero-mean Laplace prior.

$$\text{penalty}_{L1} = \lambda \sum_{i}^{N} \left| \beta_i \right| \quad , \tag{5.19}$$

whereas if $\alpha = 0$ the penalty corresponds to Ridge regularization

$$\text{penalty}_{L2} = \lambda \sum_{i}^{N} \left| \beta_i \right|^2 \quad . \tag{5.20}$$

While the Lasso regularization penalty forces some of the β_i coefficients to zero leading to sparsity in the coefficients, Ridge regression will lead to a shrinkage of coefficients and thereby avoid single coefficient to get exceedingly large (Bishop, 1992; Hastie et al., 2009).

5.2.2.3 *Goodness-of-Fit*

For linear models it is common to use the R^2, also called coefficient of determination, as a measure of the goodness-of-fit. It is defined as

$$R^2 = 1 - \frac{\sum_t \left(y_t - \hat{y}_t \right)^2}{\sum_t \left(y_t - \bar{y} \right)^2} \quad , \tag{5.21}$$

where y is the empirical data, $\bar{y}$ its mean and $\hat{y}$ the model prediction and the index t stands for a certain sample, as in our application, we consider samples across time if not mentioned otherwise. Thus, it relates the sum of squares of the residuals to the variance. If the fit is perfect, the numerator is 0 and hence $R^2 = 1$. However, if the sum of squared residuals equals the variance then $R^2 = 0$.

For nonlinear models, however, the classical coefficient of determination is not reliable. As an alternative several versions of a pseudo-R^2, henceforth denotes as $\widetilde{R}^2$, resembling the classical R^2 have been proposed. These definitions often measure the improvement of fit of the actual model (henceforth called complete model) over the null model, which is a model with just the constant intercept as regressor, or relative to the null and the saturated model, which set the lower and upper bounds for the log-likelihood respectively.

SATURATED MODEL A saturated model is a model with the same amount of parameters as degrees-of-freedom and thus, one that would yield a perfect fit. This is equivalent to one parameter per time point and thus the correct spike count prediction would be achieved per time point, in contrast to just the mean of most likely Poisson distribution. Hence, $\lambda_t \to y_t$, which is inserted into Equation 5.14 yields

$$\log \mathcal{L}_{\text{saturated}} = \sum_t y_t \left(\log y_t - 1\right) - \sum_t \log(y_t!) \quad . \tag{5.22}$$

PSEUDO-R^2 We use the following pseudo-R^2 ($\widetilde{R}^2$) definition (used in `pyglmnet` and henceforth called as such, (Goodman et al., 2019) calls it McFadden's pseudo-R^2 besides other definitions with this name)

$$\widetilde{R}^2_{\text{pyglmnet}} = 1 - \frac{\log \mathcal{L}_{\text{saturated}} - \log \mathcal{L}}{\log \mathcal{L}_{\text{saturated}} - \log \mathcal{L}_{\text{null}}} \quad , \tag{5.23}$$

where $\log \mathcal{L}$ is the log-likelihood of the model under investigation.

Note that the constant term in Equation 5.14 and Equation 5.22 drops out naturally.

If the full model fit is perfect, the numerator is 0 then $\widetilde{R}^2_{\text{pyglmnet}} = 1$, if it is merely performing as good as the null model $\widetilde{R}^2_{\text{pyglmnet}} = 0$ (Kraus et al., 2015). All other values lie in between.

Alternative pseudo-R^2 have been suggested. McFadden's pseudo-R^2 relates the complete model log-likelihood to the null model

$$\widetilde{R}^2_{\text{McFadden}} = 1 - \frac{\log \mathcal{L}_{\text{complete}}}{\log \mathcal{L}_{\text{null}}} \quad , \tag{5.24}$$

and Cox & Snell's pseudo-R^2 similarly defined

$$\widetilde{R}^2_{\text{Cox \& Snell}} = 1 - \exp\left((\log \mathcal{L}_{\text{null}} - \log \mathcal{L}_{\text{complete}}) \cdot (2/n_{\text{obs}})\right) \quad , \tag{5.25}$$

from which the latter is used by default in the python package `statsmodel`.

5.2.2.4 *Binning*

For all GLMs in this thesis, a bin size of the continuous signals and the spikes count of $\Delta t = 50\,\text{ms}$ was chosen. The choice of binning was a trade-off between temporal resolution and computational expense (i.e. computational time). Smaller bin sizes have been inspected for models with only few regressors and no qualitative difference was observed.

5.2.2.5 *Directional tuning via simple GLM per time lag*

The simplest approach to uncover the tuning of a single unit activity (SUA) to hand movement direction using a GLM is to model the firing rate as

$$\lambda_t = e^{\beta_0 + \beta_1 \cos\theta_{t-\tau} + \beta_2 \sin\theta_{t-\tau}} \quad , \tag{5.26}$$

where $\theta_{t-\tau}$ is the instantaneous movement angle at time point $t - \tau$ with τ being a fixed shift of the regressor relative to the neural activity.

This form of fit is related to the von Mises function, which has been used in (Amirikian et al., 2000) as a more flexible choice of tuning function compared to the classical cosine tuning (Georgopoulos et al., 1982).

The standard, unimodal and symmetric von Mises function is given by

$$d(\theta) = b + k \exp(\kappa \cos(\theta - \mu)) \quad , \tag{5.27}$$

with a maximum at $\theta = \mu$ (equalling the preferred direction (PD)), with κ defining the shape of the function, b is the baseline firing rate, k defines the tuning depth. The standard cosine tuning is recovered with $\kappa \ll 1$.

A re-parametrization[2] reveals the analogy to the GLM fit

$$d(\theta) = b + k \exp(\kappa_1 \cos(\theta) + \kappa_2 \sin(\theta)) \quad , \tag{5.28}$$

where $\kappa_1 = \kappa \cos(\mu)$ and $\kappa_2 = \kappa \sin(\mu)$. Hence, one can recover $\kappa = \sqrt{\kappa_1^2 + \kappa_2^2}$ and $\mu = \tan^{-1}\left(\frac{\kappa_2}{\kappa_1}\right)$. After fitting a GLM with Equation 5.26

---

[2] see `http://kordinglab.com/spykes/tutorial.html`

to a single neurons activity, we can use β_1 and β_2 instead of κ_1 and κ_2 to determine the PD.

Furthermore, in Equation 5.26 can be e^{β_0} can be factorized, revealing that it is equivalent to k. The variable b is not included in the GLM.

Note that by scanning through the shift τ, a shift-dependent tuning function can be extracted.

5.2.2.6 *Directional tuning via GLM including multiple regressors and time lags*

Instead of restricting the GLM to just one or two regressors at one specific time lag, as explained in Section 5.2.2.5, we use a more complete modeling approach to disentangle different behavioral influences. In the following, we describe the structure of this GLM and the type of regressors that were used.

The total number of regressors and thus, coefficients, to be succesfully fitted is limited by the amount of data samples. Diomedi et al. (2020) and Vaccari et al. (2021) propose as a rule of thumb to have approximately ten samples per β-coefficient. For a typical session duration of $T_{\text{session}} \approx 12\,\text{min}$ and a bin size of $\Delta t = 50\,\text{ms}$ there are $N_{\text{samples}} = \frac{T_{\text{session}}}{\Delta t} = 14400$ samples. According to the rule of thumb, we aim to build the largest model with less than ≈ 1440 regressors.

GROUPING OF REGRESSORS INTO BLOCKS In the following, we refer to a *block* as a group of regressors. To describe the neural activity, we include regressors from five different classes of external variables (Vaccari et al., 2021): *visual*, *eye position*, *saccade*, *hand position* and *movement*. For the purpose of this study, we do not include internal variables (e.g. the spike history) due to computational limitations in the number of regressors.

We group regressors belonging to one of these classes together, such that the model can be written down as:

$$\lambda_t = \exp\left(\beta_0 + \sum_{i=1}^{N_{\text{visual}}} \beta_i^{\text{visual}} X_{t,i}^{\text{visual}} + \cdots + \sum_{i=1}^{N_{\text{movement}}} \beta_i^{\text{movement}} X_{t,i}^{\text{movement}}\right) \quad . \tag{5.29}$$

REGRESSORS Here, we briefly describe the nature of the regressors per regressor block. Each regressor is a 1D-vector in time; i.e. the regressor $X_{i,t}$ constitutes i-th row of the design matrix X with t being the sample index running over time binned with the bin size $\Delta t = 50\,\text{ms}$.

Some regressors are chosen to be *dummy* variables (Vaccari et al., 2021), derived variables that are set to 1 if some condition is true and 0 if false (e.g. if a visual stimulus falls into a certain region in the visual field at a certain time).

This is necessary, because the GLM can only fit monotonic relationships between regressor and firing rate, but the response of a neuron to a certain stimulus can be non-monotonic (for example a neuron in V1 with a receptive field (RF) would have a Gaussian-like response curve in 2D).

More explicitly, the regressors were chosen in the following way:

- *visual*

  With the aim to capture neural responses to visual stimuli, we introduce two sets of visual stimuli and these enter the visual regressor block: The target position relative to the eye position and the hand position relative to the eye given in horizontal and vertical angle from the focal point of the eye. The relevant extent of target position relative to the eye position was defined to be $X^{target/hand-to-eye}_{horizontal} \in [-10, 10]^\circ$ and $X^{target/hand-to-eye}_{vertical} \in [-10, 10]^\circ$.

  To capture the eventual non-monotonic nature of the response of neurons, each of these 2D signals have been binned with a bin width of $\Delta_{\text{visual}} = 4^\circ$ horizontally and vertically, yielding each 5 bins per axis and thus each 25 bins in total. The process of obtaining these visual dummy regressors is sketched in Figure 5.1.

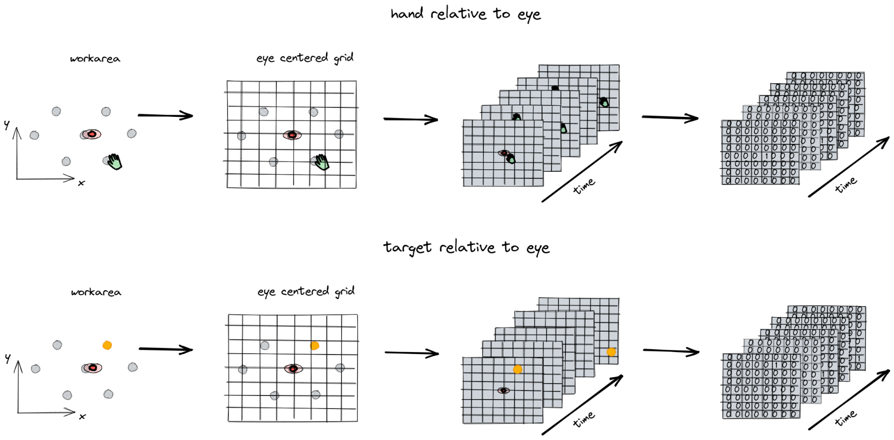

Figure 5.1: Sketch of the two types of visual regressors: Target and hand position relative to eye position.

  To account for different response latencies, time-shifted copies of these regressors have been included. We included 7 time shifts $(-1, \ldots, 5\Delta t)$. In total the visual regressor block contains $N^{\text{regressors}}_{\text{visual}} = 2 \times 25 \times 7 = 350$ regressors.

- *eye position*

  With the aim to capture eye position gain fields, the 2D eye position which differs slightly across sessions has been binned with a bin width of $\Delta_{\text{eye position}} = 4\,^\circ$ horizontally and vertically. The resulting regressors were time shifted by $(-1, \dots, 2\Delta t)$.

For session `y180116-land-001` the signal lived in the following ranges: $X^{eye}_{horizontal} \in [-17, 31]^\circ$ and $X^{eye}_{vertical} \in [-47, 22]^\circ$. The binning resulted in 84 dummy regressors. Including all time shifts we obtained $N^{\text{regressors}}_{\text{eye position}} = 84 = 252$ regressors.

- *saccade*

  We have observed saccade-related activity in some units and want to capture it by introducing regressors that contain the timing of saccades in a direction-resolved manner. Saccades directions ($\in [0, 360]^\circ$) were binned with a bin width of $\Delta_{\text{saccade}} = 18\,^\circ$. Per direction bin, we created two dummy regressors, one for saccade onset and one for saccade offset which contain a 1 at the time bin of a corresponding saccade. Furthermore, the eye velocity was standardized (z-scored) and included as a regressor. The 41 regressors were time shifted 7 times $(-1, \dots, 5\Delta t)$ yielding $N^{\text{regressors}}_{\text{saccade}} = 41 \times 7 = 287$ regressors.

- *hand position*

  With the aim to capture hand position gain fields, the 2D hand position which differs slightly across sessions has been binned with a bin width of $\Delta_{\text{hand position}} = 3\,\text{cm}$ horizontally and vertically. The resulting regressors were time shifted by $(-1, \dots, 2) \times \Delta t$.

  For session `y180116-land-001` the signal lived in the following ranges: $X^{hand}_{horizontal} \in [-16, 4]\text{cm}$ and $X^{hand}_{vertical} \in [-15, 9]\text{cm}$ with respect to the origin of the work area. The binning resulted in 56 dummy regressors. Including all time shifts we obtained $N^{\text{regressors}}_{\text{hand position}} = 56 \times 3 = 168$ regressors.

- *movement*

  We are primarily interested to uncover the neural tuning to hand movement. To achieve this we parameterized movement by a direction and velocity and added corresponding regressor.

  We first smoothed the x and y coordinates of the hand position sampled at 1 kHz with a Savitzky-Golay filter using the window length $w_{\text{SG hand}} = 101\,\text{ms}$ and the polynomial order $p_{\text{SG hand}} = 3$. From these smoothed signals, we calculated the instantaneous hand movement angle between subsequent bins t and $t+1$ as $\theta = \text{arctan2}(y_{t+1} - y_t, x_{t+1} - x_t)$. From the resulting instantaneous hand movement angle sampled at 1 kHz, we downsampled to the desired sampling period $\Delta t = 50\,\text{ms}$ by taking the circular mean within each bin.

  From the resulting signal ($\in [0, 360]^\circ$) we took the cosine and sine yielding 2 regressors.

To also capture eventual influence of the hand velocity, we added the standardized hand velocity and, additionally, dummy variables of the velocity binned with $\Delta_{\text{movement velocity}} = 2\,\text{cm/s}$, yielding $1 + 14$ regressors.

All movement regressors were time shifted $(-6, \dots, 6) \times \Delta t$ resulting in $N^{\text{regressors}}_{\text{movement}} = (2 + 1 + 14) \times 13 = 221$ regressors.

In total, our GLM comprises $N^{\text{regressors}}_{\text{total}} = 350 + 252 + 287 + 168 + 221 = 1278$ regressors.

FITTING PROCEDURE In a GLM with this amount of regressors many regressors are negligible and we resort to regularization to cope with this issue. As recommended in (Diomedi et al., 2020; Vaccari et al., 2021) we employed Lasso regularization. For the regularized fit, we thus used $\alpha = 1$.

The value of $\lambda_{\text{reg}} = 0.001$ was heuristically determined by performing the following analysis on multiple example neurons: We scanned through values of λ_{reg} and chose the value, where the cross-validated deviance of the fit is minimal.

Per neuron, we first fit the Lasso regularized GLM. The effect of the Lasso regularization is that many β-coefficient are set to zero. We then re-fit the model with just those regressors for which the β-coefficients were non-zero in the Lasso fit to obtain a goodness-of-fit measure that is not biased by the Lasso penalization term in the log-likelihood

EXTRACTION OF JUST THE INFLUENCE OF THE MOVEMENT REGRESSORS We fit this large GLM to be able to disentangle the influences of multiple behavior. To extract the directional tuning of neural firing to the instantaneous hand movement direction, we want to integrate out the impact of the regressor blocks *visual*, *eye position*, *saccade*, *hand position* and thereby avoid possible confounds.

The linear sum of regressors in the exponential leads to a multiplicative effect of each regressor. This is in line with the idea of gain modulation of eye or hand position (Paninski, 2004a). To integrate out all regressors that do not belong to the movement regressor block, we calculate

$$\lambda_t^{\text{movement}} = \frac{1}{S} \sum^{S} \exp \left(\beta_0 + \sum_{i=1}^{N_{\text{movement}}} \beta_i X_{t,i}^{\text{movement}} + \right. \tag{5.30}$$

$$\left. + \dots \text{other regressors shuffled in time} \dots \right) \quad . \tag{5.31}$$

with S the number of different shuffles inspired by (Ledergerber et al., 2021). The shuffling of the other regressors in time destroys the temporal relation between regressor and caused firing rate and thereby also destroys the potential of these regressors to be confounded as response to the movement.

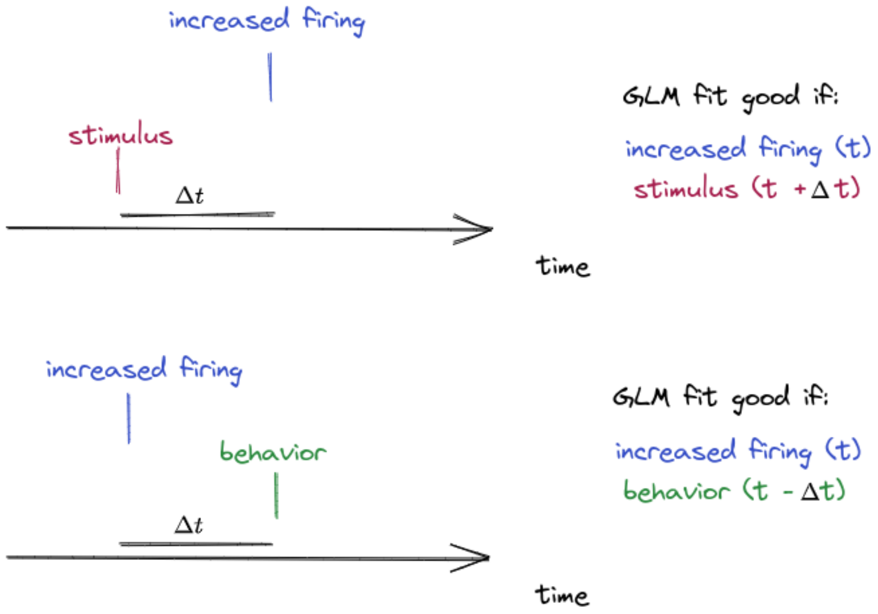

Figure 5.2: Illustration of the influence of a time shifting of the regressor variable on the goodness-of-fit in a GLM.

5.2.2.7 *Time Shift between Neural Activity and Regressors*

It is unlikely that there is an instantaneous relationship (e.g. $\tau = 0\,\text{ms}$) between neural activity and a certain regressor variable (e.g. instantaneous hand movement direction). To illustrate this consider the following two scenarios as depicted in Figure 5.2:

1. A neuron in V1 with a well-defined RF is triggered by a visual stimulus, and, as a response, increases its firing rate after a certain latency (typically around 50 ms in V1 (Schmolesky et al., 1998)). Consider a regressor for a 2D pixel at the location of that neuron's receptive field (RF) location: This regressor equals one if there is a stimulus at that location and zero otherwise. To achieve a maximal correlation between the neural response and the regressor variable, one would ideally shift the regressor by the amount of the latency.

2. A neuron in M1 indirectly (via an interneuron and a motoneuron) triggers a certain muscle activity that eventually leads to a movement of the limb in a certain direction. A regressor describing the instantaneous movement direction would need to be shifted by the latency between neural firing and the resulting movement direction.

In the first case, the neural activity lags the external stimulus, while in the second case neural activity leads the externally observed behavior.

5.2.2.8 *Relative impact of regressor block*

In the previous section Section 5.2.2.6, we explained the structure of the GLM including all regressors grouped into blocks, henceforth called the *complete model*.

We can evaluate impact of one particular regressor block on the goodness-of-fit by leaving out this regressor block from the GLM fit, then called *nested model*, and comparing it to the complete model (Diomedi et al., 2020; Vaccari et al., 2021).

We evaluate the drop in log-likelihood if one regressor block is left out (*nested model*) with respect to the *complete model* and the *null model*. The quantity that measures this is the w-value (Diomedi et al., 2020; Vaccari et al., 2021):

$$\widetilde{R}^2_{\text{relative}} = \frac{\widetilde{R}^2_{\text{nested}}}{\widetilde{R}^2_{\text{complete}}} \tag{5.32}$$

$$= \frac{\log \mathcal{L}_{\text{nested}} - \log \mathcal{L}_{\text{null}}}{\log \mathcal{L}_{\text{complete}} - \log \mathcal{L}_{\text{null}}} \tag{5.33}$$

$$w = 1 - R^2_{\text{relativepseudo}} \quad , \tag{5.34}$$

where $\log \mathcal{L}_{\text{nested}}$, exemplary, stands for the log-likelihood of the nested model.

If the nested model performs as good the complete model and thus leads to the same log-likelihood, the relativepseudo $- R^2 = 1$ and in turn $w = 0$.

On the other hand, if the nested model performs similar as the null model and the difference in their likelihoods is ϵ, the ratio relativepseudo $- R^2 = \frac{\epsilon}{\log \mathcal{L}_{\text{complete}} - \log \mathcal{L}_{\text{null}}} \gtrsim 0$ and in turn $w = 1$. In this situation, the left-out regressors are responsible for the success in the complete model.

In summary, the larger the w-value, the larger its influence on the goodness-of-fit.

5.2.2.9 *Test for Bimodality*

The Rayleigh r statistic from Batschelet (1981) was modified to determine the bimodality of the distribution of preferred directions (Scott et al., 2001a). The original r statistics measures the skewness of the distribution of angles ϕ_i's $\in [0, 360]^\circ$ with

$$r = \frac{1}{N^2} \left(\left(\sum_i \cos(\phi_i) \right)^2 + \left(\sum_i \sin(\phi_i) \right)^2 \right) \quad . \tag{5.35}$$

If all angles ϕ point into the same direction (e.g. consider $90^\circ \rightarrow \cos(90) = 1$) this measure results in $r = 1$ and consequently drops for more uniform distributions.

Similarly, it is possible to test for bimodality with precisely 180 ° in between the modes by doubling the angles:

$$r_{\text{bimodal}} = \frac{1}{N^2}\left(\left(\sum_i \cos(2\phi_i)\right)^2 + \left(\sum_i \sin(2\phi_i)\right)^2\right) \tag{5.36}$$

Given a distribution of PDs with sample size N, a p-value can be determined via bootstrapping. We use an approximation of such a bootstrap procedure supplied by `pycircstat`, the python port of (Berens, 2009). We ensured that the p-values coincide with a bootstrap distribution that was obtained by calculating the r_{bimodal} for 10^6 distributions with each N i.i.d. drawn samples from a uniform distribution. Significant bimodality was defined by a p-value < 0.05.

5.2.3 *Signal triggered distribution*

In some circumstances, the assumed causality is such that an external event/signal evokes a neuronal response. In these cases, the signal triggered distribution of firing $p(\tilde{r}^i(t)|a < \mathcal{S}(\boldsymbol{\theta}, t) < b, \tau)$, with $\tilde{r}^i(t)$ being the estimate of the instantaneous firing rate of the neuron, can be looked at. It is the distribution of firing rates observed when the signal is in a certain interval.

In the first step, the instantaneous firing rate estimate of spike train $s^i(t)$ of neuron i is obtained by a suitable convolution with a kernel $k(s)$ as $\tilde{r}^i(t) = \int s^i(t-s)k(s)ds$.

In a second step, the signal $\mathcal{S}(\boldsymbol{\theta}, t)$ is binned. For all times t_{bin} for which the signal is in the range $a < \mathcal{S}(\boldsymbol{\theta}, t) < b$ the estimated instantaneous firing rate values are stored. In this way, we get a distribution of firing rates observed when the signal is that range $p(\tilde{r}^i(t)|a < \mathcal{S}(\boldsymbol{\theta}, t) < b, \tau)$.

From this distribution, the mean $p(\tilde{r}^i(t)|a < \mathcal{S}(\boldsymbol{\theta}, t) < b, \tau) >$ can be evaluated. Repeating this for intervals covering the whole signal range and for several time-shifts (lags) τ of the instantaneous firing rate with respect to the signal, results in a lag-dependent mapping of the mean firing rate given a certain signal.

Note, that here the instantaneous firing rate is shifted with respect to the signal, while in the GLM the signals are shifted with respect to the spike count vector.

5.2.4 *Software*

All analyses were conducted using `Python`. The electrophysiological data was represented via `neo` (Garcia et al., 2014). Basic spiketrain statistics as the waveform signal-to-noise ratio (SNR) (see Section A.1) or the mean firing rates were calculated using `elephant` (Denker et al., 2018a). Automatic spike sorting, as explained in Section A.1 was performed using `SpikeInterface` (Buccino et al., 2020). `snakemake` (Köster et al., 2012) was employed to chain seperate analysis steps together into a modular analysis workflow. The GLM was fitted using `statsmodels`. However, the pseudo-R^2 was inspired from `glmnet` (Jas et al., 2020).

5.3 OUTLINE

In the results, we start by presenting a glimpse into the experimental data. In particular, we illustrate the behavioral complexity by showing an exemplary trial with all behavioral traces. After reasoning, that the behavioral data, with focus on the movements, is rich enough to extract an eventual tuning of single neuron activity to hand movement direction, we continue by determining the tuning of one exemplary neuron with classical methods and the GLM approach.

5.4 RESULTS

We analyzed neural activity from 4 sessions from monkey Enya and from 12 sessions from monkey Jazz (see Table 5.1). For the results presented in this chapter, we use single unit activity obtained according to the procedure detailed in Section 4.6 and ensuring the quality metric listed in Table A.3. A summary of the used neuron numbers per monkey and recording site is given in Table 4.3.

5.4.1 *Visually guided reaching task probes large set of behaviors*

The experimental tasks (see Section 3.4) were designed to probe natural behavior during a visually guided hand movement that requires a close and recurrent interplay between perception and action. To illustrate the interplay between different behavioral modalities, we show the recorded behavioral data for one exemplary successful trial of the landing task in Figure 5.3. Note that in the following, the discussion of results is simplified by focussing on the landing task, if not mentioned explicitly otherwise.

After the monkey is presented with a new target, it performs a saccade towards it (typically with a delay of $\sim 200\,\mathrm{ms}$) and initiates the hand movement. The temporal order of saccade and hand movement is variable (see bottom two panel rows) and seems to depend on the direction (data not shown here). The eye position signal in the top panel shows that the eye rarely hits the target position directly, but rather jumps into its vicinity and then stays there with multiple micro-saccades until the next saccade.

The hand movement can be segmented into movement segments (Section 3.2.1), for which maximal velocities are reached roughly at the

session name	subject	n_{trials}	$n_{\text{trials}}^{\text{success}}$	$n_{\text{trials}}^{\text{fail}}$	n_{LS}	T	$\bar{d}_{\text{trial}}$	$\sigma(d_{\text{trial}})$
y180116-land-001	Enya	190	121	69	8	700	3.9	0.4
y180221-land-002	Enya	178	120	58	12	656.8	3.8	0.4
y180306-land-001	Enya	176	120	56	12	657.5	3.8	0.4
y180306-draw-002	Enya	134	120	14	✗	543	3.4	0.7
j210204-land-001	Jazz	190	120	70	12	590	3.2	0.4
j210208-land-001	Jazz	268	120	148	12	733.5	3.3	0.4
j210212-land-001	Jazz	238	120	118	12	649.5	2.9	0.3
j210223-draw-002	Jazz	87	80	7	✗	320	2.7	0.3
j210301-draw-001	Jazz	122	120	2	✗	556	3.9	0.5
j210601-land-001	Jazz	317	45	272	8	559.1	3.5	0.4
j210608-land-001	Jazz	382	110	272	8	854	3.5	0.3
j210729-draw-001	Jazz	124	120	4	✗	441	2.8	0.5
j210901-draw-001	Jazz	148	120	28	✗	483	2.9	0.6
j210913-land-001	Jazz	327	120	207	12	760.4	3.2	0.4
j211007-land-001	Jazz	307	76	231	8	780	4.7	0.5
j211103-land-002	Jazz	181	80	101	8	838	7.2	0.4

Table 5.1: Information on the sessions that were used in the analysis. n_{LS} denotes the number of different landing sequences that were used. T: total session duration, $(\bar{d}_{\text{trial}}, \sigma(d_{\text{trial}}))$: mean and standard deviation across successful trial durations, respectively. The values in the last three columns are given in seconds.

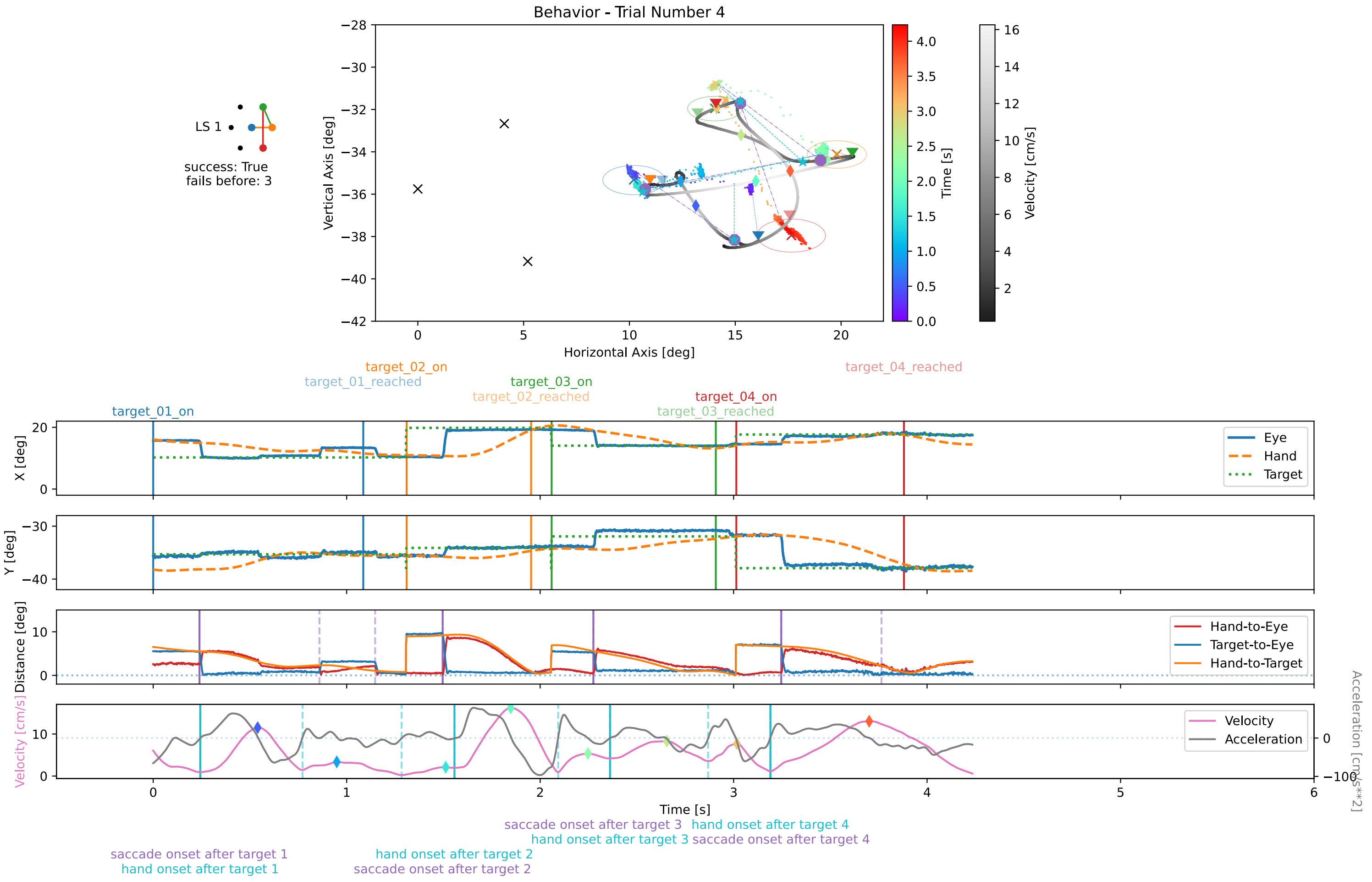

Figure 5.3: Example trial of the landing task. (Caption continues on next page.)

Figure 5.3: (Continued caption.) The presented landing sequence in this example trial is depicted on the top left. This trial was performed successfully. The previous three trial were unsuccessful. The top panel shows the 2D eye position and hand position in degrees relative to straight forward eye position. Targets are marked by crosses and colored as in the depiction of the landing sequence on the left. The logical radius plotted around the target center defines the area within which the monkey is required to land. The eye position (small colored dots) is colored according to progressing time within the trial. The hand trajectory (solid line) is shaded in gray according to the hand velocity. Relevant task events are marked on the hand trajectory with colored markers (colors match the labels below, triangle: target onset, lightly colored triangle: target reached, diamond: maximal hand movement velocity, star: saccade onset). Thin lines connect these markers to the eye position at the event's time. The bottom panel shows the behavioral data across time. The first two rows show the x and y components of the hand, eye and target. Relevant task events are marked by colored vertical lines, corresponding labels can be found above. The third row shows the distances hand-to-eye, target-to-eye and hand-to-target across time. Saccade onsets are marked by lilac vertical lines, which are solid for the first saccade onset after a target onset and dashed otherwise. The bottom row shows the hand velocity and acceleration across time. Hand movement onsets are marked by brown vertical lines, which are solid for the first hand movement onset after target onset and dashed otherwise, corresponding labels can be found below. The diamonds denote the time points of maximal velocity in the detected movement segment. Their color corresponds to the colorbar encoding time in the top panel.

halfway point when moving from one target to another. During this landing task, the hand is required to stay within the logical radius of the targets for a certain amount of time. While the hand movement is visibly slower during this landing period, the hand does not stand still. In some occasions, e.g. for the top right target landing in the presented example trial, the monkey seems to use this landing period to change the movement direction even before the next target is showing up. Note that the hand movement is constrained by the mechanics of the KINARM, which likely hinders very brisk changes in hand movement.

5.4.2 *Visually guided reaching task allows for hand movement direction tuning analysis*

Classically, directional tuning is evaluated in well-constrained tasks in which center-out movements are used and only the data during the task performance periods are analyzed (e.g. 8 center-out directions are used in Georgopoulos et al. (1982)). To enable comparison to such previous studies, the first part of each landing task trial consists of a classic center-out reach Figure 5.4**A**. Depending on our selection of the positions of subsequent targets in the landing sequences, movements in certain directions were performed more than in other directions (Figure 5.6 and Figure 5.7). The full twelve landing sequences, with three sub-trajectories each, sample a wide range of hand movement directions (see Figure 5.4**C**). Hand movement trajectories exhibit variability across the same trial type as can be seen in Figure 5.4**B**.

Similarly, multiple trials in the drawing task require the monkey to perform all hand movement directions (see Figure 5.4**D**).

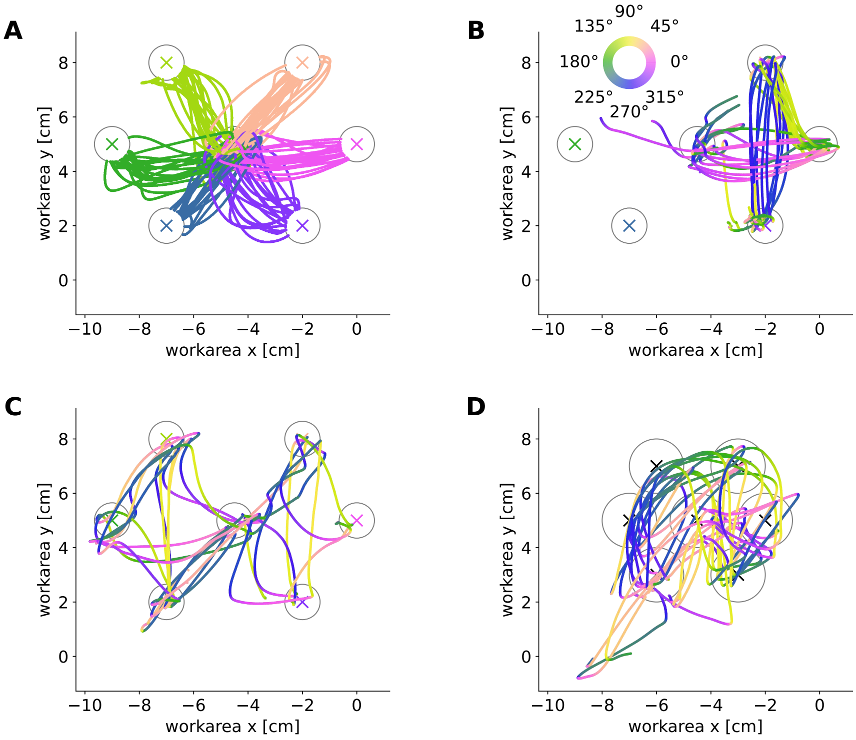

Figure 5.4: Hand movement examples. **A** Hand position trajectories on the horizontal work area during the center-out part of the landing task. Trajectories are colored according to the mean movement direction, colors coded as shown in the color wheel in the next panel. **B** shows the hand position of ten repetitions of one landing sequence, while panels **C** show the hand position during ten successive trials; the color encodes the instantaneous hand movement direction. **D** shows the hand position of ten repetitions of one drawing session. Note the larger logical radius of the targets in the drawing task.

CHOICE OF ANALYSIS TIME RANGE The two types of tasks, as illustrated above, only require the monkey to adhere to timing constraints (e.g. maximal reach time, minimal landing time), and thus, allow the monkey to perform movements with variability in the trajectories and their velocities. In consequence, the timing of events is different across repetitions of the trials of the same landing sequence, rendering classical alignment analyses (e.g. via peri-stimulus time histograms (PSTHs)) difficult. In the following, we will use a GLM approach to circumvent the need for alignments.

Such an approach, furthermore, alleviates us from the need to use only the successfully executed parts of the experiment. In line with tendencies in the field to move towards the use of neural recordings during naturalistic behavior, we decided to use the whole recording sessions at hand: That is, including unsuccessful trials, reward and inter-trial periods. Figure 5.5 illustrates the proportions of each of these different periods in the analyzed sessions. To interpret this figure see also Table 5.1. It is noteworthy, that monkey Jazz, tends to execute movements faster than Enya, at the expense of more unsuccessful trials.

One benefit of using the whole stretch of the continuous behavioral and neural recordings is the large amounts of samples: Considering only periods of movements between targets during successful trials would amount to around one third of the total duration of the recordings, which corresponds to substantially fewer samples.

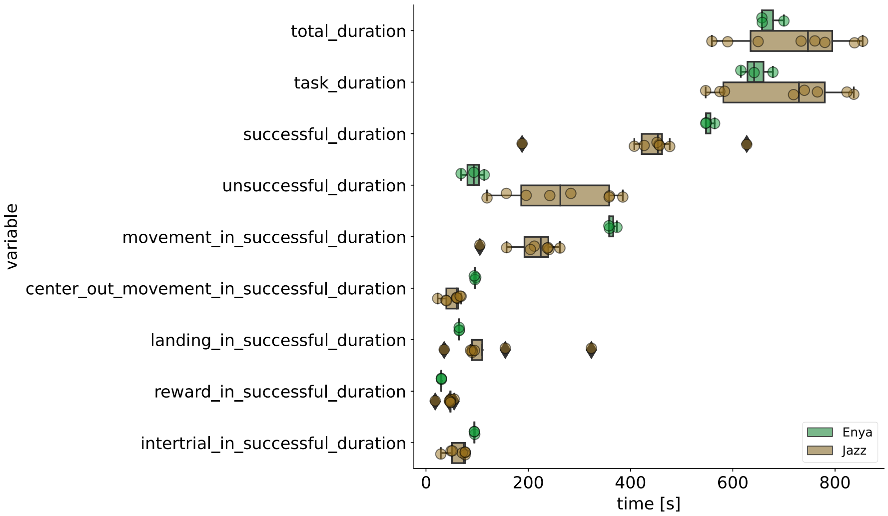

Figure 5.5: Overview over the durations of recording session, pure task execution and several epochs shown in a boxplot with overlayed single session values (circles) for the two experimnental subjects Enya and Jazz.

On the contrary, one could argue that the behavior during unsuccessful trials, as well as reward and inter-trial periods, is not controlled. Yet, in the case of the experiments in the V4A-experiments, the behavior was not strictly controlled during the task either.

Luckily, the behavioral recordings of hand position, eye position and the timing of the occurrence of targets in the work area yield a rich set of variables that can help interpret potential "uncontrolled" movements and timings of the recordings.

Hence, unsuccessful periods in the experiment were not thrown away, because the movements performed were largely valid and made up only a little fraction of the whole experimental session. Subsequent analyses, thus, contain data from uncontrolled periods during the experiment such as unsuccessful trials or eventual inter-trial periods. For future analyses it might be worth considering that different contexts (successful vs. unsuccessful) can alter the neural representation of a given movement.

BIASED DISTRIBUTIONS OF HAND MOVEMENT DIRECTIONS With the aim to extract the neural tuning to the hand movement direction, and with the argument of the previous paragraph in mind, we looked at the distribution of instantaneous movement angles samples (binned at $\Delta t = 50\,\mathrm{ms}$) during the center-out part of the landing task and the whole session (Figure 5.6**A** for Enya and Figure 5.7**A** for Jazz). In both subjects, the distribution of angles for the center-out part, is clearly biased towards the directions defined by the work area and target locations (cf. Figure 5.4**A**). Considering the complete trials and the required movements imposed by the task, certain movement directions in the 2D work-area are overrepresented due to the location of the targets (see Figure 5.6 and Figure 5.7).

Similarly, the distribution of angles across the complete sessions is biased: However, this bias is not dictated by the required movements that are demanded by the task, but seems to be aligned to a certain axis. The count of binned instantaneous movement angles depends on the velocity of movements. To resolve this dependency, panels **B** in both figures show the 2D heatmap of the distribution of angle and velocity of movements. It can be seen that the 95th-percentile of the normalized velocity distribution per direction is reached for smaller velocities in some directions. This means that movement velocities for certain movement directions (slightly differing for the two subjects) are lower and thus lead to more samples in the distribution in **A**.

The non-uniform distributions of both angles and velocities bring classical techniques (e.g. reverse correlation) to calculate the tuning curve for single unit activity to their limit and would lead to a bias (Paninski et al., 2004), that can be avoided by using a GLM approach (Pillow, 2005).

5.4.3 *Distribution of PDs for hand movement is bimodal in M1/PMd*

After having presented some characteristics of the movement behavior of the two subjects in the recorded data, we will now related the neural activity to it. We illustrate the extraction of a PD at the hand of an exemplary neuron from M1/PMd and then present the results obtained from the population of neurons.

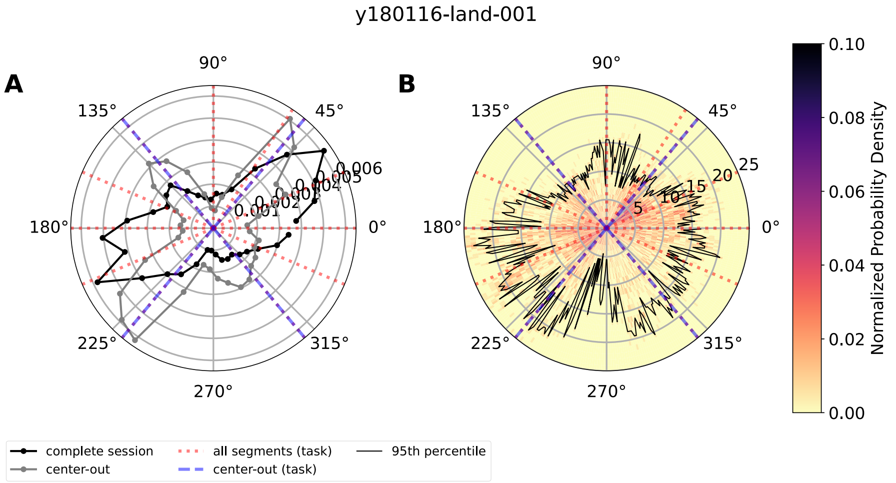

Figure 5.6: Hand movement directions distributions for session by Enya. **A** shows the normalized, circular distribution of bins (signal binned into 50 ms bins) that show a particular instantaneous hand movement direction; grey for the center-out period and black for the whole session. **B** Probability density of observing an absolute velocity in a certain direction $P(\theta, |v|)$ in polar coordinates with the radius encoding the velocity in units of cm/s. The thin black contour marks the 95^{th}-percentile of the normalized velocity distribution per direction $P\left(|v| | \theta = \hat{\theta}\right)$.

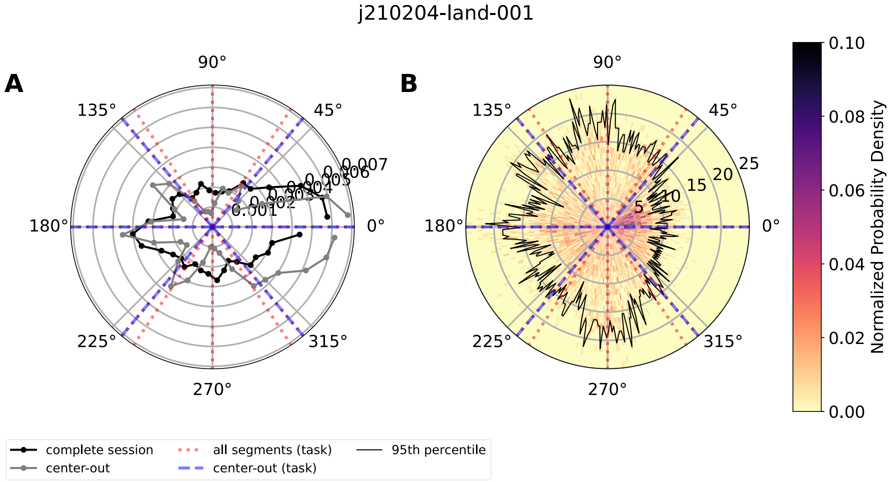

Figure 5.7: Hand movement directions distributions for session by Jazz. Same as in Figure 5.6.

5.4.3.1 *Example of single unit activity in M1/PMd*

Single unit activity in M1/PMd is known to be active during hand movement and to be modulated by the direction of movement (Georgopoulos et al., 1982). We observe such a modulation of the activity in raster plots (example shown in Figure 5.8) that visualize the spiking of a single unit across many trials triggered on a certain event (here *target_02_on*). The neuron illustrated in this example has an elevated firing rate for upward movements (e.g. LS 3/4 and LS 7/8 between *target_02_on* and *target_02_reached*) and even ceases to fire for movements to the lower right (e.g. LS 5/6 between *target_02_on* and *target_02_reached*). This directional tuning seems not to be very sensitive with regards to the starting point of a given movement (see e.g. LS 2 between *target_04_on* and *target_04_reached*).

5.4.3.2 *The classical way of extracting directional tuning*

While it is very illustrative to look at raster plots as in Figure 5.8, it is also useful to summarize the spiking activity in (smoothed) peristimulus time histograms (PSTHs). These can be estimated on a single-trial basis, but also averaged across repetitions of the same behavior (e.g. center-out hand movements in an identical direction). Figure 5.9**A** shows such an average and illustrates the variability across repetitions by showing the interquartile range. The center-out alignment is limited to 20 repetitions and thus reveals a substantial "trial-to-trial" variability. A comparison of the movement-related activity to a baseline period defined in the window from −100 ms to 100 ms, in which supposedly no movement is occurring, reveals an enhanced firing rate for upward movements and a suppression for downward movements (consistent with the observation in the raster plot shown previously).

To enhance the amount of data used to evaluate the tuning, we next segmented the hand movement behavior into a discrete set of movements with a bell-shaped velocity curve and a mean movement direction (see Section 3.2.1) and triggered the PSTH at the maximal velocity events of these segments. In the example shown in Figure 5.9**B**, the enhanced firing (relative to the mean firing rate) in the putative PD ($\sim 100\,°$) precedes the maximal velocity event, while the suppression of firing rather is maximal simultaneous to the maximal movement velocity. This highlights the dynamic nature and temporal dependence of the tuning of neural activity to hand movement.

As discussed in Section 2.3.2, neural tuning to hand movement likely also depends on velocity. In our experiment, the movement velocities are not of equal magnitude in the different direction as has been shown in Figure 5.6 and Figure 5.7. The picture in Figure 5.9, hence, might be biased.

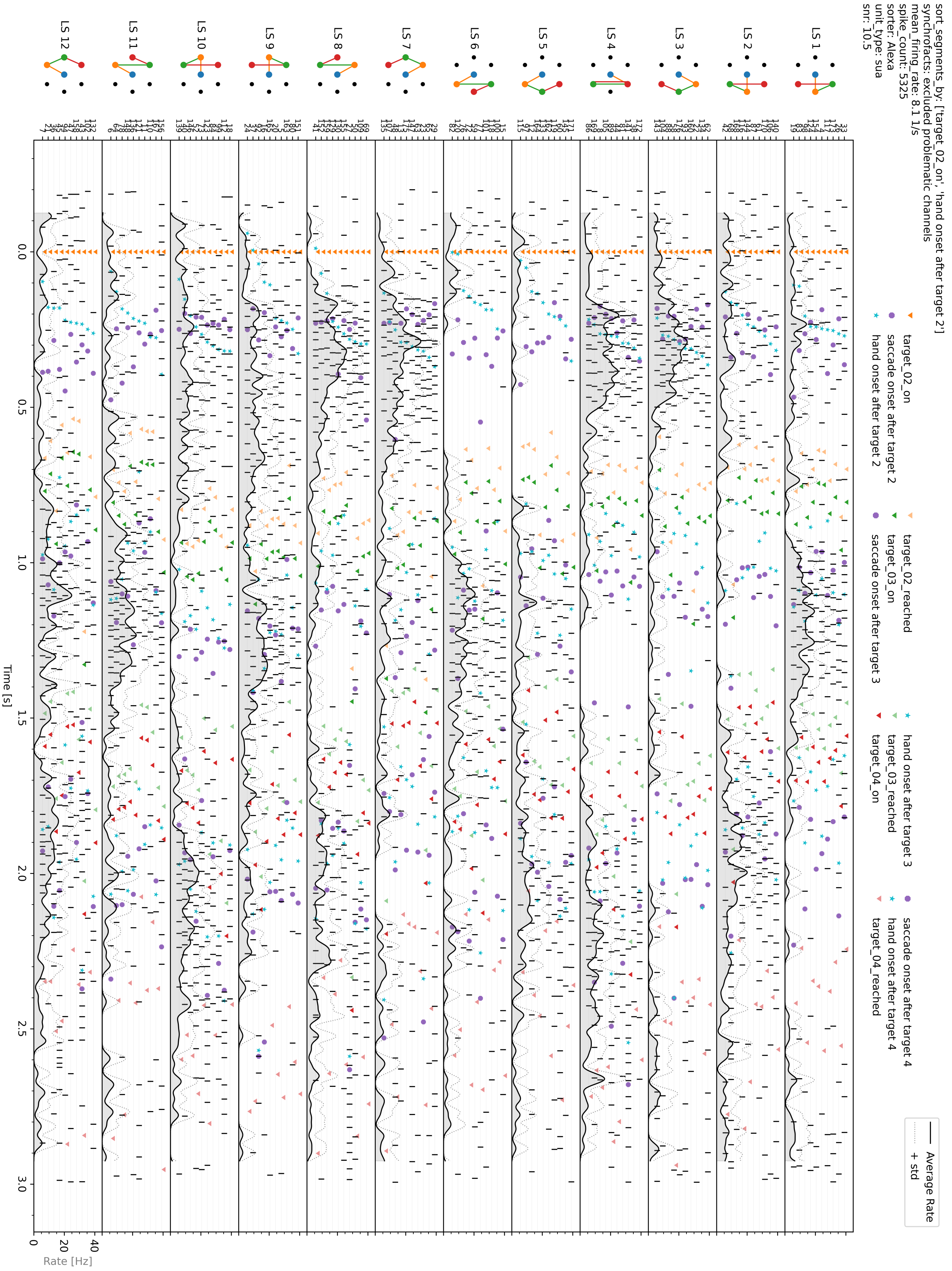

Figure 5.8: Example unit during landing task. (Caption continues on next page.)

Figure 5.8: (Continued caption.) Raster plot illustrating the spiketrains of exemplary unit M1/PMd in session `y180306-land-001` for all successful trials. Details on the unit are printed on the top left. The spiketrain is triggered on the event *target_02_on* and shown for the period from $-200\,\mathrm{ms}$ to $3000\,\mathrm{ms}$ around that event. Each row shows the spiketrain belonging to one trial (trial number printed on the y-axis) and rows are grouped into the twelve different landing sequences. The trials within one landing sequence are sorted by increasing latencies of the event *hand onset after target* 2. Further event marker are explained in the legend above the plot. Per landing sequence, the average firing rate across trials ± standard deviation are plotted with black and faint grey dotted lines, respectively (grey shade for better visibility). First, single trial firing rates were calculated by convolution with a Gaussian kernel with $\sigma = 15\,\mathrm{ms}$ and then averaged.

To deal with the non-uniformity of the behavioral data, we chose to use GLM approach to extract the tuning of single neurons to the hand movement direction.

5.4.3.3 *Extracting directional tuning via a simple GLM*

Therefore we fit a single GLM model as regressed in Section 5.2.2.5. The spike count was binned in $50\,\mathrm{ms}$ and described by a linear sum of cosine and sine of the instantaneous movement angle via an exponential link function. As described via Figure 5.9**B**, the relation between firing and, in this case, external action has a temporal dependence. To account for this, we repeat the GLM fit with time-shifted regressors (see Section 5.2.2.5 and Section 5.2.2.7).

Figure 5.10 illustrates the result obtained from multiple GLMs fits with a range of time shifts $\tau \in [-1, 1[\,\mathrm{s}$. Each "column" in Figure 5.10**B** stems from one independent fit and shows the von Mises tuning curve calculated from the fit as explained in Section 5.2.2.5. The overall pattern resembles Figure 5.9**B**, but while in the previous figure the neural activity was aligned to a behavioral event, here we "align" the behavioral data to the neural activity. For our example unit, this alignment is best for a time-shift of $\tau_{\mathrm{OTL}} = -200\,\mathrm{ms}$, also called the optimal time lag (OTL) (Mulliken et al., 2008; Paninski et al., 2004), as can be read off the goodness-of-fit measure in Figure 5.10**A**.

Note that the range of predicted firing rates in Figure 5.10**B** is substantially lower than what is observed in the classical PSTH alignment analysis (Figure 5.9). This is likely due to the fact, that we are considering data from the whole recording sessions, which might include times at which the hand is basically still, but slowly drifting into a certain direction and hence might "dilute" the extracted tuning strength.

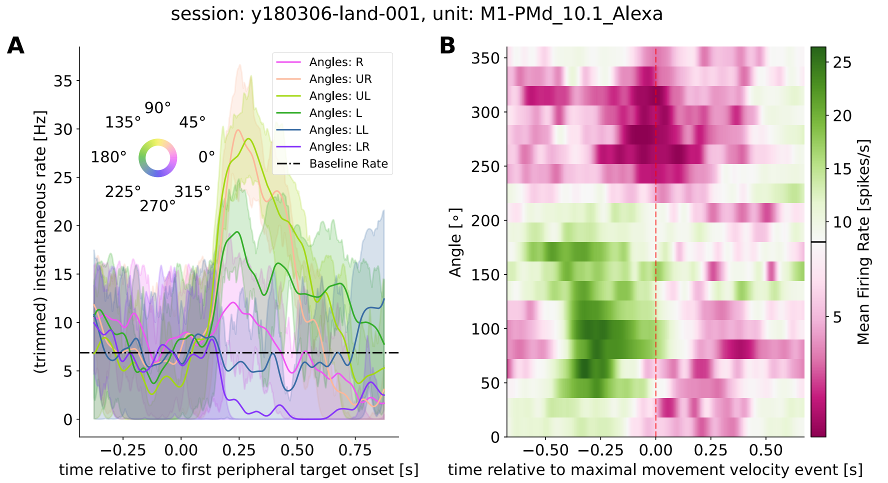

Figure 5.9: Peri-stimulus time histograms (PSTHs) triggered on center-out target onset (**A**) and maximal movement velocity event (**B**) of unit *M1*/*PMd* 10.1 sorted by Alexa on session `y180306-land-001`. PSTHs were obtained by convolution of spiketrains with Gaussian kernel with $\sigma = 25\,\text{ms}$ per event and then averaging across repetitions. Details **A**: The shaded regions span from the first to the third quartile of the data distribution across repetitions. The baseline rate in **A** was obtained in the window from $-100\,\text{ms}$ to $100\,\text{ms}$. The time windows on which the PSTHs were calculated extended from $-500\,\text{ms}$ to $-1000\,\text{ms}$ around the peripheral target onset. Yet, the displayed time ranges are shorter to avoid edge effects due to the convolution (trimming). Details **B**: PSTHs were calculated between $-800\,\text{ms}$ and $-800\,\text{ms}$ around the maximal movement velocity event. Only movement segments with a movement duration exceeding $100\,\text{ms}$ and a maximal movement velocity larger than $7\,\text{cm/s}$ were considered yielding 532 movement distributed across all directions. The colorbar is diverging (non-linearly) at the overall mean firing rate of the example neuron, with everything below and above being displayed in red green, respectively. . **A**

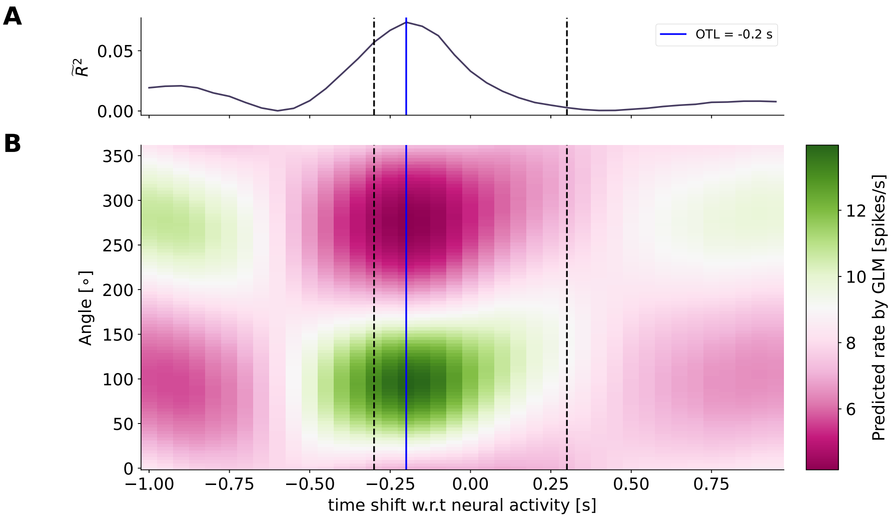

Figure 5.10: Directional tuning curve across time shifts of exemplary unit 10.1 from *M1*/*PMd* sorted by Alexa on session `y180306-land-001`. **A** Dependence of goodness-of-fit measure pseudo-R^2 (Equation 5.23) on the time shift of the instantaneous hand movement with respect to the neural activity.**B** Predicted firing rate dependence on the movement. Firing rate is encoded in color according to the colorbar. The tuning curve for a particular time shift τ is obtained by modeling the spike count vector $y^{(t)}$ via a single GLM Section 5.2.2.5, with the instantaneous movement angle regressor being shifted by τ. Blue vertical line marks the OTL. The two black vertical lines demark the time range that is focused on in Figure 5.11.

5.4.3.4 *Dynamic view on directional tuning*

Typically, units are characterized by just one single, static PD, neglecting the, sometimes strong, temporal dependence of tuning. In hommage to this view, we define the optimal time lag (OTL) as the time shift that maximizes the goodness-of-fit. We then read off a single PD read at the OTL from the corresponding effective von Mises fit (compare Section 5.2.2.5). The example unit shown in Figure 5.10 has a PD at the OTL of $\mu_{\text{OTL}} = 95.8\,^\circ$.

It is well established that the tuning of motor neurons to hand movement direction depends on the lead or lag with respect to the neural activity (Churchland et al., 2007; Hatsopoulos et al., 2007a; Mazzetti et al., 2022; Paninski et al., 2004; Suway et al., 2018). Nevertheless, the notion of having one single PD per neuron still prevails in literature.

To account for the temporal dependence, we will determine a PD per time shift (μ_τ) and weight it by a normalized modulation depth. The peak of the normalized modulation depth in general coincides with the peak in goodness-of-fit.

We define the time shift dependent modulation depth as

$$k(\tau) = \max_\theta \lambda(\tau, \theta) - \min_\theta \lambda(\tau, \theta) \tag{5.37}$$

with $\max_\theta \lambda(\tau, \theta)$ being the maximal firing rate at time shift τ across all directions θ. We normalize by the maximal modulation depth $\hat{k} = \max_\tau k(\tau)$, which in general coincides with modulation depth at OTL, and get the normalized modulation depth $\tilde{k}(\tau) = k(\tau)/\hat{k}$.

A unit can then be characterized using a distribution of (weighted) PDs accumulated across plausible time shifts (in the range of $\tau \in [-300, 300[\,\text{ms}$) as in Figure 5.11**C**,

Figure 5.11 illustrates that the PD at the OTL is a good representative for this example neuron: the largest entry to the histogram is still the PD as obtained via OTL. However, the advantage of the presented measure is, that it captures sudden switches in the PD of a unit.

5.4.3.5 *Directional tuning via a simple GLM summarized across units*

Having illustrated the way extracting the directional tuning of a single neuron that will be employed, we can proceed and summarize the distribution of these tuning across neurons. Figure 5.12 **C** shows the mean (weighted) PD distribution across all neurons pooled across all sessions, separately for Enya and Jazz. Panel **A** and **B** show the distribution of weighted PDs across neurons per time shift. Taking the marginal of these heatmaps over time yields the distribution in **C**.

To test these distributions for bimodality the Rayleigh r test for uniformity has been modified (see Section 5.2.2.9) and applied onto these distributions. We consider a bimodality to be significant if the p-value is smaller than 0.05.

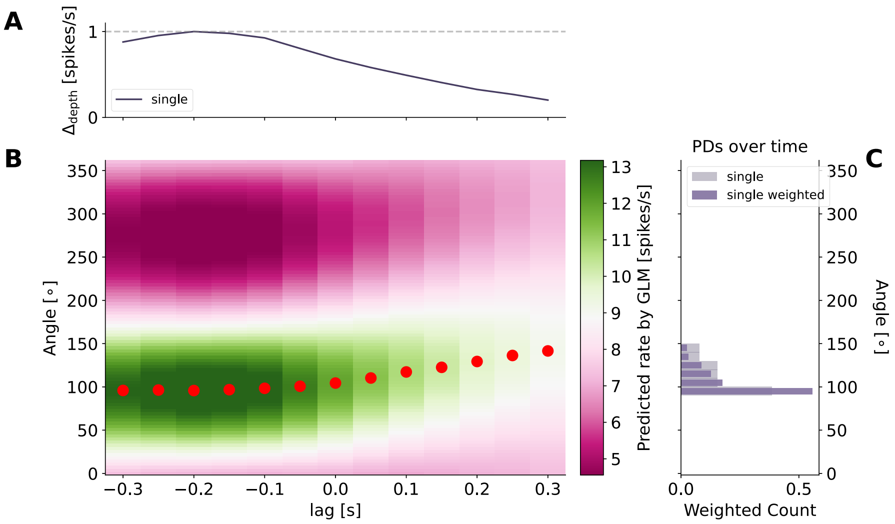

Figure 5.11: Directional tuning curve in plausible range of time shifts of exemplary motor unit *M1/PMd* 10.1 sorted by Alexa on session `y180306-land-001`. Data shown in **B** is same as within the vertical black, dashed lines in Figure 5.10. Red dots mark the PD for each time shift. **A** shows the modulation depth normalized by the maximal modulation strength observed across all time shifts (at the OTL). **C** is a histogram of the (weighted) PDs across time leads/lags, here "single" shows the unweighted histogram, while for "single weighted" each histogram entry is weighted by its corresponding normalized modulation depth.

The distributions for both monkeys are significantly bimodal (p-values reported in the figure) with the main axes of the bimodality being $\theta_{\text{Enya}} = 111.7$ and $\theta_{\text{Jazz}} = 94.7$. We hereby reproduce the bimodality of hand movement direction PDs in setups where hand movement is constraint to the horizontal plane that has been observed in M1/PMd previously by Scott et al. (2001b) and Suminski et al. (2015) and is theoretically predicted by Lillicrap et al. (2013) and Verduzco-Flores et al. (2022).

Furthermore, we resolve this distribution temporally in panels **A** and **B**, by plotting the kernel density estimate of the distribution of PDs across neurons per time lead/lag. These illustrate that the bimodality is stable across leads/lags in $\tau \in [-300, 300[$ ms.

While for Enya, the PDs very clearly cluster around the two directions of the bimodality, for Jazz the evidence is less clear. It remains to be show, whether this is an effect of the smaller sample size.

5.4.4 *Distribution of PDs for hand movement direction exhibits significant bimodality in visual and parietal areas*

To answer the question of whether a similar bimodality is also reflected in the unit activities upstream of the dorsal visual pathway, we now

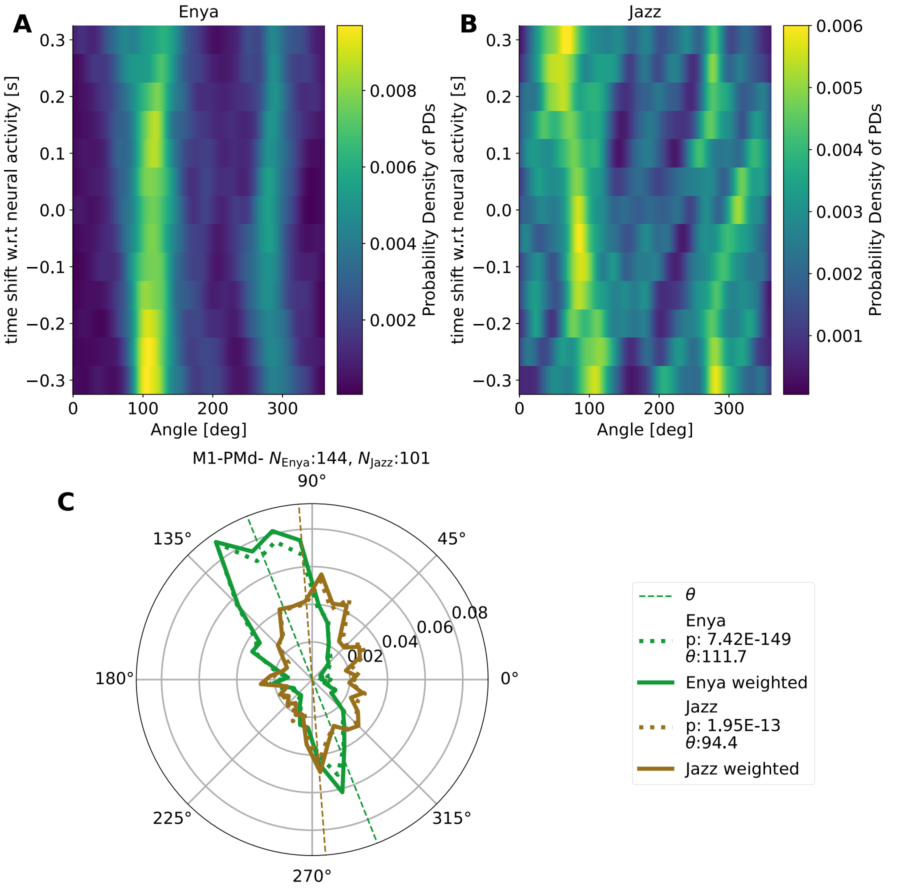

Figure 5.12: Summary of (time-resolved) distribution of PDs - M1/PMd. **A** and **B** show the time-resolved distribution of PDs for Enya and Jazz, respectively. Ro obtain a kernel density estimate (KDE), the distribution at each time shift was smoothed with kernel width $\sigma_{\text{KDE}} = 25°$. The polar distributions in panel **C** show the histogram of PDs across all units in M1 unweighted (dashed) and weighted by normalized modulation strength (solid) for Enya (green) and Jazz (brown). The main axis of skew of the distribution and p-value of the Rayleigh r test for bimodality are reported in the legend.

go beyond the analysis of units from M1/PMd and apply the same methodology to unit recorded from the visual and parietal areas.

To increase the number of analyzed units, we used two automatic spike sorters (Mountainsort4 and Tridesclous) to complement the manually sorted sessions. Details are described in Section 4.6. In the main text, we only present results based on units from Mountainsort4. The data for Trisdesclous is not shown. We observe no qualitative differences in the result and thus consider the neuroscientific finding as robust against spike sorters.

Similarly, to the situation in M1, Figure 5.13 show that distributions for the PDs are significantly bimodal for V1/V2, DP and 7a in Enya. For Jazz a significant bimodality could only observed in DP.

The lead/lag dependent KDE of PDs in Enya 7a reveals a prominent stripes centered at $\sim 100\,^\circ$ and less prominent at $\sim 300\,^\circ$. In contrast to M1, however, the PDs distribution at $\sim 100\,^\circ$ dominates for strong negative time shifts and then seems to progressively switch to $\sim 300\,^\circ$ for positive time shifts. Similar trends are observed in the other areas.

While for Enya, the lagged PDs at $\sim 100\,^\circ$ dominate, in Jazz the leading PDs at $\sim 300\,^\circ$ are stronger. The marginal distributions, integrated across time shifts, reflect these two stripes.

The similarity of time shift dependent KDE of PDs among M1/PMd, the parietal areas and even the visual areas, was not expected. The prevailing hypothesis for the origin of the bimodality M1/PMd is that for hand movements constrained to the horizontal plane particular groups of muscle are maximally contracted only in two directions (the two directions of the bimodality) (cf. Verduzco-Flores et al. (2022) and Section 5.6) and that this is reflected in the neural activity. While has been shown that this effect is observable in motor (Scott et al., 2001b) and premotor areas (Suminski et al., 2015), it would be surprising if muscle activity affects parietal and visual areas. To ensure the validity of our results, we hence need to be careful and exclude potential confounds as discussed below.

5.4.5 *The directional tuning might be biased due to confounding variables, especially in visual and parietal areas*

The GLM analyses shown in the previous section are solely based on the instantaneous hand movement direction as a regressor. This in turn, effectively leads to fitting the optimal β-coefficients over all occurrences of a certain movement angle and thus an average across all possible circumstances. Behaviors other than hand movement but occurring correlated in time with the could thus give rise to spurious hand movement tunings, especially if the neural response to other behaviors is also tuned.

In the following, we present examples of neurons that exhibit responses to other behavioral variables and argue that these might bias

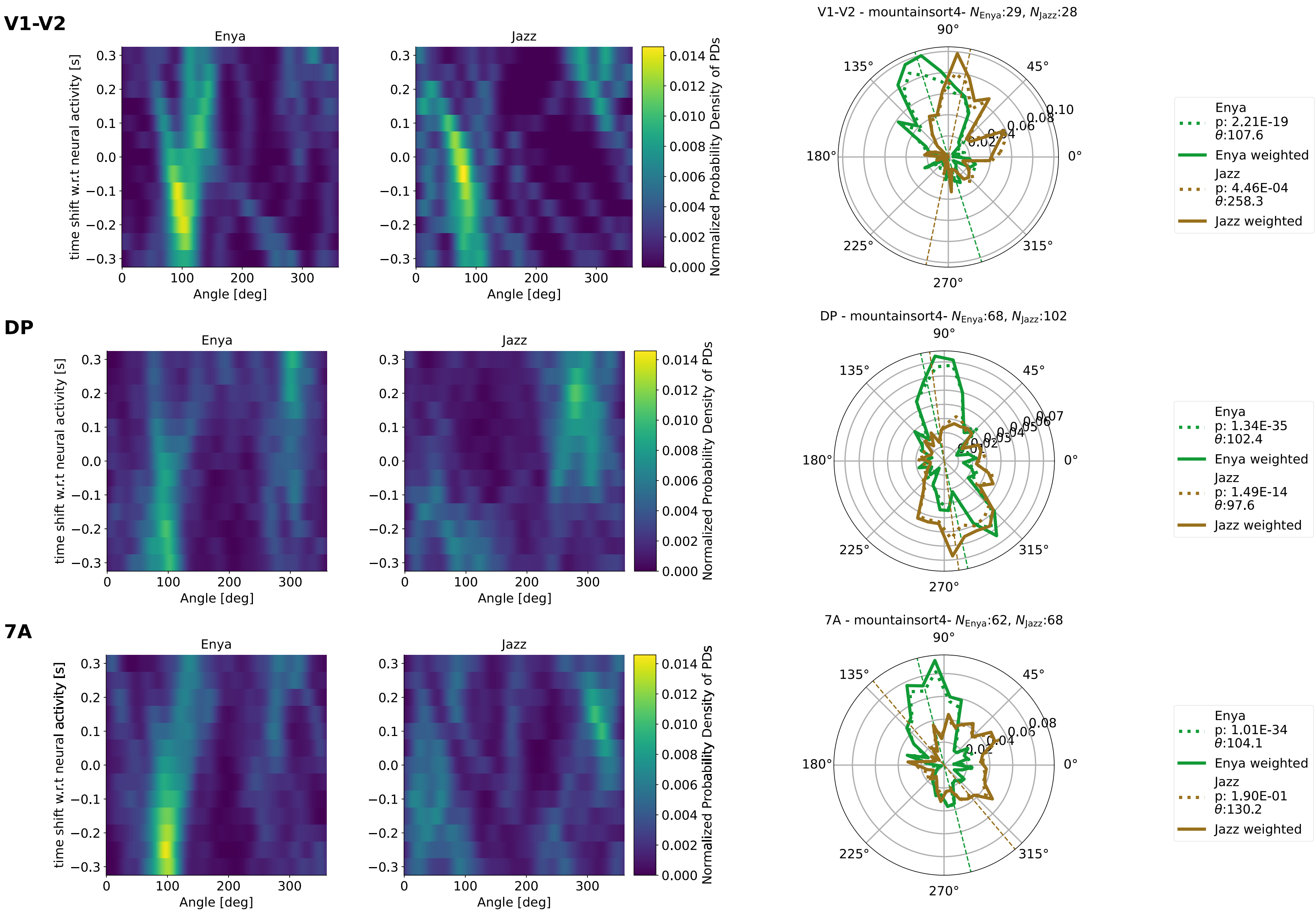

Figure 5.13: (Caption continues on next page.)

Figure 5.13: (Continued caption.) Summary of (time-resolved) distribution of PDs - visual and parietal areas. The three rows of plots show the results of areas V1/V2, DP and 7a, respectively. For an explanation of the figure elements refer to Figure 5.12.

the directional tuning analysis. Then we deal with these confounds by using a more complex variant of a GLM (see Section 5.2.2.6), briefly analyze the GLM fit outcome and present corrected distributions of PDs.

5.4.5.1 *Examples of neural responses that might lead to confounds*

V2 UNIT WITH CLEAR RECEPTIVE FIELD (RF) A preliminary receptive field mapping of online sorted single units in the visuo-parietal areas revealed that the receptive fields are located on the lower right of the fovea in V1 and V2 (data not shown) and thereby confirmed the RF location expected by retinotopic maps (see Figure 2.2).

This was confirmed by looking at the reverse correlation of both the hand and target positions relative to the eye, which is basically a signal triggered distribution of the instantaneous firing rate Section 5.2.3. We here average the means of firing rate distributions obtained for a range of time lags of the firing rate shifted with respect to the signal (e.g. hand position relative to the eye position) from 20 ms to 120 ms to isolate the neuronal response to the visual stimulus being at a certain position.

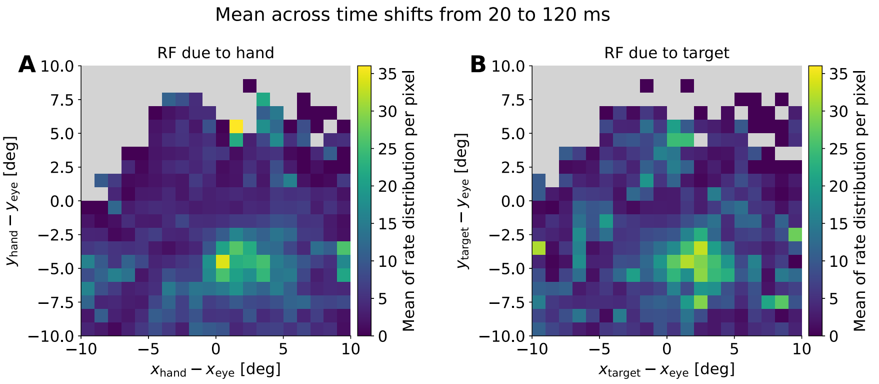

Figure 5.14: Reverse correlation analysis of an example unit from V1/V2 exhibiting a RF. **A** shows the average triggered rate distribution with the hand position relative to the eye position as signal and **B** the target position relative to the eye position.

The example neuron shown in Figure 5.14 has its RF centered at roughly 5° downward and 2° to the right with respect to the gaze point. We observe that many neurons in V2 have RFs at similar positions, but the RF size might differ (data not shown here).

Given the position of the RF, we expected responses to occur predominantly in two different situation in the landing task (see also Figure 5.15):

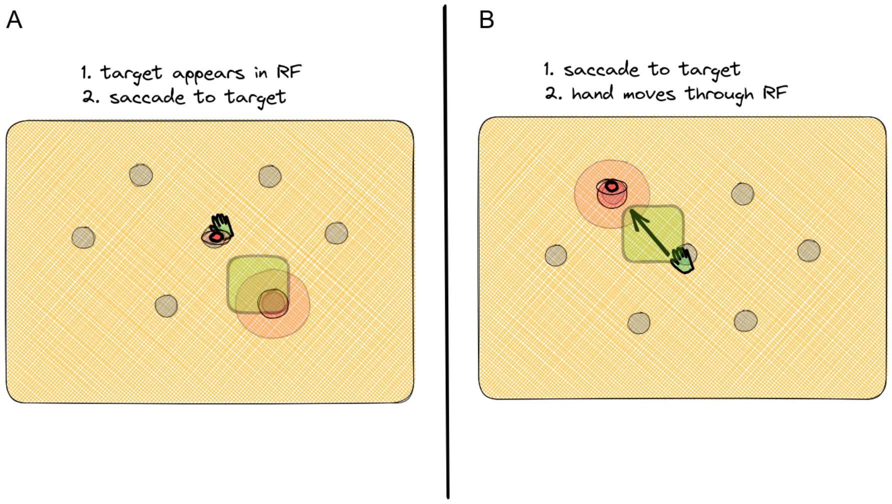

Figure 5.15: Example: V1/V2 unit with RF - Sketch of relation between RF and saccade-related activity. **A** and **B** illustrate two situations in the landing task that lead to a stimulation of the RF.

1. the target appears directly in the RF
    - consider the eye focuses the center target
    - the lower right target appears and triggers the RF
    - the monkey does a saccade towards the target (direction $\sim 300°$)
    - the monkey moves the hand towards the target (direction $\sim 300°$)
2. the hand moves through the RF
    - consider the eye focuses the center target
    - the upper left target appears
    - the monkey does a saccade towards the target (direction $\sim 100°$)
    - the monkey moves the hand towards the target (direction $\sim 100°$) and triggers the RF

Evidence for this can be found on in the direction-resolved saccade triggered PSTHs as shown in Figure 5.16. The first situation manifest as increased in activity for $\sim 300°$ after the saccade, while the second shows as activity around $\sim 100°$ prior to the saccade.

Critically, these activations give rise to hand movement directional tuning as a by-product. The origin of this artifactual hand movement directional tuning, however, is the visual stimulus. As visual stimuli

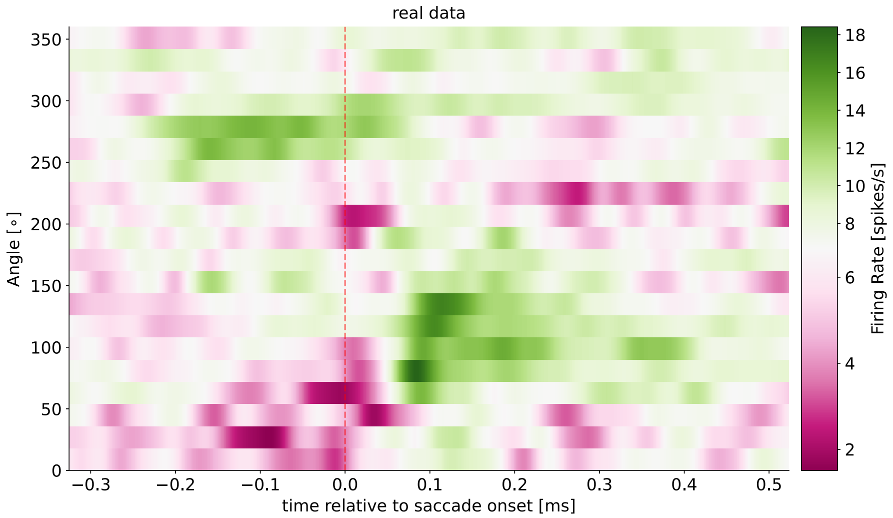

Figure 5.16: Example: V1/V2 unit with RF - Saccade triggered PSTHs. The spiketrains are aligned to the saccade onsets. Only saccades with a saccade distance exceeding 2 cm were chosen, yielding 1405 saccades and saccades were binned by their direction on the y-axis. Single trial firing rates were calculated by convolution with a Gaussian kernel with $\sigma = 15$ ms and then averaged.

and movement occur in the task in a correlated fashion, a naive extraction of hand movement PD leads to a false conclusion.

By explicitly including regressors that would capture this visual response in the GLM, we can correct this confound. In Section A.3.3.1, we convince ourselves that this actually works quite decently.

INFLUENCE OF SACCADE ACTIVITY ON HAND MOVEMENT DIRECTIONAL TUNING Similarly, we found strong responses (or suppressed firing) due to saccades in several unit recorded from area DP. Figure 5.17 shows raster diagrams of three exemplary units.

These saccade responses seem to appear for saccades in every direction. However, as can be seen in panels **A** and **B** the response is stronger for some directions. Saccade direction and hand movement direction are strongly correlated, as in the task typically both eye and hand move towards the target, and hence we want to avoid spurious movement tuning due to saccades.

In Section A.3.3.1, we demonstrate that the GLM captures the effect. By explicitly removing the saccade-related influence, it turns out, that the remaining contribution of the movement-related components becomes stronger (see Figure A.10).

EYE POSITION AND HAND POSITION GAIN FIELDS We reviewed in Section 2.4 that neurons in 7a were shown to exhibit gain modulation due to the eye and hand position. A signal triggered distribution averaged across multiple time lags in Figure 5.18) shows increased ac-

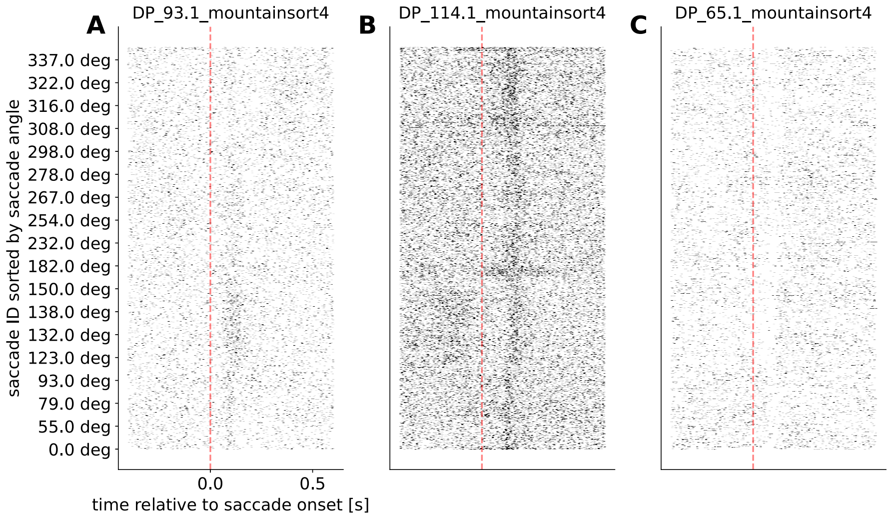

Figure 5.17: Example: Three DP units with saccade response. The spiketrains are aligned to the saccade onsets. Only saccades with a saccade distance exceeding 2 cm were chosen, yielding 1405 saccades and saccades were sorted by their direction on the y-axis.

tivity of that neurons for a certain eye position. Refer to Section A.3.3.3 to see that the complete GLM manages to reflect the activity pattern rather well.

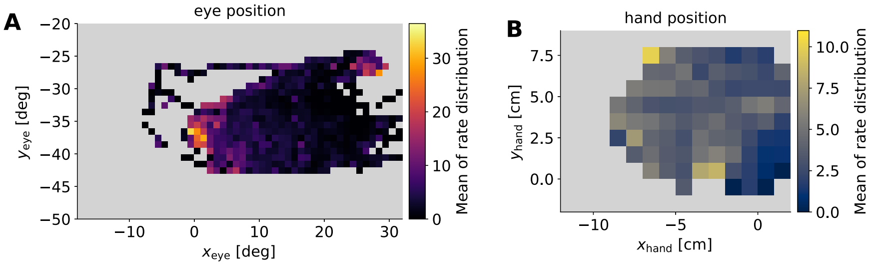

Figure 5.18: Reverse correlation analysis of an example unit from 7a unit with strong eye position gain modulation. **A** Eye position and **B** hand position gain.

5.4.5.2 *GLM reveals tendencies in neural response patterns*

In the previous section, we presented a few example neurons with a characteristic neural response. Furthermore, we argued that a GLM with well-modeled regressors is able to capture these neural responses.

Having access to such model fits, we can further analyze the impact of different behavioral variables on every single neuron. To achieve this, as described in Section 5.2.2.8, we first fit the complete model, followed by models in which we leave out a particular regressor block (nested model), and then compare the goodness-of-fit of the nested to the complete model. The measure that we are interested in is the w-

value, which measures the impact of a regressor block on the neuron's activity Equation 5.34). The set of w-values for each nested model can be seen as a *neuron fingerprint*, which shows the selectivity to the behavioral modalities (idea by Diomedi et al. (2020) and Vaccari et al. (2021)).

For the example neurons that we presented before, we obtain the fingerprints shown in Figure 5.19. The V2 unit with a clear RF shows a strong impact of the visual regressors. For the DP unit (DP_93.1_mountainsort4) the largest increase in goodness-of-fit for the unit with saccade response as achieved by adding the saccade regressor block.

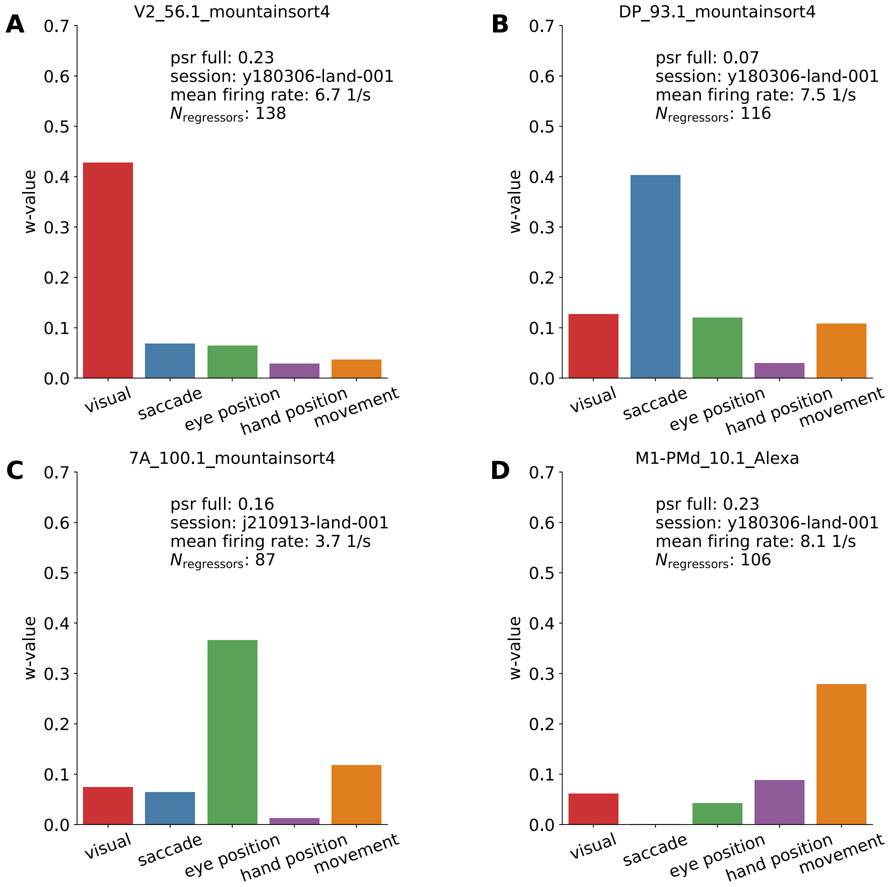

Figure 5.19: Neural fingerprints of example units. In addition to the fingerprints, the goodness-of-fit as defined by Equation 5.23, the recording session, the mean firing rate and the number of remaining regressors after Lasso regularization are reported.

OVERALL GOODNESS-OF-FIT OF THE COMPLETE GLM Figure 5.20 illustrates that the level of goodness-of-fit observed for the example neurons in Figure 5.19 is achieved for the majority of neurons. Across sessions, experimental subjects, sorters and areas, we accumulated 2053 neurons, out of which 1373 survived the rejection due to our quality metrics (see Section A.1.4). These numbers contains cases of the same unit being isolated by multiple sorters. Nevertheless, the complex GLM was fitted to all unit irrespective of whether it was later on excluded.

Comparing the outcome of two disparate spike sorting procedures is difficult due to the lack of ground truth. Having our single neuron fingerprints enables us to identify matching units that were isolated by two different sorters.

Besides the quality metrics, we use a threshold in the goodness-of-fit set at $\widetilde{R}^2 = 0.05$ to exclude units from further analysis, for which the GLM performs poorly. Goodman et al. (2019) state that a pseudo-R^2 value of $\widetilde{R}^2 = 0.05$ roughly corresponds to a regression on the trial-averaged PSTH with $R^2 = 0.08$. Requiring at least $\widetilde{R}^2 = 0.05$ was recommended in (Goodman et al., 2019; Vaccari et al., 2021) and proved to be sensible threshold judging by the visual comparison of model prediction and real data akin to Figure A.9.

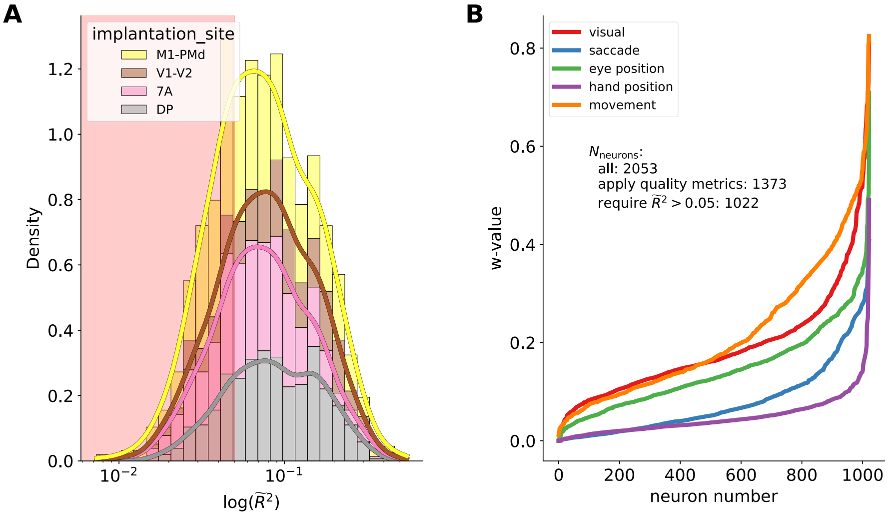

Figure 5.20: Goodness-of-fit and w-values across all analyzed neurons. **A** Distribution of pseudo-R^2 as a measure of goodness-of-fit in a histogram with logged x-scale. Contributions of the different recording areas are encoded in the stacked histogram. Unit fits with goodness-of-fit < 0.05 (red, shaded region) are excluded from analysis. **B** Sorted w-values.

In Figure 5.20**B** we see the sorted w-values from which one can easily read off how many neuron have a certain w-value or larger. The eye position and hand position regressor blocks seem to have a weaker explanatory power than the other three. Largest w-values are observed for the movement regressor block.

DISTRIBUTION OF W-VALUES PER AREA In Figure 5.21, we show the distributions of w-values per regressor block. Similarly, in Figure 5.22 we depict the distributions of w-values per recording area.

To avoid any double count of units from the same session, we here include only M1/PMd units sorted by Alexa (from Enya sessions) and Fred (from Jazz sessions) and visual-parietal unit sorted by Mountainsort4 (compare Table 4.3).

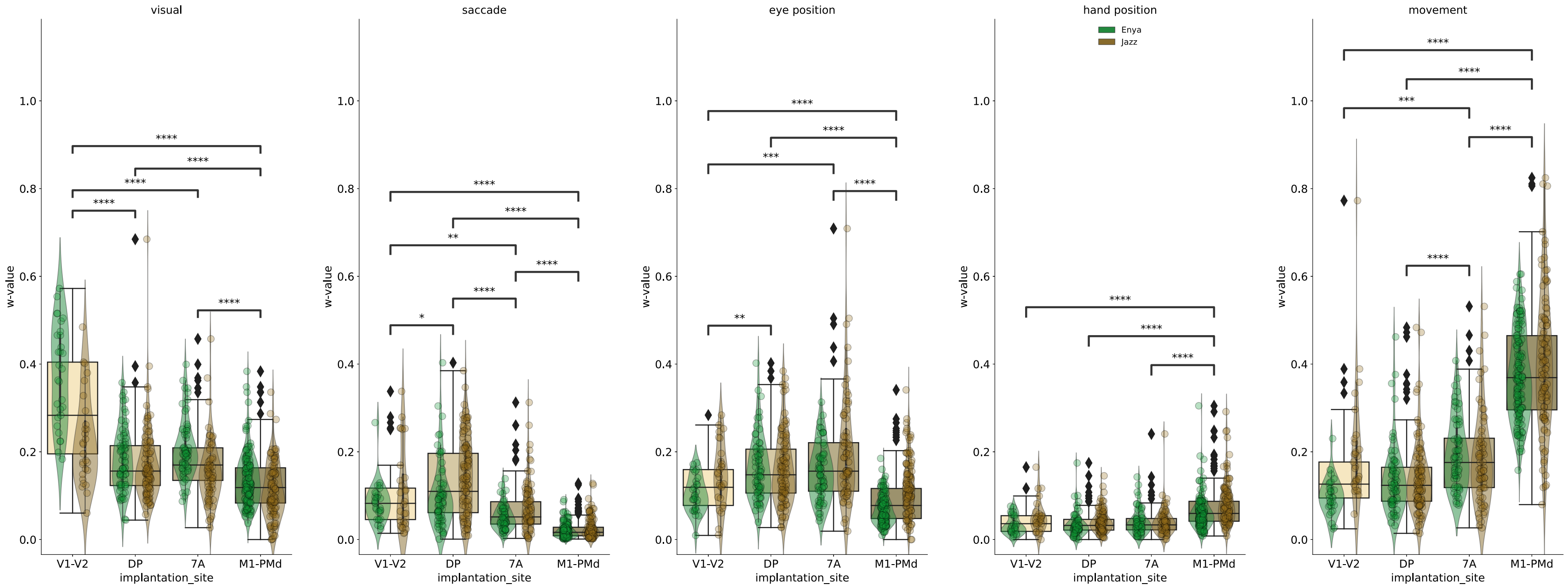

Figure 5.21: (Caption continues on next page.)

Figure 5.21: (Continued caption.) Distribution of w-values per regressor block. Within one regressor block, we report the distributions of the units from the different areas. The box plots summarize the all units from both monkeys. The violin plots shows the distributions per monkey (Enya: green, Jazz: brown) with the values of each single neuron being marked with a small circle. A two-sided Mann-Whitney-Wilcoxon test was performed on all pairs of distributions (as represented by the box plots) between areas and only significant parings were annotated. P-value annotation legend: *: $1.00e-02 < p <= 5.00e-02$, **: $1.00e-03 < p <= 1.00e-02$, $***: 1.00e-04 < p <= 1.00e-03$, ****: $p <= 1.00e-04$.

We observe a clear increase in w-values for the movement regressor block along the dorsal visual stream. Conversely, we see decreasing w-values for the visual regressor block. As far as we know, such a progression of the importance of movement variables along the dorsal visual stream and a decrease of visual variables has not been reported in literature yet.

We tested for significant difference between the distribution with a two-sided Mann-Whitney-Wilcoxon test. The information in the plot can be read as follows: The distribution of the visual regressor block w-values V1/V2 is significantly different from DP, 7a and M1/PMd. However, the distributions of the visual regressor block w-values do not significantly differ between DP, 7a. As this is not the main result of the present analysis, we will leave more in depth interpretations for future research at this point.

Noteworthy, there are some V1/V2 neurons which exhibit strong w-values for the movement regressor block (opposing the argument made in Talluri et al. (2022) and in line with findings in mice (Musall et al., 2019; Stringer et al., 2019b)).

The average fingerprints per area (Figure 5.22) reveals that:

- there is no clear dominant regressor block in DP and 7a revealing mixed selectivity
- in DP, the saccade regressor block shows slighlty higher values compared to in the other areas
- in DP the mean w-value for eye-position is strongest
- 7a shows a few neurons with strong impact of the eye position regressor block (likely reflecting eye position gain fields)
- 7a shows a few neurons with strong impact of the movement regressor block
- there is an impact of the visual regressor block on M1/PMd

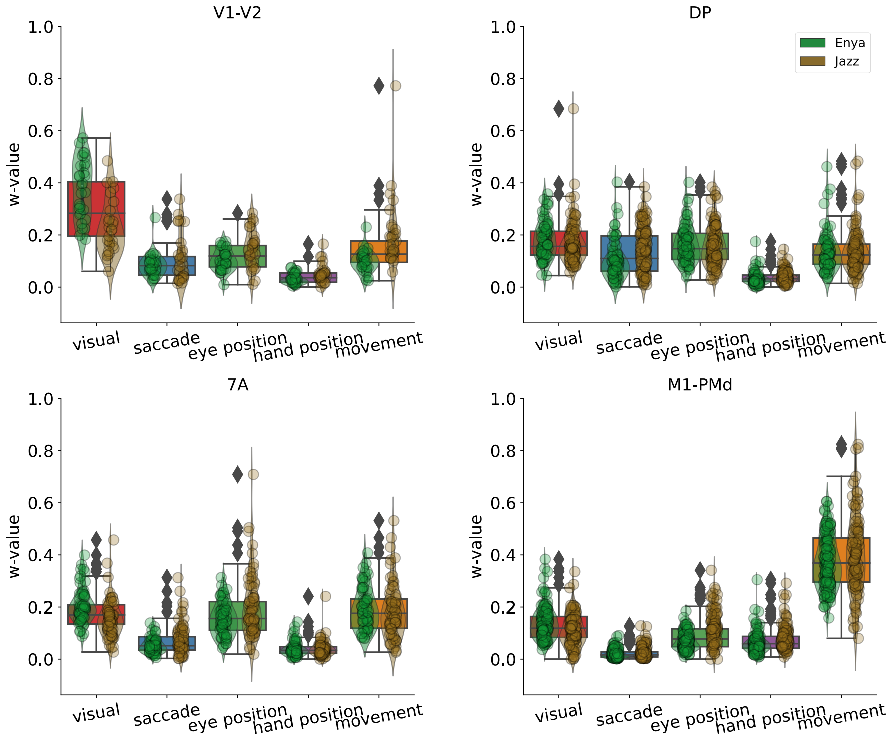

Figure 5.22: Distribution of w-values per area.

After having decided to only include neurons which have a goodness-of-fit larger then $\widetilde{R}^2 = 0.05$ and having demonstrated the effectiveness of the GLM approach, we can finally make use of the models to calculate the directional tuning and explicitely remove confounding effects. We follow the procedure detailed in Paragraph 5.2.2.6.

5.4.6 *Bimodality in visual and parietal areas prevails after correction for confounding effects*

Per unit, we follow the procedure detailed in Paragraph 5.2.2.6 to average out the effect of any regressor except for the movement regressor block. The aim of this is to avoid potentially confounding variable to cause spurious activity that would misleadingly influence the nature of the instantanteous hand movement directional tuning of single units.

Figure 5.24 presents the results of this rather intricate procedure pooled across all neurons in the visual and parietal areas. The results after exclusion of confounds for M1/PMd is shown in Figure 5.23.

We observe that the main tendencies were already visible via the simple GLM extraction of PDs as shown in Figure 5.12 and Figure 5.13.

For M1/PMd the correction lead to slightly shifted main axes of the bimodality ($\theta_{\text{Enya}} = 113.0$ and $\theta_{\text{Jazz}} = 100.1$.) and marginally decrease p-values. Only weak changes in the result were expected, as the movement regressor block by far has the greatest impact on

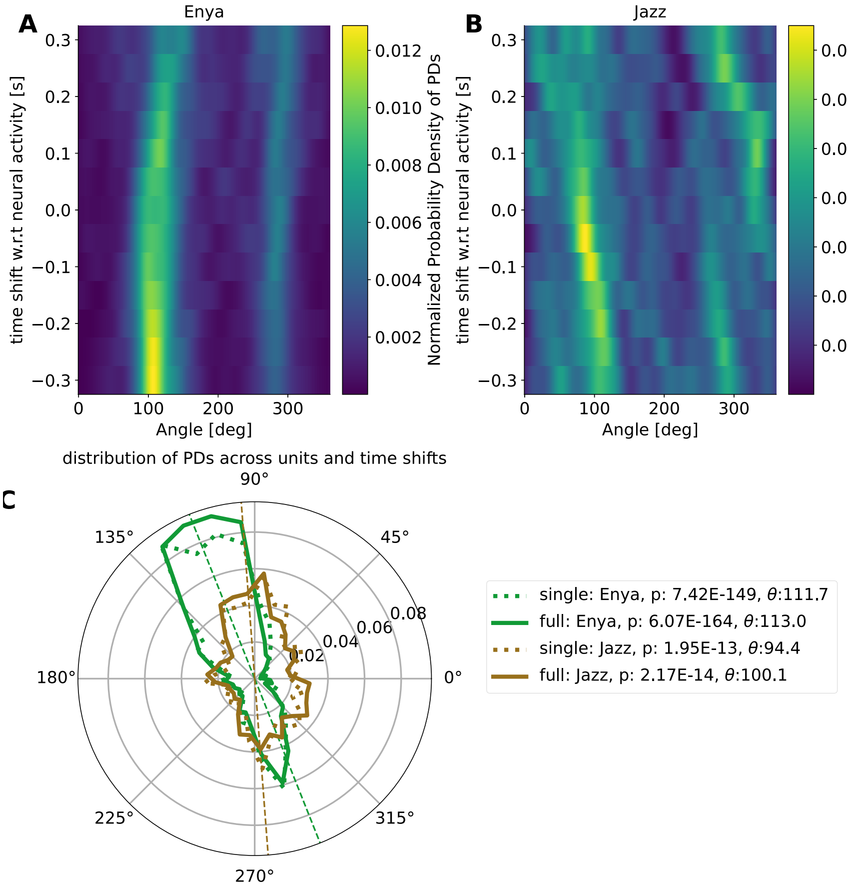

Figure 5.23: Summary of (time-resolved) distribution of PDs via complete GLM - M1/PMd. **A** and **B** show the time-resolved distribution of PDs for Enya and Jazz, respectively. Ro obtain a KDE, the distribution at each time shift was smoothed with kernel width $\sigma_{\text{KDE}} = 25°$. The polar distributions in panel **C** show the histogram of PDs across all units in M1 from single GLM (dashed, as before) and weighted by normalized modulation strength (solid) for Enya (green) and Jazz (brown). The main axis of skew of the distribution and p-value of the Rayleigh r test for bimodality are reported in the legend.

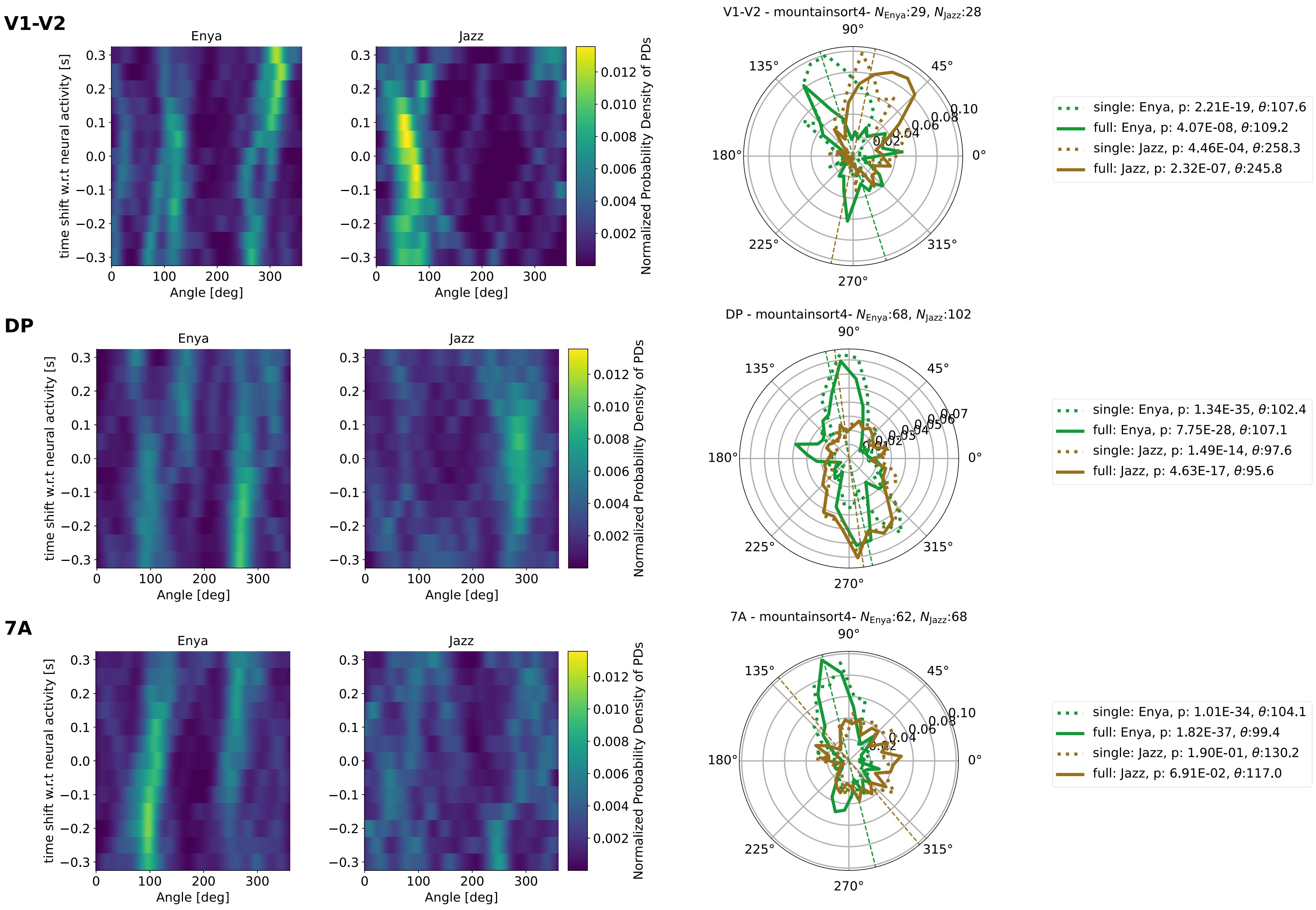

Figure 5.24: (Caption continues on next page.)

Figure 5.24: (Continued caption.) Summary of time-resolved distribution of PDs via complete GLM - visual and parietal areas. For an explanation of the figure elements refer to Figure 5.23.

units from the motor areas (see Figure 5.21). Hence, we confirm the predicted (Lillicrap et al., 2013; Scott et al., 2001b; Suminski et al., 2015; Verduzco-Flores et al., 2022) bimodality of the distribution of PDs for the hand movement direction in our monkeys, setup, and tasks.

Following the discussion upstream the dorsal visual pathway, in 7a, we still have the same picture as before: The distribution is significantly bimodal in the neuron population recorded from Enya, but not for Jazz.

Strikingly, the main axis of bimodality in Enya ($\theta_{\text{Enya, 7a}} = 99.4$) roughly points into the same direction as predicted in M1/PMd. The two pronounced bands of the time-resolved distribution as visible in M1/PMd, now are distinctly visible in Enya. Although not significant in Jazz, there is a tendency for two bands, as well. However, this might be due to the visualization which ideally should lie on a cylindrical plot instead of suggesting a discontinuity between $0°$ and $360°$.

Further upstream, DP, exhibits significant bimodalities in both monkeys which are also reflected in two pronounced bands of the time-resolved distribution. While the simple GLM result showed a stronger band around $100°$, the corrected result is visually peakier around $300°$.

Finally, in V1-V2, both distributions are significantly bimodal. The main axis of skew for Jazz, however, shifted towards $\theta_{\text{Enya, V1-V2}} = 245.8 - 180° = 65.8°$.

5.5 SUMMARY

The study presented in this chapter aimed to answer the following research question: Is the bimodality of the distribution of PDs that has been observed in M1 and PMd/PMv also present in the parietal and visual cortex of macaque monkeys that perform a visually guided reaching task with hand movement being constrained to the horizontal plane?

We investigated datasets from the V4A experiment, in which the experimenters recorded neural activity along the dorsal visual stream and motor cortex and various behavioral signals (e.g. hand position, eye position) from two monkeys that performed visually guided reaching task.

We started our analysis by reasoning, that the V4A datasets are suitable for the analysis of our question. In particular, we showed exemplary behavioral data with a focus on the hand movement and illustrated the presence of directional tuning in the neural activity of an exemplary M1/PMd unit by means of a classical trigger-alignment of the PSTH.

To avoid biases in the extraction of the tuning curve due to an observe anisotropy of the movement velocities for different directions, we first resorted to fitting an encoding model, namely a GLM (explained in Section 5.2.2). In its simple form this GLM allows to extract a von Mises tuning curve for a specific temporal relationship (time-shift) between neural activity and hand movement Section 5.2.2.5.

After having ensured, that the GLM fit yields results that are compatible with the classical tuning analyses for the example unit, we extend our analysis to all units from M1/PMd and look at the distribution of PDs across units.

By doing so, we reproduce the bimodality of the distribution of PDs that has been observed in M1 and PMd/PMv with V4A dataset. For each monkey the main axis of bimodality is consistent with the predictions.

In a next step, we went one step further, and applied the same analysis to the recording sites along the dorsal visual stream, namely v1/V2, DP and 7a. We find that that distributions for the PDs are significantly bimodal for V1/V2, DP and 7a in one monkey (Enya), however for Jazz a significant bimodality could only observed in DP.

These observations were unexpected, because the bimodality in the PD distribution is assumed to be dictated by the biomechanics of the limb and in particular the required muscle activations during hand movements in 2D. Based on this assumption, it is not trivial to see an effect of this in visual and parietal areas.

Being aware of the fact, that in our tasks, the monkeys perceive visual signals, make saccadic eye movements, and move their hand to the displayed targets, simultaneously, we had to explicitly exclude any confounding effects to further validate these surprising observations. In Section 5.4.5 we therefore presented example neurons that exhibit a RF, saccade-related activity or eye position gain field, respectively.

To achieve a removal of these confounds, we chose to fit a more complex GLMs to the neural activity that could account for the impact of various behavioral modalities (*visual*, *eye position*, *saccade*, *hand position* and *movement*) on the activity.

We then reasoned, that the more complex GLMs indeed captures the confounding influences. The GLMs gave us access to a measure of the impact of various behavioral modalities on a single neuron's activity (set of w-values that we considered as a neuron fingerprint). With these, we confirm the expectation of a progressive decrease in the influence of visual variables along the dorsal visual pathway and, conversely, an increase in the influence of hand movement variables.

Finally, the complex GLM allowed us to isolate the influence of the hand movement direction on the neural activity, and thus supplied a "corrected and unbiased" estimation of the PD of each single unit. Even after applying this correction, we are confident to answer the initial research question: We do find significantly bimodal distributions of PDs for hand movement for both monkeys in V1-V2, DP and for Enya also in 7a.

5.6 DISCUSSION

5.6.1 *Implications of the results*

BIOMECHANICS AS CAUSE FOR BIMODAL DISTRIBUTION OF PDs Recently, the biomechanistic modeling of joints and muscles received a lot of attention from the robotics and machine learning community. The open-source, physical simulations software MuJoCo (Todorov et al., 2012) is used to model the agent, that is trained via reinforcement learning algorithm to generate a broad range of movements (Fischer et al., 2021; Mukherjee et al., 2022; Schumacher et al., n.d.; Wang et al., 2022a). In line with the view that embodiment is necessary to achieve appropriate understanding of the interplay between sensory and motor systems, this could serve as a platform to create biorelatistic models driven by networks of spiking neural networks.

Modern studies (Codol et al., 2023; Verduzco-Flores et al., 2022) train such biomechanics model with neural networks (of varying complexity) to perform movement in the horizontal plane. The resulting neural activations reflect the biomality as was shown experimentally in Scott et al. (2001b) and later on modeled by Lillicrap et al. (2013).

The most precise model, to our knowledge, is presented in Verduzco-Flores et al. (2022). Their model consists of a circuit based on sensorimotor area, motor cortex, the spinal cord and muscles that learns 2D center-out reaching with biological plausible learning rules. They use this circuit as a feedback controller: In sensorimotor cortex some unit encode the acutal position (using a proprioceptive signal from the spinal cord), some the position of the target, in another layer of the sensorimotor cortex then encode the error (hand-target distance), which is then transmitted to motor cortex, where units are grouped in dual pairs accounting for positive and negative errors. These motor neurons in turn connect to the spinal cord which controls the muscles.

One of their results is, that their model reproduces the bimodality of PDs and they make the link between motor units firing preference and biomechanistic constraints even more clear: They are able to explain the bimodality as a linear combination of “directions of maximum (muscle) contraction”.

Closely related to such a picture is a study by Griffin et al. (2020) who presented evidence, that neurons in M1 generate command signals that generate “pre-movement suppression”, which in turn leads to antagonist muscles of upcoming movements to turn off.

Naselaris et al. (2006), who find an enrichment of for forward and backward PDs in 3D reaching hypothesize hyperacuity to be the cause.

The hyperacuity hypothesis states that certain movements, like forward and backward reachings, are performed more often in naturalistic behavior and thus might be overrepresented in neural activity. The accumulated evidence in favor of the hypothesis that the bimodality of PDs arises due to the biomechanics constraint in 2D movement renders this alternative hypotheses unconvincing (see also Kurtzer et al. (2007) who commented on the hyperacuity theory).

The most surprising result to us, is that we found tuning of visual neurons to the hand movement direction and that across neurons, the distribution of PDs turned out to be bimodal (at least judging based on the statistics). This raises the question of whether neurons in V1/V2 exhibits movement-related activity and if yes how strong it is.

A recent study by Musall et al. (2019) sparked interest in the community by showing that, in mice, uninstructed movements during a cognitive task execution accounted for most of the measured neural variance, also in visual cortex. Recently, Talluri et al. (2022) and Tremblay et al. (2022) investigated this hypothesis in primate data and demonstrate the effect to be present, but much weaker. Our study similarly suggests neural activity being related to movement. By chance our analysis resembles the one in Talluri et al. (2022), with the difference that they use a linear encoding model, while our encoding model is non-linear.

Our results further add evidence for an existence of such a movement-related activity even in visual cortex of primates.

Less striking, yet unexpected are the bimodalities of PDs observed in parietal cortex. PPC is known to exhibit movement-related acitivities. However, our finding raises doubts on the current understanding of the origin of the bimodality. While for M1 and also the premotor areas PMd/PMv it seems reasonable that muscular activation influences the neural activity (or vice versa) as mono- or disynaptic connections down the spinal cord exist (Strick et al., 2021), such direct connections from parietal cortex to spinal cord are less reported (notable exception (Rathelot et al., 2017)) and thus such a direct influence is not expected.

5.6.2 *Limitations of the current study*

CONTROLLED VS. NATURALISTIC TASK DESIGN Here, we chose to include data from the whole recording sessions, accepting that uncontrolled behavior during intertrial periods might happen. Still, the data largely consists of period in which the monkeys perform the task.

Our dataset thus lives in between two extremes: On the one hand, traditionally, there are very controlled settings, which likely also constraint the neural repertoire which it gives rise to. On the other hand, the trend goes to the recording of very naturalistic behavior in freely moving animals (Frey et al., 2021; Musall et al., 2019; Urai et al., 2022), probing a larger variety of neural response. While our tasks move away the very controlled settings, we are still far from completely naturalistic movements.

In Aflalo et al. (2006), for example, they used a free moving paradigm was and extracted directional tuning via a linear regression analysis. They found that the directional tuning explained a vanishingly small amount of the variance.

The advantage of a dataset like from the V4A is, that it is multipurpose and allows for data-driven analyses of various kinds, potentially revolutionizing the field. However, while this dataset allowed for the kind of analysis as presented here, I would argue that a more controlled setup/task specific to the research question (akin to hypothesis-driven research) could have simplified the analysis and would remove doubts on the removal of confound variables.

GLMS - THE SWISS ARMY KNIFE OF A NEUROSCIENTIST One challenge in the analysis of data that does not adhere to a strict trial structure is that classical alignment analysis are difficult. It is demanding to isolate the relevant events to trigger the neural activity. While the powerful GLM deals with this issue "under the hood", it starts to become a black box. Therefore, after "knowing" about response patterns from the GLM, we again resorted to visualizations based on the old fashioned alignment analyses (e.g. Figure 5.9, Figure A.10) to confirm and make sense of this black box. In Figure A.6 we took a glimpse into this black box by visualizing the β-coefficients that supposedly represent the RF of the example V1 unit. Yet, to confirm the model fit in such a way for each single unit is tedious for large-scale recordings with many single neurons.

INCLUDE REGRESSOR, THAT CAPTURE TASK PERFORMANCE For future analyses it might be worth considering that different contexts (successful vs. unsuccessful) can alter the neural representation of a given movement. It is well established that, in particular, parietal areas modulate their acitivty with attention. The task performance could be used as a proxy to capture such an effect. Ideally, we could record the pupil size (as was done for some recording sessions) and include it as regressor to describe such effects.

CHOICE OF MOVEMENT REGRESSORS In its current form, in our GLM directional tuning to hand movement is assumed to be unimodal following a von Mises function. However, we performed preliminary analysis using reverse correlation analyses and found tunings that were best fit by a bimodal single unit tuning curve. A future study should definitely incorporate regressors that allow for a bimodal tuning curve to exist.

INFLUENCE OF LEFT OUT REGRESSORS The choice of regressor variables in a large GLM is subject to a trade-off: The number of samples in a recording needs to be large enough to allow for a reasonable fit, yet you want to include as many regressors as possible to capture every possible explainable effect.

One large block of regressors, which could be added to our models, are the other neurons recorded simultaneously. This was done by Stevenson et al. (2012) with success and enable the analysis of functional connectivities. In Stevenson (2018) the same author demonstrates that omitting regressor variables might introduce a bias (very similar to our reasoning after the use of the simple GLM).

Interestingly, the models in Stevenson et al. (2012) use a time-instantaneous GLM, which drastically reduces the number of regressors and thus allows for the inclusion of parallel recorded spiketrains. In contrast, our model takes into account time shifts, which leads to a quick explosion of regressor variables.

The key point in our analysis is the presence of the bimodality of PDs and it is noteworthy that Stevenson et al. (2012) states in their paper that “However, the structure of the tuning curve (i.e. the PD, frequency, or place) remained relatively unchanged”, while the tuning modulation might change. Interestingly, this statement proofed to be miraculously true also for neurons in visual and parietal areas.

POOLING ACROSS SESSIONS IN CHRONIC RECORDINGS MIGHT INTRODUCE BIAS One major point of critique is that we pool neurons across many sessions from chronically implanted Utah arrays: One may doubt the independence of units isolated from the same channel, but on two different recording days. To weaken this critique, we aimed to choose session with substantial time in between recordings. Unfortunately, this was not always the case which might have introduced multiple counts of effectively the same neuron in the presented distributions. If present, this bias would be stronger in Jazz, as we pooled across more sessions to have a reasonable neuron count in total.

To strengthen the observations one could compare the neuron fingerprints of units recorded from the same electrodes and try to exclude matching units. To counteract an eventually reduced neuron count, we would need to expand the analysis to more sessions, in turn.

5.6.3 *Outlook*

TEST THE PREDICTIONS MADE BY BIOMECHANISTIC MODELING As reviewed above, several ways of modeling neural control of biomechanistic arm models have shown the occurrence of the bimodality of PDs. Common among the models is the prediction, that the main axis of bimodality changes with the area within which the hand movements are performed. Lillicrap et al. (2013) modelled a shift in the location of the targets and showed that the bimodality of PDs systematically shifts its main axis.

This prediction could be tested in the V4A setup as well. We propose to uncouple the actual hand movement from the visual feedback to achieve this. If the visual feedback of the hand movement is still located centered to the body, but the actual hand movement happens displaced with respect to it (e.g. to the right), we would expect to see the predicted shift of the main axis. If we see the shift of bimodality also in visual and parietal areas, this would strengthen evidence that the bimodality is a result of the movement and therefore validate the finding of the present study.

NEURON FINGERPRINT AS A MEAN TO DETECT MIXED SELECTIVITY The neuron fingerprints obtained by calculating the various nested models can be interpreted as strong evidence fo the occurrence of mixed selectivity (Rigotti et al., 2013) in all recorded area. This has been advertised by the nicely written method paper Vaccari et al. (2021) and used previously in (Diomedi et al., 2020) to uncover mixed selectivity in medial parietal cortex area V6A. A similar approach was taken by Ledergerber et al. (2021), who perform a forward model selection procedure and thereby evaluate the gain of the addition of regressor variable to assess mixed selectivity.

We observe for many neurons, in particular for neurons in the parietal cortex, that there is no single regressor block with a dominating w-value. The examples presented in Figure 5.19 rather are hand-picked exceptions for the sake of presentability. Yet, the display in Figure 5.22 this mixed selectivity. Future studies could refine this type of analysis and focus the investigation on the difference in representations across areas.

THE NOTION OF A STATIC PD Despite many unresolved controversies about what neurons in the motor cortex represent, it is well established since the first descriptions by (Georgopoulos et al., 1982) that neurons in the arm area of M1 show a cosine-like tuning toward the hand movement direction. The classical task to uncover this tuning is the center-out task, where several targets lie on a circle surrounding a central target where the hand rests at the beginning of each trial. The monkey is then trained to reach a target if presented.

In a subsequent analysis, a neuron's firing rate is then averaged across all repetitions of a reach into a certain direction.

Such task and analysis designs have the drawbacks that they assume the directional tuning to be stable (see Suway et al. (2018) for similar arguments). In our study, we represented the tuning of a neuron by the distribution of PDs per time-shift and weighted by the normalized modulation depth. A future study could systematically evaluate how good this proposed measure captures sudden changes in PDs and quantify how prevalent stable tunings are compared to switching ones.

GOODNESS-OF-FIT AND EXPLAINED VARIANCE Due to the fact that our encoding model is non-linear, we could not use classical measures for the goodness-of-fit. While closely related, it is difficult to compare absolute values with e.g. Talluri et al. (2022). Future research could define a measure that allows for the comparison of the goodness-of-fit of linear and non-linear models in the context of single unit spiking activity.

Part II

SIMULATION AND THEORETICAL DESCRIPTION OF SPIKING NEURAL NETWORKS

6

NEUROSCIENTIFIC BACKGROUND — COMPUTATIONAL NEUROSCIENCE

This part of the thesis presents the mean-field description of neuronal networks composed of leaky integrate-and-fire (LIF) neurons and an investigation into the mechanism of ultra-high frequency oscillations observed in a simulation of a microcircuit model.

The following chapter deals with the basics of how mean-field theory can be use to describe simulations of neural networks and presents a toolbox, which supplies numerical implementations for this aim. Finally, we then use this knowledge in the central chapter of this part to answer our second research question:

Are oscillatory synchronizations of the spiking activity observed as vertical stripes of raster diagrams in simulations of a microcircuit model composed of LIF neurons a valid prediction of the model? Should they be observable in experimental data, and can we mechanistically understand them?

6.1 SIMULATION OF NETWORK MODELS

In the motivation for this research question (Section 1.2.3), we briefly introduced the idea of simulating a spiking neural network.

The evolution from random networks (van Vreeswijk et al., 1996), via simple "Brunel" networks (Amit et al., 1997b; Brunel, 2000) to more complex networks involving structured connectivity and larger amounts of neurons was steadily accompanied by theoretical analyses.

In the picture of the scientific loop Figure 1.1, simulations take over the part of the experiment, and the observed activity is ideally described by appropriate analytics. This strong interplay between simulation and theory proofed to be very powerful and allowed for a deep understanding of the mechanism behind emerging properties such as oscillations.

In this section, we will have a closer look at the type of simulations that will be employed later. The following section then introduces the analytics based on mean-field theory and linear response theory.

6.1.1 *Cortical microcircuit model*

Here we want to throw a closer look at the cortical microcircuit model by Potjans et al. (2014a). The circuit network model is composed of point neurons with biologically plausible parameters and biologically constrained connectivity.

The model consists of eight populations of LIF neurons, corresponding to the excitatory and inhibitory populations of four cortical layers: 2/3E, 2/3I, 4E, 4I, 5E, 5I, 6E, and 6I (see Figure 6.1**A**). It defines the number of neurons in each population, the number of connections between the populations, the single neuron properties, and the external input. Simulations show that the model yields realistic firing rates for the different populations as observed in particular in the healthy resting-state of early sensory cortex (Potjans et al., 2014a, Table 6).

Neurons in the microcircuit model have exponentially shaped postsynaptic currents. The single neurons are modelled as LIF with governing equations:

$$\tau_m \frac{dV_{ki}(t)}{dt} = -V_{ki} + R_m I_{ki}(t) \quad , \tag{6.1}$$

$$\tau_s \frac{dI_{ki}(t)}{dt} = -I_i(t) + \tau_s \sum_{l=1}^{N} \sum_{j=1}^{M_l} w_{ki,lj} \sum_n \delta(t - t_{lj}^n - d_{ki,kl}) + \tau_s \sum_{j=1}^{M_{ext}} w_{ki,j} \sum_n \delta(t - t_j^n) \quad , \tag{6.2}$$

with V_{ki} denoting the (rescaled) membrane potential of neuron i in population k, R_m the membrane resistance, τ_m the membrane time constant and $I_{ki}(t)$ the time-dependent incoming synaptic current. τ_s is the synaptic time constant, $w_{ki,jl}$ the synaptic weight of the connection between neuron j of population l to neuron i in population k, d is the corresponding transmission delay, and $\sum_n \delta(t - t_j^n)$ describes theincoming spike train of neuron j. The index j in the first sum runs over all M_l neurons in population l, N denotes the number of populations. t_{lj}^n is the time of the n-th spike of neuron j in population l. When $V_i(t)$ reaches the threshold potential $V_{\text{threshold}}$, the membrane potential is clamped to the reset potential V_{reset} for a refractory period τ_{ref}. The reaching of the threshold with subsequent depolarization corresponds to one spiking event.

The model has been recently used in a number of other works: for example, to study network properties such as layer-dependent attentional processing (Wagatsuma et al., 2011), connectivity structure with respect to oscillations (Bos et al., 2016), and the effect of synaptic weight resolution on activity statistics (Dasbach, Tetzlaff, Diesmann, and Senk, 2021); to assess the performance of different simulator technologies such as neuromorphic hardware (van Albada et al., 2018) and GPUs (Golosio et al., 2021; Knight et al., 2018); to demonstrate forward-model prediction of local-field potentials from spiking activity (Hagen et al., 2016).

6.1.2 *Multi area model*

Furthermore, the microcircuit model served as a building block for large-scale models (Schmidt et al., 2018b). The multi-area model proposed by Schmidt et al. (2018a) is a computational model of the primate visual system that attempts to explain how visual information is processed and represented across different areas of the cortex. The model is based on neurophysiological and anatomical data from macaque monkeys and consists of a hierarchy of interconnected areas.

Multiple microcircuit models, which represent single areas, are connected according to tracing data (Markov et al., 2014). The multi-area model reproduced large-scale features observed in fMRI recordings (Schmidt et al., 2018a).

One achievement by the Potjans-Diesmann model is, that the majority of inputs to a single neuron originate in the model. By connecting multiple network models together, the dependence on external input could be further reduced.

In the next chapter, the primary visual cortex (V1) circuit from this multi-area model will be used as an alternative instantiation of the same model type. Notably, the experimental data used to infer the neuron densities and connection probabilities is updated leading to changes in activity, even if the V1 network is simulated in isolation. A comparison of the neuron counts per population is given in Table 6.1.

Networks of interacting excitatory and inhibitory populations have been shown to be amenable to analytical descriptions. While the simulations solve the full non-linear system quantitatively, mean-field and linear response theory supply us with a linear approximation of these complex networks and thus allow a rather qualitative understanding of the underlying mechanisms.

Next, we introduce this theoretical description of such network models.

	original	isolated V1
23E	20683	47386
23I	5834	13366
4E	21915	70387
4I	5479	17597
5E	4850	20740
5I	1065	4554
6E	14395	19839
6I	2948	4063
total	77169	197935

Table 6.1: Comparison of neuron numbers Potjans vs. isolated V1.

6.2 THEORETICAL DESCRIPTION OF NETWORK MODELS

Over the past few decades, the mean-field theory of neural networks has significantly improved both our analytical and intuitive comprehension of their dynamics. We developed an extendable, user-friendly open-source Python toolbox that gathers a number of mean-field approaches for the leaky integrate-and-fire neuron model in order to increase the accessibility of mean-field based analytic tools. In its present version, the Neuronal Network Mean-field Toolbox (NNMT) enables the estimation of features of large neuronal networks, such as firing rates, power spectra, and dynamical stability in mean-field and linear response approximation, without the need for simulations.

In this section, we explain the fundamental parts of the mean-field theory that are needed for the investigation of ultra-high frequency oscillations in the next chapter. For the presentation of these concepts, we focus in particular on techniques for leaky integrate-and-fire neurons and thereby reproduce previously published network model analyses from Sanzeni et al. (2020), Bos et al. (2016) and Schuecker et al. (2015).

Whenever suitable, we will apply the presented theory making use of the NNMT (Neuronal Network Meanfield Toolbox) (Layer et al., 2022b) to compare the theoretical prediction to actual simulations.

6.2.1 *Toolbox*

We created the Python toolbox NNMT (Layer et al., 2021), short for Neuronal Network Mean-field Toolbox, to make analytical tools for neuronal network model analysis available to a larger part of the neuroscientific community and to create a platform for collecting well-tested and validated implementations of such tools. NNMT is not a simulation tool; it is a set of numerically computed mean-field equations that directly connect the parameters of a microscopic network model to the statistics of its dynamics. NNMT was created to accommodate the wide range of mean-field theories, and the primary aspects we are looking for are flexibility, extensibility, and ease of use. It also includes a thorough test suite to check the correctness of the implementations, as well as rich user documentation. NNMT's current version primarily includes tools for researching networks of leaky integrate-and-fire neurons, as well as techniques for studying binary neurons and neural field models. The toolkit is open source and freely accessible on GitHub[1].

6.2.2 *Literature overview*

Large numbers of recurrently linked neurons comprise biological neural networks, with a single cortical neuron generally receiving synaptic inputs from thousands of other neurons (Braitenberg et al., 1998; DeFelipe et al., 2002). Although the inputs of different neurons are integrated in a complicated manner, such a huge number of weak synaptic inputs points to the fact that the average features of neuronal populations do not depend heavily on the contributions of individual neurons (Amit et al., 1991). On the basis of this discovery, it is feasible to create analytically tractable models of population characteristics in which the effects of individual neurons are averaged out and the complex, recurrent input to individual neurons is replaced with a self-consistent effective input(reviewed, e.g., in Gerstner et al., 2014).

In classical physics (e.g., Goldenfeld, 1992), this effective input is termed a *mean-field* since it is the self-consistent mean of a *field*, which is simply another word for the input the neuron is getting. The term *self-consistent* refers to the fact that the population of neurons that gets the effective input is the same population that contributes to this effective input in a recurring manner: the population's output controls its input and vice versa. Therefore, the stationary statistics of the effective input may be discovered in a self-consistent way: the input to a neuron must be adjusted precisely such that the caused output leads to the relevant input.

Mean-field theories have been established for a wide range of synapse, neuron, and network models. They have been effectively used to investigate average population firing rates (Amit et al., 1997b; van Vreeswijk et al., 1998; van Vreeswijk et al., 1996), and the various activity states a network of spiking neurons can exhibit, depending on the network parameters (Amit et al., 1997a; Brunel, 2000; Ostojic, 2014), as well as the effects that different kinds of synapses have on firing rates (Fourcaud et al., 2002; Lindner, 2004; Mattia et al., 2019; Schuecker et al., 2015; Schwalger et al., 2015).

---

[1] https://github.com/INM-6/nnmt

They have been used to investigate how neuronal networks respond to external inputs (Lindner et al., 2005b, 2001), and they explain why neuronal networks can track external input on much faster time scales than a single neuron could (van Vreeswijk et al., 1998; van Vreeswijk et al., 1996). Mean-field theories allow studying correlations of neuronal activity (Ginzburg et al., 1994; Lindner et al., 2005a; Sejnowski, 1976; Trousdale et al., 2012) and were able to reveal why pairs of neurons in random networks, despite receiving a high proportion of common input, can show low output correlations (Helias et al., 2014; Hertz, 2010; Renart et al., 2010; Tetzlaff et al., 2012), which for example has important implication for information processing. They describe pairwise correlations in network with spatial organization (Dahmen et al., 2022; Rosenbaum et al., 2014, 2017) and can be generalized to correlations of higher orders (Buice et al., 2013). Mean-field theories were utilized to show that neuronal networks can exhibit chaotic dynamics (Sompolinsky et al., 1988; van Vreeswijk et al., 1998; van Vreeswijk et al., 1996), in which two slightly different initial states can lead to totally different network responses, which has been linked to the network's memory capacity (Schuecker et al., 2018; Toyoizumi et al., 2011). Most of the results mentioned above have been derived for networks of either rate, binary, or spiking neurons of a linear integrate-and-fire type. But various other models have been investigated with similar tools as well; for example, just to mention a few, Hawkes processes, non-linear integrate-and-fire neurons (Brunel et al., 2003a; Fourcaud-Trocmé et al., 2003; Grabska-Barwinska et al., 2014; Montbrió et al., 2015; Richardson, 2007, 2008), or Kuramoto-type models (Stiller et al., 1998; van Meegen et al., 2018). Additionally, there is an ongoing effort showing that many of the results derived for distinct models are indeed equivalent and that those models can be mapped to each other under certain circumstances (Grytskyy et al., 2013; Ostojic et al., 2011; Senk et al., 2020).

6.2.3 *Stationary quantities in balanced networks*

Networks of excitatory and inhibitory neurons (EI networks) are widely used in computational neuroscience (Gerstner et al., 2014), e.g., to show analytically that a balanced state featuring asynchronous, irregular activity emerges dynamically in a broad region of the parameter space (Brunel, 2000; Hertz, 2010; Renart et al., 2010; van Vreeswijk et al., 1998; van Vreeswijk et al., 1996). Remarkably, such balance states emerge in inhibition dominated networks for a variety of neuron models if the indegree is large, $K \gg 1$, and the weights scale as $J \propto 1/\sqrt{K}$ (Ahmadian et al., 2021; Sanzeni et al., 2020).

Furthermore, in a balanced state, a network responds linearly to external input in the limit $K \to \infty$ (Ahmadian et al., 2021; Brunel, 2000;

Sanzeni et al., 2020; van Vreeswijk et al., 1998; van Vreeswijk et al., 1996).

The classical "Brunel" network, an EI network, as e.g. used in Sanzeni et al. (2020), consists of two populations, E and I, of identical LIF neurons with instantaneous (*delta*) synapses (Gerstner et al., 2014). The subthreshold dynamics of the membrane potential V_i of neuron i obeys

$$\tau_{\mathrm{m}} \dot{V}_i = -V_i + RI_i \quad , \tag{6.3}$$

where τ_{m} denotes the membrane time constant, R the membrane resistance, and I_i the input current. If the membrane potential exceeds a threshold V_{th}, a spike is emitted and the membrane voltage is reset to the reset potential V_0 and clamped to this value during the refractory time τ_{r}. After the refractory period, the dynamics continue according to Equation 6.3. For instantaneous synapses, the input current is given by

$$RI_i(t) = \tau_{\mathrm{m}} \sum_j J_{ij} \sum_k \delta(t - t_{j,k} - d_{ij}) \quad , \tag{6.4}$$

where J_{ij} is the synaptic weight from presynaptic neuron j to postsynaptic neuron i (with $J_{ij} = 0$ if there is no synapse), the $t_{j,k}$ are the spike times of neuron j, and d_{ij} is a synaptic delay (in this example $d_{ij} = d$ for all pairs of neurons). In total, there are N_{E} and N_{I} neurons in the respective populations. Each neuron is connected to a fixed number of randomly chosen presynaptic neurons (fixed in-degree); additionally, all neurons receive external input from independent Poisson processes with rate ν_{X}. The synaptic weights and in-degrees of recurrent and external connections are population-specific:

$$\boldsymbol{J} = \begin{pmatrix} J_{\mathrm{EE}} & -J_{\mathrm{EI}} \\ J_{\mathrm{IE}} & -J_{\mathrm{II}} \end{pmatrix} , \; \boldsymbol{J}_{\mathrm{ext}} = \begin{pmatrix} J_{\mathrm{EX}} \\ J_{\mathrm{IX}} \end{pmatrix} , \; \boldsymbol{K} = \begin{pmatrix} K_{\mathrm{EE}} & K_{\mathrm{EI}} \\ K_{\mathrm{IE}} & K_{\mathrm{II}} \end{pmatrix} , \text{ and } \boldsymbol{K}_{\mathrm{ext}} = \begin{pmatrix} K_{\mathrm{EX}} \\ K_{\mathrm{IX}} \end{pmatrix} \quad . \tag{6.5}$$

All weights are positive, implying an excitatory external input.

The core idea of mean-field theory is to approximate the input to a neuron as Gaussian white noise $\xi(t)$ with mean $\langle \xi(t) \rangle = \mu$ and noise intensity $\langle \xi(t) \xi(t') \rangle = \tau_{\mathrm{m}} \sigma^2 \delta(t - t')$. This approximation is well-suited for asynchronous, irregular network states (Amit et al., 1997b; van Vreeswijk et al., 1998; van Vreeswijk et al., 1996). For a LIF neuron driven by such Gaussian white noise, the firing rate is given by (Amit et al., 1997b; Siegert, 1951; Tuckwell, 1988)

$$\phi(\mu, \sigma) = \left(\tau_{\mathrm{r}} + \tau_{\mathrm{m}} \sqrt{\pi} \int_{\tilde{V}_0(\mu,\sigma)}^{\tilde{V}_{\mathrm{th}}(\mu,\sigma)} e^{s^2} (1 + \mathrm{erf}(s)) \mathrm{d}s \right)^{-1} \quad , \tag{6.6}$$

where the rescaled reset- and threshold-voltages are

$$\widetilde{V}_0(\mu,\sigma) = \frac{V_0 - \mu}{\sigma} \quad , \qquad \widetilde{V}_{\text{th}}(\mu,\sigma) = \frac{V_{\text{th}} - \mu}{\sigma} \quad . \tag{6.7}$$

The first term in Equation 6.6 is the refractory period and the second term is the mean first-passage time of the membrane voltage from reset to threshold. The mean and the noise intensity of the input to a neuron in a population $a \in \{E, I\}$, which control the mean first-passage time through Equation 6.7, are determined by (Amit et al., 1997b)

$$\mu_a = \tau_{\text{m}}(J_{a\text{E}}K_{a\text{E}}\nu_{\text{E}} - J_{a\text{I}}K_{a\text{I}}\nu_{\text{I}} + J_{a\text{X}}K_{a\text{X}}\nu_{\text{X}}) \quad , \tag{6.8}$$

$$\sigma_a^2 = \tau_{\text{m}}(J_{a\text{E}}^2K_{a\text{E}}\nu_{\text{E}} + J_{a\text{I}}^2K_{a\text{I}}\nu_{\text{I}} + J_{a\text{X}}^2K_{a\text{X}}\nu_{\text{X}}) \quad , \tag{6.9}$$

respectively, where each term reflects the contribution of one population,with the corresponding firing rates of the excitatory ν_{E}, inhibitory ν_{I}, and external population ν_{X}. Note that we use the letters $i, j, k, \dots$ to index single neurons and $a, b, c, \dots$ to index neuronal populations. Both μ_a and σ_a depend on the firing rate of the neurons ν_a, which is in turn given by Equation 6.6. Thus, one arrives at the self-consistency problem

$$\nu_a = \phi(\mu_a, \sigma_a) \quad , \tag{6.10}$$

which is coupled across the populations due to Equation 6.8 and Equation 6.9.

6.2.3.1 *Firing rates of microcircuit model*

Here we show the mean-field prediction of the firing rates of cortical microcircuit model by Potjans et al. (2014a) compares to simulations.

In contrast to the EI-network model that we looked at before, the neurons in the microcircuit model have exponentially shaped post-synaptic currents: Equation 6.4 is replaced by (Fourcaud et al., 2002)

$$\tau_{\text{s}}R\frac{\mathrm{d}I_i}{\mathrm{d}t}(t) = -RI_i(t) + \tau_{\text{m}}\sum_j J_{ij}\sum_k \delta(t - t_{j,k} - d_{ij}) \quad , \tag{6.11}$$

with synaptic time constant τ_{s}. Note that J_{ij} is a measure in volts here. As discussed in Section 6.2.3, in mean-field theory the second term, representing the neuronal input, is approximated by Gaussian white noise. The additional synaptic filtering leads to the membrane potential (Equation 6.3) receiving colored noise input. Fourcaud et al. (2002) developed a method for calculating the firing rate for this synapse type. They have shown that, if the synaptic time constant τ_{s}

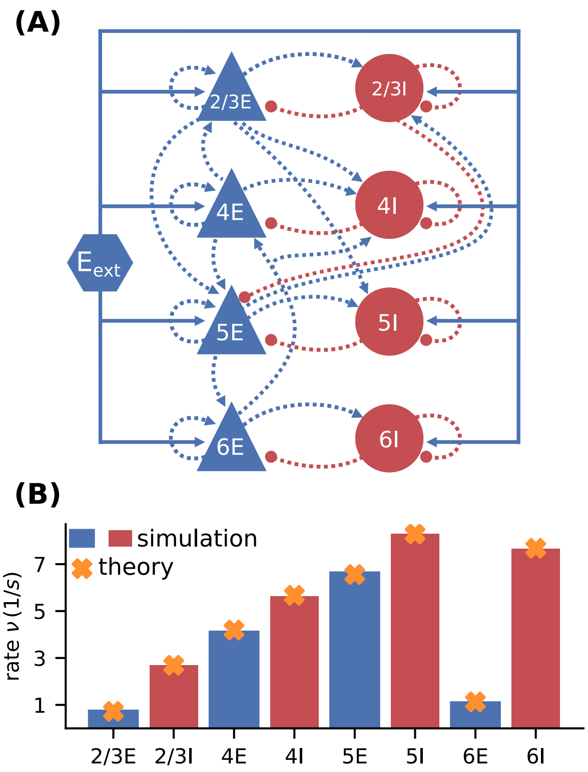

Figure 6.1: Cortical microcircuit model by Potjans et al. (2014a). **(A)** Network diagram (only the strongest connections are shown as in Figure 1 of the original publication). Network diagram with nodes and edges according to the graphical notation proposed by Senk et al. (2021). **(B)** Simulation and mean-field estimate for average population firing rates using the parameters from Bos et al. (2016).

is much smaller than the membrane time constant τ_m, the firing rate for LIF neurons with exponential synapses can be calculated using Equation 6.6 with shifted integration boundaries

$$\widetilde{V}_{\mathrm{cn},0}(\mu,\sigma) = \widetilde{V}_0(\mu,\sigma) + \frac{\alpha}{2}\sqrt{\frac{\tau_\mathrm{s}}{\tau_\mathrm{m}}} \quad , \qquad \widetilde{V}_{\mathrm{cn,th}}(\mu,\sigma) = \widetilde{V}_{\mathrm{th}}(\mu,\sigma) + \frac{\alpha}{2}\sqrt{\frac{\tau_\mathrm{s}}{\tau_\mathrm{m}}} \quad , \tag{6.12}$$

with the rescaled reset- and threshold-voltages from Equation 6.7 and $\alpha = \sqrt{2}\,|\zeta(1/2)| \approx 2.07$, where $\zeta(x)$ denotes the Riemann zeta function; the subscript cn stands for "colored noise".

6.2.3.2 *Microcircuit parameters*

The microcircuit has been implemented as an NNMT model. We here use the parameters of the circuit as published in Bos et al. (2016) which is slightly differently parameterized than the original model (see Table 6.2).

Symbol	**Value** Potjans et al. (2014a)	**Value** Bos et al. (2016)	**Description**
$K_{4\mathrm{E},4\mathrm{I}}$	795	675	In-degree from 4I to 4E
$K_{4\mathrm{E},\mathrm{ext}}$	2100	1780	External in-degree to 4E
$D(\omega)$	none	truncated Gaussian	Delay distribution
$d_e \pm \delta d_e$	$1.5 \pm 0.75\,\mathrm{ms}$	$1.5 \pm 1.5\,\mathrm{ms}$	Mean and standard deviation of excitatory delay
$d_i \pm \delta d_i$	$0.75 \pm 0.375\,\mathrm{ms}$	$0.75 \pm 0.75\,\mathrm{ms}$	Mean and standard deviation of inhibitory delay

Table 6.2: Parameter adaptions used here are introduced by Bos et al. (2016) compared to original microcircuit model. K_{ij} denotes the in-degrees from population j to population i. The delays in the simulated networks were drawn from a truncated Gaussian distribution with the given mean and standard deviation. The mean-field approximation of the microcircuit by Potjans et al. (2014a) assumes the delay to be fixed at the mean value, which is specified in the toolbox by setting the parameter `delay_dist` to `none`.

The simulated rates in Figure 6.1 have been obtained by a numerical network simulation (for simulation details see Bos et al., 2016) in which the neuron populations are connected according to the model's original connectivity rule: "random, fixed total number with multapses (autapses prohibited)", see Senk et al. (2021) as a reference for connectivity concepts. The term *multapses* refers to multiple connections between the same pair of neurons and *autapses* are self-connections; with this connectivity rule multapses can occur in a network realization but autapses are not allowed. For simplicity, the theoretical predictions assume a connectivity with a fixed in-degree for each neuron. Dasbach et al. (2021) show that simulated spike activity data of networks with these two different connectivity rules are characterized by differently shaped rate distributions ("reference" in their Figures 3d and 4d). In addition, the weights in the simulation are normally distributed while the theory replaces each distribution by its mean; this corresponds to the case $N_{\mathrm{bins}} = 1$ in Dasbach et al. (2021). Nevertheless, our mean-field theoretical estimate of the average population firing rates is in good agreement with the simulated rates (Figure 6.1**B**).

6.2.4 *Dynamical quantities*

6.2.4.1 *Transfer function*

One of the most important dynamical properties of a neuronal network is how it reacts to external input. A systematic way to study the network response is to apply an oscillatory external input current leading to a periodically modulated mean input $\mu(t) = \mu + \delta\mu \,\mathrm{Re}\left(\mathrm{e}^{\mathrm{i}\omega t}\right)$ (cf. Equation 6.8), with fixed frequency ω, phase, and amplitude $\delta\mu$, and observe the emerging frequency, phase, and amplitude of the output. If the amplitude of the external input is small compared to the stationary input, the network responds in a linear fashion: it only modifies phase and amplitude, while the output frequency equals the input frequency. This relationship is captured by the input-output transfer function $N(\omega)$ (Brunel et al., 2001, 1999; Lindner et al., 2001), which describes the frequency-dependent modulation of the output firing rate of a neuron population

$$\nu(t) = \nu + \mathrm{Re}\Big(N(\omega)\,\delta\mu\,\mathrm{e}^{\mathrm{i}\omega t}\Big) \quad .$$

Note that in this section we only study the linear response to a modulation of the mean input, although in general, a modulation of the noise intensity (Equation 6.9) can also be included (Lindner et al., 2001; Schuecker et al., 2015). The transfer function $N(\omega)$ is a complex function: Its absolute value describes the relative modulation of the firing rate. Its phase, the angle relative to the real axis, describes the phase shift that occurs between input and output. We denote the transfer function for a network of LIF neurons with instantaneous synapses in linear-response approximation as

$$N(\omega) = \frac{\sqrt{2}\nu}{\sigma}\frac{1}{1+\mathrm{i}\omega\tau_{\mathrm{m}}}\frac{\Phi'_\omega\big|_{\sqrt{2}\widetilde{V}_0}^{\sqrt{2}\widetilde{V}_{\mathrm{th}}}}{\Phi_\omega\big|_{\sqrt{2}\widetilde{V}_0}^{\sqrt{2}\widetilde{V}_{\mathrm{th}}}} \quad , \tag{6.13}$$

with the rescaled reset- and threshold-voltages $\widetilde{V}_0$ and $\widetilde{V}_{\mathrm{th}}$ as defined in Equation 6.7 and $\Phi_\omega(x) = e^{\frac{x^2}{4}}\,U\left(\mathrm{i}\omega\tau_{\mathrm{m}} - \frac{1}{2}, x\right)$ using the parabolic cylinder functions $U\left(\mathrm{i}\omega\tau_{\mathrm{m}} - \frac{1}{2}, x\right)$ as defined in (Abramowitz et al., 1974, Section 19.3) and (Olver et al., 2021, Section 12.2). Φ'_ω denotes the first derivative by x. A comparison of our notation and the transfer function given in Schuecker et al. (2015, Eq. 29) can be found in the Appendix, Paragraph 6.2.4.1.

For a neuronal network of LIF neurons with exponentially shaped post-synaptic currents, introduced in Section 6.2.3.1, Schuecker et al. (2014, 2015) show that an analytical approximation of the transfer function can be obtained by a shift of integration boundaries, akin to Equation 6.12:

$$N_{\mathrm{cn}}\left(\omega\right)=\frac{\sqrt{2}\nu}{\sigma}\frac{1}{1+\mathrm{i}\omega\tau_{\mathrm{m}}}\frac{\Phi_{\omega}'\big|_{\sqrt{2}\widetilde{V}_{\mathrm{cn},0}}^{\sqrt{2}\widetilde{V}_{\mathrm{cn,th}}}}{\Phi_{\omega}\big|_{\sqrt{2}\widetilde{V}_{\mathrm{cn},0}}^{\sqrt{2}\widetilde{V}_{\mathrm{cn,th}}}} \quad . \tag{6.14}$$

To take into account the effect of the synaptic dynamics, we include an additional low-pass filter:

$$N_{\mathrm{cn,s}}\left(\omega\right)=N_{\mathrm{cn}}\left(\omega\right)\frac{1}{1+\mathrm{i}\omega\tau_{\mathrm{s}}} \quad . \tag{6.15}$$

If the synaptic time constant is much smaller than the membrane time constant ($\tau_{\mathrm{s}} \ll \tau_{\mathrm{m}}$), an equivalent expression for the transfer function is obtained by a Taylor expansion around the original boundaries (cf. Schuecker et al. 2015, Eq. 30).

The toolbox implements both variants and offers choosing between them by setting the argument `method` of `nnmt.lif.exp.transfer_function` to either `shift` or `taylor`. Using this, we show the "shift version" of the transfer function for different means and noise intensities of the input current in Figure 6.2 and thereby reproduce Figure 4 in Schuecker et al. (2015) with the NNMT toolbox. Note that the complex-valued transfer function was split into its absolute value and phase in Figure 6.2. This illustration shows that the transfer function acts as a low-pass filter that suppresses the amplitude of high frequency activity, introduces a phase lag, and can lead to resonance phenomena for certain configurations of mean input current and noise intensity.

Note that the implemented analytical form of the transfer function by Schuecker et al. (2015) is an approximation for low frequencies, and deviations from a simulated ground truth are expected for higher frequencies ($\omega/2\pi \gtrsim 100\,\mathrm{Hz}$ at the given parameters).

TRANSFER FUNCTION NOTATIONS In Section 7.2.2.4, we introduce the analytical form of the transfer function implemented in the toolbox. Schuecker et al. (2015), derive a more general form of the transfer function, which includes a modulation of the variance of the input. Here we compare the notation used in Equation 6.13 to the notation used in Schuecker et al. (2015, Eq. 29).

Schuecker et al. (2015) define the modulations of input mean and variance as

$$\begin{aligned} \mu(t) &= \mu + \epsilon\mu\,\mathrm{e}^{\mathrm{i}\omega t} \quad , \\ \sigma^2(t) &= \sigma^2 + H\sigma^2\,\mathrm{e}^{\mathrm{i}\omega t} \quad , \end{aligned} \tag{6.16}$$

and introduce the transfer function in terms of its influence on the firing rate

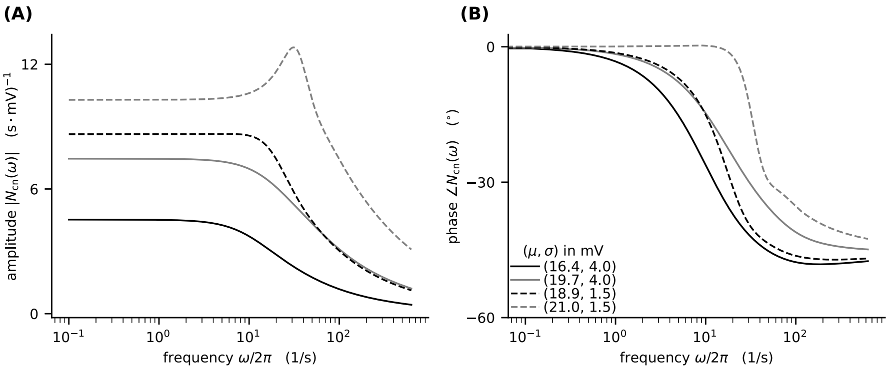

Figure 6.2: Colored-noise transfer function N_{cn} of LIF model in different regimes. **(A)** Absolute value and **(B)** phase of the "shift" version of the transfer function as a function of the log-scaled frequency. Neuron parameters are set to $V_{\mathrm{th}} = 20\,\mathrm{mV}$, $V_0 = 15\,\mathrm{mv}$, $\tau_{\mathrm{m}} = 20\,\mathrm{ms}$, and $\tau_{\mathrm{s}} = 0.5\,\mathrm{ms}$. For given noise intensities of input current, $\sigma = 4\,\mathrm{mV}$ (solid line) and $\sigma = 1.5\,\mathrm{mV}$ (dashed line), the mean input μ is chosen such that firing rates $\nu = 10\,\mathrm{Hz}$ (black) and $\nu = 30\,\mathrm{Hz}$ (gray) are obtained.

$$\nu(t)/\nu_0 = 1 + n\left(\omega\right) \mathrm{e}^{\mathrm{i}\omega t} \quad ,$$

where ν_0 is the stationary firing rate. Here the transfer function $n\left(\omega\right)$ includes contributions of both the modulation of the mean $n_G(\omega) \propto \epsilon$ and the modulation of the variance $n_H(\omega) \propto H$. We write the modulation of the mean as

$$\mu(t) = \mu + \delta\mu\, \mathrm{e}^{\mathrm{i}\omega t} \quad ,$$

implying that $\delta\mu$ corresponds to $\epsilon\mu$ in Equation 6.16. As we only consider the modulation of the mean, the firing rate can be rewritten as

$$\nu(t) = \nu + N\left(\omega\right) \delta\mu\, \mathrm{e}^{\mathrm{i}\omega t} \quad ,$$

where we moved the stationary firing rate ν to the right hand side and included it inthe definition of the transfer function $N\left(\omega\right)$.Additionally, we swap the voltage boundaries in Equation 6.13, introducing a canceling sign change in both the numerator and the denominator. This reformulation was chosen to align the presented formula with the implementation in the toolbox.

6.2.4.2 *Power Spectrum*

Another frequently studied dynamical property is the power spectrum, which describes how the power of a signal is distributed across its different frequency components, revealing oscillations of the population activity. The power is the Fourier transformed auto-correlation of the population activities (c.f. Bos et al. (2016, Eq. 16-18)). Linear response theory on top of a mean-field approximation , allows computing the power, dependent on the network architecture, the stationary firing rates, and the neurons' transfer function (Bos et al., 2016). The corresponding analytical expression for the power spectra of population a at angular frequency ω is given by the diagonal elements of the correlation matrix

$$P_a(\omega) = C_{aa}(\omega) = \left[\left(\mathbf{1} - \widetilde{\mathbf{M}}_\mathrm{d}(\omega) \right)^{-1} \mathrm{diag}\left(\boldsymbol{\nu} \oslash \boldsymbol{n} \right) \left(\mathbf{1} - \widetilde{\mathbf{M}}_\mathrm{d}(-\omega) \right)^{-\mathrm{T}} \right]_{aa} , \tag{6.17}$$

with $\oslash$ denoting the elementwise (Hadamard) division, the effective connectivity matrix

$$\widetilde{\boldsymbol{M}}_\mathrm{d}(\omega) = \tau_\mathrm{m} \boldsymbol{N}_{\mathrm{cn,s}}(\omega) \cdot \boldsymbol{J} \odot \boldsymbol{K} \odot \boldsymbol{D}(\omega) \tag{6.18}$$

where the dot denotes the scalar product, while $\odot$ denotes the elementwise (Hadamard) product, the mean population firing rates $\boldsymbol{\nu}$, and the numbers of neurons in each population $\boldsymbol{n}$. The effective connectivity combines the static, anatomical connectivity $\boldsymbol{J} \odot \boldsymbol{K}$, represented by synaptic weight matrix $\boldsymbol{J}$ and in-degree matrix $\boldsymbol{K}$, and dynamical quantities, represented by the transfer functions $N_{\mathrm{cn,s},a}(\omega)$ (Equation 6.15), and the contribution of the delays in Equation 6.11, represented by their Fourier transformed distributions $D_{ab}(\omega)$ (cf. Bos et al. (2016, Eq. 14-15)).

The toolbox permits an easy calculation of the power spectra. For a given network model, we determine the working point, which characterizes the statistics of the model's stationary dynamics. It is defined by the population firing rates, the mean, and the standard deviation of the input to a neuron of the respective population. This is necessary for determining the transfer functions. The calculation of the delay distribution matrix is then required for calculating the effective connectivity and to finally get an estimate of the power spectra. Figure 6.3 reproduces Figure 1E in Bos et al. (2016) and shows the spectra for each population of the adjusted version (see Table 6.2) of the microcircuit model.

The numerical predictions obtained from the toolbox largely coincide with simulated data taken from the original publication (Bos et al., 2016) and reveal dominant oscillations of the population activities in the low-γ range around 63 Hz. Furthermore, faster oscillations with peak power around 300 Hz are predicted with higher magnitudes in the inhibitory populations 4I, 5I, and 6I.

The deviation between predicted and simulated power spectra seen at $\sim$ 130 Hz in population 2/3E could be a harmonic of the correctly

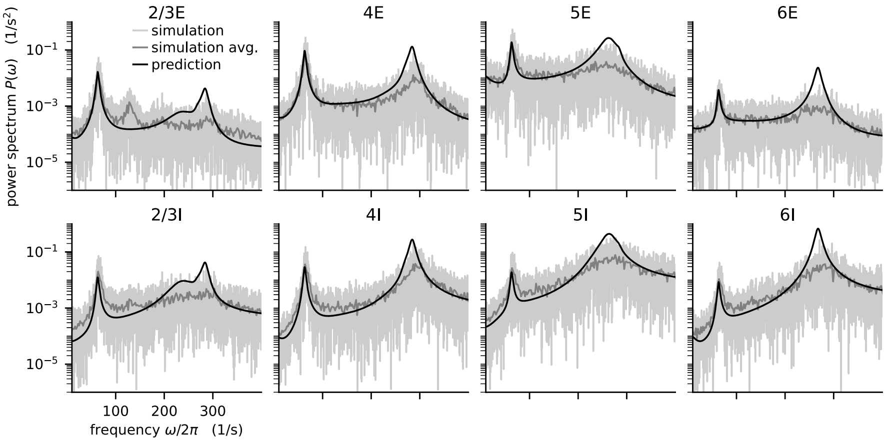

Figure 6.3: Power spectra of the population spiking activity in the adapted cortical microcircuit from Bos et al. (2016). The spiking activity of each population in a 10 s simulation of the model is binned with 1 ms resolution and the power spectrum of the resulting histogram is calculated by a fast Fourier transform (FFT; light gray curves). In addition, the simulation is split into 500 ms windows, the power spectrum calculated for each window and averaged across windows (gray curves). Black curves correspond to analytical prediction obtained with NNMT. The panels show the spectra for the excitatory (top) and inhibitory (bottom) populations within each layer of the microcircuit.

predicted, prominent 63 Hz peak; a non-linear effect not captured in linear response theory. Furthermore, the systematic overestimation of the power spectrum at large frequencies is explained by the limited validity of the analytical approximation of the transfer function for high frequencies.

6.2.4.3 *Sensitivity Measure*

The power spectra shown in the previous section exhibit prominent peaks at certain frequencies, which indicate oscillatory activity. Naturally, this begs the question: which mechanism causes these oscillations? Bos et al. (2016) expose the crucial role that the microcircuit's connectivity plays in shaping the power spectra of this network model. They have developed a method called *sensitivity measure* to directly relate the influence of the anatomical connections, especially the indegree matrix, on the power spectra.

The power spectrum of the a-th population $P_a(\omega)$ receives a contribution from each eigenvalue λ_b of the effective connectivity matrix, $P_a(\omega) \propto 1/\left(1-\lambda_b(\omega)\right)^2$. Such a contribution consequently diverges as the complex-valued λ_b approaches $1 + 0\mathrm{i}$ in the complex plane, which is referred to as the point of instability. This relation can be derived by replacing the effective connectivity matrix $\widetilde{\mathbf{M}}_\mathrm{d}(\omega)$ in Equation 6.17 by its eigendecomposition. The sensitivity measure leverages

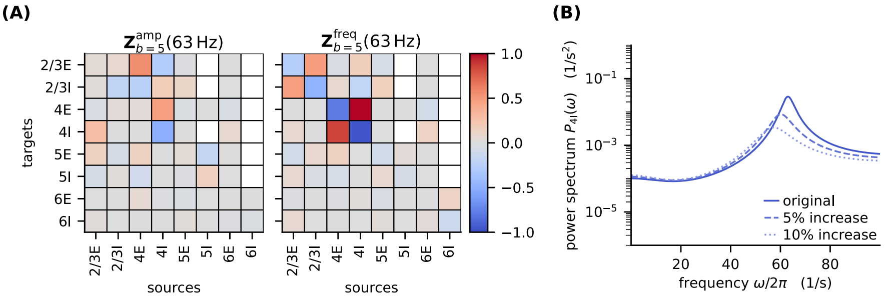

Figure 6.4: Sensitivity measure at low-γ frequency and corresponding power spectrum of microcircuit with adjusted connectivity. **(A)** Sensitivity measure of one eigenmode of the effective connectivity relevant for low-γ oscillations. The sensitivity measure for this mode is evaluated at the frequency where the corresponding eigenvalue is closest to the point of instability $1 + 0\mathrm{i}$ in complex plane. $\mathbf{Z}^{\mathrm{amp}}_{b}(\omega)$ (left subpanel) visualizes the influence of a perturbation of a connection on the peak amplitude of the power spectrum. $\mathbf{Z}^{\mathrm{freq}}_{b}(\omega)$ (right subpanel) shows the impact on the peak frequency. Non-existent connections are masked white. **(B)** Mean-field prediction of power spectrum of population 4I with original connectivity parameters (solid line), 5% increase (dashed line) and 10% increase (dotted line) in connections $K_{4\mathrm{I}\to 4\mathrm{I}}$. The increase in inhibitory input to population 4I was counteracted by and increase of the excitatory external input $K_{\mathrm{ext}\to 4\mathrm{I}}$ to maintain the working point.

this relationship and evaluates how a change in the in-degree matrix affects the eigenvalues of the effective connectivity and thus indirectly the power spectrum. Bos et al. (2016) introduce a small perturbation α_{cd} of the in-degree matrix, which allows writing the effective connectivity matrix as $\widehat{M}_{ab}(\omega) = (1 + \alpha_{cd}\delta_{ca}\delta_{db})\,\widetilde{M}_{ab}(\omega)$, where we dropped the delay subscript d. The sensitivity measure $Z_{b,cd}(\omega)$ describes how the b-th eigenvalue of the effective connectivity matrix varies when the cd-th element of the in-degree matrix is changed

$$Z_{b,cd}(\omega) = \left.\frac{\partial \lambda_b(\omega)}{\partial \alpha_{cd}}\right|_{\alpha_{cd}=0} = \frac{v_{b,c}\widetilde{M}_{cd}u_{b,d}}{\mathbf{v}_b^{\mathrm{T}} \cdot \mathbf{u}_b} \quad , \tag{6.19}$$

where $\frac{\partial \lambda_b(\omega)}{\partial \alpha_{cd}}$ is the partial derivative of the eigenvalue with respect to a change in connectivity, $\mathbf{v}_b^{\mathrm{T}}$ and $\mathbf{u}_b$ are the left and right eigenvectors of $\widetilde{\boldsymbol{M}}$ corresponding to eigenvalue $\lambda_b(\omega)$.

The complex sensitivity measure can be understood in terms of two components: $\mathbf{Z}^{\mathrm{amp}}_{b}$ is the projection of the matrix $\mathbf{Z}_b$ onto the direction in the complex plane defined by $1 - \lambda_b(\omega)$; it describes how, when the in-degree matrix is perturbed, the complex-valued $\lambda_b(\omega)$ moves towards or away from the instability $1 + 0\mathrm{i}$, and consequently how the amplitude of the power spectrum at frequency ω increases or decreases. $\mathbf{Z}^{\mathrm{freq}}_{b}$ is the projection onto the perpendicular direction and thus describes how the peak frequency of the power spectrum changes with the perturbation of the in-degree matrix. For a visualization of these projections, refer to Figure 5B in Bos et al. (2016).

According to the original publication (Bos et al., 2016), the peak around 63 Hz has contributions from one eigenvalue of the effective connectivity matrix. Figure 6.4 shows the projections of the sensitivity measure at the frequency for which this eigenvalue is closest to the instability, as illustrated in Figure 4 of Bos et al. (2016). The sensitivity measure returns one value for each connection between populations in the network model. For $\mathbf{Z}_b^{\text{amp}}$ a negative value indicates that increasing the in-degrees of a specific connection causes the amplitude of the power spectrum at the evaluated frequency to drop. If the value is positive, the amplitude is predicted to grow as the in-degrees increase. Similarly, for positive $\mathbf{Z}_b^{\text{freq}}$ the frequency of the peak in the power spectrum shifts towards higher values as in-degrees increase, and vice versa. The main finding in this analysis is that the low-γ peak seems to be affected by excitatory-inhibitory loops in layer 2/3 and layer 4.

If several eigenvalues of the effective connectivity matrix influence the power spectra in the same frequency range, adjustments of the connectivity are more involved. This is because a change in connectivity would inevitably affect all eigenvalues simultaneously. Further care has to be taken because the sensitivity measure is subject to the same constraints as the current implementation of the transfer function, which is only valid for low frequencies and enters the sensitivity measure directly.

7

VSTRIPES — ULTRA-HIGH-FREQUENCY OSCILLATIONS IN THE MICROCIRCUIT MODEL

In the previous chapter, we briefly looked at some details of biologically constrained spiking neural network models and reviewed a way of analytically approximate static and dynamical quantities of such simulations. We shall make use of the theoretical description in this chapter, as we finally tackle the second research question that we raised in Section 1.2.3:

Are oscillatory synchronizations of the spiking activity observed as vertical stripes of raster diagrams in simulations of a microcircuit model composed of leaky integrate-and-fire (LIF) neurons a valid prediction of the model? Should they be observable in experimental data, and can we mechanistically understand them?

7.1 INTRODUCTION

Randomly connected spiking neural network models with balanced excitation and inhibition exhibit sustained population-rate oscillations that are attributed to two main mechanisms, the Pyramidal Interneuron Network Gamma (PING) and the Interneuron Network Gamma (ING) (Buzsáki et al., 2012). The PING mechanism describes coupled excitatory and inhibitory populations generating oscillations at γ-frequencies ($\lesssim 70\,\mathrm{Hz}$), whereas the ING gives rise to high-γ oscillations ($\gg 70\,\mathrm{Hz}$) generated within an inhibitory population (Brunel et al., 2003b; Traub et al., 1997).

Simple model networks of leaky integrate-and-fire (LIF) neurons with balanced excitation and inhibition successfully predict experimentally observed asynchronous irregular firing of the neural activity (Brunel, 2000; Brunel et al., 1999) and confirm first order statistics as the firing rate as well as population-rate oscillations below $< 100\,\mathrm{Hz}$. In contrast, sustained high-frequency oscillations ($\sim 300\,\mathrm{Hz}$) are a robust phenomenon in models (Brunel et al., 2003b), but rarely observed in experiments of cortex.

Sustained high-frequency oscillations are also prevalent in an anatomically more realistic multi-layered model of the cortical microcircuit (Potjans et al., 2014a). This model respects the realistic densities of neurons and synapses, so doubts about the up-scaling of observed model effects are eliminated (van Albada et al., 2015).

The sustained high-frequency oscillations are not visible in individual spike trains, however, for sufficiently large neuron numbers N, are visible in raster diagrams as vertical stripes and reflected as respective peaks in the power spectrum of the population activity. While for a low number of neurons N, the auto-correlations of the spike trains (scaling with $\sim N$) dominate the power spectrum, for a large number of observed neurons the cross-correlations gain dominance (scaling with $\sim N^2$).

A few questions naturally arise: Is the omnipresence of high-frequency oscillations in our model of the cortical network an unavoidable consequence of our model architecture? What are the mechanisms that give rise to these oscillations? Are high-frequency oscillations expected to be observed in nature?

In this manuscript, we investigate the discrepancy between model prediction and, so far, missing experimental confirmation through direct simulation and mean-field analysis of the model. Despite the robustness of high-frequency oscillations to a broad range of parameter variations, a mean-field analysis uncovers that high-frequency oscillations disappear if the effective coupling is not too strong. This prediction is numerically confirmed in an anatomically better constrained model of the cortical microcircuit specific for V1.

The remainder of this chapter is organized as follows: **Visibility of ultra-high frequency oscillations in model data** describes the observation of fast oscillations of the population activity in the microcircuit model and discusses under which conditions such oscillations are visible in experimental recordings of both spiking activity (**Visibility in spiking activity**) and local field potential (**Visibility in local field potential**). Subsequently, **Mean-field theoretical description** analyzes a mean-field approximation of the microcircuit model and characterizes the dynamics of the population activity by means of linear response theory. This analytical description leads to a graphical intuition (**Intuition on behavior of eigenvalue trajectories**) for the dependence of oscillatory population activity on the effective connectivity matrix.

In **Influence of network structure**, we show that an anatomically more correct revision of the microcircuit model specific for macaque V1 (Schmidt et al., 2018c) substantially reduces fast oscillatory activity compared to the original circuit. The following sections probe the robustness of connectivity as the key promoter of fast oscillations. First, **Influence of the delay distribution** demonstrates that with respect to synaptic delays, only an exponential delay distribution has a relevant effect on fast oscillations in the original circuit. Second, **Influence of the transfer function** investigates the dependence of the phenomenon on the transfer function of the leaky integrate-and-fire neuron model summarizing all single neuron properties and the drive by external currents. The latter finding highlights how external currents exert an influence on the effective connectivity by shifting the working point of the transfer function. Finally, we discuss the limitations of presently available analytical approximations and discuss the implications of our findings (**Discussion**) for experiment, simulation, and theory.

7.2 RESULTS

Sustained high-frequency oscillations $> 300\,\mathrm{Hz}$ are observed across a broad range of models starting from two-population networks (Brunel, 2000) to more elaborate, biologically constrained networks. At the example of the Potjans-Diesmann microcircuit (Potjans et al., 2014a), we here aim to evaluate the biological plausibility of observed high-frequency oscillations in the simulated spiking activity. Therefore, we start by describing the observations in simulated data and discuss difficulties in the comparison of our findings to experimental recordings.

7.2.1 *Visibility of ultra-high frequency oscillations in model data*

In this study, we look at the cortical microcircuit as described in Section 6.1.

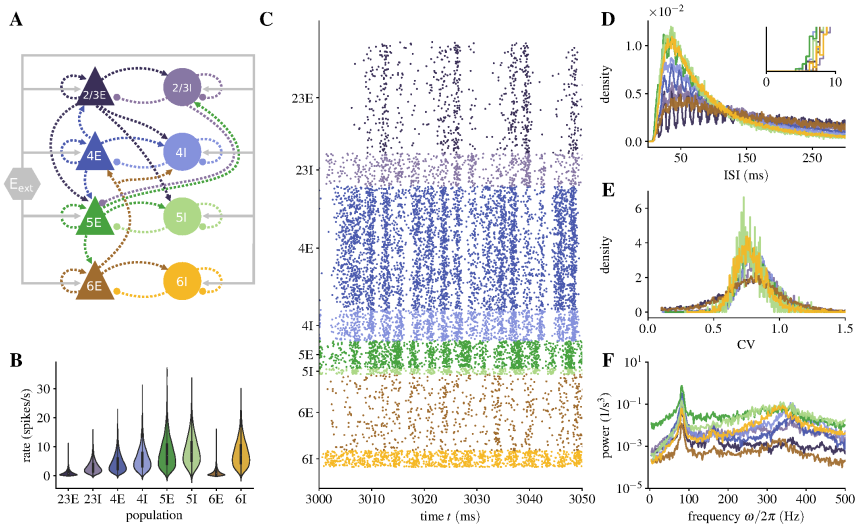

Figure 7.1: **Visibility of ultra-high frequency oscillations in simulated neural data.** **A** Sketch (according to Senk et al. (2022)) of the cortical microcircuit model by Potjans et al. (2014a). Only connections with connection probability > 0.04 are shown (as in Figure 1 of the original publication). Throughout the study colors indicate layer (2/3: purple, 4: blue, 5: green, 6: brown) and cell type (excitatory (E): dark, inhibitory (I): light), here with redundant layer-number and E/I labeling. **B** Violin plots (Hintze et al., 1998) of the firing rate distributions of each population, with the inner of the violin showing a box plot (Tukey, 1977). **C** Raster plot of 50 ms of simulated spiking activity. Spike trains are grouped by populations and vertically stacked. **D** Probability density distributions of the inter-spike interval (ISI) with inset showing shorter ISIs. **E** Probability density distributions of the coefficient of variation (CV) of the ISI. **F** Average population-rate power spectra calculated via FFT on non-overlapping 500 ms windows of the binned (bin size 1 ms) population spike count (same method as in Layer et al. (2022a)) on the time interval $[1, 10\,]$s. Data in panels **B,** **D** and **E** are calculated on the time interval $[0.3, 10\,]$s of a single simulation run with the software NEST.

A raster plot (Figure 7.1C) of the spiking activity of the microcircuit model exposes reoccurring synchronized firing of neurons within a population, visible as vertical stripes. Two different time scales dominate the activity: While in the inhibitory population of layer 4 we count roughly 17 narrow stripes within the plotted 50 ms windows, the activity of the excitatory population of layer 2/3 is shaped by four broad stripes. These broad stripes are in turn modulated by narrow stripes, similar to those in layer 4. This synchronization pattern of the spiking activity hints at superimposed oscillatory processes with different frequencies.

A neuron does not contribute a spike to every period of these oscillations as evident from the distribution of spike rates (Figure 7.1B). Similarly, the inter-spike interval (ISI) distributions (Figure 7.1D) show preferred intervals in a range from $\sim 10\,\text{ms}$ to $\sim 100\,\text{ms}$ and a long decay towards larger intervals. The distributions exhibit periodic modulations, most prominently observed in the distribution of population 2/3E, that peaks every $10 - 15\,\text{ms}$ and hence suggests an oscillation at $\sim 66 - 100\,\text{Hz}$. Faster modulation of the ISI distribution at $\sim 3\,\text{ms}$, that would correspond to the narrow stripes in the raster plots, (cf. Figure 7.1C inset) is not exhibited. The distributions of the coefficients of variation (CV) are centered at values smaller than unity, suggesting that the activity of the individual neurons is more regular than a Poisson process (Figure 7.1E). In particular, the distributions of populations 2/3E and 6E are skewed towards smaller CVs. The power spectrum of the population time histograms, however, confirms dominant frequencies at $\sim 80\,\text{Hz}$ and $\sim 340\,\text{Hz}$ (Figure 7.1F). We refer to the former as γ-oscillations and to the latter as ultra-high frequency oscillations. For populations 6E and 6I the peak in power occurs at lower frequencies compared to populations 2/3I, 4I, and 4E. While population 2/3E shows almost no elevated power at higher frequencies, populations 5I and 5E have substantial power in a broad range of high frequencies.

It has been shown that solving the differential equations for neuron dynamics on a discrete time grid can lead to an artificial synchronization of neuronal network activity (Hansel et al., 1998; Morrison et al., 2007). In Section A.5.2 we show simulations with discrete and precise spike time representation and exclude these parameters as the cause for the observed synchronizations.

7.2.1.1 *Visibility in spiking activity*

The power spectrum of the population time histogram can be decomposed into two components: the population-averaged single neuron power spectra $A_i(\omega)$ and the cross-spectra of pairs of neurons $C_{ij}(\omega)$ (Harris et al., 2011; Tetzlaff et al., 2012):

$$C(\omega) = \frac{1}{N^2}\left(\sum_{i=1}^{N} A_i(\omega) + \sum_{i=1}^{N}\sum_{j=1,j\neq i}^{N} C_{ij}(\omega)\right) \quad , \tag{7.1}$$

where $\omega = 2\pi f$ denotes the angular frequency. The first term scales with N while the second term scales with N^2.

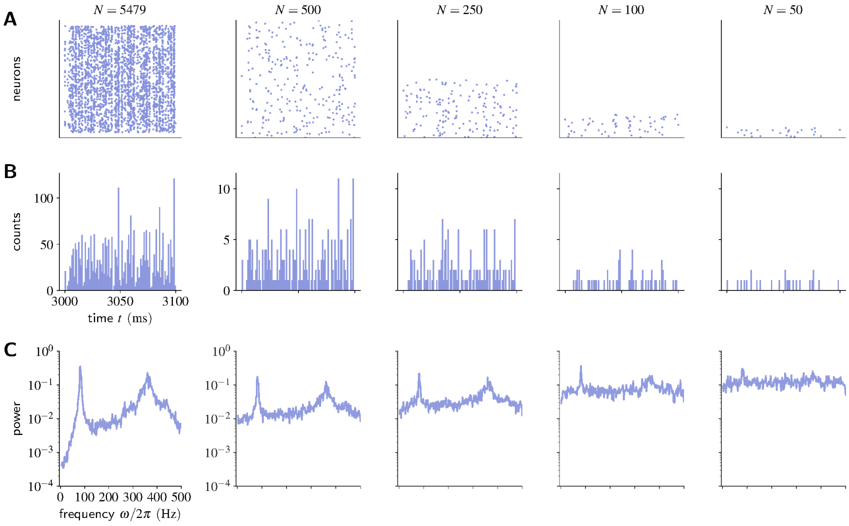

Figure 7.2: **Visibility of ultra-high frequency oscillations under subsampling.** First column displays 100 ms of activity of all $N = 5479$ neurons of population 4I of the microcircuit model (same data as in Figure 7.1). Subsequent columns show subsamples of decreasing size of these data (size indicated by column titles, identical vertical scaling but different for first column). **A** Raster plots, **B** population time histograms (bin size 1 ms) and **C** power spectra calculated as in Figure 7.1).

Figure 7.2 illustrates the consequence of the differing dependence on N of these two terms. In the raster plots and the population time histograms it becomes more difficult with decreasing N to distinguish the vertical stripe-like structure of activity from an irregular background. Equation 7.1 explains the observed phenomenon: while for large N the cross-spectra dominate, for small N the single neuron autospectra govern the population-rate power spectrum. The visibility in experimentally recorded spiking data is hence limited, as even modern recording techniques drastically subsample the local cortical network. The Utah array technology (Blackrock Microsystems, Salt Lake City, UT, USA, `www.blackrockmicro.com`) typically isolates around ~ 150 neurons. Neuropixels (Jun et al., 2017a) delivers simultaneous spike trains of hundreds of neurons, but across a larger spatial extent. As the statistics of spiking activity differs between cell types, grouping spike trains according to neuronal population would enhance the detectability of vertical stripes.

7.2.1.2 *Visibility in local field potential*

Power spectra of the population spiking activity with a sufficiently large number of neurons from the same population are hard to obtain from experimental data. A simpler, population measure that allows for comparison with simulated data is the local-field potential (LFP). Hagen et al. (2016) present a hybrid-scheme to calculate the LFP from simulations of network models based on point neurons like the microcircuit model introduced above. This hybrid scheme uses the dynamics of point-neuron networks and sends the obtained spikes into the synapses of multi-compartment neurons with cell-type and layer-specific connectivity. Those allow the computation of the transmembrane currents and thus the resulting LFP. The LFP calculated in this way indeed exposes the ultra-high frequency peak around 300 Hz of the microcircuit activity (cf. Fig. 8 of Hagen et al. (2016)) although several cell types contribute to the signal.

For a quantitative comparison of experimental data to simulated LFP power spectra, the aperiodic and periodic components of the power spectra (Donoghue et al., 2020) ideally have to be disentangled: The aperiodic component, a $1/f$-like decay observed in experimental spectra, which mostly impacts lower frequencies, according to some authors (Bédard et al., 2009) originates from ionic diffusion, which is not captured by the model of Hagen et al. (2016). Besides this aperiodic component, experimental power spectra reflect periodic components as elevated power in certain frequency bands, which are assumed to reflect the underlying spiking dynamics and in particular the synaptic currents induced by it. Traditionally, LFP spectra above 200 Hz are disregarded due to potential contamination of the high-frequency power spectrum (starting above 50 Hz) by the waveform of action potentials in the vicinity of the tip of the electrode (Zanos et al., 2011).

In summary, whether or not oscillatory activity present in the simulated spiking data is observable in experimental data depends on the number of recorded neurons. The LFP can be used as an antenna that probes the activity of thousands of neurons simultaneously. The quantitative comparison of experimental and simulated LFP, however, is hampered by various frequency-dependent filtering effects due to the extracellular medium (Bédard et al., 2004). Irrespective of whether or not ultra-high frequency oscillations are experimentally observable to date we need to investigate whether they constitute a robust signature of our understanding of cortical dynamics or rather a result of oversimplification.

7.2.2 *Mean-field theoretical description*

In order to gain a theoretical understanding of the oscillatory behavior in the microcircuit model, we resort to a mean-field description of the model and apply linear response theory to approximate the dynamics. The formalism employed here has been established in previous works (Bos et al., 2016) and was presented as part of the previous Chapter 6.

The critical quantities are the effective connectivity matrix given in Equation A.4 and the power spectra in Equation 6.17. Applying an eigenvalue decomposition to effective connectivity, allows us to see that the power spectrum of the a-th population $P_a(\omega)$ receives a contribution from each eigenvalue λ_b of the effective connectivity matrix, $P_a(\omega) \propto 1/\left(1-\lambda_b(\omega)\right)^2$.

For $\lambda_k(\omega) \rightarrow 1$ the power spectra, grow proportionally to $|1-\lambda_i(\omega)|^2$ in the vicinity of the point of instability in the complex plane $(1+i0)$, henceforth called the critical point. Figure 7.3 illustrates the contributions to the effective connectivity matrix for the microcircuit model.

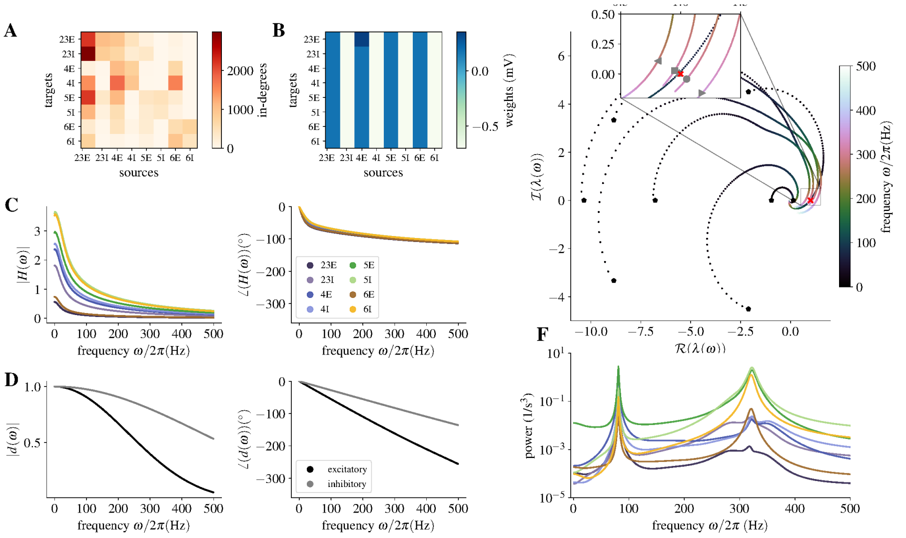

Figure 7.3: **Mean-field description of the microcircuit model.** The effective connectivity in the Fourier domain $\tilde{\boldsymbol{M}}_{\boldsymbol{d}}(\omega)$ is a 8×8 complex-valued matrix describing the interactions between the neuronal populations. $\tilde{\boldsymbol{M}}_{\boldsymbol{d}}(\omega)$ consists of a structural part and a dynamic part: The anatomical connectivity is characterized by the matrix of in-degrees $\boldsymbol{K}$ (panel **A**) and the weight matrix (panel **B**). The dynamical contributions are the transfer functions $H(\omega)$ (panel **C**; color code (legend) as in Figure 7.1 left: absolute value, right: phase) and the delay distributions (panel **D**; gray code indicates cell type (legend) left: absolute value, right: phase). **E** Frequency dependence of the eigenvalues of the effective connectivity matrix (vertical: imaginary part, horizontal: real). The eigenvalues at $f = 0\,\text{Hz}$ are marked by black pentagons and trajectories show the evolution with increasing frequency (color bar: up to 500 Hz in steps of 1 Hz). The inset highlights the closest approaches $\omega_{c,k}$ of the trajectories of five eigenvalues to the point of instability $(1+i0$, red cross) by markers (triangle left: λ_1, square: λ_2, triangle up: λ_3, disk: λ_4, triangle right: λ_5). **F** Population-rate power spectra predicted by the mean-field theory (color code as in **C**).

At zero frequency ($\omega = 0\,\text{Hz}$) all quantities are real. The delay distribution (Figure 7.3D) has an absolute value of 1 and hence doesn't affect the effective connectivity at zero frequency. The transfer function (Figure 7.3C) at zero frequency corresponds to the derivative of the firing rate with respect to the mean input to the population (Schuecker et al., 2015). The corresponding eigenvalues of the effective connectivity at zero frequency are symmetric with respect to the real axis and have complex conjugate pairs (see Figure 7.3E). Both, the transfer function and the delay distribution, effectively act as low-pass filters which suppress the absolute values with increasing frequency and additionally rotate the eigenvalues clockwise. A parameterized plot of the eigenvalue of a matrix in the complex plane is known in literature as a Nyquist plot (Oppenheim et al., 1996). As a function of the frequency, the eigenvalues form a spiraling trajectory terminating at the origin $(0 + i0)$ of the complex plane for $\omega \to \infty$. As a consequence, each trajectory comes closest to the critical point $(1 + i0)$ at some frequency $\omega_{c,k}$ (see enlargement in Figure 7.3G). At these critical frequencies the power spectrum grows as the inverse square of this distance. While four of the trajectories shown in the enlargement are responsible for the ultra-high frequency peak in the power spectrum, the fifth has its close encounter at a lower frequency and drives the γ-peak. The mean-field predictions of the power spectra in Figure 7.3E resemble the power spectra of the direct simulations Figure 7.1D. The ultra-high frequency peak of the theory is, however, more pronounced than in the simulations. How can we use the knowledge from the mean-field equations, that uncovered relationship of the network parameters and power spectrum, to understand the emergence of oscillations?

7.2.2.1 *Intuition on behavior of eigenvalue trajectories*

The distance of the eigenvalue trajectory at a certain frequency to the critical point $(1 + i0)$ in the complex plane is inversely proportional to the magnitude of the power spectrum at that frequency. This facilitates a geometrical intuition on how changes of model parameters differentially impact the emergence of oscillatory activity. Figure 7.4 illustrates global changes to the effective connectivity matrix, their effect on the eigenvalue trajectories, and the resulting power spectra. A multiplication with a real value smaller than unity leads to a contraction of the eigenvalue spiral. Conversely, a multiplication with an absolute value larger 1 expands the spiral. A multiplication by a complex number $e^{i\theta}$ with phase θ rotates the spiral in the complex plane: A positive phase rotates the spiral counterclockwise. In the exemplary sketch this rotation mainly affects the frequency at which the power spectrum reaches its maximum. In addition, the magnitude of the peak changes as the spiral's radius is smaller for higher frequencies. A multiplication of the effective connectivity matrix with a generic complex value ($z = |r|e^{i\theta}$) thus leads to a rotation combined with a contraction ($|r| < 1$) or expansion ($|r| > 1$).

In light of this intuition, we now discuss the effects of the anatomical connectivity, different delay distributions and the transfer functions on the occurrence of ultra-fast oscillations.

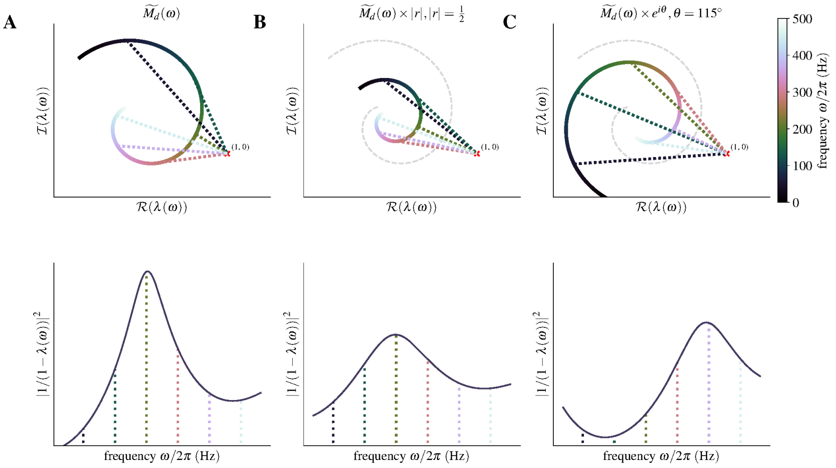

Figure 7.4: **Schematic influence of a spiraling eigenvalue on population-rate power spectra. A** Sketch of the trajectory of an eigenvalue in the complex plane (upper panel) with an implicit dependence on frequency $\omega/2\pi$ (color bar) and resulting population-rate power spectrum (lower panel). The power spectrum is proportional to $1/\left|(1-\lambda(\omega)\right|^2$, where $1-\lambda(\omega)$ is the distance of the eigenvalue trajectory to the critical point $(1+i0)$. The colored dotted lines relate the frequencies marked in the lower panel to the locations on the spiral. **B** Eigenvalue trajectory and power spectrum if effective connectivity is multiplied with an absolute value $|r| = \frac{1}{2}$ (dashed gray: original trajectory of **A** for comparison). **C** Eigenvalue trajectory and power spectrum if effective connectivity is multiplied with a complex phase factor $e^{i\theta}$ for $\theta = 115^\circ$.

7.2.2.2 *Influence of network structure*

The microcircuit model (Potjans et al., 2014a) is widely used with adapted connectivity parameters (Bos et al., 2016; Hagen et al., 2016; Schmidt et al., 2018c; van Albada et al., 2015) (see also Section 6.1.2).

The V1 circuit embedded in the multi-area model of Schmidt et al. (2018c) is one particular example. It shows no signs of a high-frequency oscillation. At the outset of the present study we hypothesized that this might be due to the intricate interplay between multiple microcircuits in the multi-area model. However, the isolated V1 circuit where external input from other cortical areas is replaced by spikes trains drawn from a Poisson process does neither exhibit vertical stripes in the raster plot nor peaks in the power spectrum (Figure 7.5). A comparison of the parameters reveals that in the V1 model the number of neurons is roughly doubled compared to the original model (Potjans et al., 2014a) to better correspond to the experimental data for the macaque, but the density of synapses in the volume is identical. As a result, the in-degrees are reduced by about a factor of two, as can be seen in Figure 7.5C. An exception is the projection from popula-

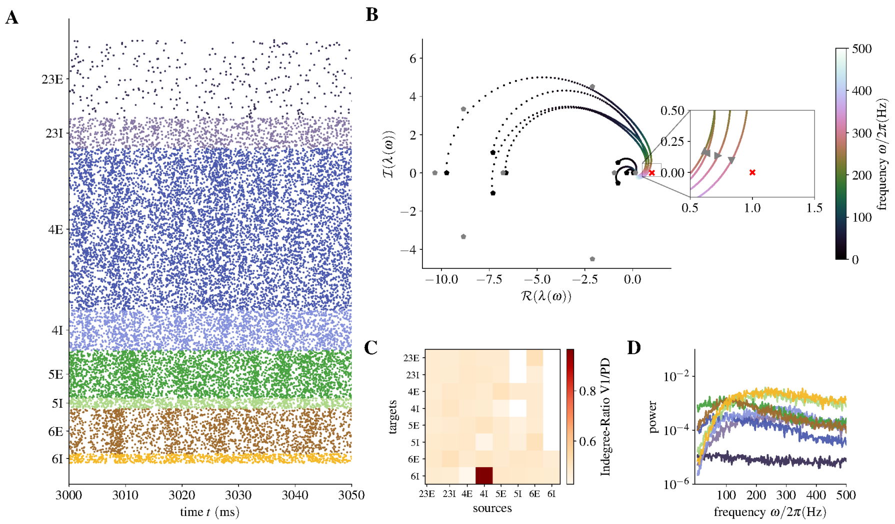

Figure 7.5: **Influence of network structure on oscillations.** Displays and color schemes as in Figure 7.3. **A** Raster plot of activity in the V1 model isolated from Schmidt et al. (2018c). **B** Eigenvalue trajectories as function of frequency; the anatomical connectivity leads to a change in the eigenvalues at 0 Hz compared to the microcircuit model (gray pentagons, cf. Figure 7.3E). **C** Ratio of in-degrees between the connectivity of the isolated V1 model and the microcircuit model. **D** Population-rate power spectra.

tion 4I to population 6I; there are very few synapses in both models and the ration remains essentially the same. Furthermore, the ratio of synaptic strengths of the inhibitory and the excitatory connections $g = J_I / J_E$ is larger in the isolated V1 circuit ($g = -11$) as compared to the original circuit ($g = -4$) . The absence of oscillations and the resulting flat spectrum for high frequencies can be understood in terms of the intuition presented in Section 7.2.2.1: The radii of the eigenvalue trajectories of the effective connectivity matrix are compressed due to the overall reduced in-degrees. At zero frequency this contraction can be observed by comparing the eigenvalues to those of the original model (see Figure 7.5B). At high frequencies, the trajectories thus pass the critical point at a larger distance. Further simulations show that the effect of the stronger inhibitory synapses does not explain the flat spectrum.

Global differences in the connectivity structure as in the V1 model compared to the original microcircuit model are expected to change network dynamics. However, also fine-grained changes in the anatomical connectivity may influence oscillatory activity. In Bos et al. (Bos et al., 2016) the impact of network structure is assessed by a quantity called 'sensitivity measure'. The sensitivity measure quantifies how an infinitesimal change in the in-degree matrix impacts the distance ($\mathbf{Z}^{\text{amp}}$) and frequency ($\mathbf{Z}^{\text{freq}}$) at which an eigenvalue trajectory of the effective connectivity matrix passes the critical point $(1 + i0)$. In Fig-

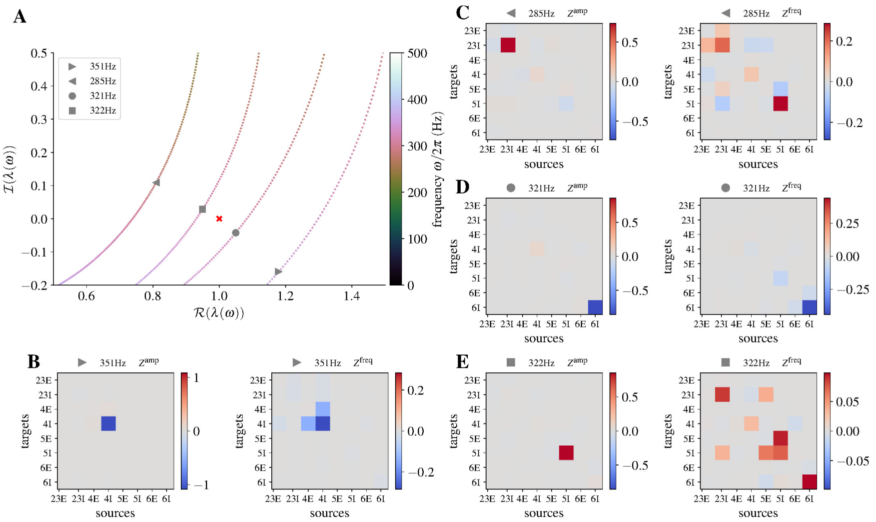

Figure 7.6: **Anatomical origin of oscillations. A** Four eigenvalue trajectories of mean-field representation of the Potjans-Diesmann model (same data as in Figure 7.3, markers (legend) indicate frequency at closest distance to critical point $1 + i0$) with ultra-high frequencies in the vicinity of the critical point. B, C, D, E Sensitivity measure for the four eigenvalues contributing to the ultra-high frequency population-rate power spectrum. Left $\mathbf{Z}^{\mathrm{amp}}$, connections contributing to the amplitude at the critical frequency (title of graph). Right $\mathbf{Z}^{\mathrm{freq}}$, connections determining frequency. Shades of blue (color bar) denote that a decrease in the in-degree leads to an increase in power or frequency, respectively; shades of red the opposite.

ure 7.6A, the inset of Figure 7.3E is enlarged to display the behavior of the eigenvalue trajectories around the critical point. At the ultra-high frequencies, there are four trajectories passing close by the critical point. These four trajectories determine the high-frequency oscillation peak. Panels B - D show that predominantly the in-degrees of the inhibitory loops 23I-23I, 4I-4I, 5I-5I and 6I-6I have a strong effect on both, the distance and the frequency, at which the relevant eigenvalue trajectory passes the critical point.

7.2.2.3 *Influence of the delay distribution*

The transmission delay from one population to another shapes the dynamics of a multi-population network. To discuss the impact of the delay distribution on the eigenvalue trajectories of the effective connectivity and thus the population-rate power spectra, we treat them as a separate factor in the Fourier domain. We study fixed delays as well as uniform, exponential, log-normal and truncated Gaussian distributions of delays (see Figure 7.7 for illustrations of the delay distributions in the time domain at the example of the microcircuit model). We ensure comparability of the distributions by matching their statistical moments where possible (for details refer to Section A.5.1). The corresponding absolute values and phases in the Fourier domain resemble those of a low-pass filter, except for the fixed delay case, where transmission is unfiltered (see 7.7). Mattia et al., 2019 recently showed analytically that the effect of the exponential delay distribution in neuronal networks is approximately equivalent to synaptic filtering.

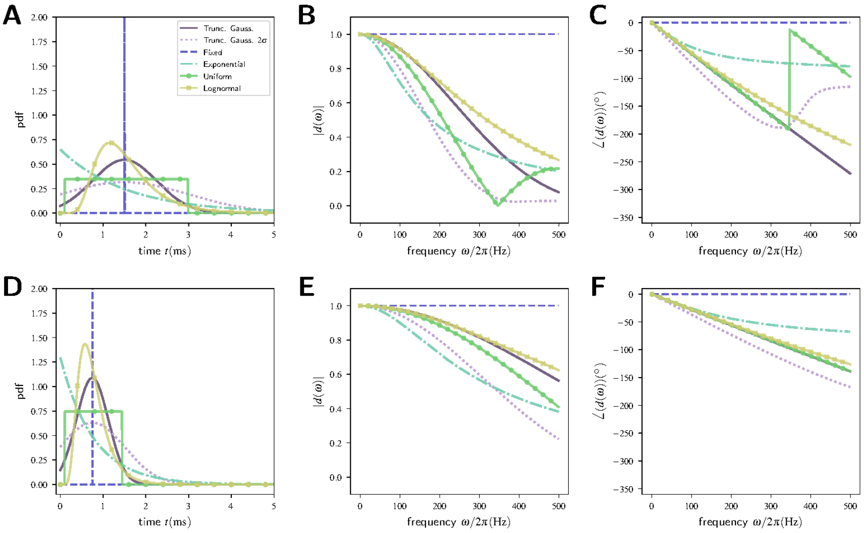

Figure 7.7: **Characteristics of common delay distributions. A** Different delay distributions in the time domain with mean and standard deviation (except for fixed delay) matched to the truncated Gaussian distribution of the excitatory connections in the microcircuit model. **B** Magnitude of delay distributions in the Fourier domain. **C** Phase of delay distributions in the Fourier domain. **D, E, F** Same as upper row for the inhibitory connections.

The mean and standard deviations of the delay distributions differ for the excitatory and inhibitory populations. A quantitative statement of the effect of the delay distribution on the eigenvalue trajectories is more involved due to the delay matrix being inhomogeneous. However, an intuition of the influence of the delay distribution can be gained by discussing deviations from a reference distribution, here taken to be the truncated Gaussian distribution.

The change of the delay distribution of a given network to an exponential distribution has a particularly strong effect on the ultra-high frequency oscillations: a prominent feature illustrated in Figure 7.7 is the slowly changing phase of the exponential distribution for higher frequencies, which corresponds to an effective counterclockwise rotation of the trajectories with respect to the truncated Gaussian trajectories. This counterclockwise rotation impacts the high-frequency oscillations in two ways: first, the frequency at which the trajectory passes the critical value is shifted towards higher frequencies and the radius of the trajectories for high-frequencies is decreases. The combined effect is a larger distance of the trajectories to the critical point. The corresponding eigenvalue trajectories of the Potjans-Diesmann model with exponential delays are shown in Figure 7.8 together with he raster plot and power spectra as resulting from direct simulations.

In Bos et al. (2016) the delay distributions of the Potjans-Diesmann model are modified to have twice as large standard deviations as in the original model in order to stabilize the dynamics of the model. The intuition of a faster compression of the eigenvalue trajectories due to a counterclockwise rotation of the trajectories explains the stabilizing effect. The uniform and log-normal distributions do not differ substantially from the reference truncated Gaussian.

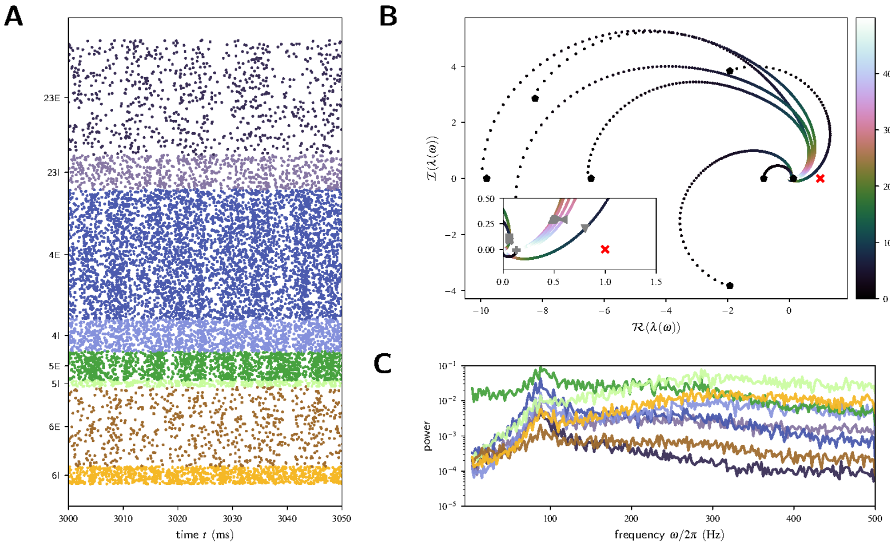

Figure 7.8: **Effect of exponential delay distribution on oscillations. A** Raster plot of a microcircuit simulation with exponentially distributed delays (same display as in Figure 7.1) with mean and standard deviation matched with the original truncated Gaussian. **B** Plot of the eigenvalue trajectories of the effective connectivity calculated with exponentially distributed delays (same display as in Figure 7.3). **C** Power spectra (same display Figure 7.1). Other model parameters as in Figure 7.1.

7.2.2.4 *Influence of the transfer function*

The transfer function describes the response of a population of leaky integrate-and-fire model neurons to a weak oscillatory input current of a given frequency on top of a stationary white noise with a certain mean and standard deviation representing the synaptic input. For synapses with an exponentially decaying current, the transfer function needs to incorporate the additional low-pass filter. From the view point of the conventional mean-field neuron model the noise is not white anymore, but colored. Expressions for the colored noise problem have been derived in Schuecker et al. (2015). These authors approximate the transfer function up to first order in $k = \sqrt{\tau_s/\tau_m}$, with τ_s and τ_m the synaptic and membrane time constants, respectively. In the limit of $\tau_s \to 0$ the white noise problem is recovered. Two equivalent methods to calculate the colored noise correction term of the transfer function linear in k consist in either shifting the boundaries of integration of the white noise transfer function or calculating the Taylor expansion (rf. Schuecker et al. (2015) for details). The two methods of calculating the transfer function differ slightly for low frequencies. Figure 7.9 shows the difference in absolute value and phase, respectively, and illustrates that the discrepancy impacts the eigenvalue trajectories and in particular the magnitude of the 70 Hz peak in the power spectrum.

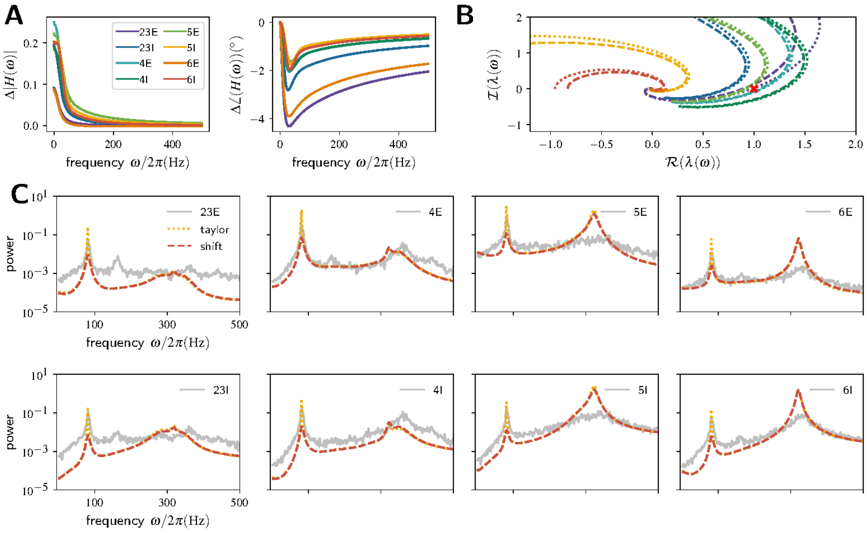

Figure 7.9: **Influence of transfer function.** **A** Differences in absolute value (left) and phase (right) of the transfer function approximations for each population ($\Delta\,|H(\omega)| = \left|H_{\text{taylor}}(\omega)\right| - |H_{\text{shift}}(\omega)|$). **B** Eigenvalue trajectories obtained by using two different approximations of the transfer function (dashed: boundary shift; dotted: Taylor expansion). **C** Impact of the transfer functions on the predicted power spectra, data from direct simulations (light gray) shown for comparison. Data representation as in previous figures.

The perturbative derivation of this expression neglects terms of order $\mathcal{O}(k^2)$ and higher. This is only valid for moderate frequencies $\omega\tau_m k \ll 1$, leading to expected deviations of the mean-field result from direct simulations of the full nonlinear system for high frequencies ($>$ 100 Hz) (Schuecker et al., 2015). In Section A.5.3, we introduce an ad-hoc correction that improves the fit of the mean-field prediction to the data for different network models. Nevertheless, the mean-field approximation to first order is accurate enough to gain qualitative insights.

It can be useful to think of the transfer function as a series of two effective low-pass filters: the filtering due to the synaptic dynamics, and a filtering due to the membrane potential dynamics including the threshold crossing process.

In the mean-field approximation, the input to a neuron is described by an effective Gaussian noise with mean μ and standard deviation σ. The statistics of the input μ, σ to a population defines its working point and the firing rate. See Figure 7.10A for comparison of the mean firing rate distributions in the simulations and the predicted mean firing rates (red markers). The contribution of the hypergeometric functions appearing in the transfer function varies quite drastically for different input statistics. In (Ledoux et al., 2011) the effect of the fraction of hypergeometric functions is discussed at the example of an E-I network with varying working points (e.g. due to external noise). It is further known that in the mean driven regime (high firing rate, low noise), resonance phenomena appear (Lindner et al., 2001; Schuecker et al., 2015).

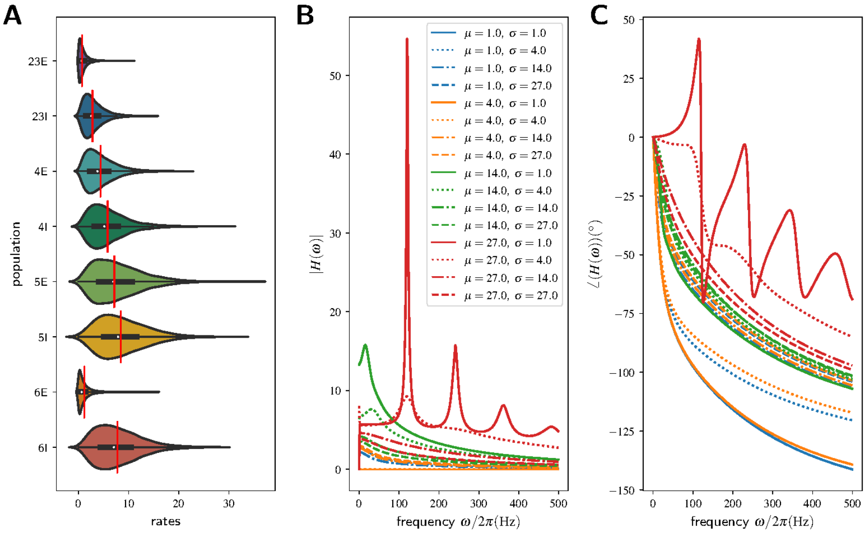

Figure 7.10: **The transfer function depends on the working point.** The working point is given by the mean input μ and its standard deviation σ. **A** Firing rate distributions (histogram of time-averaged firing rates across neurons, violine plots) for each population. Red markers denote the mean-field prediction. **B** Absolute value and **C** phase of the transfer function (shift) for different values of μ and σ.

In Figure 7.10B and C the absolute value and phase of transfer functions in the 'shift' approximation are shown for different working points. A network with fixed anatomical connectivity and biologically realistic delays can thus be driven into different regimes by modifying the working point. Furthermore, it is noteworthy, that a change in the connectivity structure will necessarily impact the transfer functions as well, as these in turn modify the working point.

7.3 DISCUSSION

The present chapter discussed the emergence of ultra-high frequency oscillations in spiking network models with a focus on potential experimental visibility and mechanistic understanding of their origins. To this aim, we take into account experiment, simulation and theory. Different interactions between these approaches lead to incremental improvement of the understanding: Experiments supply anatomical data, that can be incorporated into simulations. Large-scale simulations give rise to quantitative predictions, which can in turn be validated or falsified by experiments. A qualitative understanding of the mechanisms that govern the activity of these complex models can be gained through theoretical descriptions. A comparison of the theoretical prediction to simulations allows the control of approximations and the assessment of shortcomings in the theory. The reduced complexity and mathematical formalism of the theory, even though approximate, enable the formation of an intuition for the processes. The gained intuition can in turn inform the modeler, theoreticians, and experimenters to guide incremental improvements.

The main findings of this work are:

1. under the assumption that the model prediction of high-frequency oscillations is valid, these oscillations are (likely) not visible with state-of-the-art recordings of spiking activity, but could be noticeable in population measures, such as the local-field potential;
2. mean-field theory combined with linear response theory reveals the roles of anatomical connectivity, the delay distribution, and the the transfer function for the emergence and properties of oscillations in the model
    a) the activity of the V1 circuit of the multi-area model due to its reduced effective connection density shows no high-frequency oscillations
    b) the ultra-high frequency oscillations are sensitive to perturbations of the inhibitory-inhibitory loops in layers 2-3, 5, and 6
    c) the uniform, exponential, log-normal and truncated Gaussian delay distributions have a similar low-pass filter-like behavior, but the exponential distribution has the largest influence at high-frequencies due to a particular trend in the phase
    d) the linear response approximation of the transfer functions is expected to deviate from simulations at high-frequencies
    e) the transfer functions are sensitive to changes in the working point; the system can be driven from a non-oscillatory to an oscillatory state by varying the external input

The microcircuit model by Potjans-Diesmann, with realistic cell densities per population and experimentally extracted connectivity parameters, predicts network oscillations in the ultra-high frequency range ($\sim 340\,\text{Hz}$). These fast oscillations are clearly visible in raster plots and power spectra of the full simulation and strongest in the inhibitory populations and weakest in the populations 23E and 6E. Sustained oscillations of such high frequency are not reported in the literature. We assess the experimental visibility in electrophysiological recordings of spiking activity by sub-sampling and observe that the visibility in raster plots and power spectra decreases with the number of neurons. This is expected from the scaling of the contributions of auto-spectra and cross-spectra to the power spectrum. In modern multi-electrode recordings, the simultaneous spiking activity of roughly 100 (e.g. Utah array) to 1000 (e.g. Neuropixels) neurons are observed. The spatial extents of Utah arrays or Neuropixel probes span several layers and even brain areas, such that the activity is difficult to compare to the populations in the network model, which is supposed to model $1\,\text{mm}^2$ of cortical surface.

A hybrid-scheme of obtaining the local field potential from the microcircuit model predicts that the ultra-high frequency oscillations are visible in the local field potential. In the literature, local field potentials above $300\,\text{Hz}$ are often disregarded to avoid contamination of the signal with slow components of waveforms of nearby action potential (see Section 7.2.1.2).

Another difficulty comparing simulations and experimental data arises from the fact, that the simulation operates at one dynamical state (fixed rate of external Poisson input) and stays in that state across the time span of simulation. An oscillatory state will hence produce sustained oscillations. In nature, such a controlled state is unlikely to be realistic. In LFP and EEG literature reports of ripples $140 - 200\,\text{Hz}$ (Logothetis et al., 2012) or high-frequency oscillations (HFO, $> 80\,\text{Hz}$), that last only a couple of oscillation cycles (for a recent example see Cai et al. (2021)) can be found. These point to transient changes in the network state.

A further investigation into the theoretical underpinnings via mean-field and linear response theory led to a holistic, yet abstract understanding of the oscillatory network activity being linked to the eigenvalues of the effective connectivity matrix passing a critical point. This point of instability can be interpreted as the transition point of the Hopf-bifurcation between asynchronous irregular (AI, $\mathcal{R}(\lambda_k) < 1$) and synchronous irregular (SI, $\mathcal{R}(\lambda_k) > 1$) state (Bos et al., 2016). The eigenvalues of the effective connectivity matrix, parameterized by the frequency, form a spiral in complex plane which at some particular frequency is closest to this point of instability. As the power spectrum is proportional to the inverse squared distance of the trajectory to the point of instability, it is governed by the spiraling eigenvalue trajectories. Changes in the anatomical connectivity, the delay distribution and the transfer functions impact these eigenvalue trajectories and thus the power spectra.

The sensitivity measure defined by Bos et al. (2016) confirms the ultra-high frequency oscillations being sensitive to the connections within the inhibitory populations. Overall, lower in-degrees in the multi-area model isolated V1 microcircuit lead to an effective compression of the eigenvalue spirals radii and in consequence a reduction of high-frequency activity.

Another crucial ingredient in multi-population networks is the transmission delay from one population to another. The distribution effectively acts as a low-pass filter on the dynamics of the network. We find that the exponential distribution rotates the eigenvalues to a smaller extent compared to the truncated Gaussian delays and hence leads to a flat power spectrum for high frequencies. The uniform, log-normal and truncated Gaussian distributions have comparable effects.

Lastly, we discussed the limitations of the dynamical mean-field theory due to the transfer functions. The current state-of-the-art approximation of the transfer function for colored noise is expected to be inaccurate for large frequencies. This likely explains the mismatch between (linear) theoretical prediction and (non-linear) simulations. An ad-hoc correction in form of an additional low-pass filter on the transfer function improves correspondence of theory and simulation (see Section A.5.3). Another important observation is the dependence of the transfer function on the working point. This leads the discussion back to the dynamical state in which the network operates.

The current approach of determining the external input into the network consists in fitting the input to the network such that the resulting mean firing rates (across time and neurons within each population) fit those measured in experiment. This is probably the best we can do, as experimentally we are limited in knowing which connections are recurrent (from within the local circuitry) and which stem from external connections. As the consequence, the network operates in a dynamical state that successfully replicates the mean firing rates of the populations. To account for temporal changes in the input to the network, one could propose to define a range of dynamical states (or working points) by looking at the time-dependent population firing rates. This could be realized in the simulation model by a range of inputs to the system. The change in the network dynamics would then arise due to changes in the transfer function only. Depending on the input (or target firing rates) the network could in principle account for short, transient oscillations of high-frequencies (for a few cycles).

With larger network simulations, the dependence on external input is decreased, the networks become more self-consistent and the quantitative prediction improves. However, the intricate interactions in multi-population networks make it difficult to isolate the influence of single parameters on the network behavior. This work points at employing the network models as tools that work at the interface between theory and experiment and can help bridging intuition from theories to quantitative and testable predictions.

Part III

CONCLUSION

8

CONCLUSION

The brain is a fascinating organ, yet its precise way of function remains elusive until now. However, as it determines our way of thinking and the behavior of humans and animals alike, it is the subject of study by many researchers from different backgrounds.

In this thesis, we presented two projects that investigated the brain on two fronts: First, by recording neural activity from behaving monkeys, and second, by simulating biologically constrained spiking neural networks.

While the first project would be considered at the core of systems neuroscience, the second project belongs to the research agenda of computational neuroscientists.

Needless to say, systems neuroscience and computational neuroscience are abstract concepts of a grouping that can only be observed through the preferred way of communicating about a problem or through the constellation of researchers meeting at a conference. A computational neuroscientist, for example, with physics background, who extends current mean-field descriptions of large spiking networks to higher-order interactions, would feel "at home" at the annual Computational Neuroscience Meeting (CNS), but much less understood at the, despite its name, more systems neuroscience oriented Cosyne (Computational and Systems Neuroscience).

Yet, as the name of the Cosyne probably says, the overlap between systems and computational neuroscience is far greater than, e.g. to, cellular and molecular or cognitive neuroscience. The annual Society for Neuroscience (SfN) meeting, which attracts over 30,000 attendees annually, brings all these fields together.

However, already in our Lab at the INM-6 at Forschungszentrum Jülich, we noticed a gap worth bridging, and this thesis was an attempt in that direction.

We researched two distinct research questions and explored each subfield's intricacies:

1. Is the bimodality of the distribution of preferred directions (PDs) that has been observed in primary motor cortex (M1) and dorsal premotor cortex (PMd)/ventral premotor cortex (PMv) also present in the parietal and visual cortex of macaque monkeys that perform a visually guided reaching task?

2. Are oscillatory synchronizations of the spiking activity observed as vertical stripes of raster diagrams in simulations of a microcircuit model composed of leaky integrate-and-fire (LIF) neurons

> a valid prediction of the model? Should they be observable in experimental data, and can we mechanistically understand them?

Here, I want to summarize our research results, report on the insights gained respectively difficulties encountered, and finally suggest possible ways of bringing the two research fields closer together.

8.1 SUMMARY

8.1.1 *Analysis of electrophysiological data from the Vision-for-Action experiment*

To answer the question regarding the existence of bimodality of the distribution of PDs parietal and visual cortex of macaque monkeys that perform a visually guided reaching task, we first had to improve our understanding of the data that we were going to analyze.

In Chapter 2, we performed a literature review to get familiar with neuronal structures in the macaque brain that are relevant for eye-hand coordination. In particular, we scanned existing literature on the parietal areas dorsal prelunate (DP) and area 7a (7a), because we were to analyze neural recordings thereof. Next, in Chapter 3, we summarized joint efforts of the labs by Thomas Brochier and Sonja Grün to make the datasets from the Vision-for-Action (V4A) experiment accessible for analyses. Before using the data, however, we had to take preventative measures to avoid any bias of potential artifacts to our analysis. So, in Chapter 4, we characterized artifactual signatures in the data, hypothesized about their origin in the setup, such that they might be avoided in future evolutions of the setup, and explained the exclusion of crosstalking channels from further analyses.

Finally, we were all set to approach the research question and presented this investigation in Chapter 5. By employing a generalized linear model (GLM) fitting approach, we started reproducing the predicted bimodality of the distribution of PDs across single units in M1/PMd and could indeed find significant bimodality for the distribution for both monkeys. Further, we saw evidence for the bimodality of PD distributions in primary visual cortex (V1)/secondary visual cortex (V2), DP, and 7a, however, we doubted these results as we recognized that confounding effects might give rise to these.

To exclude these confounds, we resorted to a more holistic GLM including regressors from the behavior modalities *visual*, *eye position*, *saccade*, *hand position* and *movement*. Surprisingly, the bimodality of PDs persisted even after correction for the confounding effect. The hand movement PD distribution for both monkeys was significantly bimodal in V1-V2 and DP. Furthermore, in Enya also, area 7a (7a) showed a significant bimodality.

8.1.2 *Simulation and theoretical description of spiking neural networks*

In the second part of this thesis, we wanted to investigate ultra-fast oscillatory synchronizations (at frequencies around 340 Hz) of the spiking activity — we often times termed these vertical stripes or *vstripes* as they are visible in raster plots as such—in simulations of a microcircuit model.

We quickly noticed that the analysis of the spiking activity from large-scale networks is intricate and that cause-and-effect with parameter changes are difficult to disentangle. The solution to advancing our understanding was to resort to mean-field and linear response theory to approximate the network activity.

In the first step, we thus introduce this level of description in Chapter 6. Here, we showcased a toolbox that implements the analytical equations and supplies efficient algorithms to apply the theory to network models. During my PhD, I contributed substantially to the development of this toolbox.

In the second step, we then make use of both simulations and theoretical descriptions thereof to discuss the research question in Chapter 7. After having excluded artifacts due to the representation of time in our simulations, we evaluate whether an activity, as predicted by the model, could be observed in experimental data. While we doubt that the vertical stripes would be visible in spiking activity, we predict that population measures such as the local field potential (LFP) should exhibit a corresponding high-frequency peak in the power spectrum.

We find that the frequency power spectrum in the microcircuit model is governed essentially by three quantities: The anatomical connectivity, the employed delay distribution, and the transfer function, which in turn is subject to the external (background) input to the network. This description may not be mechanistic, yet it provides valuable intuition. For example, a structurally identical model with updated connectivity (isolated V1 circuit from (Schmidt et al., 2018b)) shows no high-frequency oscillation, an effect that can be explained in our graphical analysis through the change in connectivity.

Finally, we conclude that the simulation prediction is valid. It is, however, crucial to consider that the microcircuit model is in a stationary state with no functional input. Driving the network with additional (functional) external input would (theoretically) lead to a modified transfer function and, thus, another high-frequency power spectrum.

8.2 DISCUSSION

The scientific achievements that were summarized in the previous section have been discussed in Section 5.6 and Section 7.3, respectively. At this stage, we will zoom out and attempt a wider glance at the research topics, relate them to the scientific loop that was discussed in Chapter 1, and try to see the links between the projects.

SCIENCE IS A COMMUNITY EFFORT A glance at the Author Contribution's per chapter reveals that most of the content of this thesis was developed in a joint effort — either between the author and direct supervisors or as part of larger collaborations.

The necessity to exchange ideas and establish understanding through discussions within our lab and with close collaborators has large-scale pendants in initiatives like the Human Brain Project (HBP) (Amunts et al., 2019, 2022) in Europe, the BRAIN Initiative (Insel et al., 2013) in the US or the Brain/MINDS (Okano et al., 2015) in Japan.

The initiatives likely reflect the complexity of the matter under investigation: the brain.

VISION-FOR-ACTION EXPERIMENT — A JOINT LAB EFFORT At a smaller scale, the V4A experiment illustrates that research can't be done in isolation. As mentioned in Chapter 3, the experiment was designed jointly by a team at Forschungszentrum Jülich together with a team at Institut de Neurosciences de la Timone, Marseille. Haan et al. (2018) established an experimental setup that enables the conduction of various behavioral tasks within one setup (de Haan et al., 2018). Until we could start analyzing the first datasets, monkeys had to be trained and implanted, the behavioral recording had to be calibrated, and finally, the actual recording sessions had to be performed. Once the dataset exists in Marseille, a way of sharing the large datasets (each 12 min recording session requires roughly 12 GB) with the team in Jülich needs to be found.

However, without prior knowledge and without access to an incredible amount of metadata, such a raw dataset is basically worthless. Previous generations of PhD students at INM-6 (e.g. Sprenger (2020) and Zehl et al. (2016)) in close collaboration with the collaborators in Marseille have established automatized ways of recording and storing metadata in the attempt to publish data that is usable stand-alone (Brochier et al., 2018).

In this thesis, I aimed to present as many of the necessary prerequisites that are needed to finally tackle a research question using a neural recording dataset from behaving monkeys. A step of preprocessing that is rarely talked about in literature presenting new scientific findings, is the curation of the data prior to the analysis. This might entail complicated procedures to reduce the amount of noise (Keating et al., 2002; Lecoq et al., 2021) or the removal of artifacts (Paralikar et al., 2009) (or as shown for our setup in Chapter 4).

While only mentioned briefly in Section 3.5, one crucial ingredient to obtaining "usable" datasets is the preprocessing pipeline; its development is an ongoing effort by the joint lab. Thereby we heavily rely on software, that is supplied by the community: Consider e.g. elephant (Denker et al., 2018a), neo (Garcia et al., 2014), odml (Grewe et al., 2011), GIN[1], SpikeInterface (Buccino et al., 2020) or Snakemake (Köster et al., 2012) to name just a few.

But this reliance on tools is not unique to the analysis of experimental data in the systems neuroscience community.

THE NEURONAL MEANFIELD TOOLBOX (NNMT) For the analysis on the "vertical stripes" in Chapter 7, we heavily use the Neuronal Meanfield Toolbox (NNMT) (Layer et al., 2022b). As one of the contributing developers of the toolbox, the amount of considerations and time that flow into a well-designed tool with usable documentation and quality insurance via a testing suite, is non-negligible (see Section A.4 for further discussion on that). Yet, the collection of implementations of analytical expressions in the Neuronal Meanfield Toolbox (NNMT), is simple compared to software projects like NEST (Diesmann et al., 2002; Gewaltig et al., 2007).

8.2.1 *Uncertainty*

Throughout the projects, that I worked on, I encountered fundamental uncertainties in many research areas that can't be resolved and have to be accepted.

HOW SURE ARE WE ABOUT THE SPIKE SORTED UNITS? For the analysis of the V4A data, I was primarily interested in the spiking activity of single neurons and wanted to relate their activity to behavior. However, in extracellularly recorded data it is not always trivial to assign spikes to a single neuron identity. For a long time in the previous century, recordings were performed with single electrodes. Such recordings are often considered to be biased as the experimenter was of course tempted to search for a responsive neuron. In recordings with multi-electrode arrays, as discussed in the first part of this thesis, another challenge arises: The amount of signals for which a spike sorting has to be performed is too large and can't be done manually in reasonable amounts of time. This leads to a clash of tradition and innovation with the resistance of some researchers to accept modern, automatic spike sorting solutions. In Section A.1, we discuss both approaches and use a hybrid approach for the datasets used in Chapter 5, with the M1/PMd arrays being manually sorted and the visual-parietal arrays being automatically sorted.

The astonishing part is, however, that this very uncertain step of spike sorting, which is difficult due to the lack of ground truth, lays the foundation for almost all following analyses. To avoid that *this* uncertainty leads to an uncertainty in the neuroscientific result, I chose

---

[1] GIN, `https://gin.g-node.org/`

to apply two different automatic spike sorting algorithms. In the end, although the data is not shown in this thesis, the neuroscientific result (bimodality of PDs in visual and parietal areas) proved to be robust across sortings.

For some research questions, spike sortings will remain crucial, e.g., tuning analyses as presented in Chapter 5 or precise spike timing analyses (Grün et al., 2002; Riehle et al., 1997; Stella et al., 2019). Interestingly, for some scientific questions and analysis methods, the identity of single neurons was demonstrated to have no or little impact, e.g., Trautmann et al. (2019).

CAN WE RELY ON ANATOMICAL DATA FOR BIOLOGICALLY CONSTRAINED NEURAL NETWORKS? Biologically constrained networks rely on the experimental data that are used to constrain parameters. However, with the quickly evolving techniques, also the quality of available data evolves. Models, such as the Potjans-Diesmann microcircuit (Potjans et al., 2014b) (or e.g. Billeh et al. (2020)) need to allow for an update of the constraining data. One point of consideration is the following: Obtaining tracing data from primates (e.g. Markov et al. (2014) and Wang et al. (2022b)) requires sacrificing the animals, which is difficult under ethical consideration. In consequence, the variability within a small cohort might be large and raise the uncertainty on how representative certain data is. It is thus important that existing data can be pooled across experiments in large databases (Bakker et al., 2012; Kötter, 2004).

In Chapter 7, we encountered that an update in connectivity parameters from the original microcircuit model to the isolated V1 circuit from Schmidt et al. (2018b) indeed had an impact on the activity dynamics of a spiking neuronal network.

CAN LINEAR THEORIES CAPTURE RELEVANT PHENOMENA IN SIMULATIONS OR EVEN BIOLOGICAL BRAINS? A large part of the theoretical, mathematical descriptions of neural networks approximate the system's response to be linear. As we have seen in Chapter 6 and Chapter 7, linear theories in computational neuroscience can provide a useful framework for understanding certain aspects of cortical networks. However, it is well known that the activity of neurons in the brain is highly nonlinear, and it is not clear how well linear models can capture these nonlinear effects.

One final thought before jumping into the outlook: Given complexities that arise in any research direction, at least within systems or computational neuroscience, it is inevitable that specialized bubbles of knowledge form, and exchange beyond these bubbles is hampered. However, by clearly communicating the uncertainties each of the disciplines might struggle with, understanding across disciplines might arise.

8.3 OUTLOOK

Neurosciences as a whole develop at an incredible pace. New techniques to record neural activity (Jun et al., 2017b) record more neurons simultaneously and reduce the subsampling issue. Spiking neural network simulations grow in size, reach full biologically realistic densities of neurons (Billeh et al., 2020; Potjans et al., 2014b; Schmidt et al., 2018b) and thereby eliminate doubts on scaling.

Spatially extended spiking neural networks that reach the volume below the Utah array ($4x4\text{mm}^2$) are in development (Senk et al., 2018a) and will soon allow for interesting comparisons between experimental recordings and simulations, especially for spatially extended phenomena like traveling waves (Denker et al., 2018b; Senk et al., 2018b).

BEYOND STATIONARY ACTIVITY The type of network model that was discussed in Chapter 7 commonly operates at a certain working point, which describes the model's stationary dynamics. It is characterized by the firing rates, mean, and standard deviation of the respective population's input to a neuron. Although these networks allow for the activity to fluctuate around this "mean activity state", and might even exhibit metastable activity (Schmidt et al., 2018b), these fluctuations are not to be confused with input-driven, functionally relevant changes in the firing rate patterns and rather resemble resting state activity (Dąbrowska et al., 2021).

Functionally active biological cortical networks have in recent years been shown to exhibit a low-dimensional structure (Gao et al., 2015, 2017) and that low-dimensional representations have functional relevance (Kaufman et al., 2014; Mante et al., 2013; Matsumoto et al., 2005; Mazor et al., 2005; Vyas et al., 2020).

Interestingly, the activity of artificial recurrent neural networks (RNNs), trained via back-propagation through time (BPTT) to perform tasks, lives on suitable low-dimensional structures (Sussillo et al., 2013). In particular, for motor control, remarkable success has been achieved by comparing trained RNNs and experimental recordings (Russo et al., 2018; Saxena et al., 2022; Vyas et al., 2020). As mentioned in Figure 1.4, we started analyses elucidating the nature of neural activity state space in the V4A dataset via Hidden Markov Models or dimensionality reduction methods (Williams et al., 2018; Yu et al., 2009), but unfortunately, after the rejection of artifacts (Section 4.6) the parallel neuron count is quite low for such analyses.

In line with Williamson et al. (2018), I would argue that one way of bringing together large-scale, biologically constrained network models with functional neuronal recordings, is through a comparison of the level of their low-dimensional representations.

Currently, one limitation is imposed by the computational cost (including energy expenses) and time of large-scale networks. This hinders effective training via suitable plasticity mechanisms, which would be required for a task-relevant structure to emerge. This limitation recently sparked reasonable interest in the development and testing of neuromorphic hardware for such purposes (Rhodes et al., 2018).

In the future, we hopefully gain a proper understanding of how to effectively model neural networks, including plasticity, that make ethically difficult in vivo investigations in behaving animals redundant, yet allow us to advance our understanding of arguably the most complex organ: niarb eht.

Part IV

APPENDIX

A

APPENDIX

A.1 SPIKE SORTING

In neuroscience, it is interesting to investigate the spiketrains emitted by single neurons and relate them to the behavior. Extracellularly recorded potentials, however, do not immediately give access to the spike times of a single neuron. In an optimal case, per electrode, the action potentials of up to 4-5 neurons can be recorded.

Spike sorting is the process of assigning the action potentials recorded on one electrode to one or more units, putative neurons. Thereby we distinguish between single unit activity (SUA) and multi unit activity (MUA). While the former is used to refer to clearly separated units (i.e., the waveforms assigned to that unit have a high waveform signal-to-noise ratio (SNR), see Paragraph A.1.4), the latter is often used as a container that contains all waveforms, which could not be clearly attributed to a single neuron.

The optimal way of achieving this sorting is still an active field of research (see e.g., Buccino et al. (2022)). In the times of single electrode recordings, it was common to sort the waveforms semi-manually. With the increasing number of electrodes recorded simultaneously, this semi-manual process became increasingly time-consuming, giving rise to the development of fully automatic sorters.

Parts of Vision-for-Action (V4A) data were sorted manually by Prof. Alexa Riehle based on threshold crossings extracted during the recording by the neural signal processor (NSP). Dr. Frederic Barthelemy and MSc. Shrabasti Jana sorted sessions by thresholding the data offline. Furthermore, I employed two automatic spike sorters to sort the data from the visual and parietal areas to improve the database for the upcoming analyses. In the following, I will explain the different approaches and mention advantages, disadvantages, and challenges.

A.1.1 *Automatic spike sorting by the NSP*

Blackrock supplies a software called Cerebus Central, with which each recorded channel can be monitored during the experiment.

Based on these signals, the experimenter can set a threshold to detect spikes based on visual inspection. Here, the trade-off is to set a threshold beyond the noise floor but not too far off to not miss any putative spikes. Alternatively, and this has not been used in the V4A experiment so far, the thresholds can be set to a certain multiplier Ξ times the root mean square (RMS) of the signal (c.f. Quiroga et al. (2004)).

If the online thresholded waveforms shall be used for subsequent spike sorting, the adjustment of these thresholds prior to each recording needs to be performed. This was the case for most, but not all, recordings with *Enya*.

In the NSP, neural signals (up to here band-pass filtered between 0.3 Hz-7500 Hz) are high-pass filtered (causally, `'filt'`) with a 4-th order Butterworth filter with cutoff frequency 250 Hz for spike extraction. The real-time computer detects all threshold crossings and stores in total 38 samples (thereof ten pre-threshold samples). Threshold crossings that lie within a 30 sample range after a previously detected threshold are excluded (dead-time/refractory period).

The NSP then performs a sorting on the threshold crossings, which we did not consider reliable, and saves the results in a `.nev`-file.

A.1.2 *Manual spike sorting by the experimenter*

In the V4A experiment, two different ways of manual spike sorting were employed. The difference lies in the extraction of the threshold crossings.

SPIKE SORTING BASED ON THE THRESHOLD CROSSINGS SET DURING THE EXPERIMENT Prof. Alexa Riehle loaded the `.nev`-file generated by the online thresholding of the NSP into the Plexon Offline Sorter and re-sorted the threshold crossings in a semi-automatic fashion. Commonly, this involved a projection of the waveforms in a 2-D or 3-D principle component analysis (PCA) space, clustering of the waveforms in that space using K-Means or Template Matching and final quality control of the resulting spike trains by looking at the inter-spike interval (ISI) distributions and auto-/cross-correlation plots. For more details on the spike sorting procedure, see the description for the previous experiment in Brochier et al. (2018).

Per channel, each unit is stored under an ID. Invalidated spikes during offline sorting are assigned to unit ID $= 255$. Spikes that are considered noise are sorted into unit ID $= 0$.

SPIKE SORTING USING THE RAW DATA The sorter loads the recorded signals (0.3 Hz-7500 Hz) into the Plexon Offline Sorter, high-pass filtered the signal with a (non-causal) 4-th order Butterworth filter with cutoff frequency 500 Hz, then set the threshold offline by inspecting the noise floor, and performed the sorting as explained above.

The sorting result is then stored in a `.plx`-file, but the unit IDs are chosen analogously to the `.nev`-file.

A.1.3 *Automatic spike sorting on the raw data*

The number of sessions that are manually sorted is limited and increasing this number is a time-consuming process in the V4A-project. Per session, the manual sorter would need to sort $96 + 128 = 224$ channels: Optimistically assuming that this takes about two minutes per channel, the sorter would spend 448 min $\sim$ 7.5 h. This quickly exceeds feasibility, thus automatic sorting alternatives are required. In addition to the time argument, algorithmic solution would be beneficial for reproducibility of the sorting result.

To increase the usable database, I assembled a pipeline via Snakemake (Köster et al., 2012) that uses SpikeInterface (Buccino et al., 2020) to run automatic spike sorters.

As the number of neurons for the arrays in primary motor cortex (M1)/dorsal premotor cortex (PMd) obtained from the manually sorted sessions seemed large enough, within the scope of the thesis, I restricted the pipeline to run only on the visual and parietal arrays.

Furthermore, as detailed in Chapter 4, the signal of multiple electrodes is highly correlated, which is likely caused by crosstalk. In Section 4.4 we proposed a way to exclude these channels before running spike extraction and spike sorting. After a visual inspection of the scatter plot between the maximal correlation coefficient and the synchrofact percentage, channel exclusion thresholds on these two quantities were set manually, and hence electrodes were excluded before spike sorting.

The overall strategy for the sorting and the subsequent analysis was the following: Instead of optimizing the result for the spike sorting (a blind source separation problem (Buccino et al., 2022) which is a difficult problem due to the lack of a ground truth), we wanted to devise a sorting and analysis pipeline to show the robustness of a neuroscientific result across spike sorters.

For the scope of the thesis, we restricted this pipeline to two automatic spike sorters that were simple to set up on the local cluster and did not require GPU access: tridesclous (Garcia et al., 2015) and Mountainsort4 (Chung et al., 2017).

RUNNING SPIKEINTERFACE The practical steps to run an automatic sorting in SpikeInterface are quickly described here: SpikeInterface works with a *lazy* procedure, that mean that the steps that shall be executed are first defined and only executed if necessary. This is beneficial in the context of spike sorting, because potentially large amounts of data have to be processed at once, taking considerable amounts of time.

SpikeInterface supplies a routine to load data from Blackrock sourcefiles, which allow load raw data from the `.ns6`-files. After loading all channels, only those that survived the artifact removal are retained. These signals are then spectrally band-pass filtered between 250 Hz and 7500 Hz.

SpikeInterface allows the treatment of various recording devices, among other things high-density probes for which the probe geometry is crucial to know about the distances between probes and thus requires the defintion of a probefile. I defined a generic probefile specifying a 128-channel Utah array and filled the retained recording channels into that probe disregarding the actual positions. Generally, the distances between electrodes in the Utah array, with the distance between neighboring electrodes being $d = 0.4\,\mathrm{mm}$, are far enough apart to not record from the same neuron, justifying that simplifying approach.

Finally, the sorters are run with the parameters given in Table A.1 and Table A.2 and the sorting output is saved into separate destinations. This output can be loaded, post-processed (e.g. annotated with quality metrics) and saved in a format that is readable via `neo`, here I chose the `phy`-format.

In the chosen setup, the sorters in SpikeInterface treat the signals as if they stem from a high-density probe, assuming that the signal appearing on one electrode could also be observed on another electrode. Both tridesclous and Mountainsort4 define a template waveform per unit that is defined. This template waveform has a corresponding amplitude on each electrode, and this amplitude is maximal for the actual recording electrode, the extremum channel.

In a last step to integrate the new sortings into the preprocessed `.nix`-files, I load the the `phy`-data per sorter into `neo` and append them with the appropriate annotations to the V4A-data. Before using these automatically sorted units in the analysis I require a few quality metrics to be met. These are described in the following.

parameter	value
chunk_duration	1 s
chunk_memory	None
chunk_size	None
common_ref_removal	False
detect_sign	-1
detect_threshold	5
freq_max	7500 Hz
freq_min	250 Hz
n_jobs	1
nested_params	None
progress_bar	True
total_memory	None

Table A.1: Parameters Tridesclous.

A.1.4 *Post-processing quality metrics*

Spike sorting is a hard problem as it lacks a ground truth and faces challenges inherent to the data: For example, it might occur that

parameter	value
adjacency_radius	-1
clip_size	40
detect_interval	10
detect_sign	-1
filter	True
freq_max	7500 Hz
freq_min	250 Hz
num_workers	1
tempdir	None
whiten	True

Table A.2: Parameters Mountainsort4. The clip size parameter was previously determined by Sridhar (2020). The adjacency radius set at -1 was set as default and used. It allow spikes to be detectable on all channels. We observed in complexity distributions that this setting effectively remove any synchrofacts, including chance synchrony.

during a long recording session, the movement of the monkey leads to a slight shift of the neural tissue with respect to the electrode, such that at the beginning of the session a neuron clearly detectable, but vanishes later in the session. Or, multiple nearby neurons have very similar waveform shapes, such that they are assigned to the same unit. Furthermore, the extraction via a fixed threshold can lead to missing spikes, if due to counteracting signal fluctuations the threshold is not crossed.

Quality metrics allow an assessment of these errors and were applied with the parameters listed in Table A.3 in a post-processing step to choose units for subsequent analysis. The choice of parameters was inspired by a tutorial by the Allen Institute for Brain Science (2022).

metric	requirement
Firing rate	> 1 Hz
Waveform SNR	> 2.5
Presence ratio	> 0.9
Amplitude cutoff	< 0.1
ISI violations	< 0.5

Table A.3: Quality metrics required per spiketrain.

In the following, each parameter will be briefly explained.

FIRING RATE The firing rate is a quantity that describes the number of spikes in a given duration. To relate the activity of a single unit to the behavior as in Chapter 5, a certain amount of spikes are necessary. Effects of drift, that would lead to a decreased firing rate and require a more local-in-time measure, are neglected as recording with chronically implanted Utah arrays are assumed to be rather stable.

WAVEFORM SNR The waveform SNR is defined to quantify the reliability or consistency of the waveforms that have been assigned to a unit.

In contrast to the waveform SNR, the electrode SNR evaluates the actual recording electrode by relating the signal (e.g. peak-to-peak amplitude voltage) to the noise level (e.g. standard deviation of the recorded voltage). Here, the impedance of an electrode determines its sensitivity: The higher the impedance, the larger the needed voltage to drive a current through that electrode and vice versa.

Throughout this thesis, the following definition (Hatsopoulos et al., 2007b; Kelly et al., 2007; Nordhausen et al., 1996; Suner et al., 2005) was used:

$$\mathrm{SNR}_{\mathrm{waveform}} = \frac{\max\left(\overline{W}\right) - \min\left(\overline{W}\right)}{2 \times \overline{\mathrm{std}(W)}} \quad , \tag{A.1}$$

where the bar denotes the mean and W is a matrix containing all the waveforms. Each row of W contains a waveform

$$W = \begin{bmatrix} w^1 \\ w^2 \\ \vdots \\ w^K \end{bmatrix} \tag{A.2}$$

$$= \begin{bmatrix} v^1(\tau_1), v^1(\tau_2) \cdots v^1(\tau_S) \\ v^2(\tau_1), v^2(\tau_2) \cdots v^2(\tau_S) \\ \vdots \\ v^3(\tau_1), v^3(\tau_2) \cdots v^3(\tau_S) \end{bmatrix} \tag{A.3}$$

with $v^i(\tau_j)$ being the voltage sample the i-th threshold crossing ($i \in 1, \ldots, K$) on the j-th sample ($j \in 1, \ldots, S$, with S the number of samples per waveform) at time τ_j relative to the threshold crossing. $\mathrm{std}(W)$ is the column-wise standard deviation (per τ_j) and $\overline{\mathrm{std}(W)}$ its mean.

A weaker electrode SNR is likely to lead to a weaker waveform SNR. We aimed to focus the analysis on well-defined, stable units and wanted to reject eventual common noise artifacts (see Chapter 4). Therefore, we chose a rather strict threshold.

PRESENCE RATIO For the calculation of the presence ratio, the whole duration is split into 100 equally long epochs and the percentage of epochs containing a spike is evaluated. In principle this measure could detect units that drift out of the recording. In our dataset, it could reject units that arose due to the common noise artifacts (see Chapter 4) that drifts over time. The drawback is, that highly selective spike responses might be rejected.

AMPLITUDE CUTOFF The amplitude cutoff evaluates how strongly the distribution of spike amplitudes is truncated by the chosen threshold. If a large part of the distribution is cut off, it could mean that many spikes just fell below the threshold and the detected spike train gives incomplete information about the actual neurons firing.

According to Allen Institute for Brain Science, 2022, an amplitude cutoff of 0.1 would indicate that approximately 10 % of spikes are missing from this unit.

ISI VIOLATIONS As discussed in Section 1.1 neurons have a refractory period after emitting an action potential, that prevents further spiking during approximately 1.5 ms. If the ISI distribution has entries that are $< 1.5\,\mathrm{ms}$, this refractory period is violated and it is likely that the violating spike originates from a different neuron.

The ISI violation metric Hill et al., 2011 measures the firing rate of the contaminating neuron relative to the "true" neuron. A value of 0.5 thus indicates the contaminating spikes occur at half the rate of the "true" neuron.

A.2 VISION-FOR-ACTION - ARTIFACTS

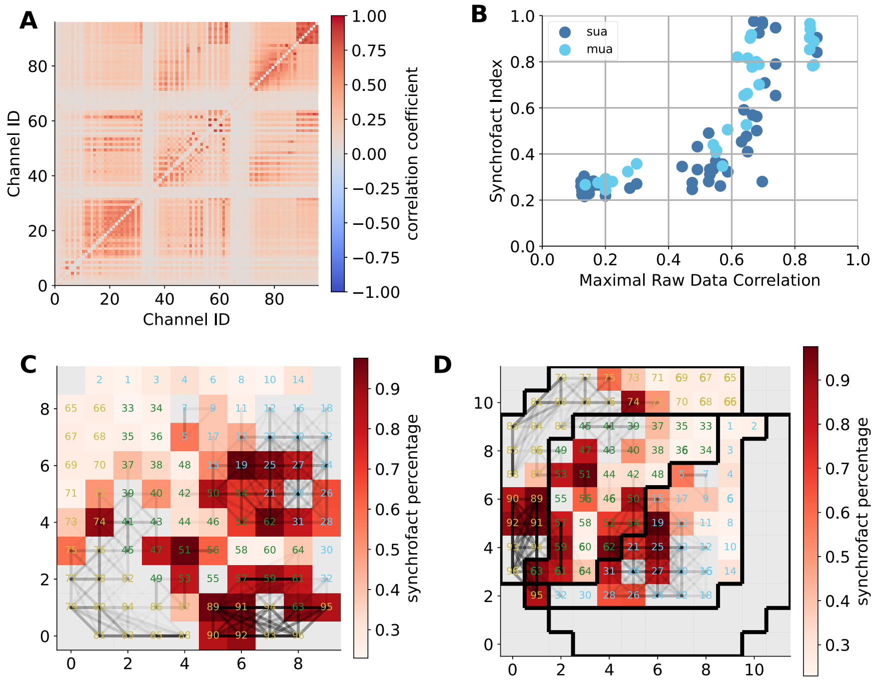

Figure A.1: Panel illustrating features of the artifact called crosstalk. The data shown in this figure stem from the motor array recorded in session `y180306-land-001`. Figure organization is the same as in Figure 4.4.

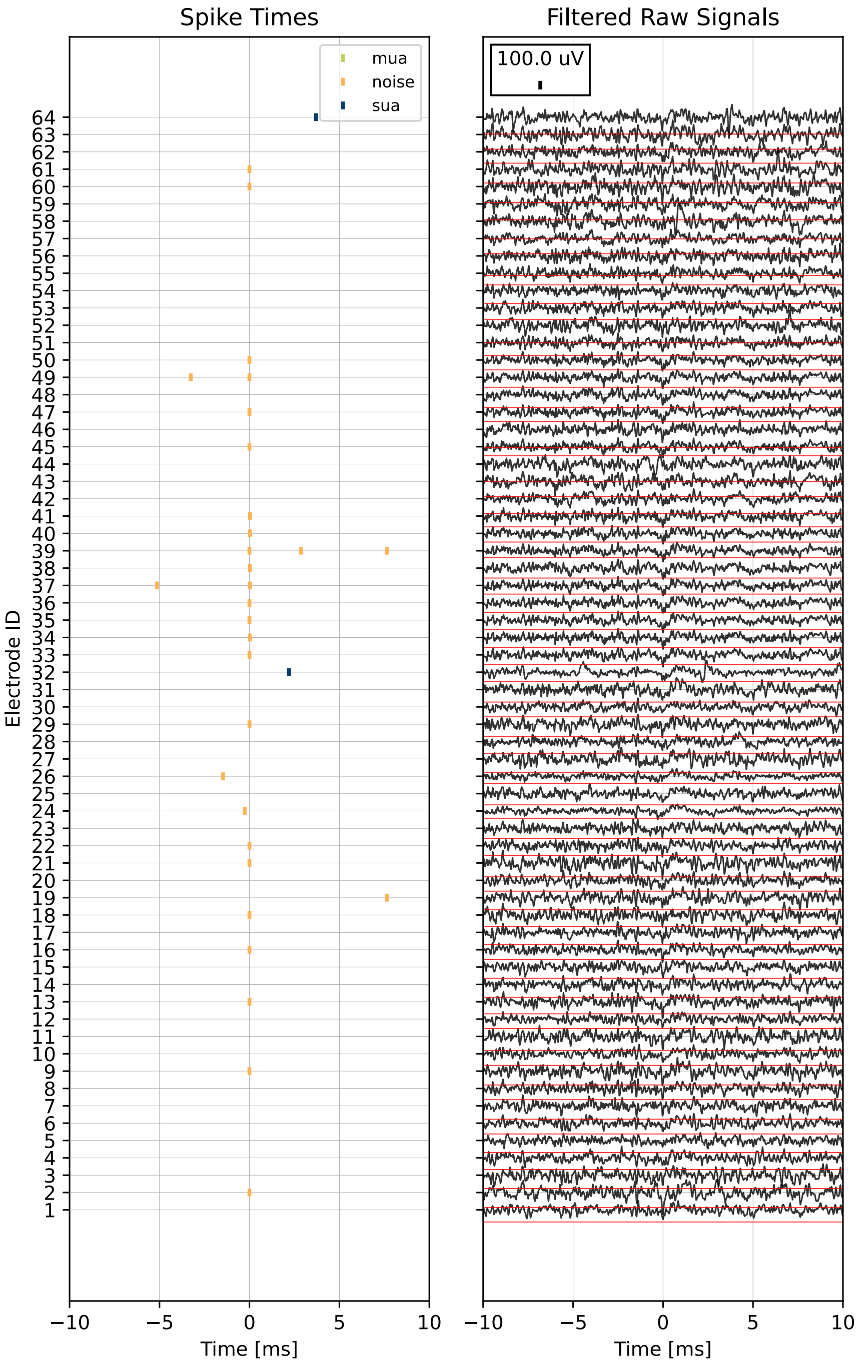

Figure A.2: Spike times and filtered raw signals showing a common noise signature called short blip. Both panels are aligned to $t = 516.0403\,\mathrm{s}$ and show data from the visual-parietal arrays in `y180306-land-001`. The figure shows the same details as Figure 4.5

A.3 VISION-FOR-ACTION - SINGLE UNIT ACTIVITY

A.3.1 *Distribution of classic preferred directions (PDs) at optimal time lag (OTL) exhibits bimodality as well*

The distribution of OTL in Figure A.3 reveals a skew towards lags, which indicates that the neural activity precedes the hand movement direction. We note that the mean lag of $\sim -96\,\text{ms}$ for Enya is larger than the lag for Jazz $\sim -23\,\text{ms}$. Possibly linked to that are overall faster reaction times (data not shown) and movement velocities in Jazz (compare e.g.Figure 5.6 and Figure 5.7).

The distribution of PDs at these OTLs Figure A.3 reproduces the bimodality that has been observed in Figure 5.12.

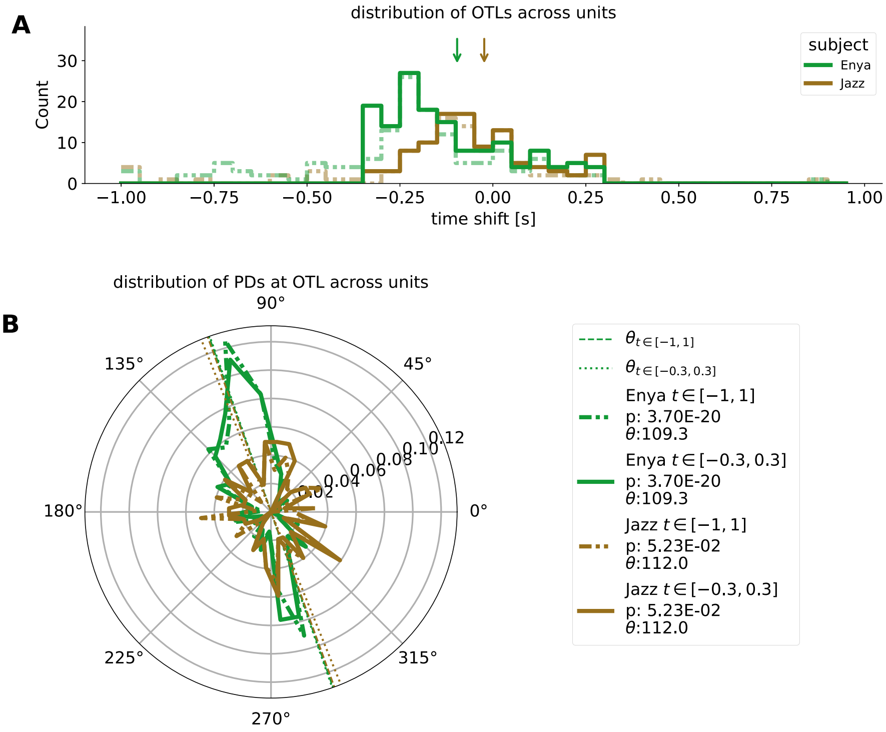

Figure A.3: Summary of directional tuning OTLs and PDs - M1/PMd. Panel **A** shows the distribution of OTL. The solid line shows a histogram of OTLs within $\tau \in [-300, 300[\,\text{ms}$. The arrows show the mean of these distributions. For the histogram in dashed this range is extended $\tau \in [-1, 1[\,\text{s}$. **B** The polar distribution the PDs at OTL across all units in M1 for both monkeys. The dashed lines show the main axis of skew of the bimodality and corresponding p-value of the Rayleigh r test for bimodality is reported in the legend.

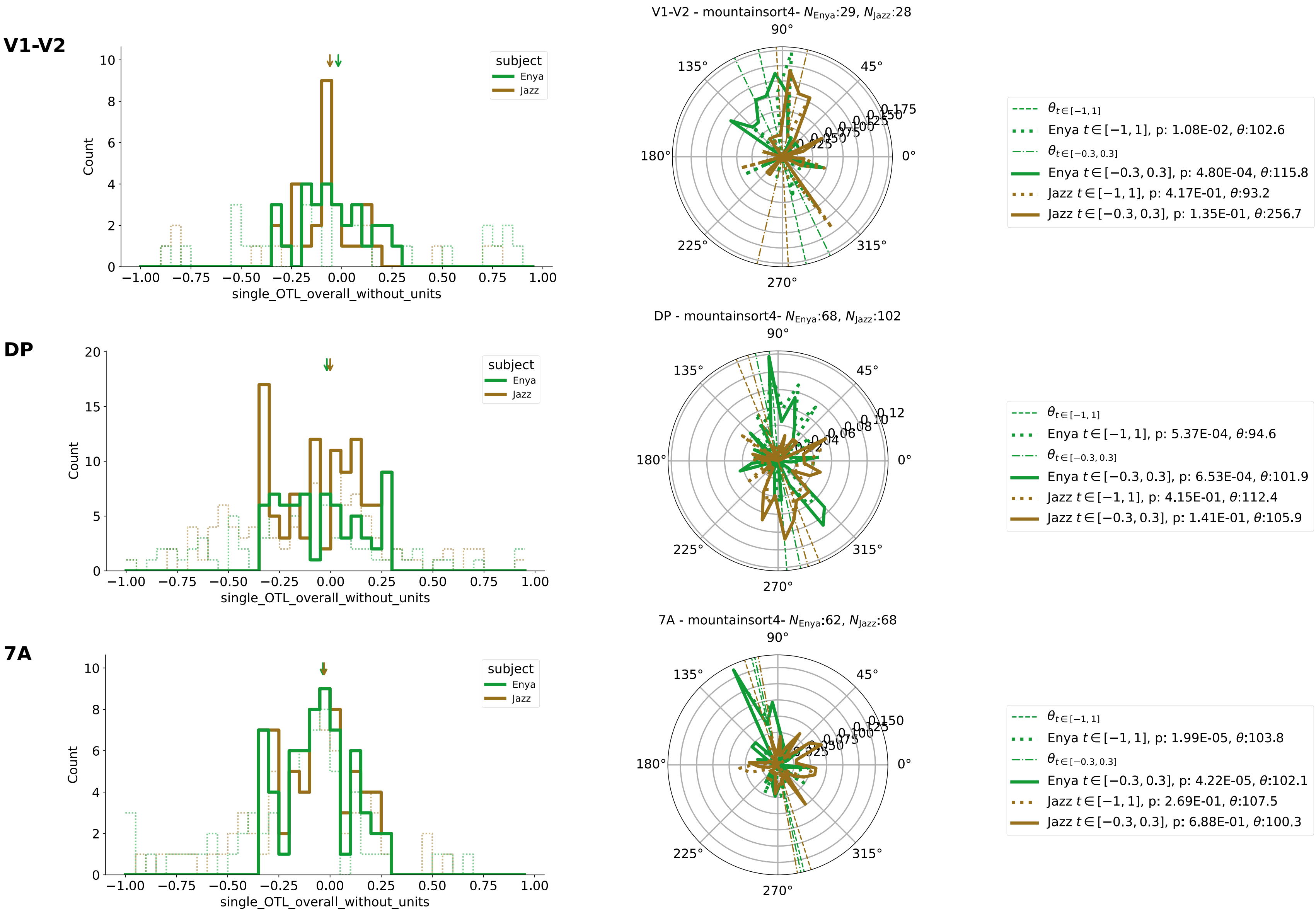

Figure A.4: (Caption continues on next page.)

Figure A.4: (Continued caption.) Summary of directional tuning OTLs and PDs - visual and parietal areas. For an explanation of the figure elements refer to Figure A.3.

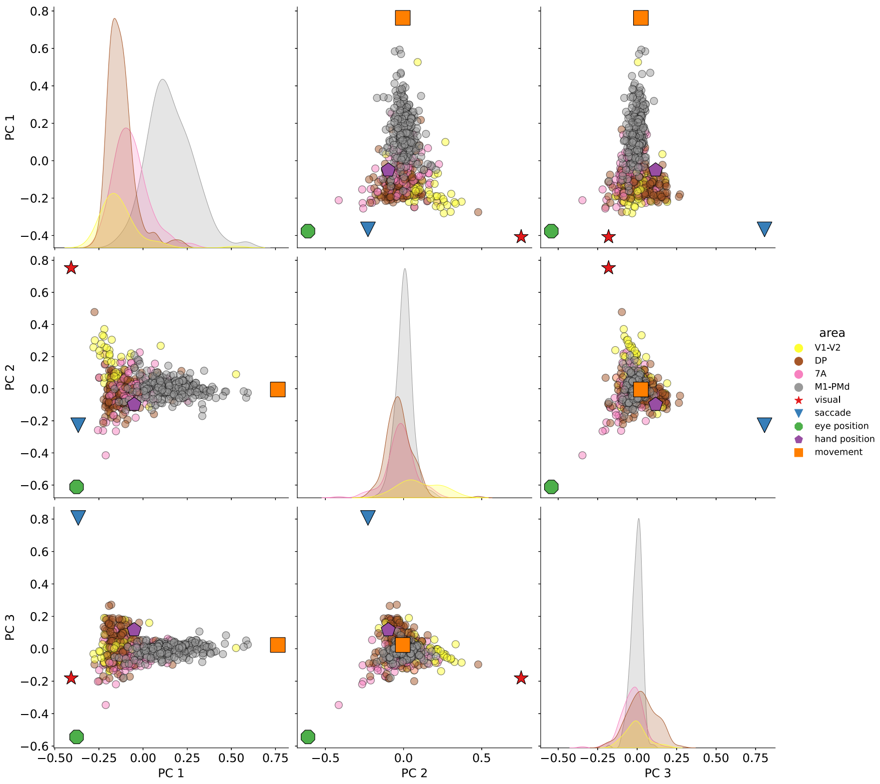

Figure A.5: PCA of w-values

A.3.2 *Neural fingerprints*

A.3.3 *Example neurons*

Here, we complement Section 5.4.5 and show a few figures, that demonstrate that the generalized linear model (GLM) with many regressors indeed captures the relevant features of the neural response.

A.3.3.1 *Visual*

The example unit from secondary visual cortex (V2) introduced in the main text exhibits a receptive field (RF) and is therefore expected to be activated by 1. a target appearing in the RF and 2. the hand traversing the RF. Another possible scenario is 3. a saccade that brings a visual stimulus into the RF. We did not find evidence for 3. scenario until the write-up of this thesis.

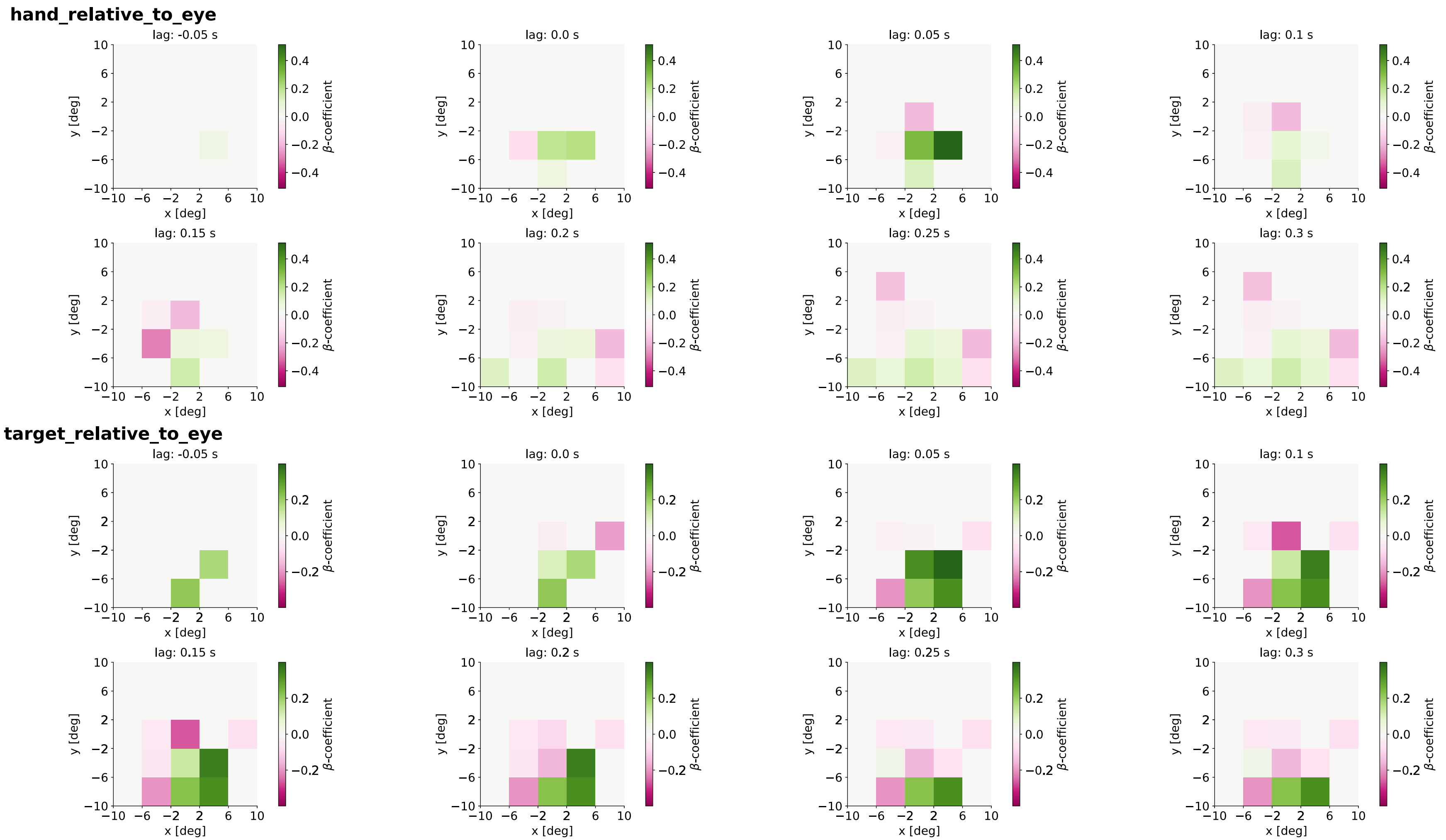

Figure A.6: (Caption continues on next page.)

Figure A.6: (Continued caption.) Example: primary visual cortex (V1)/V2 unit with RF - β-coefficients of visual regressor block. Plot shows the β-coefficients of the fitted GLM for all regressors included in the visual regressor block. As explained in Section 5.2.2.6 these are dummy variables for the possible visual stimuli for regions in the visual field.

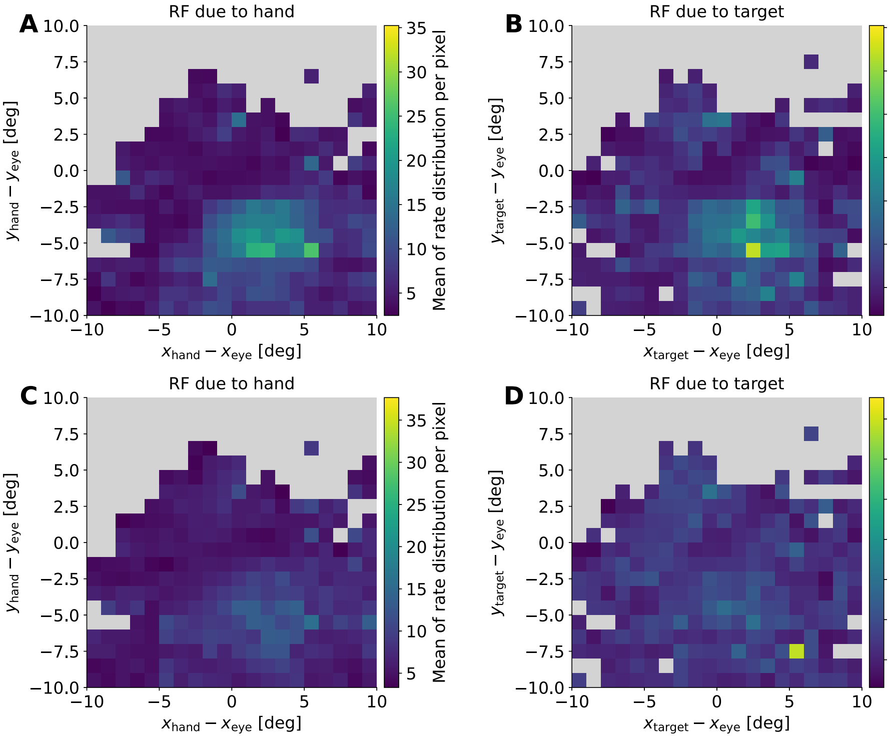

Figure A.7: Example: V1/V2 unit with RF - Complete GLM captures RF response. **A** and **B** show the complete GLM fit. Notice the resemblance with Figure 5.14. In **C** and **D** the visual regressor block was not included in the fit and consequently the RF structure was not captured by the model.

A.3.3.2 *Saccade*

A.3.3.3 *Eye position*

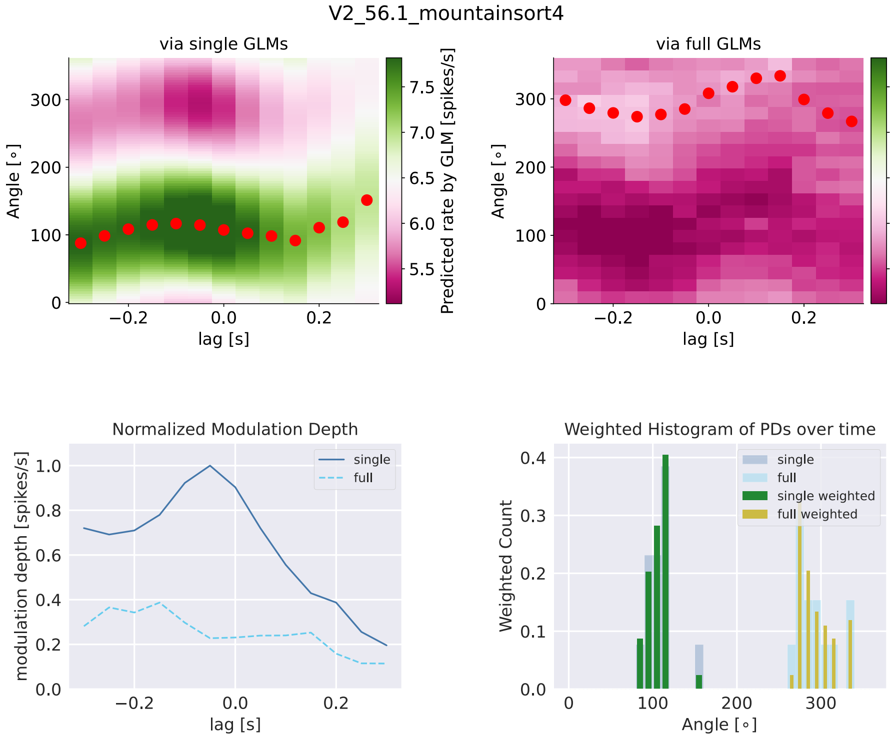

Figure A.8: Example: V1/V2 unit with RF - Direction tuning as predicted by simple and complete GLMs. Upper left panel shows the directional tuning extracted via the simple GLM ("single" regressor) while the upper right panel shows the prediction obtained from the complete GLM for which all regressors except for the movement-related ones were integrated out (see Paragraph 5.2.2.6). Lower left panel shows the normalized modulation depth in both scenarios and lower right panel show the weighted histogram of PDs.

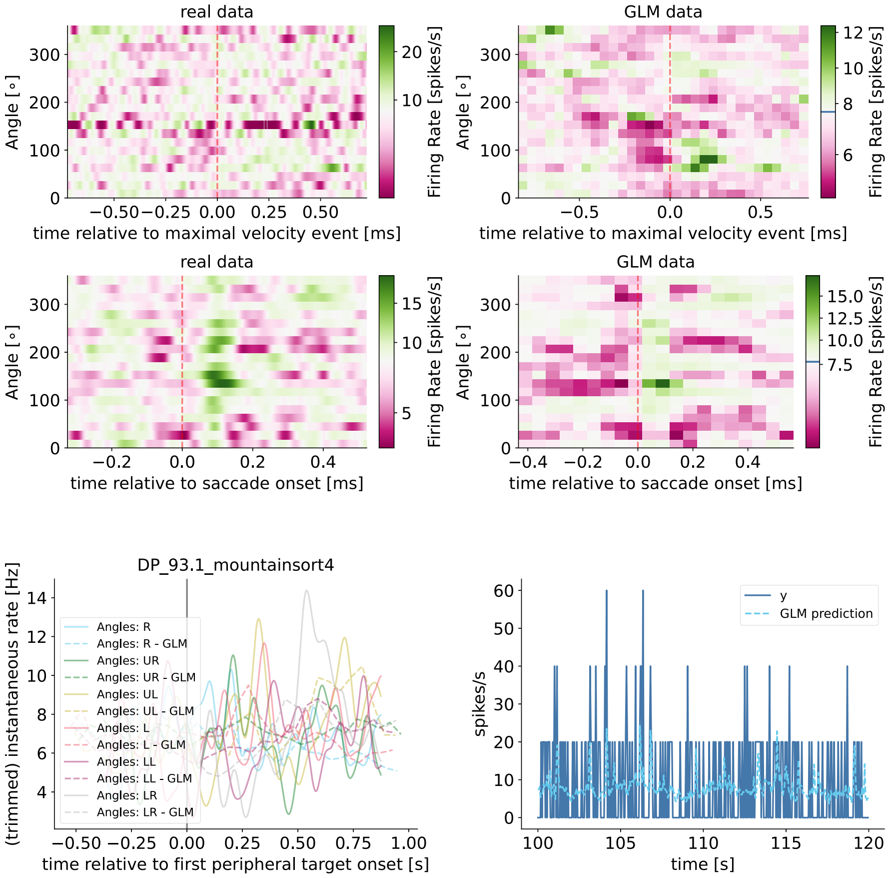

Figure A.9: Example: dorsal prelunate (DP) unit with saccade response - Comparison of peri-stimulus time histograms (PSTHs) in real data and GLM prediction.

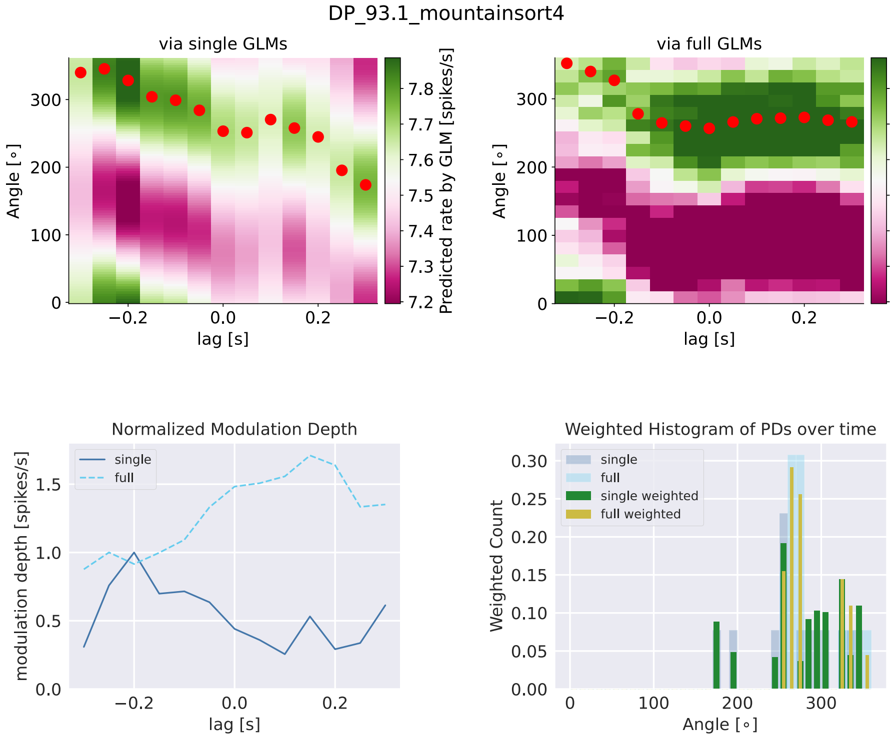

Figure A.10: Example: DP unit with saccade response - Direction tuning as predicted by simple and complete GLMs. Same figure content as Figure A.8.

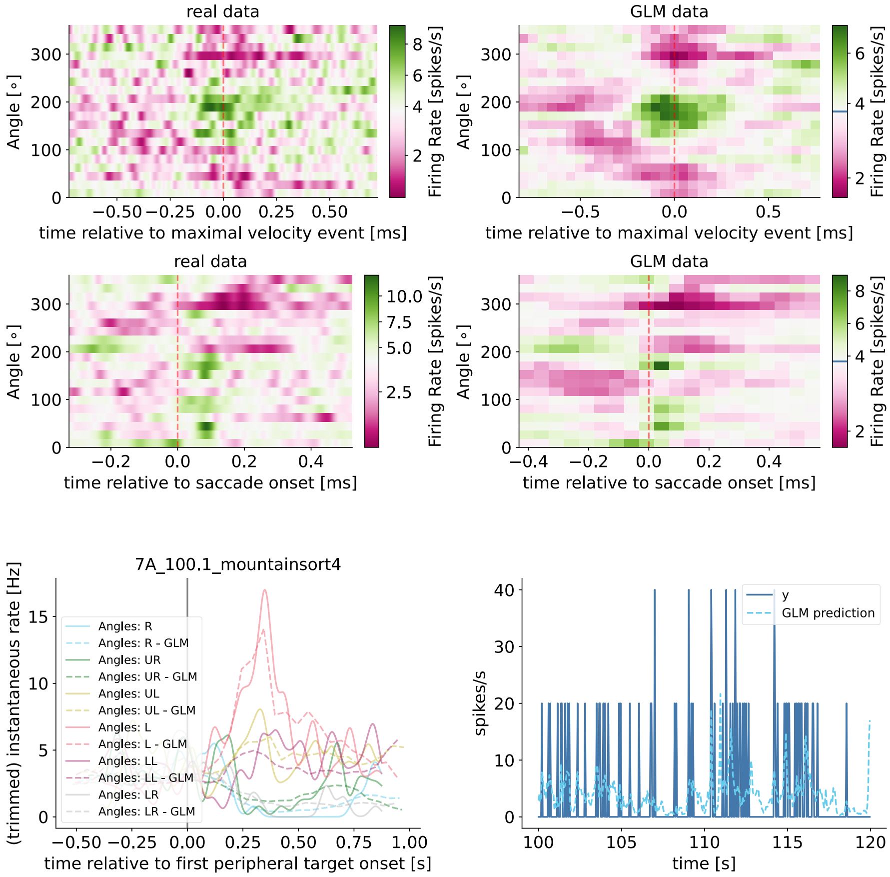

Figure A.11: Example: area 7a (7a) unit with eye position gain modulation - Comparison of PSTHs in real data and GLM prediction.

A.4 NEURONAL NETWORK MEAN-FIELD TOOLBOX (NNMT)

The content of this section has been published in Layer et al. (2022b).

Analytic theories have clearly helped to our knowledge of neural networks, and they provide a multitude of effective and efficient approaches for network model research. When comparing analytical theory predictions to simulations, experimental data, or alternative theories, a numerical implementation suitable to multiple network models is required, depending on the research objective. Such implementation is sometimes difficult and requires a significant investment of time and effort. Typically, such technologies are built as needed, and their reuse is not planned systematically and is limited to a specific lab. Not only are the neuroscientific community's efforts and resources duplicated, but many scientists are discouraged from taking full use of such methodologies, even if they may offer up new possibilities for researching their research issues.

We created the Python toolbox NNMT (Layer et al., 2021), short for Neuronal Network Mean-field Toolbox, to make analytical tools for neuronal network model analysis available to a larger part of the neuroscientific community and to create a platform for collecting well-tested and validated implementations of such tools. NNMT is not a simulation tool; it is a set of numerically computed mean-field equations that directly connect the parameters of a microscopic network model to the statistics of its dynamics. NNMT was created to accommodate the wide range of mean-field theories, and the primary aspects we are looking for are flexibility, extensibility, and ease of use. It also includes a thorough test suite to check the correctness of the implementations, as well as rich user documentation. NNMT's current version primarily includes tools for researching networks of leaky integrate-and-fire neurons, as well as techniques for studying binary neurons and neural field models. The toolkit is open source and freely accessible on GitHub[1].

DESIGN CONSIDERATIONS What are the requirements for a set of analytical approaches for neural network model analysis? To begin, it should be adaptable and modular enough to handle a broad variety of analytical approaches while avoiding code duplication and a convoluted interdependency of package components. It should simplify and clarify the application of the collected methods to various network models. It should facilitate the usage of the tools by beginners while providing specialists with rapid access to all parameters and settings. Finally, methods must be thoroughly tested and meticulously recorded.

These are the main considerations that guided the development of NNMT. Figure A.12**A**,**B** illustrate how the toolbox can be used in to

---

[1] https://github.com/INM-6/nnmt

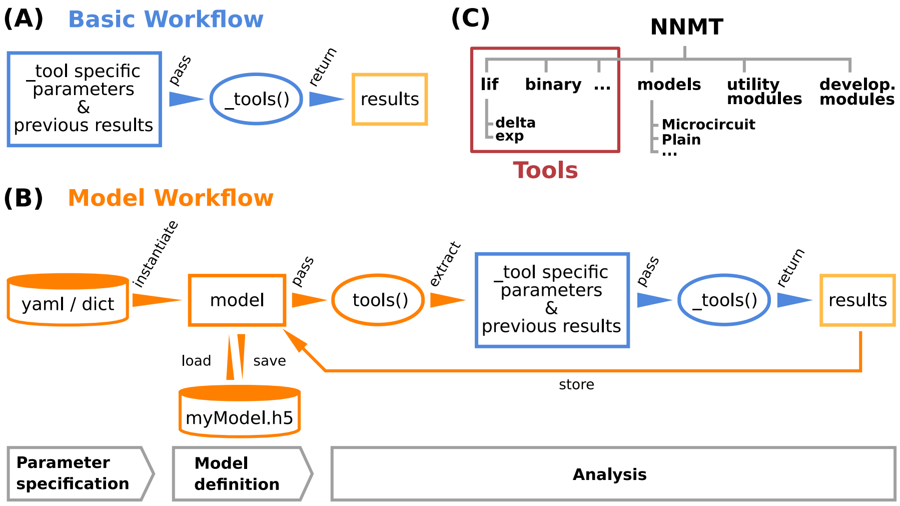

Figure A.12: Structure and workflows of the Neuronal Network Mean-field Toolbox (NNMT). **(A)** Basic workflow: individual mean-field based analysis methods are implemented as functions, called `_tools()`, that can be used directly by explicitly passing the required arguments. **(B)** Model workflow: to facilitate the handling of parameters and results, they can be stored in a model class instance, which can be passed to a `tool()`, which wraps the basic workflow of the respective `_tool()`. **(C)** Structure of the Python package. In addition to the tool collection (red frame), containing the `tools()` and the `_tools()`, and predefined model classes, the package provides utility functions for handling parameter files and unit conversions, as well as software aiding the implementation of new methods.

two different workflows, depending on the preferences and goals of the user. In the *basic workflow* the individual method implementations called *tools* are directly accessed, whereas the *model workflow* provides additional functionality for the handling of parameters and results.

Details on the structure of the toolbox can be found in the original paper (Layer et al., 2021).

COMPARISON TO OTHER TOOLS There are various approaches and corresponding tools that can help to gain a better understanding of a neuronal network model. There are numerous simulators that numerically solve the dynamical equations for concrete realizations of a network model and all its stochastic components, often focusing either on the resolution of single-neurons, for example NEST (Gewaltig et al., 2007), Brian (Stimberg et al., 2019), or Neuron (Hines et al., 2001), or on the population level, for example TheVirtualBrain (Sanz Leon et al., 2013). Similarly, general-purpose dynamical system software like XPPAUT (Ermentrout, 2002) can be used. Simulation tools, like DynaSim (Sherfey et al., 2018), come with enhanced functionality for simplifying batch analysis and parameter explorations. All these tools yield time-series of activity, and some of them even provide the methods for analyzing the generated data. However, simulations only indirectly link a model's parameters with its activity: to gain an understanding of how a model's parameters influence the statistics of their activity, it is necessary to run many simulations with different parameters and analyze the generated data subsequently.

Other approaches provide a more direct insight into a model's behavior on an abstract level: TheVirtualBrain and the Brain Dynamics Toolbox (Heitmann et al., 2018), for example, allow plotting a model's phase space vector field while the parameters can be changed interactively, allowing for exploration of low-dimensional systems defined by differential equations without the need for simulations. XPPAUT has an interface to AUTO-07P (Doedel et al., 1998), a software for performing numerical bifurcation and continuation analysis. It is worth noting that such tools are limited to models that are defined in terms of differential equations. Models specified in terms of update rules, such as binary neurons, need to be analyzed differently, for example using mean-field theory.

A third approach is to simplify the model analytically and simulate the simplified version. The simulation platform DiPDE[2] utilizes the population density approach to simulate the statistical evolution of a network model's dynamics. Schwalger et al. (2017) start from a microscopic model of generalized integrate-and-fire neurons and derive mesoscopic mean-field population equations, which reproduce the statistical and qualitative behavior of the homogeneous neuronal subpopulations. Similarly, Montbrió et al. (2015) derive a set of non-linear differential equations describing the dynamics of the rate and mean membrane potentials of a population of quadratic integrate-and-fire (QIF) neurons. The simulation platform PyRates (Gast et al., 2019) provides an implementation of this QIF mean-field model, and allows simulating them to obtain the temporal evolution of the population activity measures.

However, mean-field and related theories can go beyond such reduced dynamical equations: they can directly link model parameters to activity statistics, and they can even provide access to informative network properties that might not be accessible otherwise. The spectral bound (Rajan et al., 2006) of the effective connectivity matrix in linear response theory (Lindner et al., 2005a; Pernice et al., 2011; Trousdale et al., 2012) is an example of such a property. It is a measure for the stability of the linearized system and determines, for example, the occurrence of slow dynamics and long-range correlations (Dahmen et al., 2022). Another example is the sensitivity measure presented in Section 6.2.4.3, which directly links a network model's connectivity with the properties of its power spectrum. These measures are not accessible via simulations. They require analytical calculation.

---

[2] http://alleninstitute.github.io/dipde

Similarly, NNMT is not a simulator. NNMT is a collection of mean-field equation implementations that directly relate a model's parameters to the statistics of its dynamics or to other informative properties. It provides these implementations in a format that makes them applicable to as many network models as possible. This is not to say that NNMT does not involve numerical integration procedures; solving self-consistent equations, such as in the case of the firing rates calculations in Section 6.2.3 and Section 6.2.3.1, is a common task, and a collection of respective solvers is part of NNMT.

LIMITATIONS As a collection of analytical methods, NNMT comes with inherent limitations that apply to any toolbox for analytical methods: it is restricted to network, neuron, and synapse models, as well as observables, for which a mean-field theory exists, and the tools are based on analytical assumptions, simplifications, and approximations, restricting their valid parameter regimes and their explanatory power, which we expand upon in the next paragraphs.Analytical methods can provide good estimates of network model properties, but there are limitations that must be considered when interpreting results provided by NNMT: First of all, the employed numerical solvers introduce numerical inaccuracies, but they can be remedied by changing hyperparameters such as integration step sizes or iteration termination thresholds. More importantly, analytical methods almost always rely on approximations, which can only be justified if certain assumptions are fulfilled. Typical examples of such assumptions are fast or slow synapses, or a random connectivity. If such assumptions are not met, at least approximately, and the valid parameter regime of a tool is left, the corresponding method is not guaranteed to give reliable results. Hence, it is important to be aware of a tool's limitations, which we aim to document as thoroughly as possible.

An important assumption of mean-field theory is uncorrelated Poissonian inputs. As discussed in Section 6.2.3, asynchronous irregular activity is a robust feature of inhibition dominated networks, and mean-field theory is well-suited to describe the activity of such models. However, if a network model features highly correlated activity, or strong external input common to many neurons, approximating the input by uncorrelated noise no longer holds and mean-field estimates become unreliable.

In addition to the breakdown of such assumptions, some approaches, like linear response theory, rely on neglecting higher order terms. This restricts the tools' explanatory power, as they cannot predict higher order effects, such as the presence of higher harmonics in a network's power spectrum. Addressing these deficiencies necessitates using more elaborate analyses, and users should be aware of such limitations when interpreting the results.

Finally, a specific limitation of NNMT is that it currently only collects methods for LIF neurons. However, one of the aims of this paper is to encourage other scientists to contribute to the collection, and we outline how to do so in the following section.

A.5 VSTRIPES

A.5.1 *Delay distributions*

In Fourier space the delay term can be separated in the expression for the effective connectivity matrix, that governs the observed rate fluctuations

$$\boldsymbol{M}_{d,ij}(\omega) = \boldsymbol{M}_{ij}(\omega)e^{-i\omega d_{ij}} \quad .$$

The exponential term $e^{-i\omega d_{ij}}$ stands for the average over all possible values for the delay d_{ij}

$$e^{-i\omega d_{ij}} = \int_{-\infty}^{\infty} e^{-i\omega y} p(y) dy \quad ,$$

where $p(y)$ denotes the probability density function for the delays. Explicit expressions for delays distributed by truncated Gaussian, exponential, uniform or log-normal distributions are derived in the supplementary.

The microcircuit model by default is initialized with delays, which are drawn from a truncated Gaussian probability distribution. The truncation allows, physically and biologically necessary, only positive values for the delay.

The parameters for exponential and uniform distribution were chosen such that they match the mean of the (default) truncated Gaussian distribution, whereas the log-normal delay distribution was chosen to match its mean and standard deviation. The resulting probability density functions in time domain are shown in Figure 7.7.

The changes in the mean and the standard deviation of truncated Gaussian distribution with respect to the untruncated Gaussian are neglected for simplicity.

A.5.1.1 *Truncated Gaussian distribution*

One can define a truncated Gaussian on the interval $[a, b], a < b$ in terms of the mean μ_G and standard deviation σ_G of an un-truncated Gaussian by defining the variables

$$\alpha = \frac{a - \mu_G}{\sigma_G} \quad ,$$

$$\beta = \frac{b - \mu_G}{\sigma_G} \quad .$$

The mean of the truncated Gaussian are then be defined as

$$\mu_t = \mu_G - \sigma_G \cdot \frac{\phi(\beta) - \phi(\alpha)}{\Phi(\beta) - \Phi(\alpha)}$$

with

$$\phi(x) = \frac{1}{\sqrt{2\pi}} e^{-\frac{x^2}{2}}$$

and

$$\Phi(x) = \frac{1}{2}\left[1 + \operatorname{erf}\left(\frac{x}{\sqrt{2}}\right)\right]$$

where

$$\operatorname{erf}(x) = \frac{2}{\sqrt{\pi}} \int_0^x e^{-t^2} dt \quad .$$

A truncated Gaussian distribution can be obtained numerically by re-drawing those samples from a normal Gaussian, that fall outside the range of definition of the truncated Gaussian. The effective connectivity with truncated Gaussian delays can be written as

$$\mathbf{M}_{d,ij}(\omega) = \mathbf{M}_{ij}(\omega) \frac{1 - \Phi\left(\frac{-\mu_{ij} + i\omega\sigma_{ij}^2}{\sigma_{ij}}\right)}{1 - \Phi\left(\frac{-\mu_{ij}}{\sigma_{ij}}\right)} e^{-i\omega\mu_{ij}} e^{-\frac{\sigma_{ij}^2\omega^2}{2}} \quad .$$

A.5.1.2 *Exponential distribution*

The probability density function for the exponential distribution is given by

$$p(x; \lambda_e) = \lambda_e e^{-\lambda_e x} \quad ,$$

and hence

$$\begin{aligned}
e^{-i\omega d_{ij}} &= \int_{-\infty}^{\infty} e^{-i\omega y} p(y) dy \\
&= \int_0^{\infty} e^{-i\omega y} \lambda_e e^{-\lambda_e y} dy \\
&= \lambda_e \int_0^{\infty} e^{-(i\omega y + \lambda_e) y} dy \\
&= -\frac{\lambda_e}{i\omega + \lambda_e} \left[e^{-(i\omega y + \lambda_e) y} \right]_{y=0}^{y=\infty} \\
&= \frac{\lambda_e}{i\omega + \lambda_e} \text{if} \lambda_e, \omega \geq 0 \quad .
\end{aligned}$$

The mean and standard deviation of the exponential are both defined as $\mu_e = \sigma_e = \frac{1}{\lambda_e}$. As it is not possible to fit both parameters to those of a truncated Gaussian, just the mean was matched $\mu_t = \mu_e \rightarrow \lambda_e = \frac{1}{\mu_t}$. The effective connectivity with exponential delays can be written as

$$\mathbf{M}_{d,ij}(\omega) = \mathbf{M}_{ij}(\omega)\frac{\lambda}{i\omega + \lambda}$$

A.5.1.3 *Uniform distribution*

The probability density function for the uniform distribution is given by

$$p(x; a, b) = \frac{1}{b-a} \quad ,$$

and hence

$$\begin{aligned} e^{-i\omega d_{ij}} &= \int_{-\infty}^{\infty} e^{-i\omega y} p(y) dy \\ &= \int_{0}^{\infty} e^{-i\omega y} \frac{1}{b-a} dy \\ &= -\frac{1}{(b-a)i\omega} \left[e^{-(i\omega y + \lambda_e) y} \right]_{y=a}^{y=b} \\ &= \frac{1}{(b-a)i\omega} \left(e^{-i\omega a} - e^{-i\omega b} \right) \quad . \end{aligned}$$

The mean of a uniform distribution between a and b is given by its arithmetic mean $\mu_u = \frac{a+b}{2}$, while the standard deviation is defined as $\sigma_u = \frac{b-a}{\sqrt{12}}$. . As it is not possible to fit both parameters to those of a truncated Gaussian, just the mean was matched $\mu_t = \mu_u \rightarrow a + b = 2\mu_t$. To obtain the best correspondence between the two distributions, a was chosen to be 0, therefore $b = 2\mu_t$. The effective connectivity with uniform delays can be written as

$$\mathbf{M}_{d,ij}(\omega) = \mathbf{M}_{ij}(\omega)\frac{1}{(b-a)i\omega}\left(e^{-i\omega a} - e^{-i\omega b} \right) \quad .$$

Log-normal distribution

The probability density function for the log-normal distribution is given by

$$p(x; \mu_{log}, \sigma_{log}) = \frac{1}{x\sigma_{log}\sqrt{2\pi}} e^{-\frac{(\ln(x)-\mu)^2}{2\sigma^2}} \quad .$$

An analytic solution for the averaging could not be obtained, thus a numeric integration was performed by splitting the integral into its real and its imaginary part and integrating separately. Validity of the integration was checked by confirming the cumulative probability equaling one.

The mean of the log-normal distribution is defined by

$$\tilde{\mu}_{\log} = e^{\mu_{log}+\frac{\sigma^2_{\log}}{2}} \quad ,$$

where μ_{log}, and $\sigma^2_{\log}$are the mean and standard deviation of the normal distribution on the log-scale. The standard deviation is defined by

$$\tilde{\sigma}^2_{\log} = \left(e^{\sigma^2_{\log}} - 1\right) e^{2\mu_{log}+\sigma^2_{\log}} \quad .$$

The two parameters can be fitted such that the mean and standard deviation of log-normal distribution and truncated Gaussian are equal by solving equating $\tilde{\mu}_{\log} = \mu_t$and $\tilde{\sigma}^2_{\log} = \sigma_t^2$ which is satisfied if

$$\sigma^2_{\log} = 2\left(\ln \mu_t - \mu_{log}\right)$$

and inserting this into $\tilde{\mu}_{\log} = \mu_t$ yields

$$\mu_{log} = 2\ln\mu_t - \frac{\ln\left(\sigma_t^2 + e^{2\ln\mu_t}\right)}{2}$$

and thus leads to

$$\sigma^2_{\log} = \ln\left(\sigma_t^2 + e^{2\ln\mu_t}\right) - 2\ln\mu_t$$

$$\mathbf{M}_{d,ij}(\omega) = \int_0^\infty e^{-i\omega x}\mathbf{M}_{ij}(\omega)\frac{1}{x\sigma_{log}\sqrt{2\pi}}e^{-\frac{(\ln(x)-\mu)^2}{2\sigma^2}}dx$$

A.5.2 *Rule out simulation artifacts*

It has been shown that solving the differential equations for neuron dynamics on a discrete time grid can lead to an artificial synchronization of neuronal network activity.(Hansel et al., 1998; Morrison et al., 2007). In order to rule out this effect as cause for the observed high-frequency oscillations, control simulations have been run with all combinations of discrete or continous spiketimes and delays. Figure A.13 shows the corresponding raster plots on the left and the power spectra on the right. It is notable that the high-frequency peak in the

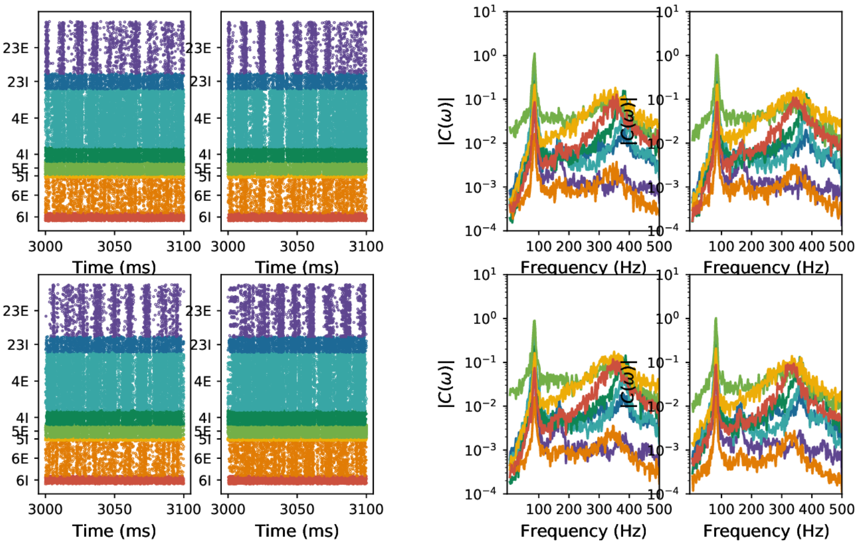

Figure A.13: Rule out simulation artifacts. (A) Continuous spiketimes, continuous delays (B) Continuous spiketimes, discrete delays, (C) discrete spiketimes, continuous delays and (D) discrete spiketimes, discrete delays

power spectrum remains visible for all simulations, suggesting that the artificial synchronization is not the causing factor. The exact realization of the spikes, however, differs as can be seen in the raster plots. Furthermore there is a slight shift of the high-frequency peak ($\sim$ 340 Hz) towards lower frequencies but larger power for the simulation with discrete spike times and continuous delays.

A.5.3 *Ad-hoc correction to align simulation and theory*

In Chapter 7, we argue that there are three main influences in our network simulations, that, if manipulated, can change the power spectrum of the population activity.

The connectivity was extracted from the experimental data to the best of the modeler's knowledge. And the mean firing rates (given the connectivity) match what is observed in experiments.

The delay distribution was shown above to have minor effects on the eigenvalue trajectories, assuming the mean delays are biologically correct.

For the transfer function, the situation is not as clear: Currently there are two ways of approximating the colored-noise transfer function up to the order $\mathcal{O}(k)$ with $k = \sqrt{\tau_s/\tau_m}$: in Schuecker et al., 2014 it is demonstrated that using effective integration boundaries in the expression of the white-noise case is equivalent to a Taylor expansion up to order $\mathcal{O}(k)$ of the full colored-noise expression. The meanfield prediction of the original Potjans-Diesmann model calculated using

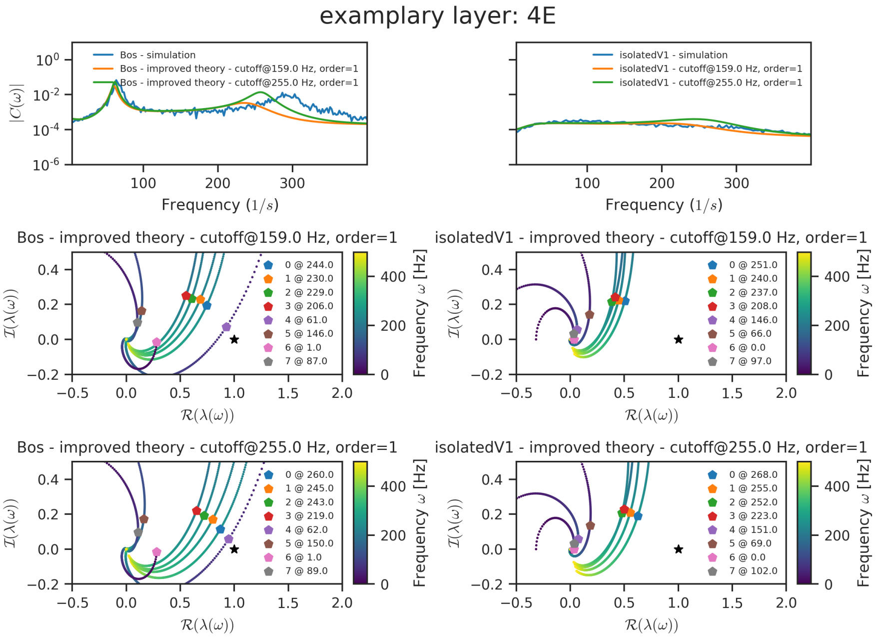

Figure A.14: Mean-field theory predict microcircuit lives in instable regime.

the shift of the integration boundary leads to one eigenvalues lying on top of the point of instability leading to exploding activity at the corresponding frequency. During the derivation of these equations, a few assumptions on the validity for high frequencies > 100 Hz are made (see 6.2.4.1). The systematic mismatch between simulations and theory mainly occurs for high frequencies and has the tendency, that the theory overestimates the activity for high frequencies.

As a consequence, we propose that an additional low-pass filter can be applied to the effective connectivity matrix, which leads to a shifting of the eigenvalues towards smaller real values and thus away from the instability and such that they pass it on the left. For a number of simulated circuit, such an ad-correction yields a better prediction of the resulting power spectra as the original theory (see FigureA.14).

The adapted effective connectivity matrix is then given by:

$$\widetilde{\boldsymbol{M}}_{\mathrm{d}}(\omega) = \tau_{\mathrm{m}} \boldsymbol{N}'_{\mathrm{cn,s}}(\omega) \cdot \boldsymbol{J} \odot \boldsymbol{K} \odot \boldsymbol{D}(\omega) \tag{A.4}$$

with a modified transfer function $\boldsymbol{N}'_{\mathrm{cn,s}}(\omega)$ that contains an additional low-pass filter with cutoff-frequency ω_c.

Figure A.14 shows a comparison of power spectra for the simulates Bos model and isolated V1 the prediction produced by the modified transfer functions with additional low-pass filter using two different cutoff-frequencies ω_c. It is visible that the power spectra peak for high-frequencies now has a similar magnitude as the peak from the simulations. and eigenvalue trajectories behaved as expected an effectively rotated away from the point of instability.

BIBLIOGRAPHY

Abeles, Moshe, Yifat Prut, Hagai Bergman, and Eilon Vaadia (1994). "Synchronization in Neuronal Transmission and Its Importance for Information Processing." In: *Temporal Coding in the Brain*. Ed. by G. Buzsaki et al. Berlin, Heidelberg: Springer-Verlag, pp. 39–50 (cit. on p. 8).

Abramowitz, Milton and Irene A. Stegun (1974). *Handbook of Mathematical Functions: with Formulas, Graphs, and Mathematical Tables*. New York: Dover Publications. DOI: 10.1119/1.15378. URL: https://doi.org/10.1119/1.15378 (cit. on p. 131).

Aflalo, Tyson N. and Michael S. A. Graziano (Feb. 2006). "Partial Tuning of Motor Cortex Neurons to Final Posture in a Free-Moving Paradigm." In: *Proceedings of the National Academy of Sciences* 103.8, pp. 2909–2914. ISSN: 0027-8424, 1091-6490. DOI: 10.1073/pnas.0511139103. (Visited on 11/04/2022) (cit. on p. 114).

Ahmadian, Yashar and Kenneth D Miller (2021). "What is the dynamical regime of cerebral cortex?" In: *Neuron* 109.21, pp. 3373–3391 (cit. on p. 126).

Allen Institute for Brain Science (2022). *Allen Software Development Kit*. (Visited on 02/10/2023) (cit. on pp. 176, 178).

Amirikian, Bagrat and Apostolos P Georgopulos (Jan. 2000). "Directional Tuning Profiles of Motor Cortical Cells." In: *Neuroscience Research* 36.1, pp. 73–79. ISSN: 01680102. DOI: 10.1016/S0168-0102(99)00112-1. (Visited on 03/04/2022) (cit. on pp. 66, 73).

Amit, D. J. and M. V. Tsodyks (1991). "Quantitative study of attractor neural network retrieving at low spike rates I: Substrate – spikes, rates and neuronal gain." In: *Network* 2, p. 259 (cit. on p. 125).

Amit, Daniel J. and Nicolas Brunel (1997a). "Dynamics of a recurrent network of spiking neurons before and following learning." In: *Netw. Comput. Neural Syst.* 8.4, pp. 373–404. DOI: 10.1088/0954-898x_8_4_003. URL: https://doi.org/10.1088/0954-898x_8_4_003 (cit. on p. 125).

– (Apr. 1997b). "Model of Global Spontaneous Activity and Local Structured Activity During Delay periods in the Cerebral Cortex." In: *Cereb. Cortex* 7, pp. 237–252. DOI: 10.1093/cercor/7.3.237. URL: https://doi.org/10.1093/cercor/7.3.237 (cit. on pp. 11, 121, 125, 127, 128).

Amunts, Katrin, Alois C. Knoll, Thomas Lippert, Cyriel M. A. Pennartz, Philippe Ryvlin, Alain Destexhe, Viktor K. Jirsa, Egidio D'Angelo, and Jan G. Bjaalie (July 2019). "The Human Brain Project—Synergy between Neuroscience, Computing, Informatics, and Brain-Inspired Technologies." In: *PLOS Biology* 17.7, e3000344. ISSN: 1545-7885. DOI:

10.1371/journal.pbio.3000344. (Visited on 04/05/2023) (cit. on p. 164).

Amunts, Katrin et al. (Mar. 2022). "Linking Brain Structure, Activity, and Cognitive Function through Computation." In: *eneuro* 9.2, ENEURO.0316–21.2022. ISSN: 2373-2822. DOI: 10.1523/ENEURO.0316-21.2022. (Visited on 12/27/2022) (cit. on p. 164).

Andersen, R. A., C. Asanuma, G. Essick, and R. M. Siegel (June 1990a). "Corticocortical Connections of Anatomically and Physiologically Defined Subdivisions within the Inferior Parietal Lobule." In: *The Journal of Comparative Neurology* 296.1, pp. 65–113. ISSN: 0021-9967, 1096-9861. DOI: 10.1002/cne.902960106. (Visited on 03/20/2022) (cit. on pp. 28, 29).

Andersen, Ra, Rm Bracewell, S Barash, Jw Gnadt, and L Fogassi (Apr. 1990b). "Eye Position Effects on Visual, Memory, and Saccade-Related Activity in Areas LIP and 7a of Macaque." In: *The Journal of Neuroscience* 10.4, pp. 1176–1196. ISSN: 0270-6474, 1529-2401. DOI: 10.1523/JNEUROSCI.10-04-01176.1990. (Visited on 08/05/2022) (cit. on p. 28).

Andersen, Richard A. (Dec. 1987). "Inferior Parietal Lobule Function in Spatial Perception and Visuomotor Integration." In: *Comprehensive Physiology*. Ed. by Ronald Terjung. First. Wiley, pp. 483–518. ISBN: 978-0-470-65071-4. DOI: 10.1002/cphy.cp010512. (Visited on 08/03/2022) (cit. on p. 28).

Andersen, Richard A., Tyson Aflalo, Luke Bashford, David Bjånes, and Spencer Kellis (Jan. 2022). "Exploring Cognition with Brain–Machine Interfaces." In: *Annual Review of Psychology* 73.1, pp. 131–158. ISSN: 0066-4308, 1545-2085. DOI: 10.1146/annurev-psych-030221-030214. (Visited on 08/03/2022) (cit. on p. 27).

Andersen, Richard A. and Christopher A. Buneo (Mar. 2002). "Intentional Maps in Posterior Parietal Cortex." In: *Annual Review of Neuroscience* 25.1, pp. 189–220. ISSN: 0147-006X, 1545-4126. DOI: 10.1146/annurev.neuro.25.112701.142922. (Visited on 08/03/2022) (cit. on pp. 27, 28).

Andersen, Richard A., Greg K. Essick, and Ralph M. Siegel (Oct. 1985). "Encoding of Spatial Location by Posterior Parietal Neurons." In: *Science* 230.4724, pp. 456–458. ISSN: 0036-8075, 1095-9203. DOI: 10.1126/science.4048942. (Visited on 08/05/2022) (cit. on pp. 28, 30).

Andersen, Richard A., Spencer Kellis, Christian Klaes, and Tyson Aflalo (Sept. 2014). "Toward More Versatile and Intuitive Cortical Brain–Machine Interfaces." In: *Current Biology* 24.18, R885–R897. ISSN: 09609822. DOI: 10.1016/j.cub.2014.07.068. (Visited on 08/14/2022) (cit. on p. 27).

Arcaro, M. J., M. A. Pinsk, X. Li, and S. Kastner (Feb. 2011). "Visuotopic Organization of Macaque Posterior Parietal Cortex: A Functional Magnetic Resonance Imaging Study." In: *Journal of Neuroscience* 31.6, pp. 2064–2078. ISSN: 0270-6474, 1529-2401. DOI: 10.1523/JNEUROSCI.3334-10.2011. (Visited on 03/20/2022) (cit. on p. 29).

Asanuma, C., R. A. Andersen, and W. M. Cowan (Nov. 1985). "The Thalamic Relations of the Caudal Inferior Parietal Lobule and the Lateral Prefrontal Cortex in Monkeys: Divergent Cortical Projections from Cell Clusters in the Medial Pulvinar Nucleus." In: *The Journal of Comparative Neurology* 241.3, pp. 357–381. ISSN: 0021-9967, 1096-9861. DOI: 10.1002/cne.902410309. (Visited on 12/27/2022) (cit. on p. 29).

Avila, Eric, Kaushik J Lakshminarasimhan, Gregory C DeAngelis, and Dora E Angelaki (Aug. 2019). "Visual and Vestibular Selectivity for Self-Motion in Macaque Posterior Parietal Area 7a." In: *Cerebral Cortex* 29.9, pp. 3932–3947. ISSN: 1047-3211, 1460-2199. DOI: 10.1093/cercor/bhy272. (Visited on 03/15/2022) (cit. on p. 28).

Bahill, A.Terry, Michael R. Clark, and Lawrence Stark (Jan. 1975). "The Main Sequence, a Tool for Studying Human Eye Movements." In: *Mathematical Biosciences* 24.3-4, pp. 191–204. ISSN: 00255564. DOI: 10.1016/0025-5564(75)90075-9. (Visited on 12/14/2022) (cit. on p. 24).

Baillière, J. B. (1839). "De La Maladie Sacrée." In: *Oeuvres Complètes d'Hippocrate: Traduction Nouvelle Avec Le Texte Grec en Regard*. Tome 6. Paris. (Visited on 12/09/2022) (cit. on p. 1).

Bakker, Rembrandt, Wachtler Thomas, and Markus Diesmann (2012). "CoCoMac 2.0 and the future of tract-tracing databases." In: *Front. Neuroinform.* 6, p. 30. DOI: 10.3389/fninf.2012.00030 (cit. on p. 166).

Barash, S., R. M. Bracewell, L. Fogassi, J. W. Gnadt, and R. A. Andersen (Sept. 1991). "Saccade-Related Activity in the Lateral Intraparietal Area. I. Temporal Properties; Comparison with Area 7a." In: *Journal of Neurophysiology* 66.3, pp. 1095–1108. ISSN: 0022-3077, 1522-1598. DOI: 10.1152/jn.1991.66.3.1095. (Visited on 07/26/2022) (cit. on p. 28).

Barthélemy, Frédéric V. (2023). In: *In Preparation* (cit. on p. 32).

Batschelet, Edward (1981). *Circular Statistics in Biology*. Mathematics in Biology. New York: Academic Press. ISBN: 0120810506 (cit. on p. 79).

Battaglia-Mayer, Alexandra (Feb. 2019). "A Brief History of the Encoding of Hand Position by the Cerebral Cortex: Implications for Motor Control and Cognition." In: *Cerebral Cortex* 29.2, pp. 716–731. ISSN: 1047-3211, 1460-2199. DOI: 10.1093/cercor/bhx354. (Visited on 08/16/2022) (cit. on pp. 27, 30).

Battaglia-Mayer, Alexandra, Philippe S. Archambault, and Roberto Caminiti (Jan. 2006). "The Cortical Network for Eye–Hand Coordination and Its Relevance to Understanding Motor Disorders of Parietal Patients." In: *Neuropsychologia* 44.13, pp. 2607–2620. ISSN: 00283932. DOI: 10.1016/j.neuropsychologia.2005.11.021. (Visited on 08/16/2022) (cit. on p. 27).

Battaglia-Mayer, Alexandra, Stefano Ferraina, Takashi Mitsuda, Barbara Marconi, Aldo Genovesio, Paolo Onorati, Francesco Lacquaniti, and Roberto Caminiti (Apr. 2000). "Early Coding of Reaching in the Parietooccipital Cortex." In: *Journal of Neurophysiology* 83.4, pp. 2374–2391. ISSN: 0022-3077, 1522-1598. DOI: `10.1152/jn.2000.83.4.2374`. (Visited on 08/16/2022) (cit. on p. 66).

Battaglia-Mayer, Alexandra, Massimo Mascaro, Emiliano Brunamonti, and Roberto Caminiti (May 2005). "The Over-representation of Contralateral Space in Parietal Cortex: A Positive Image of Directional Motor Components of Neglect?" In: *Cerebral Cortex* 15.5, pp. 514–525. ISSN: 1460-2199, 1047-3211. DOI: `10.1093/cercor/bhh151`. (Visited on 08/16/2022) (cit. on p. 28).

Battaglia-Mayer, Alexandra, Massimo Mascaro, and Roberto Caminiti (June 2007). "Temporal Evolution and Strength of Neural Activity in Parietal Cortex during Eye and Hand Movements." In: *Cerebral Cortex* 17.6, pp. 1350–1363. ISSN: 1460-2199, 1047-3211. DOI: `10.1093/cercor/bhl046`. (Visited on 08/16/2022) (cit. on pp. 29, 66).

Bédard, C. and A. Destexhe (2009). "Macroscopic models of local field potentials and the apparent 1/f noise in brain activity." In: *Biophys. J.* 96.7, pp. 2589–2603. DOI: `10.1016/j.bpj.2008.12.3951` (cit. on p. 145).

Bédard, Claude, Helmut Kröger, and Alain Destexhe (2004). "Modeling extracellular field potentials and the frequency-filtering properties of extracellular space." In: *Biophys. J.* 86.3, pp. 1829–1842. DOI: `10.1016/S0006-3495(04)74250-2` (cit. on p. 145).

Berens, Philipp (2009). "**CircStat** : A *MATLAB* Toolbox for Circular Statistics." In: *Journal of Statistical Software* 31.10. ISSN: 1548-7660. DOI: `10.18637/jss.v031.i10`. (Visited on 09/08/2022) (cit. on p. 80).

Billeh, Yazan N. et al. (May 2020). "Systematic Integration of Structural and Functional Data into Multi-scale Models of Mouse Primary Visual Cortex." In: *Neuron* 106.3, 388–403.e18. ISSN: 08966273. DOI: `10.1016/j.neuron.2020.01.040`. (Visited on 05/18/2020) (cit. on pp. 166, 167).

Bishop, Christopher M. (1992). *Pattern Recognition & Machine Learning*. Elsevier. ISBN: 978-0-12-058830-5. DOI: `10.1016/C2009-0-22409-3` (cit. on p. 71).

Borra, Elena, Marzio Gerbella, Stefano Rozzi, and Giuseppe Luppino (Apr. 2017). "The Macaque Lateral Grasping Network: A Neural Substrate for Generating Purposeful Hand Actions." In: *Neuroscience and Biobehavioral Reviews* 75, pp. 65–90. ISSN: 1873-7528. DOI: `10.1016/j.neubiorev.2017.01.017` (cit. on p. 28).

Bos, Hannah, Markus Diesmann, and Moritz Helias (Oct. 2016). "Identifying Anatomical Origins of Coexisting Oscillations in the Cortical Microcircuit." In: *PLOS Comput. Biol.* 12.10, e1005132. DOI: `10.1371/journal.pcbi.1005132`. URL: `http://doi.org/10.1371\%2Fjournal.pcbi.1005132` (cit. on pp. xx, xxii, 123, 124, 129, 130, 134–137, 145, 148, 149, 152, 156, 157).

Braitenberg, Valentin and Almut Schüz (1998). *Cortex: Statistics and Geometry of Neuronal Connectivity*. 2nd. Berlin: Springer-Verlag. ISBN: 3-540-63816-4. DOI: `10.1007/978-3-662-03733-1` (cit. on p. 125).

Breitenfeld, T., M. J. Jurasic, and D. Breitenfeld (Sept. 2014). "Hippocrates: The Forefather of Neurology." In: *Neurological Sciences* 35.9, pp. 1349–1352. ISSN: 1590-1874, 1590-3478. DOI: `10.1007/s10072-014-1869-3`. (Visited on 07/11/2022) (cit. on p. 1).

Bremmer, Pouget, and K. P. Hoffmann (Jan. 1998). "Eye Position Encoding in the Macaque Posterior Parietal Cortex." In: *European Journal of Neuroscience* 10.1, pp. 153–160. ISSN: 0953-816X, 1460-9568. DOI: `10.1046/j.1460-9568.1998.00010.x`. (Visited on 03/23/2022) (cit. on p. 28).

Brewer, Alyssa A., William A. Press, Nikos K. Logothetis, and Brian A. Wandell (Dec. 2002). "Visual Areas in Macaque Cortex Measured Using Functional Magnetic Resonance Imaging." In: *The Journal of Neuroscience* 22.23, pp. 10416–10426. ISSN: 0270-6474, 1529-2401. DOI: `10.1523/JNEUROSCI.22-23-10416.2002`. (Visited on 01/13/2023) (cit. on p. 21).

Brochier, Thomas, Lyuba Zehl, Yaoyao Hao, Margaux Duret, Julia Sprenger, Michael Denker, Sonja Grün, and Alexa Riehle (Apr. 2018). "Massively parallel recordings in macaque motor cortex during an instructed delayed reach-to-grasp task." In: *Sci. Data* 5, p. 180055. DOI: `10.1038/sdata.2018.55`. URL: `https://doi.org/10.1038/sdata.2018.55` (cit. on pp. 56, 164, 173).

Brodmann, Korbinian (1909). *Vergleichende Lokalisationslehre der Großhirnrinde in ihren Prinzipien dargestellt auf Grund des Zellenbaues*. Leipzig: Johann Ambrosius Barth (cit. on pp. 26, 27).

Brunel, Nicolas (2000). "Dynamics of sparsely connected networks of excitatory and inhibitory spiking neurons." In: *J. Comput. Neurosci.* 8.3, pp. 183–208. DOI: `10.1023/a:1008925309027`. URL: `https://doi.org/10.1023/a:1008925309027` (cit. on pp. 11, 121, 125, 126, 140, 141).

Brunel, Nicolas, Frances S. Chance, Nicolas Fourcaud, and L. F. Abbott (Mar. 2001). "Effects of Synaptic Noise and Filtering on the Frequency Response of Spiking Neurons." In: *Phys. Rev. Lett.* 86.10, pp. 2186–2189. DOI: `10.1103/physrevlett.86.2186`. URL: `https://doi.org/10.1103/physrevlett.86.2186` (cit. on p. 131).

Brunel, Nicolas and Vincent Hakim (Oct. 1999). "Fast Global Oscillations in Networks of Integrate-and-Fire Neurons with Low Firing Rates." In: *Neural Comput.* 11.7, pp. 1621–1671. DOI: `10.1162/089976699300016179` (cit. on pp. 131, 140).

Brunel, Nicolas and Peter Latham (2003a). "Firing rate of the noisy quadratic integrate-and-fire neuron." In: *Neural Comput.* 15.10, pp. 2281–2306 (cit. on p. 126).

Brunel, Nicolas and Xiao-Jing Wang (2003b). "What Determines the Frequency of Fast Network Oscillations With Irregular Neural Discharges? I. Synaptic Dynamics and Excitation-Inhibition Balance." In: *J. Neurophysiol.* 90, pp. 415–430 (cit. on pp. 139, 140).

Buccino, Alessio P, Samuel Garcia, and Pierre Yger (Apr. 2022). "Spike Sorting: New Trends and Challenges of the Era of High-Density Probes." In: *Progress in Biomedical Engineering* 4.2, p. 022005. ISSN: 2516-1091. DOI: `10.1088/2516-1091/ac6b96`. (Visited on 08/23/2022) (cit. on pp. 172, 174).

Buccino, Alessio P, Cole L Hurwitz, Samuel Garcia, Jeremy Magland, Joshua H Siegle, Roger Hurwitz, and Matthias H Hennig (Nov. 2020). "SpikeInterface, a Unified Framework for Spike Sorting." In: *eLife* 9, e61834. ISSN: 2050-084X. DOI: `10.7554/eLife.61834`. (Visited on 01/09/2023) (cit. on pp. 58, 81, 165, 174).

Buice, Michael A and Carson C Chow (2013). "Beyond mean field theory: statistical field theory for neural networks." In: *J. Stat. Mech. Theory Exp.* 2013.03, P03003 (cit. on p. 126).

Buneo, Christopher A. and Richard A. Andersen (July 2012). "Integration of Target and Hand Position Signals in the Posterior Parietal Cortex: Effects of Workspace and Hand Vision." In: *Journal of Neurophysiology* 108.1, pp. 187–199. ISSN: 0022-3077, 1522-1598. DOI: `10.1152/jn.00137.2011`. (Visited on 12/04/2022) (cit. on p. 28).

Buzsáki, György and Xiao Jing Wang (July 2012). "Mechanisms of Gamma Oscillations." In: *Annu. Rev. Neurosci.* 35.1, pp. 203–225. DOI: `10.1146/annurev-neuro-062111-150444`. URL: `https://doi.org/10.1146/annurev-neuro-062111-150444` (cit. on p. 139).

Cai, Zhengxiang, Abbas Sohrabpour, Haiteng Jiang, Shuai Ye, Boney Joseph, Benjamin H. Brinkmann, Gregory A. Worrell, and Bin He (Apr. 2021). "Noninvasive high-frequency oscillations riding spikes delineates epileptogenic sources." en. In: *Proc. Natl. Acad. Sci. USA* 118.17, e2011130118. ISSN: 0027-8424, 1091-6490. DOI: `10.1073/pnas.2011130118`. URL: `http://www.pnas.org/lookup/doi/10.1073/pnas.2011130118` (visited on 04/21/2021) (cit. on p. 156).

Caminiti, R, Pb Johnson, and A Urbano (July 1990). "Making Arm Movements within Different Parts of Space: Dynamic Aspects in the Primate Motor Cortex." In: *The Journal of Neuroscience* 10.7, pp. 2039–2058. ISSN: 0270-6474, 1529-2401. DOI: `10.1523/JNEUROSCI.10-07-02039.1990`. (Visited on 09/01/2022) (cit. on pp. 10, 66).

Campbell, P.K., K.E. Jones, R.J. Huber, K.W. Horch, and R.A. Normann (Aug./1991). "A Silicon-Based, Three-Dimensional Neural Interface: Manufacturing Processes for an Intracortical Electrode Array." In: *IEEE Transactions on Biomedical Engineering* 38.8, pp. 758–768. ISSN: 00189294. DOI: `10.1109/10.83588`. (Visited on 01/06/2023) (cit. on p. 33).

Caspers, Svenja, Simon B. Eickhoff, Tobias Rick, Anette von Kapri, Torsten Kuhlen, Ruiwang Huang, Nadim J. Shah, and Karl Zilles (Sept. 2011). "Probabilistic Fibre Tract Analysis of Cytoarchitectonically Defined Human Inferior Parietal Lobule Areas Reveals

Similarities to Macaques." In: *NeuroImage* 58.2, pp. 362–380. ISSN: 10538119. DOI: 10.1016/j.neuroimage.2011.06.027. (Visited on 12/15/2022) (cit. on p. 27).

Chung, Jason E., Jeremy F. Magland, Alex H. Barnett, Vanessa M. Tolosa, Angela C. Tooker, Kye Y. Lee, Kedar G. Shah, Sarah H. Felix, Loren M. Frank, and Leslie F. Greengard (Sept. 2017). "A Fully Automated Approach to Spike Sorting." In: *Neuron* 95.6, 1381–1394.e6. ISSN: 08966273. DOI: 10.1016/j.neuron.2017.08.030. (Visited on 01/09/2023) (cit. on p. 174).

Churchland, Mark M. and Krishna V. Shenoy (June 2007). "Temporal Complexity and Heterogeneity of Single-Neuron Activity in Premotor and Motor Cortex." In: *Journal of Neurophysiology* 97.6, pp. 4235–4257. ISSN: 0022-3077, 1522-1598. DOI: 10.1152/jn.00095.2007. (Visited on 11/04/2022) (cit. on p. 94).

Clark, Mary Ann, Matthew Douglas, and Jung Choi (Mar. 2018). *Biology 2e*. Houston, Texas: OpenStax (cit. on pp. 4, 5).

Clarke, Edwin and Jerry Stannard (1963). "Aristotle on the Anatomy of the Brain." In: *Journal of the History of Medicine and Allied Sciences* 18.2, pp. 130–148. ISSN: 0022-5045. JSTOR: 24621747. (Visited on 12/09/2022) (cit. on p. 1).

Clower, Dottie M, Robert A West, James C Lynch, and Peter L Strick (n.d.). "The Inferior Parietal Lobule Is the Target of Output from the Superior Colliculus, Hippocampus, and Cerebellum." In: () (cit. on p. 28).

Codol, Olivier, Jonathan A. Michaels, Mehrdad Kashefi, J. Andrew Pruszynski, and Paul L. Gribble (Feb. 2023). *MotorNet: A Python Toolbox for Controlling Differentiable Biomechanical Effectors with Artificial Neural Networks*. Preprint. Neuroscience. DOI: 10.1101/2023.02.17.528969. (Visited on 02/27/2023) (cit. on pp. 11, 66, 112).

Cody, Patrick A., James R. Eles, Carl F. Lagenaur, Takashi D.Y. Kozai, and X. Tracy Cui (2018). "Unique Electrophysiological and Impedance Signatures between Encapsulation Types: An Analysis of Biological Utah Array Failure and Benefit of a Biomimetic Coating in a Rat Model." In: *Biomaterials* 161, pp. 117–128. ISSN: 18785905. DOI: 10.1016/j.biomaterials.2018.01.025 (cit. on p. 57).

Cohen, Yale E. and Richard A. Andersen (July 2002). "A Common Reference Frame for Movement Plans in the Posterior Parietal Cortex." In: *Nature Reviews Neuroscience* 3.7, pp. 553–562. ISSN: 1471-003X, 1471-0048. DOI: 10.1038/nrn873. (Visited on 08/19/2022) (cit. on p. 30).

Connors, Barry W. and Michael A. Long (2004). "Electrical synapses in the mammalian brain." In: *Annu. Rev. Neurosci.* 27.1, pp. 393–418. DOI: 10.1146/annurev.neuro.26.041002.131128. URL: https://doi.org/10.1146/annurev.neuro.26.041002.131128 (cit. on p. 6).

Constantinidis, C. and M. A. Steinmetz (Aug. 1996). "Neuronal Activity in Posterior Parietal Area 7a during the Delay Periods of a

Spatial Memory Task." In: *Journal of Neurophysiology* 76.2, pp. 1352–1355. ISSN: 0022-3077, 1522-1598. DOI: `10.1152/jn.1996.76.2.1352`. (Visited on 03/15/2022) (cit. on p. 28).

Constantinidis, C. and M. A. Steinmetz (July 2001). "Neuronal Responses in Area 7a to Multiple-stimulus Displays: I. Neurons Encode the Location of the Salient Stimulus." In: *Cerebral Cortex* 11.7, pp. 581–591. ISSN: 1047-3211, 1460-2199. DOI: `10.1093/cercor/11.7.581`. (Visited on 03/15/2022) (cit. on p. 28).

Côté, Sandrine L., Adjia Hamadjida, Stephan Quessy, and Numa Dancause (June 2017). "Contrasting Modulatory Effects from the Dorsal and Ventral Premotor Cortex on Primary Motor Cortex Outputs." In: *The Journal of Neuroscience* 37.24, pp. 5960–5973. ISSN: 0270-6474, 1529-2401. DOI: `10.1523/JNEUROSCI.0462-17.2017`. (Visited on 12/19/2022) (cit. on p. 26).

Crawford, J. Douglas, Denise Y.P. Henriques, and W. Pieter Medendorp (July 2011). "Three-Dimensional Transformations for Goal-Directed Action." In: *Annual Review of Neuroscience* 34.1, pp. 309–331. ISSN: 0147-006X, 1545-4126. DOI: `10.1146/annurev-neuro-061010-113749`. (Visited on 12/07/2022) (cit. on p. 29).

Curcio, Christine A., Kenneth R. Sloan, Robert E. Kalina, and Anita E. Hendrickson (Feb. 1990). "Human Photoreceptor Topography." In: *The Journal of Comparative Neurology* 292.4, pp. 497–523. ISSN: 0021-9967, 1096-9861. DOI: `10.1002/cne.902920402`. (Visited on 01/04/2023) (cit. on p. 19).

Dąbrowska, Paulina Anna, Nicole Voges, Michael von Papen, Junji Ito, David Dahmen, Alexa Riehle, Thomas Brochier, and Sonja Grün (May 2021). "On the Complexity of Resting State Spiking Activity in Monkey Motor Cortex." In: *Cereb. Cortex Commun.* 2.3. tgab033. ISSN: 2632-7376. DOI: `10.1093/texcom/tgab033`. eprint: `https://academic.oup.com/cercorcomms/article-pdf/2/3/tgab033/38889970/tgab033.pdf`. URL: `https://doi.org/10.1093/texcom/tgab033` (cit. on p. 167).

Dahmen, David, Moritz Layer, Lukas Deutz, Paulina Anna Dąbrowska, Nicole Voges, Michael von Papen, Thomas Brochier, Alexa Riehle, Markus Diesmann, Sonja Grün, et al. (2022). "Global organization of neuronal activity only requires unstructured local connectivity." In: *eLife* 11, e68422 (cit. on pp. 126, 192).

Dai, Weiwei, Ivan Selesnick, John-Ross Rizzo, Janet Rucker, and Todd Hudson (Dec. 2016). "A Parametric Model for Saccadic Eye Movement." In: *2016 IEEE Signal Processing in Medicine and Biology Symposium (SPMB)*. Philadelphia, PA: IEEE, pp. 1–6. ISBN: 978-1-5090-6713-8. DOI: `10.1109/SPMB.2016.7846860`. (Visited on 12/13/2022) (cit. on p. 24).

Dasbach, Stefan, Tom Tetzlaff, Markus Diesmann, and Johanna Senk (2021). "Dynamical Characteristics of Recurrent Neuronal Networks Are Robust Against Low Synaptic Weight Resolution." In: *Front.*

Neurosci. 15, p. 757790. DOI: 10.3389/fnins.2021.757790. URL: http://doi.org/10.3389/fnins.2021.757790 (cit. on pp. 123, 130).

De Cheveigné, Alain and Lucas C. Parra (2014). “Joint Decorrelation, a Versatile Tool for Multichannel Data Analysis.” In: *NeuroImage* 98, pp. 487–505. ISSN: 10959572. DOI: 10.1016/j.neuroimage.2014.05.068 (cit. on p. 58).

De Schutter, Erik (May 2008). “Why Are Computational Neuroscience and Systems Biology So Separate?” In: *PLoS Computational Biology* 4.5. Ed. by Karl J. Friston, e1000078. ISSN: 1553-7358. DOI: 10.1371/journal.pcbi.1000078. (Visited on 04/06/2023) (cit. on p. 2).

De Haan, Marcel Jan, Thomas Brochier, Sonja Grün, Alexa Riehle, and Frédéric V. Barthélemy (2018). “Real-time visuomotor behavior and electrophysiology recording setup for use with humans and monkeys.” en. In: *J. Neurophysiol.* 120.2, pp. 539–552. ISSN: 0022-3077 and 1522-1598. DOI: 10.1152/jn.00262.2017. URL: https://www.physiology.org/doi/10.1152/jn.00262.2017 (cit. on pp. 32, 33, 36, 37, 40).

DeFelipe, J., L. Alonso-Nanclares, and J.I. Arellano (2002). “Microstructure of the neocortex: comparative aspects.” In: *J. Neurocytol.* 31, pp. 299–316. DOI: 10.1023/A:1024130211265. URL: https://doi.org/10.1023/A:1024130211265 (cit. on p. 125).

Delepine, Chloe, Jennifer Shih, Keji Li, Pierre Gaudeaux, and Mriganka Sur (Mar. 2023). “Differential Effects of Astrocyte Manipulations on Learned Motor Behavior and Neuronal Ensembles in the Motor Cortex.” In: *The Journal of Neuroscience*, JN–RM–1982–22. ISSN: 0270-6474, 1529-2401. DOI: 10.1523/JNEUROSCI.1982-22.2023. (Visited on 03/27/2023) (cit. on p. 6).

Denagamage, Sachira, Mitchell P. Morton, John H. Reynolds, Monika P. Jadi, and Anirvan S. Nandy (Jan. 2021). *Laminar Mechanisms of Saccadic Suppression in Primate Visual Cortex*. Preprint. Neuroscience. DOI: 10.1101/2021.01.09.426063. (Visited on 04/15/2022) (cit. on pp. 23, 24).

Denker, M., A. Yegenoglu, and S. Grün (2018a). “Collaborative HPC-enabled workflows on the HBP Collaboratory using the Elephant framework.” In: *Neuroinformatics 2018*, P19. DOI: 10.12751/incf.ni2018.0019. URL: https://abstracts.g-node.org/abstracts/023bec4e-0c35-4563-81ce-2c6fac282abd (cit. on pp. 80, 165).

Denker, Michael, Lyuba Zehl, Bjørg E. Kilavik, Markus Diesmann, Thomas Brochier, Alexa Riehle, and Sonja Grün (2018b). “LFP Beta Amplitude Is Linked to Mesoscopic Spatio-Temporal Phase Patterns.” In: *Scientific Reports* 8.1, pp. 1–21. ISSN: 20452322. DOI: 10.1038/s41598-018-22990-7. arXiv: 1703.09488 (cit. on p. 167).

Diesmann, Markus and Marc-Oliver Gewaltig (2002). “NEST: An Environment for Neural Systems Simulations.” In: *Forschung und wisschenschaftliches Rechnen, Beiträge zum Heinz-Billing-Preis 2001*. Ed. by

Theo Plesser and Volker Macho. Vol. 58. GWDG-Bericht. Göttingen: Ges. für Wiss. Datenverarbeitung, pp. 43–70 (cit. on p. 165).

Diomedi, S., F.E. Vaccari, C. Galletti, K. Hadjidimitrakis, and P. Fattori (Oct. 2021). "Motor-like Neural Dynamics in Two Parietal Areas during Arm Reaching." In: *Progress in Neurobiology* 205, p. 102116. ISSN: 03010082. DOI: `10.1016/j.pneurobio.2021.102116`. (Visited on 10/20/2021) (cit. on p. 66).

Diomedi, Stefano, Francesco E. Vaccari, Matteo Filippini, Patrizia Fattori, and Claudio Galletti (Oct. 2020). "Mixed Selectivity in Macaque Medial Parietal Cortex during Eye-Hand Reaching." In: *iScience* 23.10, p. 101616. ISSN: 25890042. DOI: `10.1016/j.isci.2020.101616`. (Visited on 08/14/2022) (cit. on pp. 27, 67, 74, 77, 79, 103, 116).

Doedel, Eusebius J and B Oldeman (1998). "Auto-07p: continuation and bifurcation software." In: *WARNING: Not A Journal* (cit. on p. 192).

Donoghue, Thomas et al. (Dec. 2020). "Parameterizing neural power spectra into periodic and aperiodic components." en. In: *Nat. Neurosci.* 23.12, pp. 1655–1665. ISSN: 1097-6256, 1546-1726. DOI: `10.1038/s41593-020-00744-x`. URL: `http://www.nature.com/articles/s41593-020-00744-x` (visited on 04/07/2021) (cit. on p. 145).

Dougherty, Robert F., Volker M. Koch, Alyssa A. Brewer, Bernd Fischer, Jan Modersitzki, and Brian A. Wandell (Oct. 2003). "Visual Field Representations and Locations of Visual Areas V1/2/3 in Human Visual Cortex." In: *Journal of Vision* 3.10, p. 1. ISSN: 1534-7362. DOI: `10.1167/3.10.1`. (Visited on 01/13/2023) (cit. on p. 21).

Duhamel, Jean-René, Carol L. Colby, and Michael E. Goldberg (Jan. 1992). "The Updating of the Representation of Visual Space in Parietal Cortex by Intended Eye Movements." In: *Science* 255.5040, pp. 90–92. ISSN: 0036-8075, 1095-9203. DOI: `10.1126/science.1553535`. (Visited on 12/14/2022) (cit. on p. 23).

Ermentrout, Bard (2002). *Simulating, Analyzing, and Animating Dynamical Systems: A Guide to Xppaut for Researchers and Students (Software, Environments, Tools)*. Soc for Industrial & Applied Math. ISBN: 898715067 (cit. on p. 191).

Erö, Csaba, Marc-Oliver Gewaltig, Daniel Keller, and Henry Markram (Nov. 2018). "A Cell Atlas for the Mouse Brain." In: *Frontiers in Neuroinformatics* 12, p. 84. ISSN: 1662-5196. DOI: `10.3389/fninf.2018.00084`. (Visited on 04/03/2023) (cit. on p. 6).

Evarts, E. V. (1968). "Relation of pyramidal tract activity to force exerted during voluntary movement." In: *J. Neurophysiol.* 31.1, pp. 14–27 (cit. on p. 25).

Farhoodi, Sahand and Uri Eden (Aug. 2021). "The Problem of Perfect Predictors in Statistical Spike Train Models." In: *Neurons, Behavior, Data analysis, and Theory* 5.3. ISSN: 2690-2664. DOI: `10.51628/001c.27667`. arXiv: `2102.00574 [stat]`. (Visited on 11/25/2022) (cit. on p. 71).

Felleman, Daniel J and David C Van Essen (1991). “Distributed Hierachical Processing in the Primate Cerebral Cortex.” In: *Cerebral Cortex* 1.1, pp. 1–47. ISSN: 1047-3211. DOI: `10.1093/cercor/1.1.1` (cit. on pp. 18, 20, 29, 65).

Fischer, Florian, Miroslav Bachinski, Markus Klar, Arthur Fleig, and Jörg Müller (July 2021). “Reinforcement Learning Control of a Biomechanical Model of the Upper Extremity.” In: *Scientific Reports* 11.1, p. 14445. ISSN: 2045-2322. DOI: `10.1038/s41598-021-93760-1`. (Visited on 12/18/2022) (cit. on p. 112).

Fogassi, Leonardo, Pier Francesco Ferrari, Benno Gesierich, Stefano Rozzi, Fabian Chersi, and Giacomo Rizzolatti (Apr. 2005). “Parietal Lobe: From Action Organization to Intention Understanding.” In: *Science* 308.5722, pp. 662–667. ISSN: 0036-8075, 1095-9203. DOI: `10.1126/science.1106138`. (Visited on 12/27/2022) (cit. on p. 28).

Fourcaud-Trocmé, N., D. Hansel, C. van Vreeswijk, and N. Brunel (2003). “How spike generation mechanisms determine the neuronal response to fluctuating inputs.” In: *J. Neurosci.* 23, pp. 11628–11640 (cit. on p. 126).

Fourcaud, Nicolas and Nicolas Brunel (2002). “Dynamics of the firing probability of noisy integrate-and-fire neurons.” In: *Neural Comput.* 14, pp. 2057–2110. DOI: `10.1162/089976602320264015`. URL: `https://doi.org/10.1162/089976602320264015` (cit. on pp. 125, 128).

Frey, Markus et al. (Aug. 2021). “Interpreting Wide-Band Neural Activity Using Convolutional Neural Networks.” In: *eLife* 10, e66551. ISSN: 2050-084X. DOI: `10.7554/eLife.66551`. (Visited on 04/02/2023) (cit. on p. 113).

Fukushima, Kunihiko (Jan. 1988). “Neocognitron: A Hierarchical Neural Network Capable of Visual Pattern Recognition.” In: *Neural Networks* 1.2, pp. 119–130. ISSN: 08936080. DOI: `10.1016/0893-6080(88)90014-7`. (Visited on 04/04/2023) (cit. on p. 20).

Fukutomi, Matasaburo and Bruce A. Carlson (July 2020). “A History of Corollary Discharge: Contributions of Mormyrid Weakly Electric Fish.” In: *Frontiers in Integrative Neuroscience* 14, p. 42. ISSN: 1662-5145. DOI: `10.3389/fnint.2020.00042`. (Visited on 12/14/2022) (cit. on p. 23).

Gaboian, Jerry (2000). “A Statistical Survey of Common-Mode Noise.” In: (cit. on p. 57).

Gallese, Vittorio, Luciano Fadiga, Leonardo Fogassi, and Giacomo Rizzolatti (1996). “Action Recognition in the Premotor Cortex.” In: *Brain* 119.2, pp. 593–609. ISSN: 0006-8950, 1460-2156. DOI: `10.1093/brain/119.2.593`. (Visited on 12/20/2022) (cit. on p. 28).

Gamberini, Michela, Lauretta Passarelli, Matteo Filippini, Patrizia Fattori, and Claudio Galletti (Dec. 2021). “Vision for Action: Thalamic and Cortical Inputs to the Macaque Superior Parietal Lobule.” In: *Brain Structure and Function* 226.9, pp. 2951–2966. ISSN: 1863-

2653, 1863-2661. DOI: 10.1007/s00429-021-02377-7. (Visited on 03/20/2022) (cit. on p. 27).

Gao, Peiran and Surya Ganguli (2015). "On Simplicity and Complexity in the Brave New World of Large-Scale Neuroscience." In: *Current Opinion in Neurobiology* 32, pp. 148–155. ISSN: 18736882. DOI: 10.1016/j.conb.2015.04.003. arXiv: 1503.08779 (cit. on p. 167).

Gao, Peiran, Eric Trautmann, Byron M. Yu, Gopal Santhanam, Stephen I. Ryu, Krishna V. Shenoy, and Surya Ganguli (2017). "A Theory of Multineuronal Dimensionality, Dynamics and Measurement." In: *bioRxiv*, p. 214262. ISSN: 08870446. DOI: 10.1101/214262 (cit. on p. 167).

Garcia, Samuel and Christophe Pouzat (2015). *Trisdesclous: Spike Sorting with a French Touch.* tridesclous. (Visited on 01/09/2023) (cit. on p. 174).

Garcia, Samuel et al. (2014). "Neo: An Object Model for Handling Electrophysiology Data in Multiple Formats." In: *Frontiers in Neuroinformatics* 8.February, pp. 1–10. ISSN: 1662-5196. DOI: 10.3389/fninf.2014.00010 (cit. on pp. 80, 165).

Gast, Richard, Daniel Rose, Christoph Salomon, Harald E Möller, Nikolaus Weiskopf, and Thomas R Knösche (2019). "PyRates - A Python framework for rate-based neural simulations." In: *PLOSONE* 14.12, e0225900 (cit. on p. 192).

Gautrais, Jacques and Simon Thorpe (1998). "Rate coding versus temporal order coding: a theoretical approach." In: *BioSystems* 48, pp. 57–65 (cit. on p. 8).

Georgopoulos, A. P., R. Caminiti, J. F. Kalaska, and J. T. Massey (1983). "Spatial coding of movement: A hypothesis concerning the coding of movement direction by motor cortical populations." In: *Exp. Brain Res. Suppl.* 7, pp. 327–336 (cit. on p. 25).

Georgopoulos, A. P., R. E. Kettner, and A. B. Schwartz (1988). "Primate motor cortex and free arm movements to visual targets in three-dimensional space. II. Coding of the direction of movement by a neuronal population." In: *J. Neurosci.* 8.8, pp. 2928–2937 (cit. on p. 25).

Georgopoulos, A.P., A.B. Schwartz, and R.E. Kettner (1986). "Neuronal population coding of movement direction." In: *Science* 4771.233, pp. 1416–1419. DOI: 10.1126/science.3749885 (cit. on p. 25).

Georgopoulos, Ap, Jf Kalaska, R Caminiti, and Jt Massey (Nov. 1982). "On the Relations between the Direction of Two-Dimensional Arm Movements and Cell Discharge in Primate Motor Cortex." In: *The Journal of Neuroscience* 2.11, pp. 1527–1537. ISSN: 0270-6474, 1529-2401. DOI: 10.1523/JNEUROSCI.02-11-01527.1982. (Visited on 03/15/2022) (cit. on pp. 8, 10, 25, 66, 73, 84, 89, 116).

Gerstner, Wulfram, Werner M. Kistler, Richard Naud, and Liam Paninski (2014). *Neuronal Dynamics. From Single Neurons to Networks and*

Models of Cognition. Cambridge: Cambridge University Press. DOI: 10.1017/cbo9781107447615 (cit. on pp. 7, 125–127).

Gewaltig, Marc-Oliver and Markus Diesmann (2007). "NEST (NEural Simulation Tool)." In: *Scholarpedia J.* 2.4, p. 1430. DOI: 10.4249/scholarpedia.1430. URL: https://doi.org/10.4249/scholarpedia.1430 (cit. on pp. 165, 191).

Gibaldi, Agostino and Silvio P. Sabatini (Feb. 2021). "The Saccade Main Sequence Revised: A Fast and Repeatable Tool for Oculomotor Analysis." In: *Behavior Research Methods* 53.1, pp. 167–187. ISSN: 1554-3528. DOI: 10.3758/s13428-020-01388-2. (Visited on 12/13/2022) (cit. on p. 24).

Ginzburg, Iris and Haim Sompolinsky (1994). "Theory of correlations in stochastic neural networks." In: *Phys. Rev. E* 50 (4), pp. 3171–3191. DOI: 10.1103/PhysRevE.50.3171. URL: https://link.aps.org/doi/10.1103/PhysRevE.50.3171 (cit. on p. 126).

Glaser, Joshua I., Matthew G. Perich, Pavan Ramkumar, Lee E. Miller, and Konrad P. Kording (Dec. 2018). "Population Coding of Conditional Probability Distributions in Dorsal Premotor Cortex." In: *Nature Communications* 9.1, p. 1788. ISSN: 2041-1723. DOI: 10.1038/s41467-018-04062-6. (Visited on 08/17/2022) (cit. on p. 26).

Goldenfeld, Nigel (1992). *Lectures on phase transitions and the renormalization group*. Reading, Massachusetts: Perseus books (cit. on p. 125).

Golgi, Camillo (1873). "Sulla struttura della sostanza grigia del cervello." In: *Gaz. Med. Ital. Lomb.* 33, pp. 244–46 (cit. on pp. 1, 8).

Golosio, Bruno, Gianmarco Tiddia, Chiara De Luca, Elena Pastorelli, Francesco Simula, and Pier Stanislao Paolucci (Feb. 2021). "Fast Simulations of Highly-Connected Spiking Cortical Models Using GPUs." In: *Front. Comput. Neurosci.* 15, p. 627620. DOI: 10.3389/fncom.2021.627620. URL: https://doi.org/10.3389/fncom.2021.627620 (cit. on p. 123).

Goodale, M. A. and A. D. Milner (Jan. 1992a). "Separate Visual Pathways for Perception and Action." In: *Trends in Neurosciences* 15.1, pp. 20–25. ISSN: 0166-2236. DOI: 10.1016/0166-2236(92)90344-8 (cit. on p. 18).

– (Jan. 1992b). "Separate Visual Pathways for Perception and Action." In: *Trends Neurosci.* 15.1, pp. 20–25. ISSN: 0166-2236. DOI: 10.1016/0166-2236(92)90344-8 (cit. on p. 65).

Goodman, James M., Gregg A. Tabot, Alex S. Lee, Aneesha K. Suresh, Alexander T. Rajan, Nicholas G. Hatsopoulos, and Sliman Bensmaia (Dec. 2019). "Postural Representations of the Hand in the Primate Sensorimotor Cortex." In: *Neuron* 104.5, 1000–1009.e7. ISSN: 08966273. DOI: 10.1016/j.neuron.2019.09.004. (Visited on 08/17/2022) (cit. on pp. 72, 104).

Grabska-Barwinska, A. and P. Latham (2014). "How well do mean field theories of spiking quadratic-integrate-and-fire networks work in realistic parameter regimes?" In: *J. Comput. Neurosci.* 36.3, pp. 469–81 (cit. on p. 126).

Gray, Henry, and Warren H Lewis (1918). *Anatomy of the Human Body*. Philadelphia: Lea & Febiger, 1918, p. 1396 (cit. on p. 18).

Graziano, Michael S.A. and Tyson N. Aflalo (Oct. 2007). "Mapping Behavioral Repertoire onto the Cortex." In: *Neuron* 56.2, pp. 239–251. ISSN: 08966273. DOI: `10.1016/j.neuron.2007.09.013`. (Visited on 11/04/2022) (cit. on p. 26).

Gregoriou, Georgia G., Elena Borra, Massimo Matelli, and Giuseppe Luppino (May 2006). "Architectonic Organization of the Inferior Parietal Convexity of the Macaque Monkey." In: *The Journal of Comparative Neurology* 496.3, pp. 422–451. ISSN: 0021-9967, 1096-9861. DOI: `10.1002/cne.20933`. (Visited on 08/16/2022) (cit. on pp. 27, 28).

Grewe, Jan, Thomas Wachtler, and Jan Benda (2011). "A Bottom-up Approach to Data Annotation in Neurophysiology." In: *Frontiers in Neuroinformatics* 5.August, pp. 1–18. ISSN: 1662-5196. DOI: `10.3389/fninf.2011.00016` (cit. on p. 165).

Griffin, Darcy M. and Peter L. Strick (Aug. 2020). "The Motor Cortex Uses Active Suppression to Sculpt Movement." In: *Science Advances* 6.34, eabb8395. ISSN: 2375-2548. DOI: `10.1126/sciadv.abb8395`. (Visited on 11/25/2022) (cit. on pp. 26, 112).

Grün, Sonja, Markus Diesmann, and Ad Aertsen (2002). "Unitary events in multiple single-neuron spiking activity: I. Detection and significance." In: *Neural Comput.* 14.1, pp. 43–80 (cit. on p. 166).

Grytskyy, D., T. Tetzlaff, M. Diesmann, and M. Helias (2013). "A unified view on weakly correlated recurrent networks." In: *Front. Comput. Neurosci.* 7, p. 131. DOI: `10.3389/fncom.2013.00131` (cit. on p. 126).

Haan, Marcel Jan De and Den Helder (2018). "Cortical Network Dynamics during Visually-Guided Motor Behavior : Setup Development and Preliminary Analyses." PhD thesis (cit. on p. 164).

Hadjidimitrakis, Kostas, Sophia Bakola, Yan T. Wong, and Maureen A. Hagan (Mar. 2019). "Mixed Spatial and Movement Representations in the Primate Posterior Parietal Cortex." In: *Frontiers in Neural Circuits* 13, p. 15. ISSN: 1662-5110. DOI: `10.3389/fncir.2019.00015`. (Visited on 03/20/2022) (cit. on p. 27).

Hagen, Espen, David Dahmen, Maria L. Stavrinou, Henrik Lindén, Tom Tetzlaff, Sacha J. van Albada, Sonja Grün, Markus Diesmann, and Gaute T. Einevoll (Oct. 2016). "Hybrid scheme for modeling local field potentials from point-neuron networks." In: *Cereb. Cortex* 26.12, pp. 4461–4496. DOI: `10.1093/cercor/bhw237`. URL: `https://doi.org/10.1093/cercor/bhw237` (cit. on pp. 123, 144, 145, 148).

Hansel, D., G. Mato, C. Meunier, and L. Neltner (1998). "On numerical simulations of integrate-and-fire neural networks." In: *Neural Comput.* 10.2, pp. 467–483. URL: `https://doi.org/10.1162/089976698300017845` (cit. on pp. 143, 198).

Harris, Kenneth D. and Alexander Thiele (2011). "Cortical state and attention." In: *Nat. Rev. Neurosci.* 12, pp. 509–523. DOI: `10.1038/nrn3084` (cit. on p. 143).

Hastie, Trevor, Robert Tibshirani, Jerome H Friedman, and Jerome H Friedman (2009). *The elements of statistical learning: data mining, inference, and prediction*. Vol. 2. Springer (cit. on p. 71).

Hatsopoulos, N. G., Q. Xu, and Y. Amit (2007a). "Encoding of Movement Fragments in the Motor Cortex." In: *Journal of Neuroscience* 27.19, pp. 5105–5114. ISSN: 0270-6474. DOI: `10.1523/JNEUROSCI.3570-06.2007` (cit. on p. 94).

Hatsopoulos, Nicholas G., Qingqing Xu, and Yali Amit (2007b). "Encoding of Movement Fragments in the Motor Cortex." In: *J. Neurosci.* 27.19, pp. 5105–5114 (cit. on p. 177).

Heider, B. (Apr. 2005). "Functional Architecture of Retinotopy in Visual Association Cortex of Behaving Monkey." In: *Cerebral Cortex* 15.4, pp. 460–478. ISSN: 1047-3211, 1460-2199. DOI: `10.1093/cercor/bhh148`. (Visited on 03/20/2022) (cit. on pp. 28, 29).

Heider, Barbara, Anushree Karnik, Nirmala Ramalingam, and Ralph M. Siegel (Dec. 2010). "Neural Representation During Visually Guided Reaching in Macaque Posterior Parietal Cortex." In: *Journal of Neurophysiology* 104.6, pp. 3494–3509. ISSN: 0022-3077, 1522-1598. DOI: `10.1152/jn.01050.2009`. (Visited on 10/20/2021) (cit. on p. 28).

Heider, Barbara and Ralph M. Siegel (Mar. 2014). "Optical Imaging of Visually Guided Reaching in Macaque Posterior Parietal Cortex." In: *Brain Structure and Function* 219.2, pp. 495–509. ISSN: 1863-2653, 1863-2661. DOI: `10.1007/s00429-013-0513-y`. (Visited on 03/27/2022) (cit. on p. 28).

Heitmann, Stewart, Matthew J Aburn, and Michael Breakspear (2018). "The brain dynamics toolbox for Matlab." In: *Neurocomputing* 315, pp. 82–88 (cit. on p. 192).

Helias, Moritz, Tom Tetzlaff, and Markus Diesmann (2014). "The correlation structure of local cortical networks intrinsically results from recurrent dynamics." In: *PLOS Comput. Biol.* 10.1, e1003428. DOI: `10.1371/journal.pcbi.1003428`. URL: `https://doi.org/10.1371/journal.pcbi.1003428` (cit. on p. 126).

Hertz, John (2010). "Cross-Correlations in High-Conductance States of a Model Cortical Network." In: *Neural Comput.* 22, pp. 427–447 (cit. on p. 126).

Herz, Andreas V. M., Tim Gollisch, Christian K. Machens, and Dieter Jaeger (2006). "Modeling Single-Neuron Dynamics and Computations: A Balance of Detail and Abstraction." In: *Science* 314, pp. 80–84 (cit. on p. 7).

Hill, D. N., S. B. Mehta, and D. Kleinfeld (June 2011). "Quality Metrics to Accompany Spike Sorting of Extracellular Signals." In: *Journal of Neuroscience* 31.24, pp. 8699–8705. ISSN: 0270-6474, 1529-2401. DOI:

10.1523/JNEUROSCI.0971-11.2011. (Visited on 02/10/2023) (cit. on p. 178).

Hines, Michael L. and Nicholas T. Carnevale (2001). "NEURON: a tool for neuroscientists." In: *Neuroscientist* 7.2, pp. 123–135. DOI: 10.1177/107385840100700207 (cit. on p. 191).

Hintze, Jerry L. and Ray D. Nelson (1998). "Violin Plots: A Box Plot-Density Trace Synergism." In: *Am. Stat.* 52.2, pp. 181–184. DOI: 10.1080/00031305.1998.10480559 (cit. on p. 142).

Hodgkin, A. L. and A. F. Huxley (1952). "A Quantitative Description of Membrane Current and Its Application to Conduction and Excitation in Nerve." In: *J. Physiol.* 117, pp. 500–544. DOI: 10.1113/jphysiol.1952.sp004764 (cit. on p. 7).

Hoerl, Arthur E. and Robert W. Kennard (Feb. 1970). "Ridge Regression: Biased Estimation for Nonorthogonal Problems." In: *Technometrics* 12.1, pp. 55–67. ISSN: 0040-1706. DOI: 10.1080/00401706.1970.10488634. (Visited on 03/13/2023) (cit. on p. 71).

Hubel, D. H. and T. N. Wiesel (1959). "Receptive fields of single neurones in the cat's striate cortex." In: *J. Physiol.* 148, pp. 574–591 (cit. on p. 20).

– (Jan. 1962). "Receptive Fields, Binocular Interaction and Functional Architecture in the Cat's Visual Cortex." In: *The Journal of Physiology* 160.1, pp. 106–154. ISSN: 00223751. DOI: 10.1113/jphysiol.1962.sp006837. (Visited on 03/16/2022) (cit. on p. 8).

Hyvärinen, Juhani and Antti Poranen (Dec. 1974). "Function of the Parietal Associative Area 7 as Revealed from Cellular Discharges in Alert Monkeys." In: *Brain* 97.4, pp. 673–692. ISSN: 0006-8950. DOI: 10.1093/brain/97.4.673. (Visited on 01/04/2023) (cit. on p. 28).

Insel, T. R., S. C. Landis, and F. S. Collins (May 2013). "The NIH BRAIN Initiative." In: *Science* 340.6133, pp. 687–688. ISSN: 0036-8075, 1095-9203. DOI: 10.1126/science.1239276. (Visited on 04/05/2023) (cit. on p. 164).

Izhikevich, EM (2003). "Simple model of spiking neurons." In: *IEEE Trans. Neural Netw.* 14.6, pp. 1569–1572. DOI: 10.1109/TNN.2003.820440 (cit. on p. 7).

Jas, Mainak et al. (Mar. 2020). "Pyglmnet: Python Implementation of Elastic-Net Regularized Generalized Linear Models." In: *Journal of Open Source Software* 5.47, p. 1959. ISSN: 2475-9066. DOI: 10.21105/joss.01959. (Visited on 10/05/2022) (cit. on pp. 71, 81).

Jun, James J. et al. (2017a). "Fully Integrated Silicon Probes for High-Density Recording of Neural Activity." In: *Nature* 551.7679, pp. 232–236. ISSN: 0028-0836, 1476-4687. DOI: 10.1038/nature24636 (cit. on p. 144).

– (Nov. 2017b). "Fully Integrated Silicon Probes for High-Density Recording of Neural Activity." In: *Nature* 551.7679, pp. 232–236. ISSN: 0028-0836, 1476-4687. DOI: 10.1038/nature24636. (Visited on 09/24/2022) (cit. on p. 167).

Kandel, Eric R., James H. Schwartz, and Thomas M. Jessel (1991). *Principles of neural science*. 3rd ed. New York: Elsevier. ISBN: 0-444-01562-0 (cit. on p. 18).

Kandel, Eric R., James H. Schwartz, Thomas M. Jessell, Steven A. Siegelbaum, A.J. Hudspeth, and Sarah Mack (2013). *Principles of Neural Science*. 5th ed. New York: McGraw-Hill. ISBN: 978-0-071-39011-8 (cit. on pp. 4, 5, 19, 20, 22–26, 29, 30).

Karkhanis, Anushree N., Barbara Heider, Fabian Muñoz Silva, and Ralph M. Siegel (Aug. 2014). "Spatial Effects of Shifting Prisms on Properties of Posterior Parietal Cortex Neurons: Prism Effects on Macaque Parietal Neurons." In: *The Journal of Physiology* 592.16, pp. 3625–3646. ISSN: 00223751. DOI: `10.1113/jphysiol.2014.270942`. (Visited on 12/15/2022) (cit. on p. 28).

Kato, Rikako, Takuya Hayashi, Kayo Onoe, Masatoshi Yoshida, Hideo Tsukada, Hirotaka Onoe, Tadashi Isa, and Takuro Ikeda (Dec. 2021). "The Posterior Parietal Cortex Contributes to Visuomotor Processing for Saccades in Blindsight Macaques." In: *Communications Biology* 4.1, p. 278. ISSN: 2399-3642. DOI: `10.1038/s42003-021-01804-z`. (Visited on 03/27/2022) (cit. on p. 22).

Kaufman, Matthew T, Mark M Churchland, Stephen I Ryu, and Krishna V Shenoy (Mar. 2014). "Cortical Activity in the Null Space: Permitting Preparation without Movement." In: *Nature Neuroscience* 17.3, pp. 440–448. ISSN: 1097-6256, 1546-1726. DOI: `10.1038/nn.3643`. (Visited on 01/25/2021) (cit. on p. 167).

Kaufman, Matthew T., Mark M. Churchland, and Krishna V. Shenoy (Aug. 2013). "The Roles of Monkey M1 Neuron Classes in Movement Preparation and Execution." In: *Journal of Neurophysiology* 110.4, pp. 817–825. ISSN: 0022-3077, 1522-1598. DOI: `10.1152/jn.00892.2011`. (Visited on 03/25/2022) (cit. on p. 26).

Keating, J.G, G.L Gerstein, P.G Musial, S.N Baker, and E.A King (Mar. 2002). "Signal-to-Noise Ratio Improvement in Multiple Electrode Recording." In: *Journal of Neuroscience Methods* 115.1, pp. 29–43. ISSN: 01650270. DOI: `10.1016/s0165-0270(01)00516-7` (cit. on p. 164).

Kelly, R. C., M. A. Smith, J. M. Samonds, A. Kohn, A. B. Bonds, J. A. Movshon, and T. Sing Lee (Jan. 2007). "Comparison of Recordings from Microelectrode Arrays and Single Electrodes in the Visual Cortex." In: *Journal of Neuroscience* 27.2, pp. 261–264. ISSN: 0270-6474, 1529-2401. DOI: `10.1523/JNEUROSCI.4906-06.2007`. (Visited on 12/08/2022) (cit. on p. 177).

Knight, James C. and Thomas Nowotny (Dec. 2018). "GPUs Outperform Current HPC and Neuromorphic Solutions in Terms of Speed and Energy When Simulating a Highly-Connected Cortical Model." In: *Front. Neurosci.* 12, pp. 1–19. DOI: `10.3389/fnins.2018.00941`. URL: `https://doi.org/10.3389/fnins.2018.00941` (cit. on p. 123).

Köster, Johannes and Sven Rahmann (2012). "Snakemake—a scalable bioinformatics workflow engine." In: *Biochemistry* 28.19, pp. 2520–

2522. DOI: 10.1093/bioinformatics/bts480 (cit. on pp. 43, 81, 165, 174).

Kötter, R. (2004). "Online retrieval, processing, and visualization of primate connectivity data from the CoCoMac database." In: *Neuroinformatics* 2.2, pp. 127–144 (cit. on p. 166).

Kraus, Benjamin J., Mark P. Brandon, Robert J. Robinson, Michael A. Connerney, Michael E. Hasselmo, and Howard Eichenbaum (Nov. 2015). "During Running in Place, Grid Cells Integrate Elapsed Time and Distance Run." In: *Neuron* 88.3, pp. 578–589. ISSN: 08966273. DOI: 10.1016/j.neuron.2015.09.031. (Visited on 10/24/2022) (cit. on p. 72).

Kuffler, Stephen W. (Jan. 1953). "DISCHARGE PATTERNS AND FUNCTIONAL ORGANIZATION OF MAMMALIAN RETINA." In: *Journal of Neurophysiology* 16.1, pp. 37–68. ISSN: 0022-3077, 1522-1598. DOI: 10.1152/jn.1953.16.1.37. (Visited on 12/13/2022) (cit. on p. 19).

Kurtzer, Isaac and Troy M. Herter (June 2007). "Contrasting Interpretations of the Nonuniform Distribution of Preferred Directions Within Primary Motor Cortex." In: *Journal of Neurophysiology* 97.6, pp. 4390–4390. ISSN: 0022-3077, 1522-1598. DOI: 10.1152/jn.00032.2007. (Visited on 08/16/2022) (cit. on p. 113).

Kusunoki, Makoto and Michael E. Goldberg (Mar. 2003). "The Time Course of Perisaccadic Receptive Field Shifts in the Lateral Intraparietal Area of the Monkey." In: *Journal of Neurophysiology* 89.3, pp. 1519–1527. ISSN: 0022-3077, 1522-1598. DOI: 10.1152/jn.00519.2002. (Visited on 08/18/2022) (cit. on p. 23).

Layer, Moritz, Johanna Senk, Simon Essink, Alexander van Meegen, Hannah Bos, and Moritz Helias (Dec. 2021). *NNMT 1.0.0*. Version 1.0.0. DOI: 10.5281/zenodo.5779549. URL: https://doi.org/10.5281/zenodo.5779549 (cit. on pp. 124, 190, 191).

– (2022a). "NNMT: Mean-Field Based Analysis Tools for Neuronal Network Models." In: *Front. Neuroinform.* 16, p. 835657. DOI: 10.3389/fninf.2022.835657 (cit. on p. 142).

Layer, Moritz, Johanna Senk, Simon Essink, Alexander van Meegen, Hannah Bos, and Moritz Helias (May 2022b). "NNMT: Mean-Field Based Analysis Tools for Neuronal Network Models." In: *Frontiers in Neuroinformatics* 16, p. 835657. ISSN: 1662-5196. DOI: 10.3389/fninf.2022.835657. (Visited on 06/21/2022) (cit. on pp. xiv, 124, 165, 190).

LeCun, Yann, Yoshua Bengio, and Geoffrey Hinton (May 2015). "Deep Learning." In: *Nature* 521.7553, pp. 436–444. ISSN: 0028-0836, 1476-4687. DOI: 10.1038/nature14539. (Visited on 04/04/2023) (cit. on p. 20).

Lecoq, Jérôme, Michael Oliver, Joshua H. Siegle, Natalia Orlova, Peter Ledochowitsch, and Christof Koch (Nov. 2021). "Removing Independent Noise in Systems Neuroscience Data Using DeepInterpolation." In: *Nature Methods* 18.11, pp. 1401–1408. ISSN: 1548-7091, 1548-7105.

DOI: 10.1038/s41592-021-01285-2. (Visited on 01/08/2023) (cit. on p. 164).

Ledergerber, Debora, Claudia Battistin, Jan Sigurd Blackstad, Richard J. Gardner, Menno P. Witter, May-Britt Moser, Yasser Roudi, and Edvard I. Moser (May 2021). "Task-Dependent Mixed Selectivity in the Subiculum." In: *Cell Reports* 35.8, p. 109175. ISSN: 22111247. DOI: 10.1016/j.celrep.2021.109175. (Visited on 08/25/2022) (cit. on pp. 77, 116).

Ledoux, E and N Brunel (2011). "Dynamics of networks of excitatory and inhibitory neurons in response to time-dependent inputs." In: *Front. Comput. Neurosci.* 5.25, pp. 1–17 (cit. on p. 154).

Lepage, Kyle Q., Christopher J. MacDonald, Howard Eichenbaum, and Uri T. Eden (Apr. 2012). "The Statistical Analysis of Partially Confounded Covariates Important to Neural Spiking." In: *Journal of Neuroscience Methods* 205.2, pp. 295–304. ISSN: 01650270. DOI: 10.1016/j.jneumeth.2011.12.021. (Visited on 11/23/2022) (cit. on p. 67).

Lewis, James W. and David C. Van Essen (Dec. 2000). "Corticocortical Connections of Visual, Sensorimotor, and Multimodal Processing Areas in the Parietal Lobe of the Macaque Monkey." In: *The Journal of Comparative Neurology* 428.1, pp. 112–137. ISSN: 0021-9967, 1096-9861. DOI: 10.1002/1096-9861(20001204)428:1<112::AID-CNE8>3.0.CO;2-9. (Visited on 03/15/2022) (cit. on p. 28).

Li, Chao-yi, Masafumi Tanaka, and O.D. Creutzfeldt (Sept. 1989). "Attention and Eye Movement Related Activation of Neurons in the Dorsal Prelunate Gyrus (Area DP)." In: *Brain Research* 496.1-2, pp. 307–313. ISSN: 00068993. DOI: 10.1016/0006-8993(89)91078-0. (Visited on 05/17/2022) (cit. on p. 29).

Li, Yuhui, Yong Wang, and He Cui (Mar. 2022). "Posterior Parietal Cortex Predicts Upcoming Movement in Dynamic Sensorimotor Control." In: *Proceedings of the National Academy of Sciences* 119.13, e2118903119. ISSN: 0027-8424, 1091-6490. DOI: 10.1073/pnas.2118903119. (Visited on 08/15/2022) (cit. on p. 28).

Lillicrap, Timothy P. and Stephen H. Scott (Jan. 2013). "Preference Distributions of Primary Motor Cortex Neurons Reflect Control Solutions Optimized for Limb Biomechanics." In: *Neuron* 77.1, pp. 168–179. ISSN: 08966273. DOI: 10.1016/j.neuron.2012.10.041. (Visited on 03/30/2022) (cit. on pp. 11, 66, 95, 110, 112, 115).

Lindner, Benjamin (2004). "Interspike interval statistics of neurons driven by colored noise." In: *Phys. Rev. E* 69, pp. 0229011–0229014 (cit. on p. 125).

Lindner, Benjamin, Brent Doiron, and André Longtin (Dec. 2005a). "Theory of oscillatory firing induced by spatially correlated noise and delayed inhibitory feedback." In: *Phys. Rev. E* 72.6, p. 061919. DOI: 10.1103/physreve.72.061919. URL: https://doi.org/10.1103/physreve.72.061919 (cit. on pp. 126, 192).

Lindner, Benjamin and Andre Longtin (2005b). “Effect of an exponentially decaying threshold on the firing statistis of a stochastic integate-and-fire neuron.” In: *J. Theor. Biol.* 232, pp. 505–521 (cit. on p. 126).

Lindner, Benjamin and Lutz Schimansky-Geier (Apr. 2001). “Transmission of noise coded versus additive signals through a neuronal ensemble.” In: *Phys. Rev. Lett.* 86, pp. 2934–2937. DOI: `10.1103/physrevlett.86.2934`. URL: `https://doi.org/10.1103/physrevlett.86.2934` (cit. on pp. 126, 131, 154).

Logothetis, Nikos K, O Eschenko, Y Murayama, M Augath, T Steudel, HC Evrard, M Besserve, and A Oeltermann (2012). “Hippocampal-cortical interaction during periods of subcortical silence.” In: *Nature* 491.7425, pp. 547–553 (cit. on p. 156).

Louis, Sebastien, Christian Borgelt, and Sonja Grün (2010). “Complexity distribution as a measure for assembly size and temporal precision.” In: *Neural Netw.* 23, pp. 705–712 (cit. on p. 46).

Luppino, G and G Rizzolatti (2000). “The Organization of the Frontal Motor Cortex.” In: *News Physiol Sci* 15.October, pp. 219–224. ISSN: 0886-1714. DOI: `10.1093/cercor/bhg093` (cit. on p. 26).

MacKay, W. A. (May 1992). “Properties of Reach-Related Neuronal Activity in Cortical Area 7A.” In: *Journal of Neurophysiology* 67.5, pp. 1335–1345. ISSN: 0022-3077, 1522-1598. DOI: `10.1152/jn.1992.67.5.1335`. (Visited on 08/16/2022) (cit. on p. 28).

Maguire, W. M. and J. S. Baizer (July 1984). “Visuotopic Organization of the Prelunate Gyrus in Rhesus Monkey.” In: *Journal of Neuroscience* 4.7, pp. 1690–1704. ISSN: 0270-6474, 1529-2401. DOI: `10.1523/JNEUROSCI.04-07-01690.1984`. (Visited on 09/17/2022) (cit. on p. 29).

Mante, Valerio, David Sussillo, Krishna V. Shenoy, and William T. Newsome (Nov. 2013). “Context-Dependent Computation by Recurrent Dynamics in Prefrontal Cortex.” In: *Nature* 503.7474, pp. 78–84. ISSN: 0028-0836, 1476-4687. DOI: `10.1038/nature12742`. (Visited on 11/15/2020) (cit. on p. 167).

Markov, N. T. et al. (Jan. 2014). “A Weighted and Directed Interareal Connectivity Matrix for Macaque Cerebral Cortex.” In: *Cerebral Cortex* 24.1, pp. 17–36. ISSN: 1460-2199, 1047-3211. DOI: `10.1093/cercor/bhs270`. (Visited on 10/07/2022) (cit. on pp. 123, 166).

Marr, David (1982). *Vision: A Computational Investigation into the Human Representation and Processing of Visual Information*. MIT press (cit. on p. 20).

Matelli, Massimo, Giuseppe Luppino, and Giacomo Rizzolatti (Nov. 1985). “Patterns of Cytochrome Oxidase Activity in the Frontal Agranular Cortex of the Macaque Monkey.” In: *Behavioural Brain Research* 18.2, pp. 125–136. ISSN: 01664328. DOI: `10.1016/0166-4328(85)90068-3`. (Visited on 04/04/2023) (cit. on p. 26).

Matsumoto, Narihisa, Masato Okada, Yasuko Sugase-Miyamoto, Shigeru Yamane, and Kenji Kawano (2005). “Population Dynamics of Face-Responsive Neurons in the Inferior Temporal Cortex.” In: *Cerebral Cortex* 15.8, pp. 1103–1112. ISSN: 10473211. DOI: `10.1093/cercor/bhh209` (cit. on p. 167).

Mattia, Maurizio, Matteo Biggio, Andrea Galluzzi, and Marco Storace (Oct. 2019). “Dimensional reduction in networks of non-Markovian spiking neurons: Equivalence of synaptic filtering and heterogeneous propagation delays.” In: *PLOS Comput. Biol.* 15.10. Ed. by Bard Ermentrout, e1007404. ISSN: 1553-7358. DOI: `10.1371/journal.pcbi.1007404`. URL: `https://dx.plos.org/10.1371/journal.pcbi.1007404` (visited on 04/12/2021) (cit. on pp. 125, 151).

May, J.G. and R.A. Andersen (July 1986). “Different Patterns of Corticopontine Projections from Separate Cortical Fields within the Inferior Parietal Lobule and Dorsal Prelunate Gyrus of the Macaque.” In: *Experimental Brain Research* 63.2. ISSN: 0014-4819, 1432-1106. DOI: `10.1007/BF00236844`. (Visited on 07/18/2022) (cit. on p. 29).

Mazor, Ofer and Gilles Laurent (2005). “Transient Dynamics versus Fixed Points in Odor Representations by Locust Antennal Lobe Projection Neurons.” In: *Neuron* 48.4, pp. 661–73. ISSN: 0896-6273. DOI: `10.1016/j.neuron.2005.09.032`. PMID: `16301181` (cit. on p. 167).

Mazzetti, Caterina, Alessandro Sarti, and Giovanna Citti (Aug. 2022). *Functional Architecture of M1 Cells Encoding Movement Direction*. arXiv: `arXiv:2208.03352`. (Visited on 11/04/2022) (cit. on p. 94).

McCullagh, P. and J. A. Nelder (1989a). *Generalized Linear Models*. Boston, MA: Springer US. ISBN: 978-0-412-31760-6 978-1-4899-3242-6. DOI: `10.1007/978-1-4899-3242-6`. (Visited on 11/24/2022) (cit. on p. 67).

– (1989b). *Generalized Linear Models*. 37th ed. Monographs on Statistics and Applied Probability. CRC Press (cit. on p. 68).

McDowell, Jennifer E., Kara A. Dyckman, Benjamin P. Austin, and Brett A. Clementz (Dec. 2008). “Neurophysiology and Neuroanatomy of Reflexive and Volitional Saccades: Evidence from Studies of Humans.” In: *Brain and Cognition* 68.3, pp. 255–270. ISSN: 02782626. DOI: `10.1016/j.bandc.2008.08.016`. (Visited on 10/07/2022) (cit. on p. 22).

McFarland, James M., Adrian G. Bondy, Richard C. Saunders, Bruce G. Cumming, and Daniel A. Butts (Nov. 2015). “Saccadic Modulation of Stimulus Processing in Primary Visual Cortex.” In: *Nature Communications* 6.1, p. 8110. ISSN: 2041-1723. DOI: `10.1038/ncomms9110`. (Visited on 12/14/2022) (cit. on p. 23).

McPeek, Robert M and Edward L Keller (July 2004). “Deficits in Saccade Target Selection after Inactivation of Superior Colliculus.” In: *Nature Neuroscience* 7.7, pp. 757–763. ISSN: 1097-6256, 1546-1726. DOI: `10.1038/nn1269`. (Visited on 01/15/2023) (cit. on p. 23).

Medathati, N. V. Kartheek, Heiko Neumann, Guillaume S. Masson, and Pierre Kornprobst (Sept. 2016). "Bio-Inspired Computer Vision: Towards a Synergistic Approach of Artificial and Biological Vision." In: *Computer Vision and Image Understanding* 150, p. 1. ISSN: 10773142. DOI: 10.1016/j.cviu.2016.04.009. (Visited on 12/18/2022) (cit. on pp. 20, 21).

Merchant, Hugo, Alexandra Battaglia-Mayer, and Apostolos P. Georgopoulos (Feb. 2004). "Neural Responses in Motor Cortex and Area 7a to Real and Apparent Motion." In: *Experimental Brain Research* 154.3, pp. 291–307. ISSN: 0014-4819, 1432-1106. DOI: 10.1007/s00221-003-1664-5. (Visited on 12/05/2022) (cit. on pp. 28, 29).

Mineault, Patrick J (Dec. 2011). *Denoising and Spike Detection in a Utah Array*. (Visited on 02/11/2023) (cit. on p. 53).

Montbrió, Ernest, Diego Pazó, and Alex Roxin (2015). "Macroscopic Description for Networks of Spiking Neurons." In: *Phys. Rev. X* 5 (2), p. 021028. DOI: 10.1103/PhysRevX.5.021028. URL: http://link.aps.org/doi/10.1103/PhysRevX.5.021028 (cit. on pp. 126, 192).

Morrison, Abigail, Sirko Straube, Hans Ekkehard Plesser, and Markus Diesmann (Jan. 2007). "Exact Subthreshold Integration with Continuous Spike Times in Discrete-Time Neural Network Simulations." In: *Neural Comput.* 19.1, pp. 47–79. DOI: 10.1162/neco.2007.19.1.47. URL: https://doi.org/10.1162/neco.2007.19.1.47 (cit. on pp. 143, 198).

Mountcastle, V. B., J. C. Lynch, A. Georgopoulos, H. Sakata, and C. Acuna (July 1975). "Posterior Parietal Association Cortex of the Monkey: Command Functions for Operations within Extrapersonal Space." In: *Journal of Neurophysiology* 38.4, pp. 871–908. ISSN: 0022-3077, 1522-1598. DOI: 10.1152/jn.1975.38.4.871. (Visited on 08/03/2022) (cit. on p. 27).

Mountcastle, Vernon B. (1997). "The columnar organization of the neocortex." In: *Brain* 120, pp. 701–722 (cit. on p. 8).

Mukherjee, Sayak, Daniel Perez-Rapela, Jason Forman, and Matthew B. Panzer (Sept. 2022). "Generating Human Arm Kinematics Using Reinforcement Learning to Train Active Muscle Behavior in Automotive Research." In: *Journal of Biomechanical Engineering*. ISSN: 0148-0731, 1528-8951. DOI: 10.1115/1.4055680. (Visited on 12/18/2022) (cit. on p. 112).

Mulliken, G. H., S. Musallam, and R. A. Andersen (June 2008). "Forward Estimation of Movement State in Posterior Parietal Cortex." In: *Proceedings of the National Academy of Sciences* 105.24, pp. 8170–8177. ISSN: 0027-8424, 1091-6490. DOI: 10.1073/pnas.0802602105. (Visited on 01/11/2022) (cit. on p. 91).

Musall, Simon, Matthew T. Kaufman, Ashley L. Juavinett, Steven Gluf, and Anne K. Churchland (Oct. 2019). "Single-Trial Neural Dynamics Are Dominated by Richly Varied Movements." In: *Nature*

Neuroscience 22.10, pp. 1677–1686. ISSN: 1097-6256, 1546-1726. DOI: `10.1038/s41593-019-0502-4`. (Visited on 09/12/2022) (cit. on pp. 65, 106, 113).

Nakamura, Kae and Carol L. Colby (Mar. 2002). "Updating of the Visual Representation in Monkey Striate and Extrastriate Cortex during Saccades." In: *Proceedings of the National Academy of Sciences* 99.6, pp. 4026–4031. ISSN: 0027-8424, 1091-6490. DOI: `10.1073/pnas.052379899`. (Visited on 09/08/2022) (cit. on p. 23).

Naselaris, Thomas, Hugo Merchant, Bagrat Amirikian, and Apostolos P. Georgopoulos (Dec. 2006). "Large-Scale Organization of Preferred Directions in the Motor Cortex. I. Motor Cortical Hyperacuity for Forward Reaching." In: *Journal of Neurophysiology* 96.6, pp. 3231–3236. ISSN: 0022-3077, 1522-1598. DOI: `10.1152/jn.00487.2006`. (Visited on 08/16/2022) (cit. on pp. 10, 112).

Niknam, Kaiser, Amir Akbarian, Kelsey Clark, Yasin Zamani, Behrad Noudoost, and Neda Nategh (Sept. 2019). "Characterizing and Dissociating Multiple Time-Varying Modulatory Computations Influencing Neuronal Activity." In: *PLOS Computational Biology* 15.9. Ed. by Brent Doiron, e1007275. ISSN: 1553-7358. DOI: `10.1371/journal.pcbi.1007275`. (Visited on 08/18/2022) (cit. on p. 24).

Niu, Meiqi (2022). "Architecture and Connectivity of the Human Angular Gyrus and of Its Homolog Region in the Macaque Brain." In: *Brain Structure and Function* (cit. on p. 27).

Niu, Meiqi, Lucija Rapan, Thomas Funck, Seán Froudist-Walsh, Ling Zhao, Karl Zilles, and Nicola Palomero-Gallagher (May 2021). "Organization of the Macaque Monkey Inferior Parietal Lobule Based on Multimodal Receptor Architectonics." In: *NeuroImage* 231, p. 117843. ISSN: 10538119. DOI: `10.1016/j.neuroimage.2021.117843`. (Visited on 07/15/2022) (cit. on pp. 27, 28).

Noel, Jean-Paul, Edoardo Balzani, Eric Avila, Kaushik Janakiraman Lakshminarasimhan, Stefania Bruni, Panos Alefantis, Cristina Savin, and Dora E Angelaki (Oct. 2022). "Coding of Latent Variables in Sensory, Parietal, and Frontal Cortices during Closed-Loop Virtual Navigation." In: *eLife* 11. Ed. by Kristine Krug, e80280. ISSN: 2050-084X. DOI: `10.7554/eLife.80280`. (Visited on 10/26/2022) (cit. on p. 65).

Nordhausen, Craig T, Edwin M Maynard, and Richard A Normann (1996). "Single Unit Recording Capabilities of a 100 Microelectrode Array." In: *Brain Research*, p. 12 (cit. on pp. 33, 177).

Numssen, Ole, Danilo Bzdok, and Gesa Hartwigsen (Mar. 2021). "Functional Specialization within the Inferior Parietal Lobes across Cognitive Domains." In: *eLife* 10, e63591. ISSN: 2050-084X. DOI: `10.7554/eLife.63591`. (Visited on 08/15/2022) (cit. on p. 27).

Okano, Hideyuki, Atsushi Miyawaki, and Kiyoto Kasai (May 2015). "Brain/MINDS: Brain-Mapping Project in Japan." In: *Philosophical Transactions of the Royal Society B: Biological Sciences* 370.1668,

p. 20140310. ISSN: 0962-8436, 1471-2970. DOI: 10.1098/rstb.2014.0310. (Visited on 04/05/2023) (cit. on p. 164).

Olver, F. W. J., A. B. Olde Daalhuis, D. W. Lozier, B. I. Schneider, R. F. Boisvert, C. W. Clark, B. R. Miller, B. V. Saunders, H. S. Cohl, and M. A. McClain (2021). *NIST Digital Library of Mathematical Functions*. http://dlmf.nist.gov/, Release 1.1.2 of 2021-06-15. URL: http://dlmf.nist.gov (cit. on p. 131).

Omrani, Mohsen, Matthew T. Kaufman, Nicholas G. Hatsopoulos, and Paul D. Cheney (Sept. 2017). "Perspectives on Classical Controversies about the Motor Cortex." In: *Journal of Neurophysiology* 118.3, pp. 1828–1848. ISSN: 0022-3077, 1522-1598. DOI: 10.1152/jn.00795.2016. (Visited on 08/11/2022) (cit. on p. 25).

Oppenheim, AV and AS Wilsky (1996). *Systems and signals*. Prentice Hall (cit. on p. 147).

Ostojic, Srdjan (Feb. 2014). "Two types of asynchronous activity in networks of excitatory and inhibitory spiking neurons." In: *Nat. Neurosci.* 17, pp. 594–600. DOI: 10.1038/nn.3658. URL: https://doi.org/10.1038/nn.3658 (cit. on p. 125).

Ostojic, Srdjan and Nicolas Brunel (2011). "From Spiking Neuron Models to Linear-Nonlinear Models." In: *PLOS Comput. Biol.* 7.1, e1001056 (cit. on p. 126).

Pandya, Deepak N. and Benjamin Seltzer (Jan. 1982). "Intrinsic Connections and Architectonics of Posterior Parietal Cortex in the Rhesus Monkey." In: *The Journal of Comparative Neurology* 204.2, pp. 196–210. ISSN: 0021-9967, 1096-9861. DOI: 10.1002/cne.902040208. (Visited on 07/18/2022) (cit. on p. 27).

Paninski, L. (Sept. 2004a). "Superlinear Population Encoding of Dynamic Hand Trajectory in Primary Motor Cortex." In: *Journal of Neuroscience* 24.39, pp. 8551–8561. ISSN: 0270-6474, 1529-2401. DOI: 10.1523/JNEUROSCI.0919-04.2004. (Visited on 11/25/2022) (cit. on p. 77).

Paninski, Liam (Jan. 2004b). "Maximum Likelihood Estimation of Cascade Point-Process Neural Encoding Models." In: *Network: Computation in Neural Systems* 15.4, pp. 243–262. ISSN: 0954-898X, 1361-6536. DOI: 10.1088/0954-898X_15_4_002. (Visited on 08/17/2022) (cit. on p. 70).

Paninski, Liam, Matthew R. Fellows, Nicholas G. Hatsopoulos, and John P. Donoghue (Jan. 2004). "Spatiotemporal Tuning of Motor Cortical Neurons for Hand Position and Velocity." In: *Journal of Neurophysiology* 91.1, pp. 515–532. ISSN: 0022-3077, 1522-1598. DOI: 10.1152/jn.00587.2002. (Visited on 01/11/2022) (cit. on pp. 87, 91, 94).

Paralikar, Kunal J., Chinmay R. Rao, and Ryan S. Clement (June 2009). "New Approaches to Eliminating Common-Noise Artifacts in Recordings from Intracortical Microelectrode Arrays: Inter-electrode Correlation and Virtual Referencing." In: *Journal of Neuroscience*

Methods 181.1, pp. 27–35. ISSN: 01650270. DOI: 10.1016/j.jneumeth.2009.04.014 (cit. on p. 164).

Patel, Paras R. et al. (Aug. 2022). *Utah Array Characterization and Histological Analysis of a Multi-Year Implant in Non-Human Primate Motor and Sensory Cortices*. Preprint. Bioengineering. DOI: 10.1101/2022.08.27.505114. (Visited on 12/08/2022) (cit. on p. 45).

Pernice, Volker, Benjamin Staude, Stefano Cardanobile, and Stefan Rotter (2011). "How Structure Determines Correlations in Neuronal Networks." In: *PLOS Comput. Biol.* 7.5, e1002059 (cit. on p. 192).

Pillow, J. W. (Nov. 2005). "Prediction and Decoding of Retinal Ganglion Cell Responses with a Probabilistic Spiking Model." In: *Journal of Neuroscience* 25.47, pp. 11003–11013. ISSN: 0270-6474, 1529-2401. DOI: 10.1523/JNEUROSCI.3305-05.2005. (Visited on 11/29/2022) (cit. on p. 87).

Potjans, Tobias C. and Markus Diesmann (Mar. 2014a). "The Cell-Type Specific Cortical Microcircuit: Relating Structure and Activity in a Full-Scale Spiking Network Model." In: *Cereb. Cortex* 24.3, pp. 785–806. DOI: 10.1093/cercor/bhs358. URL: https://doi.org/10.1093/cercor/bhs358 (cit. on pp. xx, 11, 122, 128–130, 140–142, 148).

– (2014b). "The Cell-Type Specific Cortical Microcircuit: Relating Structure and Activity in a Full-Scale Spiking Network Model." In: *Cerebral Cortex* 24.3, pp. 785–806. ISSN: 10473211. DOI: 10.1093/cercor/bhs358 (cit. on pp. xxii, 166, 167).

Purves, Dale, George J Augustine, David Fitzpatrick, Lawrence C Katz, Anthony-Samuel LaMantia, James O McNamara, and S. Mark Williams (2018). *Neuroscience*. Oxford University Press (cit. on pp. 3, 4).

Quiroga, R. Quian, Z. Nadasdy, and Y. Ben-Shaul (2004). "Unsupervised spike detection and sorting with wavelets and superparamagnetic clustering." In: *Neural Comput.* 16.8, pp. 1661–87 (cit. on p. 172).

Quraishi, S., B. Heider, and R. M. Siegel (Aug. 2007). "Attentional Modulation of Receptive Field Structure in Area 7a of the Behaving Monkey." In: *Cerebral Cortex* 17.8, pp. 1841–1857. ISSN: 1047-3211, 1460-2199. DOI: 10.1093/cercor/bhl093. (Visited on 12/15/2022) (cit. on p. 28).

Raffi, M. and Ralph M. Siegel (May 2005). "Functional Architecture of Spatial Attention in the Parietal Cortex of the Behaving Monkey." In: *Journal of Neuroscience* 25.21, pp. 5171–5186. ISSN: 0270-6474, 1529-2401. DOI: 10.1523/JNEUROSCI.5201-04.2005. (Visited on 12/15/2022) (cit. on p. 28).

Raffi, Milena and Ralph M. Siegel (Feb. 2007). "A Functional Architecture of Optic Flow in the Inferior Parietal Lobule of the Behaving Monkey." In: *PLoS ONE* 2.2. Ed. by Laurent Itti, e200. ISSN: 1932-6203. DOI: 10.1371/journal.pone.0000200. (Visited on 05/17/2022) (cit. on p. 28).

Rajan, K. and L. F. Abbott (2006). “Eigenvalue spectra of random matrices for neural networks.” In: *Phys. Rev. Lett.* 97, p. 188104 (cit. on p. 192).

Ramón y Cajal, Santiago (1888). “Estructura de los centros nerviosos de las aves.” In: *Rev. Trim. Histol. Norm. Pat.* 1, pp. 1–10 (cit. on pp. 1, 8).

Rapan, Lucija (2021). “Multimodal 3D Atlas of the Macaque Monkey Motor and Premotor Cortex.” In: (cit. on pp. 26, 28).

Rasmussen, Rune Nguyen, Antonis Asiminas, Eva Maria Meier Carlsen, Celia Kjaerby, and Nathan Anthony Smith (Mar. 2023). “Astrocytes: Integrators of Arousal State and Sensory Context.” In: *Trends in Neurosciences*, S0166223623000504. ISSN: 01662236. DOI: `10.1016/j.tins.2023.03.003`. (Visited on 04/03/2023) (cit. on p. 6).

Rathelot, Jean-Alban, Richard P. Dum, and Peter L. Strick (Apr. 2017). “Posterior Parietal Cortex Contains a Command Apparatus for Hand Movements.” In: *Proceedings of the National Academy of Sciences* 114.16, pp. 4255–4260. ISSN: 0027-8424, 1091-6490. DOI: `10.1073/pnas.1608132114`. (Visited on 12/19/2022) (cit. on p. 113).

Renart, Alfonso, Jaime De La Rocha, Peter Bartho, Liad Hollender, N’estor Parga, Alex Reyes, and Kenneth D. Harris (Jan. 2010). “The asynchronous State in Cortical Circuits.” In: *Science* 327, pp. 587–590. DOI: `10.1126/science.1179850`. URL: `https://doi.org/10.1126/science.1179850` (cit. on p. 126).

Rhodes, Oliver et al. (2018). “sPyNNaker: A Software Package for Running PyNN Simulations on SpiNNaker.” In: *Front. Neurosci.* 12. DOI: `10.3389/fnins.2018.00816`. URL: `https://doi.org/10.3389/fnins.2018.00816` (cit. on p. 168).

Richardson, Magnus J. E. (2007). “Firing-rate response of linear and nonlinear integrate-and-fire neurons to modulated current-based and conductance-based synaptic drive.” In: *Phys. Rev. E* 76.021919, pp. 1–15 (cit. on p. 126).

– (2008). “Spike-train spectra and network response functions for non-linear integrate-and-fire neurons.” In: *Biol. Cybern.* 99, pp. 381–392 (cit. on p. 126).

Riehle, Alexa, Sonja Grün, Markus Diesmann, and Ad Aertsen (1997). “Spike synchronization and rate modulation differentially involved in motor cortical function.” In: *Science* 278.5345, pp. 1950–1953. DOI: `10.1126/science.278.5345.1950` (cit. on p. 166).

Rigotti, Mattia, Omri Barak, Melissa R. Warden, Xiao-Jing Wang, Nathaniel D. Daw, Earl K. Miller, and Stefano Fusi (May 2013). “The Importance of Mixed Selectivity in Complex Cognitive Tasks.” In: *Nature* 497.7451, pp. 585–590. ISSN: 0028-0836, 1476-4687. DOI: `10.1038/nature12160`. (Visited on 09/16/2022) (cit. on pp. 27, 116).

Rizzolatti (Aug. 1994). “Space and Selective Attention.” In: DOI: `10.7551/mitpress/1478.003.0016`. (Visited on 08/03/2022) (cit. on p. 28).

Rizzolatti, Giacomo, Luigi Cattaneo, Maddalena Fabbri-Destro, and Stefano Rozzi (Apr. 2014). "Cortical Mechanisms Underlying the Organization of Goal-Directed Actions and Mirror Neuron-Based Action Understanding." In: *Physiological Reviews* 94.2, pp. 655–706. ISSN: 0031-9333, 1522-1210. DOI: `10.1152/physrev.00009.2013`. (Visited on 08/03/2022) (cit. on pp. 26, 28).

Rizzolatti, Giacomo and Laila Craighero (July 2004). "THE MIRROR-NEURON SYSTEM." In: *Annual Review of Neuroscience* 27.1, pp. 169–192. ISSN: 0147-006X, 1545-4126. DOI: `10.1146/annurev.neuro.27.070203.144230`. (Visited on 12/17/2022) (cit. on p. 28).

Rizzolatti, Giacomo, Luciano Fadiga, Vittorio Gallese, and Leonardo Fogassi (Mar. 1996). "Premotor Cortex and the Recognition of Motor Actions." In: *Cognitive Brain Research* 3.2, pp. 131–141. ISSN: 09266410. DOI: `10.1016/0926-6410(95)00038-0`. (Visited on 12/20/2022) (cit. on p. 28).

Rockland, Kathleen S. (Jan. 2022). "Notes on Visual Cortical Feedback and Feedforward Connections." In: *Frontiers in Systems Neuroscience* 16, p. 784310. ISSN: 1662-5137. DOI: `10.3389/fnsys.2022.784310`. (Visited on 12/13/2022) (cit. on p. 20).

Rockland, Kathleen S. and Deepak N. Pandya (Dec. 1979). "Laminar Origins and Terminations of Cortical Connections of the Occipital Lobe in the Rhesus Monkey." In: *Brain Research* 179.1, pp. 3–20. ISSN: 00068993. DOI: `10.1016/0006-8993(79)90485-2`. (Visited on 12/20/2022) (cit. on p. 20).

Rosenbaum, Robert and Brent Doiron (2014). "Balanced Networks of Spiking Neurons with Spatially Dependent Recurrent Connections." In: *Phys. Rev. X* 4.2, p. 021039. DOI: `10.1103/PhysRevX.4.021039`. URL: `https://doi.org/10.1103/physrevx.4.021039` (cit. on p. 126).

Rosenbaum, Robert, Mathew A. Smith, Adam Kohn, Jonathan E. Rubin, and Brent Doiron (Oct. 2017). "The spatial structure of correlated neuronal variability." In: *Nat. Neurosci.* 20.1, pp. 107–114. DOI: `10.1038/nn.4433`. URL: `https://doi.org/10.1038/nn.4433` (cit. on p. 126).

Rozzi, Stefano, Roberta Calzavara, Abdelouahed Belmalih, Elena Borra, Georgia G. Gregoriou, Massimo Matelli, and Giuseppe Luppino (Oct. 2006). "Cortical Connections of the Inferior Parietal Cortical Convexity of the Macaque Monkey." In: *Cerebral Cortex* 16.10, pp. 1389–1417. ISSN: 1460-2199, 1047-3211. DOI: `10.1093/cercor/bhj076`. (Visited on 12/15/2022) (cit. on p. 28).

Rozzi, Stefano, Pier Francesco Ferrari, Luca Bonini, Giacomo Rizzolatti, and Leonardo Fogassi (Oct. 2008). "Functional Organization of Inferior Parietal Lobule Convexity in the Macaque Monkey: Electrophysiological Characterization of Motor, Sensory and Mirror Responses and Their Correlation with Cytoarchitectonic Areas." In: *European Journal of Neuroscience* 28.8, pp. 1569–1588. ISSN: 0953816X, 14609568. DOI: 10.1111/j.1460-9568.2008.06395.x. (Visited on 07/15/2022) (cit. on pp. 28, 29).

Rushmore, R. Jarrett, Sylvain Bouix, Marek Kubicki, Yogesh Rathi, Douglas L. Rosene, Edward H. Yeterian, and Nikos Makris (June 2021). "MRI-based Parcellation and Morphometry of the Individual Rhesus Monkey Brain: The Macaque Harvard-Oxford Atlas (mHOA), a Translational System Referencing a Standardized Ontology." In: *Brain Imaging and Behavior* 15.3, pp. 1589–1621. ISSN: 1931-7557, 1931-7565. DOI: 10.1007/s11682-020-00357-9. (Visited on 08/26/2022) (cit. on p. 19).

Russo, Abigail A. et al. (Feb. 2018). "Motor Cortex Embeds Muscle-like Commands in an Untangled Population Response." In: *Neuron* 97.4, 953–966.e8. ISSN: 08966273. DOI: 10.1016/j.neuron.2018.01.004. (Visited on 08/11/2022) (cit. on p. 167).

Sanz Leon, Paula, Stuart Knock, M. Woodman, Lia Domide, Jochen Mersmann, Anthony McIntosh, and Viktor Jirsa (2013). "The Virtual Brain: a simulator of primate brain network dynamics." In: *Front. Neuroinform.* 7, p. 10. DOI: 10.3389/fninf.2013.00010. URL: https://doi.org/10.3389/fninf.2013.00010 (cit. on p. 191).

Sanzeni, Alessandro, Mark H Histed, and Nicolas Brunel (2020). "Response nonlinearities in networks of spiking neurons." In: *PLOS Comput. Biol.* 16.9, e1008165 (cit. on pp. 124, 126, 127).

Saxena, Shreya, Abigail A Russo, John Cunningham, and Mark M Churchland (May 2022). "Motor Cortex Activity across Movement Speeds Is Predicted by Network-Level Strategies for Generating Muscle Activity." In: *eLife* 11, e67620. ISSN: 2050-084X. DOI: 10.7554/eLife.67620. (Visited on 06/17/2022) (cit. on p. 167).

Schmidt, Maximilian, Rembrandt Bakker, Claus C. Hilgetag, Markus Diesmann, and Sacha J. van Albada (Apr. 2018a). "Multi-scale account of the network structure of macaque visual cortex." In: *Brain Struct. Funct.* 223.3, pp. 1409–1435. ISSN: 1863-2661. DOI: 10.1007/s00429-017-1554-4. URL: https://doi.org/10.1007/s00429-017-1554-4 (cit. on p. 123).

Schmidt, Maximilian, Rembrandt Bakker, Claus C. Hilgetag, Markus Diesmann, and Sacha J. van Albada (Apr. 2018b). "Multi-Scale Account of the Network Structure of Macaque Visual Cortex." In: *Brain Structure and Function* 223.3, pp. 1409–1435. ISSN: 1863-2653, 1863-2661. DOI: 10.1007/s00429-017-1554-4. (Visited on 12/11/2022) (cit. on pp. 123, 163, 166, 167).

Schmidt, Maximilian, Rembrandt Bakker, Kelly Shen, Gleb Bezgin, Markus Diesmann, and Sacha Jennifer van Albada (2018c). "A multi-scale layer-resolved spiking network model of resting-state dynamics in macaque visual cortical areas." In: *PLOS Comput. Biol.* 14.10, e1006359. DOI: 10.1371/journal.pcbi.1006359. URL: https://doi.org/10.1371/journal.pcbi.1006359 (cit. on pp. 141, 148, 149).

Schmolesky, Matthew T., Youngchang Wang, Doug P. Hanes, Kirk G. Thompson, Stefan Leutgeb, Jeffrey D. Schall, and Audie G. Leventhal (June 1998). “Signal Timing Across the Macaque Visual System.” In: *Journal of Neurophysiology* 79.6, pp. 3272–3278. ISSN: 0022-3077, 1522-1598. DOI: `10.1152/jn.1998.79.6.3272`. (Visited on 12/05/2022) (cit. on p. 78).

Schuecker, Jannis, Markus Diesmann, and Moritz Helias (2014). “Reduction of colored noise in excitable systems to white noise and dynamic boundary conditions.” In: *ArXiv*, p. 1410.8799. URL: `https://arxiv.org/abs/1410.8799` (cit. on pp. 131, 199).

– (Nov. 2015). “Modulated escape from a metastable state driven by colored noise.” In: *Phys. Rev. E* 92 (5), p. 052119. DOI: `10.1103/PhysRevE.92.052119`. URL: `https://doi.org/10.1103/physreve.92.052119` (cit. on pp. 124, 125, 131, 132, 146, 152–154).

Schuecker, Jannis, Sven Goedeke, and Moritz Helias (2018). “Optimal Sequence Memory in Driven Random Networks.” In: *Phys. Rev. X* 8 (4), p. 041029. DOI: `10.1103/PhysRevX.8.041029`. URL: `https://link.aps.org/doi/10.1103/PhysRevX.8.041029` (cit. on p. 126).

Schumacher, Pierre, Daniel Häufle, Dieter Büchler, and Syn Schmitt (n.d.). “DEP-RL: Embodied Exploration for Reinforcement Learning in Overactuated and Musculoskeletal Systems.” In: () (cit. on p. 112).

Schwalger, Tilo, Moritz Deger, and Wulfram Gerstner (2017). “Towards a theory of cortical columns: From spiking neurons to interacting neural populations of finite size.” In: *PLOS Comput. Biol.* 13.4, e1005507. DOI: `10.1371/journal.pcbi.1005507`. URL: `https://doi.org/10.1371/journal.pcbi.1005507` (cit. on p. 192).

Schwalger, Tilo, Felix Droste, and Benjamin Lindner (2015). “Statistical structure of neural spiking under non-Poissonian or other non-white stimulation.” In: *J. Comput. Neurosci.* 39, p. 29 (cit. on p. 125).

Schwartz, Ab, Re Kettner, and Ap Georgopoulos (Aug. 1988). “Primate Motor Cortex and Free Arm Movements to Visual Targets in Three-Dimensional Space. I. Relations between Single Cell Discharge and Direction of Movement.” In: *The Journal of Neuroscience* 8.8, pp. 2913–2927. ISSN: 0270-6474, 1529-2401. DOI: `10.1523/JNEUROSCI.08-08-02913.1988`. (Visited on 04/04/2023) (cit. on pp. 10, 66).

Schwartz, Andrew B. (1994). “Direct cortical representation of drawing.” In: *Science* 265.5171, pp. 540–542 (cit. on p. 25).

Scott, S.H., P.L. Gribble, K.M. Graham, and D.W. Cabel (2001a). “Dissociation between hand motion and population vectors from neural activity in motor cortex.” In: *Nature* 413.6852, pp. 161–165 (cit. on p. 79).

Scott, Stephen H., Paul L. Gribble, Kirsten M. Graham, and D. William Cabel (Sept. 2001b). “Dissociation between Hand Motion and Population Vectors from Neural Activity in Motor Cortex.” In: *Nature* 413.6852, pp. 161–165. ISSN: 0028-0836, 1476-4687. DOI: `10.1038/`

35093102. (Visited on 04/05/2022) (cit. on pp. 10, 66, 95, 97, 110, 112).

Scott, Stephen H. and John F. Kalaska (Feb. 1997). "Reaching Movements With Similar Hand Paths But Different Arm Orientations. I. Activity of Individual Cells in Motor Cortex." In: *Journal of Neurophysiology* 77.2, pp. 826–852. ISSN: 0022-3077, 1522-1598. DOI: 10.1152/jn.1997.77.2.826. (Visited on 09/01/2022) (cit. on pp. 10, 66).

Sejnowski, TJ (1976). "On the stochastic dynamics of neuronal interaction." In: *Biol. Cybern.* 22.4, pp. 203–211 (cit. on p. 126).

Senk, Johanna, Espen Hagen, Sacha van Albada, and Markus Diesmann (2018a). *A Mesoscopic Layered Cortical Network Model for Spiking Activity and Local Field Potentials* (cit. on p. 167).

Senk, Johanna, Karolína Korvasová, Jannis Schuecker, Espen Hagen, Tom Tetzlaff, Markus Diesmann, and Moritz Helias (2018b). "Conditions for Traveling Waves in Spiking Neural Networks." In: pp. 1–42. arXiv: 1801.06046 (cit. on p. 167).

Senk, Johanna, Karolína Korvasová, Jannis Schuecker, Espen Hagen, Tom Tetzlaff, Markus Diesmann, and Moritz Helias (May 2020). "Conditions for wave trains in spiking neural networks." In: *Phys. Rev. Res.* 2.2. DOI: 10.1103/physrevresearch.2.023174. URL: https://doi.org/10.1103/physrevresearch.2.023174 (cit. on p. 126).

Senk, Johanna, Birgit Kriener, Mikael Djurfeldt, Nicole Voges, Han-Jia Jiang, Lisa Schüttler, Gabriele Gramelsberger, Markus Diesmann, Hans E. Plesser, and Sacha J. van Albada (2021). "Connectivity Concepts in Neuronal Network Modeling." In: *ArXiv*, 2110.02883 [q–bio.NC] (cit. on pp. 129, 130).

– (2022). "Connectivity Concepts in Neuronal Network Modeling." In: *PLOS Comput. Biol.* 18.9, e1010086. DOI: 10.1371/journal.pcbi.1010086 (cit. on p. 142).

Sergio, Lauren E., Catherine Hamel-Pâquet, and John F. Kalaska (Oct. 2005). "Motor Cortex Neural Correlates of Output Kinematics and Kinetics During Isometric-Force and Arm-Reaching Tasks." In: *Journal of Neurophysiology* 94.4, pp. 2353–2378. ISSN: 0022-3077, 1522-1598. DOI: 10.1152/jn.00989.2004. (Visited on 08/16/2022) (cit. on p. 25).

Shadlen, Michael N. and William T. Newsome (1994). "Noise, neural codes and cortical organization." In: *Curr. Opin. Neurobiol.* 4.4, pp. 569–579 (cit. on p. 8).

Sherfey, Jason S, Austin E Soplata, Salva Ardid, Erik A Roberts, David A Stanley, Benjamin R Pittman-Polletta, and Nancy J Kopell (2018). "DynaSim: a MATLAB toolbox for neural modeling and simulation." In: *Front. Neuroinform.* 12, p. 10 (cit. on p. 191).

Shimoura, Renan Oliveira, Rodrigo F. O. Pena, Vinicius Lima, Nilton L. Kamiji, Mauricio Girardi-Schappo, and Antonio C. Roque (June 2021). "Building a model of the brain: from detailed connectivity maps to network organization." In: *Eur. Phys. J. Spec. Top.* 230.14-15, pp. 2887–2909. DOI: 10.1140/epjs/s11734-021-00152-7. URL:

https://doi.org/10.1140/epjs/s11734-021-00152-7 (cit. on p. 11).

Siegel, Ralph M., Milena Raffi, Raymond E. Phinney, Jessica A. Turner, and Gábor Jandó (Aug. 2003). "Functional Architecture of Eye Position Gain Fields in Visual Association Cortex of Behaving Monkey." In: *Journal of Neurophysiology* 90.2, pp. 1279–1294. ISSN: 0022-3077, 1522-1598. DOI: 10.1152/jn.01179.2002. (Visited on 08/26/2022) (cit. on p. 28).

Siegert, Arnold J.F. (1951). "On the first passage time probability problem." In: *Phys. Rev.* 81.4, pp. 617–623 (cit. on p. 127).

Soechting, J F and M Flanders (1992). "Moving in Three-Dimensional Space: Frames of Reference, Vectors, and Coordinate Systems." In: p. 25 (cit. on p. 29).

Sommer, Marc A. and Edward J. Tehovnik (Sept. 1997). "Reversible Inactivation of Macaque Frontal Eye Field:" in: *Experimental Brain Research* 116.2, pp. 229–249. ISSN: 0014-4819. DOI: 10.1007/PL00005752. (Visited on 01/15/2023) (cit. on p. 23).

Sommer, Marc A. and Robert H. Wurtz (May 2002). "A Pathway in Primate Brain for Internal Monitoring of Movements." In: *Science* 296.5572, pp. 1480–1482. ISSN: 0036-8075, 1095-9203. DOI: 10.1126/science.1069590. (Visited on 12/14/2022) (cit. on p. 23).

Sompolinsky, H., A. Crisanti, and H. J. Sommers (1988). "Chaos in Random Neural Networks." In: *Phys. Rev. Lett.* 61 (3), pp. 259–262. DOI: 10.1103/PhysRevLett.61.259. URL: http://link.aps.org/doi/10.1103/PhysRevLett.61.259 (cit. on p. 126).

Sponheim, Caleb, Vasileios Papadourakis, Jennifer L Collinger, John Downey, Jeffrey Weiss, Lida Pentousi, Kaisa Elliott, and Nicholas G. Hatsopoulos (Dec. 2021). "Longevity and Reliability of Chronic Unit Recordings Using the Utah, Intracortical Multi-Electrode Arrays." In: *Journal of Neural Engineering* 18.6, p. 066044. ISSN: 1741-2560, 1741-2552. DOI: 10.1088/1741-2552/ac3eaf. (Visited on 12/08/2022) (cit. on p. 45).

Sprenger, Julia (2014). "Spatial Dependence of the Spike-Related Component of the Local Field Potential in Motor Cortex." PhD thesis (cit. on pp. 49, 56).

– (2020). "Tools and Workflows for Data & Metadata Management of Complex Experiments : Building a Foundation for Reproducible & Collaborative Analysis in the Neurosciences." PhD thesis (cit. on p. 164).

Sridhar, Shashwat (2020). "Evaluation of Automatic Spike Sorting Algorithms: Reproducible Workflows for Comparison with Ground Truth and Surrogate Data." PhD thesis (cit. on p. 176).

Steinmetz, M A, C E Connor, C Constantinidis, and J R McLaughlin (1994). "Covert Attention Suppresses Neuronal Responses in Area 7a of the Posterior Parietal Cortex." In: p. 4 (cit. on p. 28).

Stella, Alessandra, Pietro Quaglio, Emiliano Torre, and Sonja Grün (2019). "3d-SPADE: Significance Evaluation of Spatio-Temporal Patterns of Various Temporal Extents." In: *BioSystems* 185, p. 104022. ISSN: 0303-2647. DOI: `10.1016/j.biosystems.2019.104022`. URL: `https://juser.fz-juelich.de/record/864994` (cit. on p. 166).

Stepniewska, Iwona, Christine E. Collins, and Jon H. Kaas (June 2005). "Reappraisal of DL/V4 Boundaries Based on Connectivity Patterns of Dorsolateral Visual Cortex in Macaques." In: *Cerebral Cortex* 15.6, pp. 809–822. ISSN: 1460-2199, 1047-3211. DOI: `10.1093/cercor/bhh182`. (Visited on 08/15/2022) (cit. on p. 28).

Stevenson, Ian H. (Dec. 2018). "Omitted Variable Bias in GLMs of Neural Spiking Activity." In: *Neural Computation* 30.12, pp. 3227–3258. ISSN: 0899-7667, 1530-888X. DOI: `10.1162/neco_a_01138`. (Visited on 11/17/2022) (cit. on pp. 71, 115).

Stevenson, Ian H. et al. (Nov. 2012). "Functional Connectivity and Tuning Curves in Populations of Simultaneously Recorded Neurons." In: *PLoS Computational Biology* 8.11. Ed. by Tim Behrens, e1002775. ISSN: 1553-7358. DOI: `10.1371/journal.pcbi.1002775`. (Visited on 11/25/2022) (cit. on p. 115).

Stiller, JC and G Radons (1998). "Dynamics of nonlinear oscillators with random interactions." In: *Phys. Rev. E* 58.2, p. 1789 (cit. on p. 126).

Stimberg, Marcel, Romain Brette, and Dan FM Goodman (Aug. 2019). "Brian 2, an intuitive and efficient neural simulator." In: *eLife* 8. DOI: `10.7554/elife.47314`. URL: `https://doi.org/10.7554/elife.47314` (cit. on p. 191).

Stricanne, B., R. A. Andersen, and P. Mazzoni (Sept. 1996). "Eye-Centered, Head-Centered, and Intermediate Coding of Remembered Sound Locations in Area LIP." In: *Journal of Neurophysiology* 76.3, pp. 2071–2076. ISSN: 0022-3077, 1522-1598. DOI: `10.1152/jn.1996.76.3.2071`. (Visited on 08/03/2022) (cit. on p. 30).

Strick, Peter L., Richard P. Dum, and Jean-Alban Rathelot (July 2021). "The Cortical Motor Areas and the Emergence of Motor Skills: A Neuroanatomical Perspective." In: *Annual Review of Neuroscience* 44.1, pp. 425–447. ISSN: 0147-006X, 1545-4126. DOI: `10.1146/annurev-neuro-070918-050216`. (Visited on 08/03/2022) (cit. on pp. 26, 65, 113).

Stringer, Carsen, Marius Pachitariu, Nicholas Steinmetz, Matteo Carandini, and Kenneth D Harris (2019a). "High-dimensional geometry of population responses in visual cortex." In: *Nature* 571.7765, pp. 361–365 (cit. on p. 65).

Stringer, Carsen, Marius Pachitariu, Nicholas Steinmetz, Charu Bai Reddy, Matteo Carandini, and Kenneth D Harris (2019b). "Spontaneous Behaviors Drive Multidimensional, Brainwide Activity." In: *Science (New York, N.Y.)* 364.6437, p. 255. ISSN: 1095-9203. DOI: `10.1126/science.aav7893`. PMID: `31000656` (cit. on p. 106).

Suminski, Aaron J., Philip Mardoum, Timothy P. Lillicrap, and Nicholas G. Hatsopoulos (Apr. 2015). "Temporal Evolution of Both Premotor and Motor Cortical Tuning Properties Reflect Changes in Limb Biomechanics." In: *Journal of Neurophysiology* 113.7, pp. 2812–2823. ISSN: 0022-3077, 1522-1598. DOI: `10.1152/jn.00486.2014`. (Visited on 08/11/2022) (cit. on pp. 11, 66, 95, 97, 110).

Sun, Linus D. and Michael E. Goldberg (Oct. 2016). "Corollary Discharge and Oculomotor Proprioception: Cortical Mechanisms for Spatially Accurate Vision." In: *Annual Review of Vision Science* 2.1, pp. 61–84. ISSN: 2374-4642, 2374-4650. DOI: `10.1146/annurev-vision-082114-035407`. (Visited on 07/18/2022) (cit. on p. 23).

Suner, S., M.R. Fellows, C. Vargas-Irwin, G.K. Nakata, and J.P. Donoghue (Dec. 2005). "Reliability of Signals from a Chronically Implanted, Silicon-Based Electrode Array in Non-Human Primate Primary Motor Cortex." In: *IEEE Transactions on Neural Systems and Rehabilitation Engineering* 13.4, pp. 524–541. ISSN: 1534-4320, 1558-0210. DOI: `10.1109/TNSRE.2005.857687`. (Visited on 12/11/2022) (cit. on p. 177).

Sunkin, Susan M, Lydia Ng, Chris Lau, Tim Dolbeare, Terri L Gilbert, Carol L Thompson, Michael Hawrylycz, and Chinh Dang (2012). "Allen Brain Atlas: an integrated spatio-temporal portal for exploring the central nervous system." In: *Nucleic Acids Res.* 41.D1, pp. D996–D1008 (cit. on p. 6).

Sussillo, David and Omri Barak (2013). "Opening the Black Box: Low-Dimensional Dynamics in High-Dimensional Recurrent Neural Networks." In: *Neural Comput.* 25.3, pp. 626–649 (cit. on p. 167).

Suway, S B, J Orellana, A J C McMorland, G W Fraser, Z Liu, M Velliste, S M Chase, R E Kass, and A B Schwartz (July 2018). "Temporally Segmented Directionality in the Motor Cortex." In: *Cerebral Cortex* 28.7, pp. 2326–2339. ISSN: 1047-3211, 1460-2199. DOI: `10.1093/cercor/bhx133`. (Visited on 08/11/2022) (cit. on pp. 94, 116).

Talluri, Bharath C., Incheol Kang, Adam Lazere, Katrina R. Quinn, Nicholas Kaliss, Jacob L. Yates, Daniel A. Butts, and Hendrikje Nienborg (Sept. 2022). *Activity in Primate Visual Cortex Is Minimally Driven by Spontaneous Movements*. Preprint. Neuroscience. DOI: `10.1101/2022.09.08.507006`. (Visited on 10/22/2022) (cit. on pp. 65, 106, 113, 117).

Tetzlaff, Tom, Moritz Helias, Gaute T. Einevoll, and Markus Diesmann (2012). "Decorrelation of Neural-Network Activity by Inhibitory Feedback." In: *PLOS Comput. Biol.* 8.8. Ed. by Nicolas Brunel, e1002596. DOI: `10.1371/journal.pcbi.1002596`. URL: `https://doi.org/10.1371/journal.pcbi.1002596` (cit. on pp. 126, 143).

Thiele, A., P. Henning, M. Kubischik, and K.-P. Hoffmann (Mar. 2002). "Neural Mechanisms of Saccadic Suppression." In: *Science* 295.5564, pp. 2460–2462. ISSN: 0036-8075, 1095-9203. DOI: 10.1126/science.1068788. (Visited on 12/14/2022) (cit. on p. 24).

Tibshirani, Robert (1996). "Regression Shrinkage and Selection via the Lasso." In: *Journal of the Royal Statistical Society. Series B (Methodological)* 58.1, pp. 267–288. ISSN: 0035-9246. JSTOR: 2346178. (Visited on 03/13/2023) (cit. on p. 71).

Todorov, Emanuel (2003). "On the Role of Primary Motor Cortex in Arm Movement Control." In: *Progress in motor control III* 6, pp. 125–166 (cit. on p. 25).

Todorov, Emanuel, Tom Erez, and Yuval Tassa (Oct. 2012). "MuJoCo: A Physics Engine for Model-Based Control." In: *2012 IEEE/RSJ International Conference on Intelligent Robots and Systems*. Vilamoura-Algarve, Portugal: IEEE, pp. 5026–5033. ISBN: 978-1-4673-1736-8 978-1-4673-1737-5 978-1-4673-1735-1. DOI: 10.1109/IROS.2012.6386109. (Visited on 12/19/2022) (cit. on p. 112).

Torre, Emiliano, Pietro Quaglio, Michael Denker, Thomas Brochier, Alexa Riehle, and Sonja Grün (2016). "Synchronous spike patterns in macaque motor cortex during an instructed-delay reach-to-grasp task." In: *J. Neurosci.* 36.32, pp. 8329–8340. DOI: 10.1523/jneurosci.4375-15.2016 (cit. on pp. 8, 47, 60).

Toyoizumi, Taro and Larry F Abbott (2011). "Beyond the edge of chaos: Amplification and temporal integration by recurrent networks in the chaotic regime." In: *Phys. Rev. E* 84.5, p. 051908 (cit. on p. 126).

Traub, Roger D., John G. R. Jefferys, and Miles A. Whittington (1997). "Simulation of gamma rhythms in networks of interneurons and pyramidal cells." en. In: *J. Comput. Neurosci.* 4.2, pp. 141–150. ISSN: 0929-5313, 1573-6873. DOI: 10.1023/A:1008839312043. (Visited on 08/21/2015) (cit. on p. 139).

Trautmann, Eric M. et al. (June 2019). "Accurate Estimation of Neural Population Dynamics without Spike Sorting." In: *Neuron* 103.2, 292–308.e4. ISSN: 10974199. DOI: 10.1016/j.neuron.2019.05.003 (cit. on p. 166).

Tremblay, Sébastien, Camille Testard, Ron W. DiTullio, Jeanne Inchauspé, and Michael Petrides (Sept. 2022). *Neural Cognitive Signals during Spontaneous Movements in the Macaque*. Preprint. Neuroscience. DOI: 10.1101/2022.09.05.506681. (Visited on 09/12/2022) (cit. on p. 113).

Trousdale, J, Y Hu, E Shea-Brown, and K Josic (2012). "Impact of network structure and cellular response on spike time correlations." In: *PLOS Comput. Biol.* 8.3, e1002408 (cit. on pp. 126, 192).

Truccolo, Wilson, Uri T. Eden, Matthew R. Fellows, John P. Donoghue, and Emery N. Brown (Feb. 2005). "A Point Process Framework for Relating Neural Spiking Activity to Spiking History, Neural Ensemble, and Extrinsic Covariate Effects." In: *Journal of Neurophysiology* 93.2, pp. 1074–1089. ISSN: 0022-3077, 1522-1598. DOI: 10.1152/jn.00697.2004. (Visited on 08/17/2022) (cit. on p. 67).

Tuckwell, Henry C. (1988). *Introduction to Theoretical Neurobiology*. Vol. 2. Cambridge: Cambridge University Press (cit. on p. 127).

Tukey, John W. (1977). *Exploratory data analysis*. Addison-Wesley (cit. on p. 142).

Umeno, Marc M. and Michael E. Goldberg (Sept. 1997). "Spatial Processing in the Monkey Frontal Eye Field. I. Predictive Visual Responses." In: *Journal of Neurophysiology* 78.3, pp. 1373–1383. ISSN: 0022-3077, 1522-1598. DOI: `10.1152/jn.1997.78.3.1373`. (Visited on 12/14/2022) (cit. on p. 23).

Ungerleider, L. G. and M. Mishkin (1982). "Two cortical visual systems." In: *Analysis of Visual Behavior*. Ed. by David J. Ingle, Melvyn A. Goodale, and Richard J. W. Mansfield. The MIT Press, pp. 549–586 (cit. on pp. 18, 65).

Urai, Anne E., Brent Doiron, Andrew M. Leifer, and Anne K. Churchland (Jan. 2022). "Large-Scale Neural Recordings Call for New Insights to Link Brain and Behavior." In: *Nature Neuroscience* 25.1, pp. 11–19. ISSN: 1097-6256, 1546-1726. DOI: `10.1038/s41593-021-00980-9`. (Visited on 08/23/2022) (cit. on p. 113).

Vaccari, Francesco Edoardo, Stefano Diomedi, Matteo Filippini, Claudio Galletti, and Patrizia Fattori (June 2021). "A Poisson Generalized Linear Model Application to Disentangle the Effects of Various Parameters on Neurophysiological Discharges." In: *STAR Protocols* 2.2, p. 100413. ISSN: 26661667. DOI: `10.1016/j.xpro.2021.100413`. (Visited on 01/11/2022) (cit. on pp. 67, 74, 77, 79, 103, 104, 116).

Van Albada, Sacha J., Andrew G. Rowley, Johanna Senk, Michael Hopkins, Maximilian Schmidt, Alan B. Stokes, David R. Lester, Markus Diesmann, and Steve B. Furber (May 2018). "Performance Comparison of the Digital Neuromorphic Hardware SpiNNaker and the Neural Network Simulation Software NEST for a Full-Scale Cortical Microcircuit Model." In: *Front. Neurosci.* 12, p. 291. DOI: `10.3389/fnins.2018.00291`. URL: `https://doi.org/10.3389/fnins.2018.00291` (cit. on p. 123).

Van Albada, Sacha Jennifer, Moritz Helias, and Markus Diesmann (2015). "Scalability of Asynchronous Networks Is Limited by One-to-One Mapping between Effective Connectivity and Correlations." In: *PLOS Comput. Biol.* 11.9. Ed. by Peter E. Latham, e1004490. DOI: `10.1371/journal.pcbi.1004490`. URL: `https://doi.org/10.1371/journal.pcbi.1004490` (cit. on pp. 140, 148).

Van Meegen, Alexander and Benjamin Lindner (2018). "Self-Consistent Correlations of Randomly Coupled Rotators in the Asynchronous State." In: *Phys. Rev. Lett.* 121.25, p. 258302. DOI: `10.1103/PhysRevLett.121.258302` (cit. on p. 126).

Van Vreeswijk, C. and H. Sompolinsky (1998). "Chaotic Balanced State in a Model of Cortical Circuits." In: *Neural Comput.* 10.6, pp. 1321–1371. DOI: `10.1162/089976698300017214`. URL: `https://doi.org/10.1162/089976698300017214` (cit. on pp. 11, 125–127).

Van Vreeswijk, Carl and Haim Sompolinsky (Dec. 1996). “Chaos in Neuronal Networks with Balanced Excitatory and Inhibitory Activity.” In: *Science* 274, pp. 1724–1726. DOI: `10.1126/science.274.5293.1724`. URL: `https://doi.org/10.1126/science.274.5293.1724` (cit. on pp. 11, 121, 125–127).

Verduzco-Flores, Sergio Oscar and Erik De Schutter (Nov. 2022). “Self-Configuring Feedback Loops for Sensorimotor Control.” In: *eLife* 11, e77216. ISSN: 2050-084X. DOI: `10.7554/eLife.77216`. (Visited on 11/24/2022) (cit. on pp. 11, 66, 95, 97, 110, 112).

Vogt, Cécile and Oskar Vogt (1919). *Allgemeine Ergebnisse unserer Hirnforschung*. J.A. Barth (cit. on p. 27).

Von Bonin, Gerhardt and Percival Bailey (1947). *The Neocortex of Macaca Mulatta*. Illinois. Urbana: Univ. of Illinois Press (cit. on p. 27).

Vyas, Saurabh, Matthew D. Golub, David Sussillo, and Krishna V. Shenoy (July 2020). “Computation Through Neural Population Dynamics.” In: *Annual Review of Neuroscience* 43.1, pp. 249–275. ISSN: 0147-006X, 1545-4126. DOI: `10.1146/annurev-neuro-092619-094115`. (Visited on 07/16/2020) (cit. on pp. 26, 167).

Wagatsuma, Nobuhiko, Tobias C. Potjans, Markus Diesmann, and Tomoki Fukai (2011). “Layer-dependent attentional processing by top-down signals in a visual cortical microcircuit model.” In: *Front. Comput. Neurosci.* 5, p. 31. DOI: `10.3389/fncom.2011.00031`. URL: `https://doi.org/10.3389/fncom.2011.00031` (cit. on p. 123).

Walker, M. F., E. J. Fitzgibbon, and M. E. Goldberg (May 1995). “Neurons in the Monkey Superior Colliculus Predict the Visual Result of Impending Saccadic Eye Movements.” In: *Journal of Neurophysiology* 73.5, pp. 1988–2003. ISSN: 0022-3077, 1522-1598. DOI: `10.1152/jn.1995.73.5.1988`. (Visited on 12/14/2022) (cit. on p. 23).

Wang, Huawei, Vittorio Caggiano, Guillaume Durandau, Massimo Sartori, and Vikash Kumar (May 2022a). “MyoSim: Fast and Physiologically Realistic MuJoCo Models for Musculoskeletal and Exoskeletal Studies.” In: *2022 International Conference on Robotics and Automation (ICRA)*. Philadelphia, PA, USA: IEEE, pp. 8104–8111. ISBN: 978-1-72819-681-7. DOI: `10.1109/ICRA46639.2022.9811684`. (Visited on 12/18/2022) (cit. on p. 112).

Wang, Mingli et al. (Apr. 2022b). *Retinotopic Organization of Feedback Projections in Primate Early Visual Cortex: Implications for Active Vision*. Preprint. Neuroscience. DOI: `10.1101/2022.04.27.489651`. (Visited on 12/20/2022) (cit. on pp. 20, 28, 29, 65, 166).

Wang, Tianwei, Yun Chen, and He Cui (July 2022c). “From Parametric Representation to Dynamical System: Shifting Views of the Motor Cortex in Motor Control.” In: *Neuroscience Bulletin* 38.7, pp. 796–808. ISSN: 1673-7067, 1995-8218. DOI: `10.1007/s12264-022-00832-x`. (Visited on 11/15/2022) (cit. on p. 26).

Wells-Gray, E M, S S Choi, A Bries, and N Doble (Aug. 2016). “Variation in Rod and Cone Density from the Fovea to the Mid-Periphery in

Healthy Human Retinas Using Adaptive Optics Scanning Laser Ophthalmoscopy." In: *Eye* 30.8, pp. 1135–1143. ISSN: 0950-222X, 1476-5454. DOI: `10.1038/eye.2016.107`. (Visited on 01/04/2023) (cit. on p. 19).

Williams, Alex H., Tony Hyun Kim, Forea Wang, Saurabh Vyas, Stephen I. Ryu, Krishna V. Shenoy, Mark Schnitzer, Tamara G. Kolda, and Surya Ganguli (June 2018). "Unsupervised Discovery of Demixed, Low-Dimensional Neural Dynamics across Multiple Timescales through Tensor Component Analysis." In: *Neuron* 98.6, 1099–1115.e8. ISSN: 08966273. DOI: `10.1016/j.neuron.2018.05.015` (cit. on p. 167).

Williamson, Ryan C, Brent Doiron, Matthew A Smith, and Byron M Yu (2018). "Bridging Large-Scale Neuronal Recordings and Large-Scale Network Models Using Dimensionality Reduction." In: *Peer Preprints* 55, pp. 1–14. ISSN: 09594388. DOI: `10.7287/peerj.preprints.27340v1` (cit. on p. 167).

Woeppel, Kevin, Christopher Hughes, Angelica J. Herrera, James R. Eles, Elizabeth C. Tyler-Kabara, Robert A. Gaunt, Jennifer L. Collinger, and Xinyan Tracy Cui (Dec. 2021). "Explant Analysis of Utah Electrode Arrays Implanted in Human Cortex for Brain-Computer-Interfaces." In: *Frontiers in Bioengineering and Biotechnology* 9, p. 759711. ISSN: 2296-4185. DOI: `10.3389/fbioe.2021.759711`. (Visited on 10/07/2022) (cit. on p. 45).

Wurtz, Robert H. (Sept. 2015). "Using Perturbations to Identify the Brain Circuits Underlying Active Vision." In: *Philosophical Transactions of the Royal Society B: Biological Sciences* 370.1677, p. 20140205. ISSN: 0962-8436, 1471-2970. DOI: `10.1098/rstb.2014.0205`. (Visited on 12/17/2022) (cit. on p. 22).

Yael, Dorin, Jacob J. Vecht, and Izhar Bar-Gad (2018). "Filter-Based Phase Shifts Distort Neuronal Timing Information." In: *eNeuro* 5.2, pp. 1–8. ISSN: 23732822. DOI: `10.1523/ENEURO.0261-17.2018` (cit. on p. 39).

Yokoyama, Chihiro, Joonas A. Autio, Takuro Ikeda, Jérôme Sallet, Rogier B. Mars, David C. Van Essen, Matthew F. Glasser, Norihiro Sadato, and Takuya Hayashi (Dec. 2021). "Comparative Connectomics of the Primate Social Brain." In: *NeuroImage* 245, p. 118693. ISSN: 10538119. DOI: `10.1016/j.neuroimage.2021.118693`. (Visited on 12/15/2022) (cit. on p. 28).

Yoonessi, Ali and Ahmad Yoonessi (2011). "Functional Assessment of Magno, Parvo and Konio-Cellular Pathways; Current State and Future Clinical Applications." In: *JOURNAL OF OPHTHALMIC AND VISION RESEARCH* 6.2 (cit. on p. 20).

Yu, Byron M., John P. Cunningham, Gopal Santhanam, Stephen I. Ryu, Krishna V. Shenoy, and Maneesh Sahani (July 2009). "Gaussian-Process Factor Analysis for Low-Dimensional Single-Trial Analysis of Neural Population Activity." In: *Journal of Neurophysiology* 102.1, pp. 614–635. ISSN: 0022-3077. DOI: 10.1152/jn.90941.2008. arXiv: 1011.1669v3 (cit. on p. 167).

Zanos, T. P., P. J. Mineault, D. Guitton, and C. C. Pack (Aug. 2016). "Mechanisms of Saccadic Suppression in Primate Cortical Area V4." In: *Journal of Neuroscience* 36.35, pp. 9227–9239. ISSN: 0270-6474, 1529-2401. DOI: 10.1523/JNEUROSCI.1015-16.2016. (Visited on 04/15/2022) (cit. on p. 23).

Zanos, Theodoros P., Patrick J. Mineault, and Christopher C. Pack (Jan. 2011). "Removal of Spurious Correlations Between Spikes and Local Field Potentials." en. In: *J. Neurophysiol.* 105.1, pp. 474–486. ISSN: 0022-3077, 1522-1598. DOI: 10.1152/jn.00642.2010. URL: https://www.physiology.org/doi/10.1152/jn.00642.2010 (visited on 04/07/2021) (cit. on p. 145).

Zehl, Lyuba, Florent Jaillet, Adrian Stoewer, Jan Grewe, Andrey Sobolev, Thomas Wachtler, Thomas G. Brochier, Alexa Riehle, Michael Denker, and Sonja Grün (July 2016). "Handling Metadata in a Neurophysiology Laboratory." In: *Front. Neuroinform.* 10, p. 26. DOI: 10.3389/fninf.2016.00026. URL: https://doi.org/10.3389/fninf.2016.00026 (cit. on p. 164).

Zhang, Carey Y., Tyson Aflalo, Boris Revechkis, Emily R. Rosario, Debra Ouellette, Nader Pouratian, and Richard A. Andersen (Aug. 2017). "Partially Mixed Selectivity in Human Posterior Parietal Association Cortex." In: *Neuron* 95.3, 697–708.e4. ISSN: 08966273. DOI: 10.1016/j.neuron.2017.06.040. (Visited on 08/08/2022) (cit. on p. 27).

Zhaoping, Li (July 2014). *Understanding Vision: Theory, Models, and Data*. Illustrated edition. Oxford, United Kingdom ; New York, NY, United States of America: Oxford University Press. ISBN: 978-0-19-956466-8 (cit. on p. 23).

Zipser, David and Richard A. Andersen (Feb. 1988). "A Back-Propagation Programmed Network That Simulates Response Properties of a Subset of Posterior Parietal Neurons." In: *Nature* 331.6158, pp. 679–684. ISSN: 0028-0836, 1476-4687. DOI: 10.1038/331679a0. (Visited on 08/03/2022) (cit. on p. 30).

Zou, Hui and Trevor Hastie (2005). "Regularization and Variable Selection via the Elastic Net." In: *Journal of the Royal Statistical Society. Series B (Statistical Methodology)* 67.2, pp. 301–320. ISSN: 1369-7412. JSTOR: 3647580. (Visited on 03/13/2023) (cit. on p. 71).

de Haan, Marcel Jan, Thomas Brochier, Sonja Grün, Alexa Riehle, and Frédéric V. Barthélemy (2018). "Real-Time Visuomotor Behavior and Electrophysiology Recording Setup for Use with Humans and Monkeys." In: *Journal of Neurophysiology* 120.2, pp. 539–552. ISSN: 0022-3077. DOI: 10.1152/jn.00262.2017 (cit. on p. 164).